Universiteit Antwerpen

First-Principles Studies of Novel Two-Dimensional Materials and Their Physical Properties

---

First-Principles Studies van Nieuwe Tweedimensionale Materialen en hun Fysische Eigenschappen

Proefschrift voorgelegd tot het behalen van de graad van doctor in de wetenschappen aan de Universiteit Antwerpen te verdedigen door

Yierpan Aierken

Supervisors: Prof. Dr. François M. Peeters
Dr. Ortwin Leenaerts
Dr. Deniz Çakır

Departement Fysica, Universiteit Antwerpen

Antwerpen, België Oktober 2017

Members of the Jury:

Chairman

Prof. Dr. Dirk Lamoen, Universiteit Antwerpen, Belgium

Supervisors

Prof. Dr. François Peeters, Universiteit Antwerpen, Belgium

Dr. Ortwin Leenaerts, Universiteit Antwerpen, Belgium

Dr. Deniz Çakır, University of North Dakota, USA

Members

Prof. Dr. Sandra Van Aert, Universiteit Antwerpen, Belgium

Prof. Dr. Michel Houssa, Katholieke Universiteit Leuven, Belgium

Contact Information:

Yierpan Aierken
G.U. 212
Groenenborgerlaan 171
2020 Antwerpen
Belgium
yierpan.aierken@uantwerpen.be

Reseach Units:

NANO Centre of Excellence nano

CMT Condensed Matter Theory University of Antwerp

Funding Agency:

fwo Fonds Wetenschappelijk Onderzoek Vlaanderen
Opening new horizons

I would like to dedicate this thesis

to my loving parents Arkin and Perwin,

to my belored wife Adila,

to my cherished sons Efran and Wildan.

Acknowledgements

I would like to express my utmost gratitude to Professor Francois Peeters for giving me the opportunity to work in the condensed matter theory (CMT) group at the University of Antwerp. I truly appreciate both his academical and financial support during my PhD study, without which this thesis would not have been completed. I would like to thank Dr. Ortwin Leenaerts and Dr. Deniz Çakır for their guidance in various of the practical aspects of this work. I have learned a lot from their expertise in the field of first-principles calculations. I would also like to thank all the professors, students and administrative staff in the CMT group for their help in every possible way during my PhD study. Finally, I would like to thank my family for being supportive all the time.

Abstract

This thesis is a collection of works aimed at exploring the physical properties of novel two-dimensional (2D) materials using advanced first-principles calculations in the framework of density functional theory (DFT). 2D materials have an atomic thickness. Because of this reduction of the dimensions, quantum confinement effects will have an important influence on the properties of the material. The field of 2D materials is expanding with the continued introduction of new members and the new phenomena they bring. DFT is a powerful tool that can be used to investigate these exciting materials and their properties.

By performing advanced DFT calculations, this thesis proposes several new 2D materials. These materials are stable and have distinct properties as compared to their bulk form. The discovery of new 2D materials involves separating known layered materials in their bulk form into monolayers or rationally designing materials with tailored properties at the atomic level. Full characterizations are given to introduce these new materials to the 2D materials community.

In addition to the basic properties of these materials that can be obtained by a single step DFT calculation, this thesis increases the level of the characterization by introducing additional approximations on top of the DFT calculations. This usually requires several calculations to be done under different conditions, e.g. mechanical strains, to find the relation between these results. By doing so, the properties related to more dynamical processes of the materials can be understood.

This thesis also introduces several effective ways to modify the determined properties. Questions like "What is the effect of the interlayer interaction for a few-layer system?" and "How a particular material responds to the application of strain?" are answered throughout the thesis.

Table of contents

List of figures

List of tables

List of abbreviations

2D	two-dimensional
3D	three-dimensional
AEMHs	alkaline earth metal hydroxides
CBM	conduction band minimum
cNEB	climbing-image nudge elastic band
CVD	Chemical vapor deposition
DFPT	density functional perturbation theory
DOS	density of states
DPC	deformation potential constant
EP	electrostatic potential
GGA	generalized gradient approximation
HF	Hartree-Fock
HSE	Heyd-Scuseria-Ernzerhof
LDA	local density approximation
MAE	mean absolute error
NEGF	non-equilibrium Green's functions
PAW	projected-augemeted wave

pDOS partial density of states

PES potential energy surface

PNT phosphorene nanotubes

QHA quasi-harmonic approximation

SOC spin-orbit coupling

TEC thermal expansion coefficients

TMDs Transition metal dichalcogenides

VASP Vienna *Ab initio* Simulation Package

VBM valence band maximum

vdW van der Waals

Chapter 1

Computational methods

Theories behind the calculations are the core component in the theoretical determination of material properties. Its correctness, accuracy and implementation directly influence the quality of its predictions. In this chapter, I will introduce relevant theoretical models, approximations and their implementations in commonly used software packages.

1.1 Theory

1.1.1 Density Functional Theory

Density functional theory (DFT) is one of the most widely used quantum mechanical methods to calculate the properties of materials. Its applicable length and time scales are in nanometre and picoseconds, respectively. These scales are longer than that for quantum Monte Carlo simulations but lower than that for semi- or full-empirical methods. This is also true in the accuracy verse size-of-the-system plot in Fig. 1.1. In this figure, four types of popular computational methods are compared. They each have a total number of atoms that they can handle and a typical magnitude of error can be expected in the total energy of the system under study. For these methods, generally, the more atoms one method can compute, the larger the error it contains. However, this dose not affect to make some qualitative conclusions or study the property of the system at a larger length scale. However, the accuracy of the different methods can be higher than what is shown in the figure, this is because a large part of the error can also be

attributed to uncertainties of the experimental results with which these methods are compared[1]. As I will discuss further, if a DFT method is compared with a highly accurate theoretical benchmark method, DFT will have typically a precision around 1 meV/atom. Particularly, for bulk or nanostructures, DFT can be therefore used to even quantitatively predict the properties of materials. Since DFT is based on the Hohenberg-Kohn theorems[2] and Kohn-Sham equations[3], I will briefly give an overview of them without putting too much stress on their derivations which have been extensively documented in textbooks.

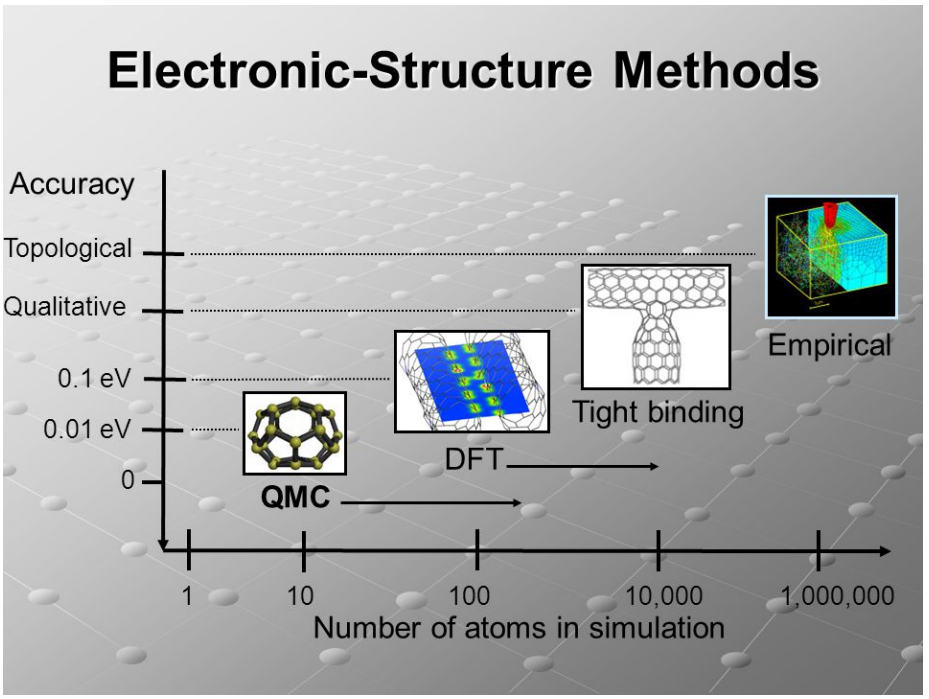

Fig. 1.1 Comparison of the accuracy and the size of different electronic structure calculation methods. Image source: Ref. [4]

Materials are made from atoms that contain electrons and nuclei. The type of nuclei and the interactions between these give rise to various materials and their properties. The interactions are mainly electrostatic or Coulombic. While electrons must be described with quantum mechanics, the nuclei can be treated as classical particles. The equation governing the electron behaviour is the Schrödinger

equation. It can be written as follows:[1]

$$\begin{aligned}
&\hat{H}\,\Psi_\alpha(\vec{r_1}\sigma_1,\ldots,\vec{r_N}\sigma_N) \\
&\quad= \left[-\frac{1}{2}\sum_{i=1}^{N}\nabla_i^2+\sum_{i=1}^{N}\upsilon(\vec{r_i})+\frac{1}{2}\sum_{i=1}\sum_{j\neq i}\frac{1}{|\vec{r_i}-\vec{r_j}|}\right]\Psi_\alpha(\vec{r_1}\sigma_1,\ldots,\vec{r_N}\sigma_N) \\
&\quad= \left(\hat{T}+\hat{V}_{ext}+\hat{V}_{ee}\right)\Psi_\alpha(\vec{r_1}\sigma_1,\ldots,\vec{r_N}\sigma_N) \\
&\quad= E_\alpha\,\Psi_\alpha(\vec{r_1}\sigma_1,\ldots,\vec{r_N}\sigma_N).
\end{aligned} \tag{1.1}$$

In the above equation, $\hat{H}$ is the total Hamiltonian, $\hat{T}$ is the kinetic energy, $\hat{V}_{ext}$ is the interaction between electrons and nuclei. Here we already started with the first approximation: Born–Oppenheimer approximation[5]. This approximation neglects the dynamics of nuclei, thus electrons are considered moving in a static potential generated by their interaction with all nuclei. $\hat{V}_{ee}$ is the Coulomb interaction between electrons. The first two terms sum over all N electrons, and the last one sums over all pairs of N electrons. $\vec{r}$ is the electron position, and σ is the z-component of the electron spin (+$\frac{1}{2}$,-$\frac{1}{2}$). Ψ is the N-electron wave function, which should be antisymmetric under the interchange of the orbital and the spin coordinates of two electrons (i.e. fermionic character of electrons) and it should also satisfy the boundary condition of the system (e.g. quantum confinement in a low-dimensional system). E is the total energy, and α is the complete set of N-electron quantum numbers.

Following the constrained search algorithm introduced by M. Levy[6], the ground-state energy E can be found by minimizing the expectation value of the total Hamiltonian with respect to the wave function:

$$E=\min_{\Psi}\left\langle\Psi\right|\hat{H}\left|\Psi\right\rangle. \tag{1.2}$$

Here we take two steps for the minimization. For the first step, we minimize with respect to all wave functions that give the same density $n(\vec{r})$:

$$E=\min_{\Psi\to n}\left\langle\Psi\right|\hat{T}+\hat{V}_{ee}\left|\Psi\right\rangle+\int dr^3\upsilon(\vec{r})n(\vec{r}). \tag{1.3}$$

[1]Equations in this chapter are written using atomic units: fundamental constants $\hbar$, e and m_e are set to unity.

Then with the resulting wave function Ψ_n^{min} that yields the minimum energy E, an overall electron density $n(\vec{r})$ is associated. We can construct the universal functional $F[n(\vec{r})]$:

$$\min_{\Psi \to n} \langle \Psi | \hat{T} + \hat{V}_{ee} | \Psi \rangle = \langle \Psi_n^{min} | \hat{T} + \hat{V}_{ee} | \Psi_n^{min} \rangle = F[n(\vec{r})]. \tag{1.4}$$

For the second step, we minimize with respect to the density $n(\vec{r})$:

$$E = \min_n \left\{ F[n(\vec{r})] + \int d r^3 v(\vec{r}) n(\vec{r}) \right\}, \tag{1.5}$$

where $v(\vec{r})$ is kept fixed during the minimization. The resulting density is the ground-state density that gives the ground state energy. This is known as the density variational principle, which is also the main idea of the Hohenberg-Kohn theorems. For completeness I present the theorems below:

Theorem 1 *The external potential, $V_{ext}(\vec{r})$, of any system of interacting particles is uniquely determined (up to a constant) by the particle density, $n_0(\vec{r})$, of the ground state.*

Theorem 2 *The ground state energy of a system with an external potential $V_{ext}(\vec{r})$ is given by the minimum value of the energy functional $E_{HK}[n]$ and the density for which this minimum is reached corresponds with the ground state density $n_0(\vec{r})$.*

Now, the main problem is to find an approximate expression for $F[n(\vec{r})]$. The Kohn-Sham equation is an elegant way to do this. It aims to construct a non-interacting system where the kinetic energy can be calculated exactly, and a local external potential $V_{KS}(\vec{r})$ is added. The functional $F[n]$ decomposes into the following, where $E_{XC}[n]$ is the exchange-correlation (XC) energy:

$$F[n] = T_s[n] + E_H[n] + E_{XC}[n], \tag{1.6}$$

where $T_s[n]$ is the non-interacting kinetic energy functional, and $E_H[n]$ is the Hartree energy functional:

$$E_H[n] = \frac{1}{2} \int d^3 r \int d^3 r' \frac{n(\vec{r}) n(\vec{r'})}{|\vec{r} - \vec{r'}|}. \tag{1.7}$$

Apart from the last term, $E_{XC}[n]$, everything else can be calculated exactly for a non-interacting system for given density. By imposing a normalisation constraint on the electron density, $\int n(\vec{r})d\vec{r} = N$, we have

$$\frac{\delta F[n]}{\delta n(\vec{r})} = -v(\vec{r}). \tag{1.8}$$

Therefore, the effective local potential $V_{KS}(\vec{r})$ will be

$$V_{KS}(\vec{r}) = v(\vec{r}) + \frac{\delta E_H[n]}{\delta n(\vec{r})} + \frac{\delta E_{XC}[n]}{\delta n(\vec{r})}, \tag{1.9}$$

and the Kohn-Sham equation reads

$$\left[-\frac{1}{2}\nabla_i^2 + v(\vec{r}) + \frac{\delta E_H[n]}{\delta n(\vec{r})} + \frac{\delta E_{XC}[n]}{\delta n(\vec{r})}\right]\psi_\alpha(\vec{r}\sigma) = \varepsilon_\alpha\psi_\alpha(\vec{r}\sigma), \tag{1.10}$$

with ground-state electron density given by

$$n(\vec{r}) = \sum_{\alpha}^{occ.}\sum_{\sigma}|\psi_\alpha(\vec{r}\sigma)|^2. \tag{1.11}$$

These set of equations can be solved self-consistently. An initial guess of the density $n(\vec{r})$ determines the effective potential $V_{KS}(\vec{r})$, then the wave functions $\psi_\alpha(\vec{r}\sigma)$ can be calculated from equation (1.10), a new density is calculated through equation (1.11). This procedure is repeated until self-consistency is reached.

1.1.2 Exchange-correlation functional

The XC energy functional is not known exactly and therefore needs to be approximated. The choice of it directly influences the accuracy of the results. This is because, although it is often a small fraction of the total energy, its contribution to the chemical bonding and the formation energy is relatively important. For the XC approximation, the generalized gradient approximation (GGA) has become popular in solid state calculations. It is a further upgrade of its previous version, the local density approximation (LDA). The LDA has the following form:

$$E_{XC}^{LDA}[n] = \int n(\vec{r})\epsilon_{XC}[n(\vec{r})]d\vec{r}. \tag{1.12}$$

$\epsilon_{XC}[n(\vec{r})]$ is the XC energy for an homogeneous electron gas having density n, and it is usually taken from quantum Monte Carlo calculations. The GGA further includes the derivative of the density, $\nabla n(\vec{r})$, as an argument for ϵ_{XC}, thus it reads

$$E_{XC}^{GGA}[n] = \int \epsilon_{XC}[n(\vec{r}), \nabla n(\vec{r})] d\vec{r}. \tag{1.13}$$

In contrast to LDA, there is no unique input for $\epsilon_{XC}[n(\vec{r}), \nabla n(\vec{r})]$. Different constructions for GGA usually named after the corresponding authors, e.g. PW91-GGA stands for Perdew and Wang's GGA construction in 1991[7, 8] and PBE-GGA stands for Perdew et al. [9]'s construction. They are the most popular GGA approximations for solid state systems.

Jacob's ladder

Jacob's ladder is a ladder connecting earth and heaven that biblical Patriarch Jacob dreamed about. Professor John P. Perdew, who is known for his profound contributions to DFT and XC functionals, used it analogously to describe the hierarchy of density functional approximations in terms of their accuracies[10], see Fig. 1.2. Each rung is a level of approximation constructed with different formalisms. From LDA and GGA as mentioned before to meta-GGA which includes the Kohn-Sham kinetic energy density. The next method up the ladder is the hybrid functionals which incorporate a part of the exact exchange from Hartree-Fock (HF) theory and result in Heyd-Scuseria-Ernzerhof (HSE) functionals. For example, the PBE0 functional[12] has the following definition:

$$E_{XC}^{PBE0} = \frac{1}{4} E_X^{HF} + \frac{3}{4} E_X^{PBE} + E_C^{PBE}. \tag{1.14}$$

The HSE06[13] takes into account the screened Coulomb potential for the exact part:

$$E_{XC}^{HSE} = \beta E_X^{HF,SR}(\omega) + (1-\beta) E_X^{PBE,SR}(\omega) + E_X^{PBE,LR}(\omega) + E_C^{PBE}, \tag{1.15}$$

where β is the mixing parameter and ω is the parameter to control the screening range which defines the short-range, SR, and long-range, LR, parts. The values $\beta = 1/4$ and $\omega = 0.2$ are typically used in the HSE06 functional which turns out to give accurate band gaps and lattice constants, see the mean absolute

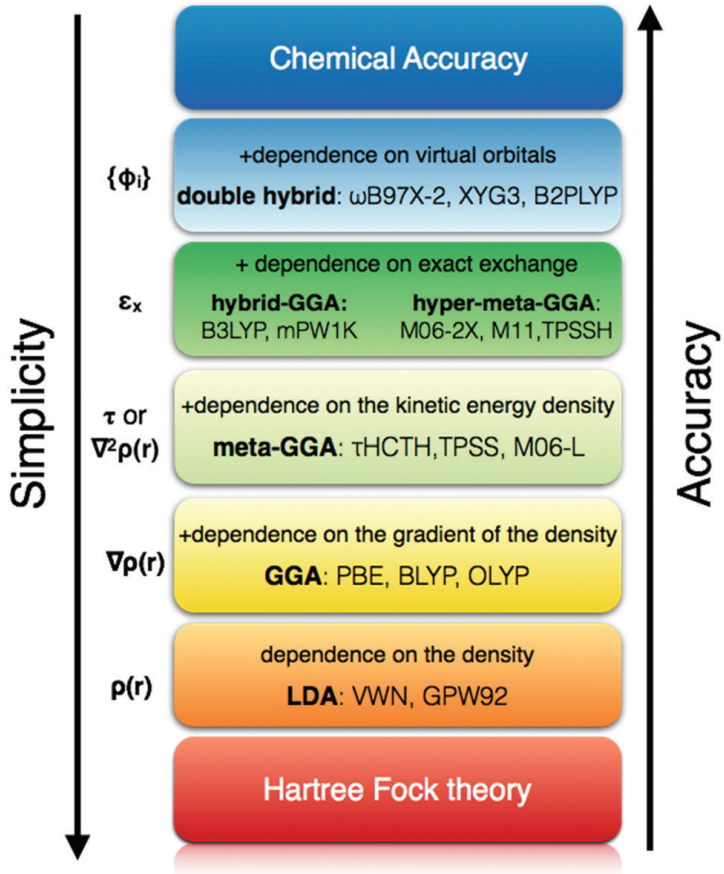

Fig. 1.2 Jacob's ladder for DFT approximations. Image source: Ref. [11]

error (MAE) of different functionals in Fig. 1.3. The highest ranked funcional is the double hybrid which includes the unoccupied orbitals as well, e.g. Random Phase Approximation[15].

Band gap problem

As shown in Fig. 1.3, band gaps estimated in LDA and GGA are quite poor. This can be attributed to the highly non-analytical and non-local behaviour of the XC energy functional. To understand this, let's look at the definition of the band gap E_g:

$$E_g = I - A = \varepsilon_{N+1}^{KS,HOMO} - \varepsilon_N^{KS,HOMO}, \tag{1.16}$$

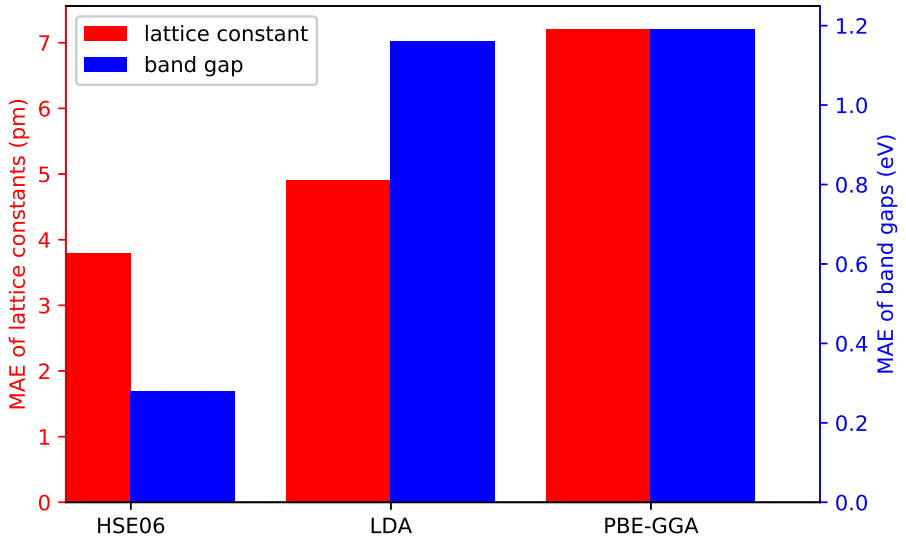

Fig. 1.3 MAE of the equilibrium lattice constants and band gaps of different functionals on SC40 solid test set[1]. Data source: [14]

where I is the ionization energy, which is the energy change by removing one valence electron. A is the electron affinity, which is the energy change by adding one electron to a neutral system. ε_N^{KS} is the Kohn-Sham orbital energy for N-electron system. $HOMO$ and $LUMO$ stand for the highest and the lowest occupied molecular orbital, respectively. For a non-interacting Kohn-Sham system, E_g^{KS} can be calculated as follows:

$$E_g^{KS} = \varepsilon_N^{KS,LUMO} - \varepsilon_N^{KS,HOMO}. \tag{1.17}$$

This leads to

$$E_g = E_g^{KS} + \Delta_{XC}, \tag{1.18}$$

where Δ_{XC} is the orbital shift caused by adding an extra electron: $\varepsilon_{N+1}^{KS,HOMO} - \varepsilon_N^{KS,LUMO}$. The Δ_{XC} exclusively depends on the non-analyticity of the XC potential $\frac{\delta E_{XC}[n]}{\delta n(\vec{r})}$, since the Hartree potential explicitly depends on the density. In other words, it means the energy increase by adding an extra electron in the extended system is of the order of 1 eV, even though, it is an infinitesimal density change. If

[1]The SC40 test set is a collection of 40 elementary and binary solid compounds of various structures having a wide range of band gaps.

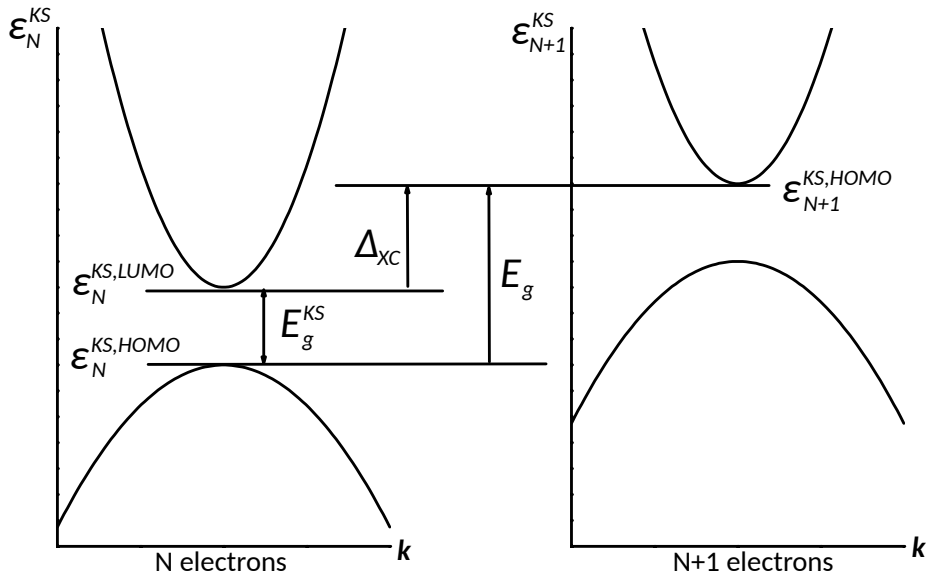

Fig. 1.4 Schematic illustration of the relation between E_g and E_g^{KS}. Image is adapted from Ref. [16].

the XC energy functional were analytic, the infinitesimal density variation would not introduce a large potential change, hence Δ_{XC} is small or equals to zero, and $E_g \approx E_g^{KS}$. The accuracy of the band gap, when compared to experiment, would be only limited by the error that is inherent to the different functionals. However, Δ_{XC} usually is not zero and it is responsible for the 80% of the LDA band gap error[17].

1.2 Implementation

The implementations of the above theory are crucial and not straightforward. Many of the quantities are represented with technically easy-implemented functions, and they have to be finite in size or quantity. A question will rise on how large the size or the resolution has to be. This is equivalent to the computational convergence. Here we review two of the most important convergence parameters: number of **k** points and cut-off energy of the basis set.

k points

According to Bloch's theorem, the solution of the Schrödinger equation for a periodic system, e.g. a crystal with a well-defined unit cell, can be expressed as follows:

$$\phi_{\mathbf{k}}(\mathbf{r}) = e^{i\mathbf{k}\cdot\mathbf{r}} u_{\mathbf{k}}(\mathbf{r}), \tag{1.19}$$

where ϕ is the wave function, u is a function having the same periodicity as the crystal. The vectors **r** and **k** are associated with the real and the reciprocal space (**k** space), respectively. Particularly, each point in **k** space is associated with a unique **k** vector and is usually called a **k** point. Making use of the translational symmetry of the system, all inequivalent **k** points are contained inside a finite subspace of **k** space, called the first Brillouin zone (FBZ). Quantity evaluations are mostly done through the integration of wave functions, or other functions having **k** dependence, over the FBZ. This integration has to be done numerically since the explicit relation of ϕ and **k** is unknown. In practice, the FBZ is discretized into a grid defined by the mesh of the k-points. This mesh has to be large enough for accurate sampling of the FBZ, yet it should be small enough to reduce the computational time and computer memory. This is one of the convergence tests that need to be done in order to obtain reliable results. Usually, metals need more k-points than semiconductors. This is because the highest occupied valence band crosses the Fermi energy in metals, hence the integration for all occupied states is done for a discontinuous function that excludes unoccupied states. Whereas for a semiconductor or insulator, the highest occupied valence band is completely occupied, therefore the integration is for a continuous function. Smearing is one of the ways to transform a discontinuous function in a metal into a continuous one by smearing out the edge using a smearing function, e.g. a Fermi-Dirac function. The range of smearing has to compromise between the computation efficiency and correctness: Too large will give wrong integration results of the total energy, while too small becomes useless, therefore one again needs more k-points.

Basis set, cut-off energy

Now let us look back at equation (1.19). There we can identify $e^{i\mathbf{k}\cdot\mathbf{r}}$ as a plane wave, $u_{\mathbf{k}}(\mathbf{r})$ is periodic in space and it can be expanded in terms of a set of plane

waves as well:

$$u_{\mathbf{k}}(\mathbf{r}) = \sum_{\mathbf{G}} c_{\mathbf{G}} e^{i\mathbf{G}\cdot\mathbf{r}}, \tag{1.20}$$

where $c_{\mathbf{G}}$ is the coefficient that determines the magnitude of the plane wave $e^{i\mathbf{G}\cdot\mathbf{r}}$. Equation (1.19) can now exclusively be represented as a sum over plane waves:

$$\phi_{\mathbf{k}}(\mathbf{r}) = \sum_{\mathbf{G}} c_{\mathbf{k}+\mathbf{G}} e^{i\mathbf{k}+\mathbf{G}\cdot\mathbf{r}}. \tag{1.21}$$

The summation in the above equation, for practical reasons, has to be truncated. The truncation is usually done for the kinetic energy:

$$E = \frac{1}{2}|\mathbf{k} + \mathbf{G}|^2. \tag{1.22}$$

The maximum kinetic energy, E_{cut}, is associated with a **G** vector and defines the limit of the summations. Here we arrived at another convergence parameter: the plane wave cut-off energy. Similar to the number of **k** points, it has to be large enough for the total energy to be converged in an acceptable precision range. While too large will cost more computational resources without additional benefits.

Pseudopotentials and projected augmented-wave method

Considering the chemical inertness of the core electrons and their highly oscillating wave functions, their impact on the valence electrons is generally approximated by pseudopotentials in order to optimize the computational efficiency. It is a smooth function and has the ability to reconstruct the original core electron properties. Transferability of a pseudopotential is one of the most important factors that determine the performance of the potentials. In practice, a pseudopotential is usually constructed for one isolated atom of one element, while being used in complex multi-elements systems, the potentials with higher transferability can simulate a real atom within different environments. Ultrasoft [18] and projected augmented-wave (PAW) [19, 20] are two types of the most popular pseudopotentials-based methods used in materials simulations. They are well-balanced between accuracy and computational cost. In this thesis, the PAW method is exclusively used for all calculations. This method combines the ideas

of the pseudopotential methods and all-electron methods. Similar as in the case of pseudopotentials, in PAW, the true wave function $|\Psi_n\rangle$ that is obtained from all-electron methods can be transformed into a smooth auxiliary function $|\tilde{\Psi}_n\rangle$ by a linear transformation operator $\mathcal{T}$. The partial waves $|\phi_i\rangle$ form the complete basis set in which the wave function is expanded and it can be also related to auxiliary partial waves $|\tilde{\phi}_i\rangle$:

$$|\phi_i\rangle = \mathcal{T}\,|\tilde{\phi}_i\rangle\,, \tag{1.23}$$

where i is a complete set of quantum numbers. The true and the auxiliary wave functions are identical outside the cut-off radius r_c:

$$\phi_i(\mathbf{r}) = \tilde{\phi}_i(\mathbf{r}), \text{ for } |\mathbf{r} - \mathbf{R}| > r_c, \tag{1.24}$$

where $\mathbf{R}$ is the position of the atom. The transformation operator $\mathcal{T}$ takes the following form:

$$\mathcal{T} = 1 + \sum_i (|\phi_i\rangle - |\tilde{\phi}_i\rangle)\,\langle\tilde{p}_i|\,, \tag{1.25}$$

where $\tilde{p}_i$ are the projector functions that capture the character of the true wave function within a radius of r_c. Now the all-electron wave functions can be reconstructed through the smooth auxiliary functions and projector functions :

$$|\Psi_n\rangle = |\tilde{\Psi}_n\rangle + \sum_i (|\phi_i\rangle - |\tilde{\phi}_i\rangle)\,\langle\tilde{p}_i|\tilde{\Psi}_n\rangle\,. \tag{1.26}$$

The PAW method expresses the true all-electron wave functions with smooth functions that can be easily implemented and perform more efficiently as compared to the all-electron wave functions. Moreover, the accuracy of the calculations are comparable to that for the all-electron ones.

1.2.1 Software Packages

There are more than 70 different software packages capable of performing density functional theory calculations according to Wikipedia[21]. They mainly differ in the type of pseudopotentials, the type of basis set that is used to expand the wave function, in which programming language it is written and whether or not it is free or commercial etc. Lejaeghere et al. [22] have compared 40 different implementations and their accuracy by comparing their results to a highly accurate

all-electron method. They concluded that all codes or methods yield generally consistent results. The accuracy of the codes which were developed in recent years is higher than the earlier ones. The Vienna *Ab initio* Simulation Package (VASP)[23, 24] with its PAW method is one of the most accurate codes that was investigated in this study. Its well-optimized performance on supercomputers gives good results in less time as compared with the others. Therefore, this code will be used as the main tool for all the calculations done in this thesis.

Chapter 2

General physical properties of 2D materials

In this thesis, the properties of materials are divided into a preliminary and an advanced category, where the latter will be presented in the next chapter as the main results of this thesis. In this chapter, I will focus on the preliminary properties of 2D materials, namely structural, electronic, vibrational and mechanical properties. These properties can be used to test the methodology and form the foundation upon which the advanced properties are calculated. They are composed both of my original calculations and from results of the literature. Emphasis will be on the characteristic properties of 2D materials that are different from three-dimensional (3D) materials.

2.1 Structural properties

2.1.1 Layered structure: from multi- to monolayer

As discussed in **??**, layered bulk materials are closely related to 2D materials. A single layer of a layered bulk material is a 2D material. This anisotropic nature is attributed to the weak interlayer bonds and the strong intralayer bonds. vdW interaction [25] is the main source of the weak interlayer bonds. vdW interactions consist of attraction and repulsion between atomic or molecular entities caused by dipole-dipole, dipole-induced dipole and instantaneous induced dipole-induced dipole forces. The definition is sometimes extended to include

all dispersion forces between molecules. For 2D materials, the vdW interaction becomes important when the number of layers is larger than one; i.e. few-layer materials having typically less than ten layers. They also belong to the family of 2D materials since the thickness of the materials is still small and quantum confinement effects are very important. As in its layered bulk counterpart, a few-layer system is a stack of monolayers hold together through vdW forces. When no other bonding types are present, interlayer vdW interaction determines the changes when going from a single layer to multilayer, and its impact on the electronic structure can be significant. For example, from monolayer to bilayer graphene, the low energy linear dispersion relation of energy E as a function of k around the K point evolves into a parabolic-like spectrum[26, 27].

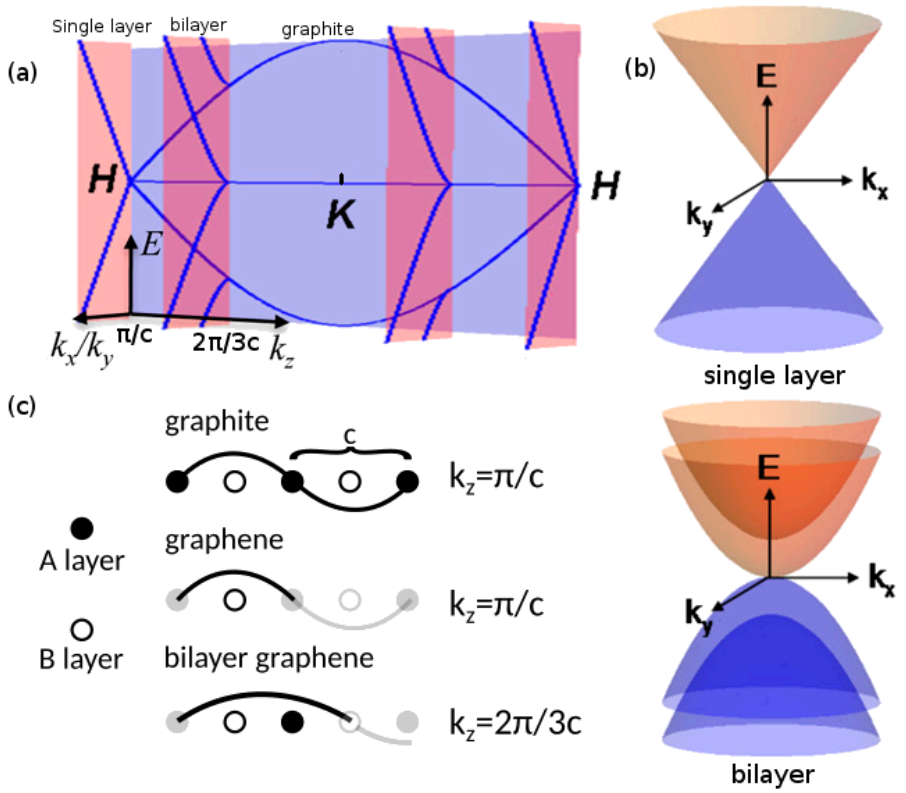

Fig. 2.1 (a) Energy-momentum dispersion relations of single layer and bilayer graphene as approximated by plane intersections of 3D graphite dispersion relation and (b) their 3D dispersion relations around the K point. (c) Matching of the wavelength in graphite to that in single layer and bilayer graphene. Image is adapted from Ref. [27].

In Fig. 2.1(a), the dispersion relation of graphite along the z direction, that is the HKH line in the Brillouin zone, is shown on the blue plane. This direction is perpendicular to the graphite layers. Because of quantum confinement in a few-layer system, standing waves are presented with a finite number of wave vectors. If only the intralayer and interlayer interactions between the nearest neighbour atoms were considered, the dispersion relation in few-layer graphene can be approximated as those on the cross-section of virtual planes (the red planes in Fig. 2.1(a)) with the 3D graphite dispersion relation. These planes are perpendicular to the z direction and intersect with the HKH line at limited points. This is called the quantization[1] of dispersion relations[28]. These points are illustrated in Fig. 2.1(c). Quantum confinement in a few-layer system requires that the wave functions vanish at the imaginary layer right outside the surface of the system, the systems will have well-defined wave vectors. Then, the dispersion relations of graphene and bilayer graphene will be on the red planes that intersect the HKH line at $k_z = \pi/c$ and at $kz = 2(\pi/3c)$, respectively, where c is the lattice constant of graphite that is vertical to the graphite plane. Having the knowledge of the 3D band structure of graphite, one can approximate the dispersion relation of few-layer systems in this way. As shown in the red plane in Fig. 2.1(a) and the 3D version in Fig. 2.1(b), graphene has a linear dispersion relation and bilayer graphene has two parabolic-like bands. Moreover, the bilayer structure will never pass through the H point where graphene has passed to have a linear dispersion relation. This is because the standing waves in a bilayer will have a wave vector $k = 2(n\pi/3c)$, where n is a positive integer: 1, 2, ... , n. This will never be equal to π/c for any integer number of n. More generally, systems with an even number of layers will not have a linear dispersion relation, and vice versa for systems that have an odd number of layers. Further, if other interactions were considered, an overlap of those bands touching each other would have occurred[26]. This overlap increases with the number of layers. Eventually, maximum overlap is reached in graphite.

Another example of the importance of interlayer interactions in few-layer 2D materials is seen for MoS_2. As mentioned in **??**, when going from layered bulk to monolayer, MoS_2 transforms from an indirect band gap to a direct one. Here again, we can make use of the quantization scheme to approximate the band

[1]Sometimes it is also referred as zone-folding.

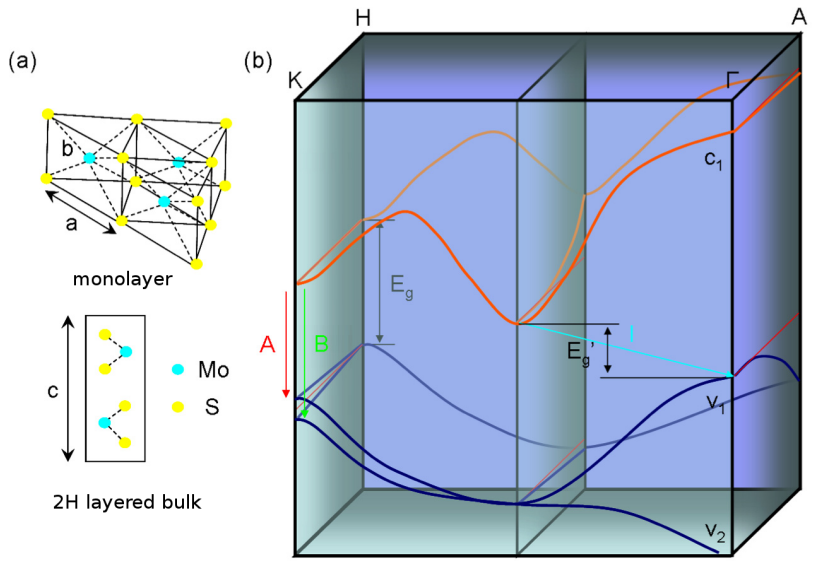

Fig. 2.2 (a) The atomic structures of monolayer and layered bulk MoS_2. (b) The energy-momentum dispersion relation of monolayer MoS_2 as a plane intersection of the 3D dispersion relation. Image is adapted from Ref. [29].

structure of the monolayer from that of its layered bulk. The monolayer and the layered bulk structure of the 2H phase are shown in Fig. 2.2(a). In Fig. 2.2(b), let us focus on the planes parallel to the page that pass through the KΓ line and the HA line (simply call them KΓ plane and HA plane below). Similar to the previously discussed graphite, 2H layered bulk MoS_2 has two layers per unit cell. Therefore, according to the standing wave arguments that we have used for the graphene case above, HA plane represents the monolayer. E_g and E'_g are the band gaps of the monolayer and the layered bulk structures. Here, not only the magnitude of the band gap is increased as going from layered bulk to monolayer, the character of the band gap has changed as well. It is clearly shown that this is due to the shifting of the band edges. VBM at Γ and CBM at the middle of the ΓK line are brought closer as they go from monolayer to layered bulk. This corresponds to the widening of the band width and it is coming from the splitting of the VB and CB when more and more layers interact with each other through the interlayer interactions. Therefore, the band gap in the layered bulk is defined by these two band edges, which in the monolayer was defined by the band edges at K. In contrast to this, the band edges at the K point are not affected too much by the interlayer interaction. So why do the band edges react differently

to the interlayer interactions? If we look into the orbital composition of the band edges, we will find the ones that have widened the most, i.e. VBM at Γ, have the largest contribution from S p_z and Mo d_{z^2} orbitals. These out-of-plane orbitals are orientated vertically to the plane and thus have maximum overlap with the others from an adjacent layer. Therefore, band splitting is more profound for these band edges and causes an increase of their band width. In contrast, both the CBM and VBM at K are largely composed of S p_x and p_y orbitals and Mo d_{xy} and $d_{x^2-y^2}$ orbitals. All of them are in-plane orientated orbitals and thus have limited effect on the interlayer interaction[30].

2.1.2 sp^n hybridization

After discussing layered structures and the importance of interlayer interaction, let us look into some detail in the in-plane structure and how sp^n hybridization gives rise to various structures for 2D materials, where n is the hybridization index that will be discussed in the following. When atoms come together to form bonds, the orientation of bonding orbitals are decisive for the final structure. The hybridization of s and p orbitals is a good example of this. It mainly exists in three different variants: sp, sp^2 and sp^3, see Fig. 2.3. The hybridization index n in sp^n stands for the relative amount of p character in the resulting hybridized orbital. For example, sp^2 has 1/3 s character and 2/3 p character. Hybridized orbitals tend to maximize their distance to reduce the energy raised by the repulsion of electrons. As shown in Fig. 2.3, this results in a tetrahedral structure of sp^3 orbitals, as in diamond, trigonal planar structure of sp^2 orbitals, as in graphene or graphite and linear structure of sp orbitals, as in ethyne molecules. This is, for example, useful to explain the buckled structure of graphane and fluorographene. Because the sp^3 character is induced when the fourth electron is bonded with H or F atoms, and as a result buckling appears in these systems.

Coulson and Moffitt [32] generalized the relation of bond angle with n as follows:

$$1 = -\sqrt{n_1 n_2}\, cos\theta_{12}, \tag{2.1}$$

where θ_{12} is the bond angle between orbital 1 and 2. If orbital 1 and 2 have different sp hybridization n_1 and n_2, we still need one more constraint to solve the equation (2.1) for the hybridization indices n. This constraint is that, in the

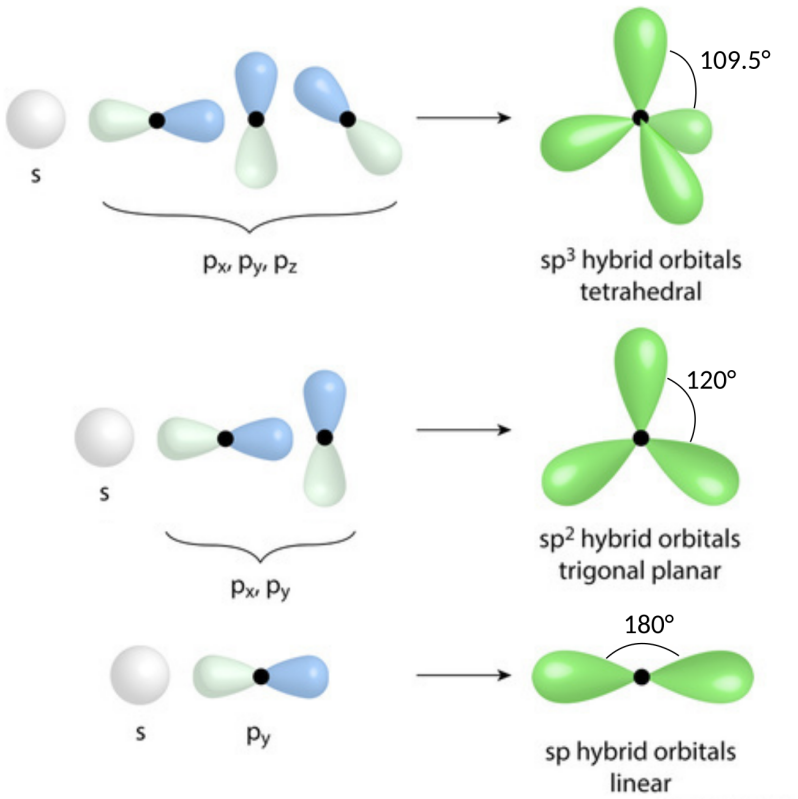

Fig. 2.3 Three types of sp hybridized orbitals. Image is adapted from Ref. [31].

case of carbon atoms, the total portion of s orbitals should be equal to 1, while it should be 3 for the p orbitals. With these pieces of knowledge, equation (2.1) can be solved, and each orbital from one atom can be assigned with n. This formula is useful to determine the s and p fractions of the bonds. For example, $\theta_{12} = 90^o$ gives $n \to \infty$, which means it is a pure p orbital; $\theta_{12} = 120^o$ gives $n = 2$, that is a sp^2 hybridized orbital. Generally, the wider the bond angle, the larger the s contribution. Accordingly, bond angles are ordered as sp > sp^2 > sp^3. Of course, equation (2.1) is more useful when the bond angle takes values other than those three types of hybridized orbitals mentioned, then it can be used to explain the resulting geometry.

2.2 Electronic properties

The electronic properties are among the first features we would like to know of new materials, not only because semiconductors and metals play different roles in applications, but also because details of the electronic structure set the direction for further exploration. One example from my experience is that by monitoring electronic structure variations under strain, we can predict how the mobility of the carriers can be tuned. This will be discussed in later chapters. Therefore, it is important to understand this property of a new material to fully reveal its potential. Electronic properties are usually characterized by the band structure (BS) and the density of states (DOS). These calculations are standard calculations in common first-principles codes from where all subsequent calculations start. After solving the Kohn-Sham equation with properly defined cut-off energy, number of k points etc., we will have the eigenenergy of each state, indexed by a k point in the Brillouin zone and a band number. The DOS counts such states at a specific energy. The BS is the plot of the eigenenergies along lines in the Brillouin zone that connect high symmetry k points. 2D materials have a vast variation of electronic properties, from semimetallic graphene to semiconducting MoS_2 and insulating BN. I will briefly discuss this at the end of this section. The purpose of this section is to point out some of the interesting electronic properties of some 2D materials. We will start with a brief introduction of the electronic properties of graphene.

2.2.1 Graphene

As mentioned before, the orbitals of the C atoms in graphene are sp^2 hybridized. Each one of these sp^2 orbitals, coloured in green in Fig. 2.4, is composed of s, p_x and p_y orbitals, whereas the p_z orbital, coloured in yellow in the figure, is left unchanged. One sp^2 hybridized orbital with the one from an adjacent atom forms a strong σ bond, while p_z orbitals form π bonds. It may look like alternative single and double bonds between atoms, however, according to Clar's theory, the bond order, i.e. the number of chemical bonds between a pair of atoms, in graphene is 4/3 and is uniform[33]. This has to do with the high symmetry of the graphene lattice.

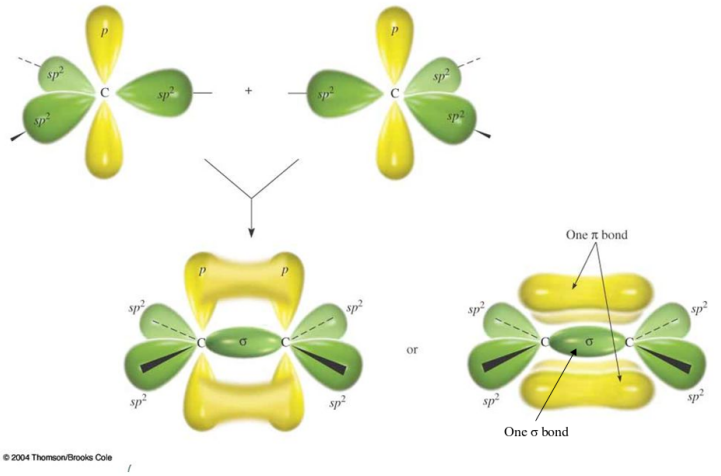

Fig. 2.4 The formation of sp^2 σ and p_z π double bond. Image source: Ref. [34]

Every C atom has the same local environment in graphene. However, adjacent atoms are not equivalent from a symmetry point of view. They belong to different hexagonal sublattices, A and B, as indicated with blue and yellow colors in Fig. 2.5. a_1 and a_2 are the basis vectors in real space connecting equivalent lattice sites. On the left, b_1 and b_2 are the basis vectors in reciprocal space connecting equivalent k points. The hexagon in reciprocal space is the first Brillouin zone where all inequivalent k points are contained. These k points correspond to different parallel lines of atoms and thus their directions in reciprocal space are associated with different directions in real space. The k wave vectors near the Γ point have longer wave length than those away from it. While those at the boundary of the first Brillouin zone have wave lengths that are twice the unit cell dimension in the direction specified by the k points. For example, the most interesting k points for graphene are the K and K′ points. These directions correspond to the a_1 and a_2 directions in real space. It is only at these k points in the Brillouin zone that the antibonding and the bonding π bands touch each other.

In contrast to π bonds, the σ bonds originate from a strong overlap of sp^2 orbitals. The interaction is so strong that the splitting of bonding and antibonding orbitals is large. This makes the σ bonding orbitals having large negative energies, or in other words, makes the σ bond strong and difficult to break. This feature contributes the most to the mechanical strength of graphene. On the other

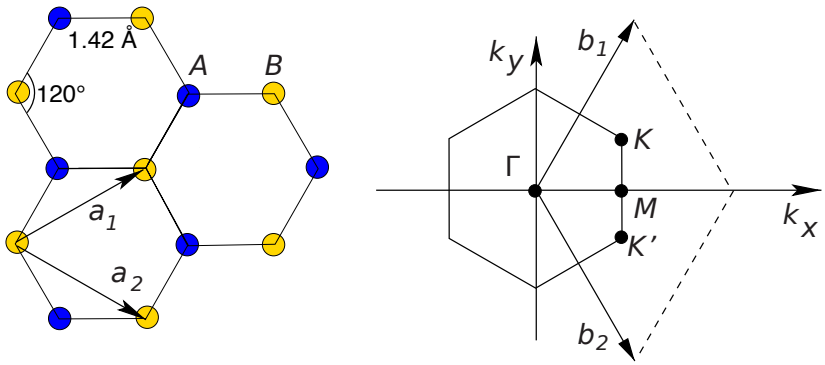

Fig. 2.5 Graphene lattice and its Brillouin zone. Image source: Ref. [35]

hand, p_z orbitals are less overlapping. This makes the π bond energy close to the Fermi level, i.e. the highest occupied state. Therefore, they contribute the most to the electronic properties of graphene.

2.2.2 Dirac cone and symmetry

We have seen that graphene, silicene and germanene have an interesting electronic structure: forming Dirac cones. We also have listed the consequences of having such a feature: high mobility, massless carriers etc. In this section, we will discuss the symmetry condition for the existence of Dirac cones. This knowledge can be used to discover more materials exhibiting a Dirac cone. According to the

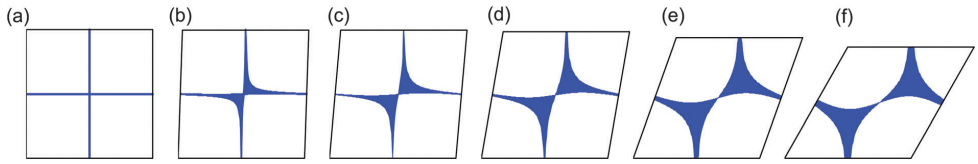

Fig. 2.6 Possible positions for the second atom (blue area) in order to guarantee the existence of Dirac cones as going from (a) square lattice to (f) hexagonal lattice. The first atom is located at the corners of the unit cell. Image source: Ref. [36]

von Neumann-Wigner theorem[2], the space-time inversion symmetry is crucial for the existence and protection of Dirac cones[37]. It is a combination of space inversion and time reversal symmetries. These two are equally important and

[2]This theorem describes the probability of a finite-dimensional matrix to have degenerate eigenvalues.

have to act simultaneously for the possible formation of Dirac cones. A more restrictive condition that guarantees the existence of Dirac cones has to deal with relations of hopping integrals[36, 38]. A study by Liu et al. [36] revealed that the hexagonal lattice has the most favourable structure to form Dirac cones. The probability decreases as one goes from a hexagonal lattice to a square lattice, as shown in Fig. 2.6. Therefore, since most of the 2D materials have hexagonal symmetry, there will be a higher chance of finding materials with Dirac cones in this category.

2.2.3 Examples: 2D-hBN, 2D-MoS_2 and graphene

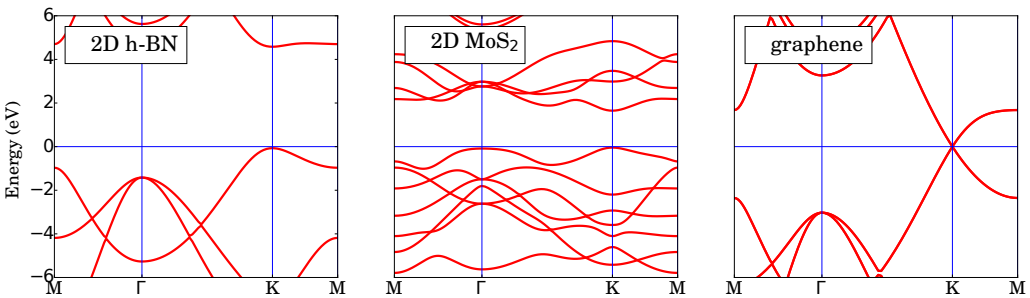

Fig. 2.7 Electronic band structures of 2D-hBN, 2D-MoS_2 and graphene calculated with PBE-GGA functional.

Three typical examples of the band structure of 2D materials are shown in Fig. 2.7. The 2D h-BN is an insulator due to a large band gap in the ultraviolet range, therefore it is suitable to serve as a dielectric layer in an electronic device. The 2D TMDs have a band gap ranging from 1.0-2.5 eV which is in the visible and the near infrared range of light, therefore, they are suitable for optoelectronic device applications. Furthermore, as we compare the dispersion curves along the MΓ and KΓ directions, we can see that the electronic structure is generally the same along these paths which correspond to different crystallographic directions. This means that these materials are highly isotropic, thus we would expect the same for their physical properties. In the result chapters of this thesis, we will investigate some new 2D materials that are highly anisotropic. Their discoveries enrich the features of the physical properties of 2D materials.

2.3 Vibrational properties

The vibrational properties form an important aspect of materials, especially at finite temperature. Thermal expansion, thermal conductivity and electron mobility are all vibrational related topics. Therefore, it is crucial to understand the characterization of this in computational modelling. The force $\vec{F_I}$ on the atom I at the position $\vec{R}$ can be calculated from the wave functions Ψ_0 evaluated from DFT thanks to the Hellmann-Feynman theorem as follows:

$$-\vec{F_I} = \langle \Psi_0(\vec{R}) | \nabla_I H(\vec{R}) | \Psi_0(\vec{R}) \rangle . \tag{2.2}$$

When searching for the equilibrium geometry of the materials, one basically tries different positions of atoms to find a geometry that minimizes all the forces. This usually is the first thing to do for new materials, since different codes, implementations and, more importantly, different functionals will give different results. Despite the fact that the differences are usually small, an unrelaxed geometry will have residual forces on the atoms. This is particularly important when vibrational properties are concerned. Vibrational properties are characterized through the energy (usually expressed in terms of frequency) versus vibrational wave vector dispersion relation. In crystals, all atoms vibrate around their equilibrium positions. The vibrational modes are quantized into phonons. Each phonon represents a periodic, collective vibration with a well-defined vibrational mode and wave vector. The forces (F) that restore the atoms when they deviate from their equilibrium positions can be calculated from DFT either by introducing small displacements or from perturbation theory. Then, the force constants, Φ, can be constructed by monitoring the change in forces through the displacements, u, of atoms in the following way:

$$\Phi_{i\alpha,j\beta} = \frac{\partial F_{j\beta}}{\partial u_{i\alpha}}, \tag{2.3}$$

where the i, j indices are the labels for atoms, α, β are the Cartesian directions: x, y and z. The Fourier transformation of the force constants at wave vector $\mathbf{q}$ is the dynamical matrix $D(\mathbf{q})$ that is related to the frequency of the phonon through the eigenvalue problem:

$$\omega^2(\mathbf{q}, n)\mathbf{e}(\mathbf{q}, n) = D(\mathbf{q})\mathbf{e}(\mathbf{q}, n), \tag{2.4}$$

where $\omega(\mathbf{q}, n)$ is the frequency of the phonon in mode n having wave vector $\mathbf{q}$, and $\mathbf{e}(\mathbf{q}, n)$ is the corresponding eigenvector[39, 40]. Depending on whether atoms in the unit cell are vibrating in-phase or out-of-phase, phonon modes are categorized into acoustic and optical, respectively. For polar materials, charged atoms that vibrate with respect to each other can interact with light, which is the reason that these types of vibrations are called optical modes. Further, considering the respective directions of the wave ($\mathbf{e}$) and vibration ($\mathbf{q}$), the modes are subcategorized into transverse optical (TO) modes and transvers acoustice (TA) modes, where $\mathbf{q} \perp \mathbf{e}$), and longitudinal optical (LO) and longitudinal acoustic (LA) modes, where $\mathbf{q} \parallel \mathbf{e}$. These modes are all in-plane vibrations for 2D materials. For 2D materials, another direction is different from those in-plane ones, namely the $\mathbf{c}$ lattice vector direction perpendicular to the 2D plane. Special modes exist: out-of-plane transverse optical (ZO) and out-of-plane transverse acoustic (ZA) ($\mathbf{q} \perp \mathbf{e}$ and $\mathbf{q} \parallel c$). The total number of acoustic modes is three, that of optical modes is 3N-3, where N is the total number of atoms in the unit cell.

2.3.1 Example: 2D-MoS_2

Let us now take layered bulk and monolayer MoS_2 as examples to highlight some of the important details of the phonon dispersion relations in 2D materials. A comparison of vibrational modes between layered bulk and monolayer MoS_2 is presented in Fig. 2.8(a). First of all, the number of atoms in the unit cell reduces from six to three from layered bulk to monolayer. Therefore, the number of optical modes will be reduced as well from 15 in layered bulk to six in the monolayer. In Fig. 2.8(a) it is shown, as the material is transformed to the monolayer, that several modes merge with others that only differ by whether the vibration in different layers is in-phase or out-of-phase. Secondly, a characteristic feature of phonon dispersions for layered bulk and 2D materials has appeared, namely the quadratic ZA mode (flexural mode). It is usually linear in 3D bulk materials because of strong interlayer interactions. Because in layered bulk, the interlayer interactions are weak and absent in 2D materials, therefore, it will cost less energy

for the out-of-plane vibration and a quadratic dispersion will appear[41]. This feature is closely related to the formation of the intrinsic ripples in 2D materials, e.g. graphene[42] and MoS_2[43]. As shown in Fig. 2.8(b), phonons with longer wave lengths, i.e. around Γ, in ZA mode have smaller frequencies or energies. This means this mode is more easily excited at low temperature and forms ripples which can be often observed in 2D materials. The formation of ripples is crucial for the stability of 2D materials at finite temperature. Lastly, in the projected DOS, the projections of mode eigenvectors to in-plane (XY) and out-of-plane (Z) components are shown. The modes with Z components, i.e. ZO_1, ZO_2 and ZA, contribute the most to the Z projections, and vice versa for the longitudinal and acoustic modes to the XY projection.

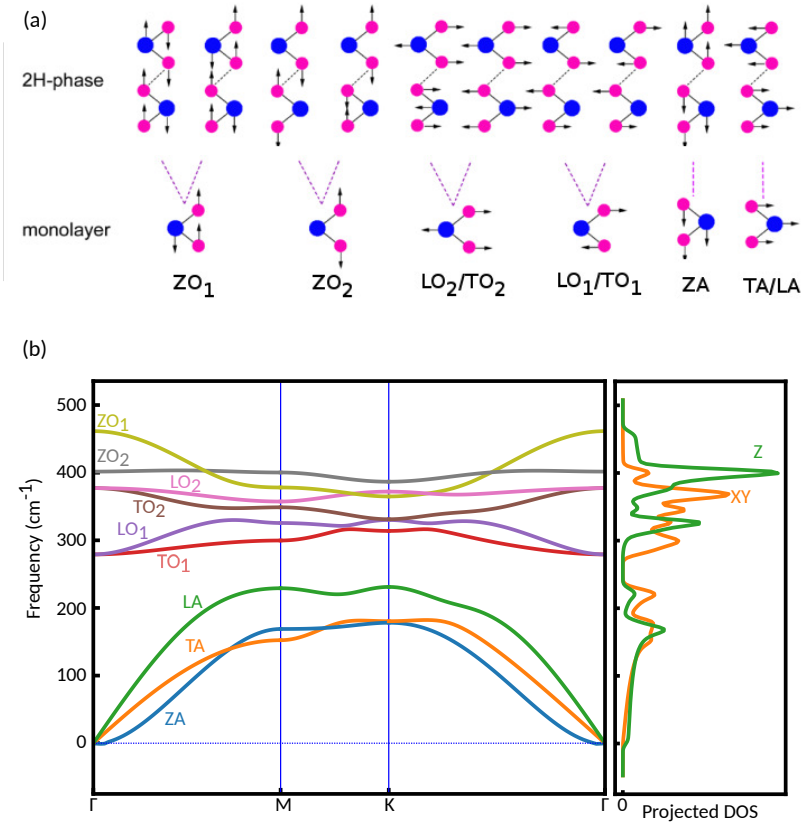

Fig. 2.8 (a) Phonon modes of layered bulk (first row) and monolayer (second row) MoS_2 at the Γ point. (b) Phonon dispersion and projected DOS of monolayer MoS_2.

2.3.2 Dynamic stability from phonon dispersion

One of the most useful features of the phonon dispersion is the possibility to check the dynamical stability of the structure. An unstable structure is usually indicated by the presence of imaginary frequencies which are usually plotted as negative frequency in the phonon spectrum in some part of the Brillouin zone, see Fig. 2.9 for example.

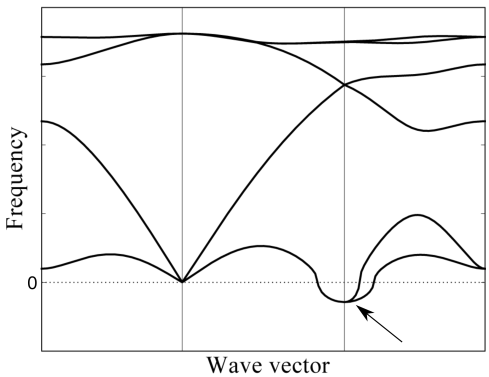

Fig. 2.9 Imaginary frequencies are shown as negative frequencies in a phonon dispersion plot

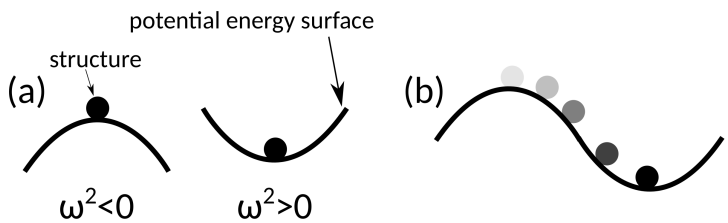

Fig. 2.10 (a) A structure at the convex (left) and the concave (right) of the PES. (b) Searching for a stable structure (phase transition).

Now let us try to understand this and make use of it to convert an unstable to a stable structure. Consider a relaxed structure in which the forces on all atoms have vanished. This could be locally at the maximum or the minimum of the potential energy surface (PES), see Fig. 2.10. Note that, in both situations, the forces, the derivative of the PES curves, are zero. Therefore, both situations can occur when the structure is relaxed by only following the forces. In the case of a convex PES, the dynamical matrix $D(\mathbf{q})$ will have negative components because the direction of the force is the same as the displacement. We have seen

from equation (2.4) that $D(\mathbf{q})$ is related to the square of the frequency ω, hence imaginary frequencies are the only solutions. However, a structure with imaginary frequencies near the Γ point does not necessarily mean it is not stable. Since a large supercell consisting of multiples of the unit cell is typically used to do phonon calculations, it may be that the size of the supercell is not large enough to correctly describe long wavelength phonons. In contrast to this, a structure with imaginary frequencies that appear around other q points than the Γ point would imply a structure instability or a structural phase transition. The lowering of the energy with some vibrational modes means that the structure prefers a modulation as induced by the vibration, therefore if we calculate the energy of the modulated structure we will have a lower energy structure. With advanced techniques in phonon software[e.g. 44], it is possible to perturb such a structure based on the vibration mode which has an imaginary frequency to find a lower energy state and stabilize the structure, as schematically illustrated in Fig. 2.10(b).

2.4 Mechanical properties

In **??**, we have discussed the stiffness and strength of some of the 2D materials. These are some of the mechanical properties of materials. The force on the atoms or the stress $\boldsymbol{\sigma}$ on the unit cells under a finite strain $\boldsymbol{\epsilon}$ are typical outputs from common first-principles codes. Within the elastic regime of the stress-strain relation, they can be related through the elastic constant $\boldsymbol{C}$: $\boldsymbol{\sigma} = \boldsymbol{C}\boldsymbol{\epsilon}$, this is Hooke's law. $\boldsymbol{C}$ is a 6×6 matrix with matrix elements C_{ij}. The elements measure the resistance of a material in the i direction to a deformation in the j direction, where i and j are the index of stress and strain tensors, respectively, and refer to particular directions. With the Voigt notations, the indices have the following correspondence: 1→ xx, 2→ yy, 3→ zz, 4→ yz, 5→ zx, 6→ xy. The elastic constants can be simplified if the crystal symmetry and dimension are taken into account. For example, for 2D hexagonal lattice symmetry, Hook's law reads:

$$\begin{pmatrix} \sigma_1 \\ \sigma_2 \\ \sigma_6 \end{pmatrix} = \begin{pmatrix} C_{11} & C_{12} & 0 \\ C_{12} & C_{11} & 0 \\ 0 & 0 & (C_{11} - C_{12})/2 \end{pmatrix} \begin{pmatrix} \epsilon_1 \\ \epsilon_2 \\ \epsilon_6 \end{pmatrix}. \tag{2.5}$$

In this way, all elastic constants can be extracted from stress-strain data using first-principles calculations. Generally, it is more convenient to have a single quantity to describe a particular aspect of the mechanical properties of the material. This is where the Young's modulus Y, shear modulus G and Poisson's ratio ν become useful. Following previous notations, they are defined as

$$Y_\alpha = \frac{1}{S_{\alpha\alpha}}, \quad \alpha = 1, 2, 3 \ . \tag{2.6}$$

$$\nu_{\alpha\beta} = -Y_\beta S_{\alpha\beta}, \quad \alpha, \beta = 1, 2, 3 \ \ (\alpha \neq \beta) \ . \tag{2.7}$$

$$G_{\gamma\gamma} = \frac{1}{S_{\gamma\gamma}}, \quad \gamma = 4, 5, 6 \ , \tag{2.8}$$

where $\boldsymbol{S} = \boldsymbol{C}^{-1}$ is the compliance matrix [e.g. 45]. The Young's modulus and shear modulus give the stiffness of the material when it responds to a stretching and shearing deformation in particular directions and they stand for the hardness of the material. Their unit in 2D is J/m^2 or N/m. To make them comparable to conventional 3D materials, 2D moduli usually are converted into 3D ones by dividing the former by the thickness of the sheet. Poisson's ratio gives the ratio of the transverse to the axial strain. It represents how easy it is to change the shape of the material with respect to changing the volume. Liquid and rubber have a Poisson's ratio close to 0.5, which is the theoretical upper limit of this quantity and making them the easiest materials to change shape over volume. In contrast, a cork has a Poisson's ratio close to zero, meaning zero lateral expansion when compressed in other directions. The breaking strength/strain is a measure of the maximum load limit that a material can withstand and it is used to characterize the strength of a material. This quantity is usually obtained by continuously deforming the material until they break and recording the maximum stress/strain. This can be done both experimentally and through simulations.

2.4.1 Examples: graphene, 2D-hBN and 2D-MoS_2

In table 2.1, the mechanical properties of several 2D materials are listed, as well as that of steel for comparison. As mentioned, graphene is the strongest ma-

terial ever measured. This is due to its strong σ bonding. With similar bonding in BN, it shows comparable results to graphene. MoS_2 has lower stiffness and strength than the previous two due to weaker bonding, nevertheless, it is still much stronger than steel. The Poisson's ratio has an inverse relation with Young's modulus. This means graphene acts more like cork than rubber as compared to MoS_2.

Table 2.1 Mechanical properties of graphene, 2D-hBN and 2D-MoS_2

material	Young's modulus[3] TPa	Breaking strength GPa	Poisson's ratio
graphene[46]	1.0±0.1	130±10	0.149[47]
2D-hBN [48]	0.71–0.97	120–165	0.210
2D-MoS_2[49]	0.27± 0.10	23	0.29 [50]
A36 steel[51]	0.2	0.4–0.55	0.26

2.4.2 Mechanical stability: Born stability criteria

Mechanical stability is a criterion for unstressed crystal stability, which is additional to dynamical stability. It was first pointed out by Born [52] in the 1940's, and is therefore often called "Born stability criteria". Its core concept is that the elastic energy should be positive for any non-zero strains. The elastic energy U is related to the elastic constants C_{ij} in the following way:

$$U = U_0 + \frac{1}{2} V_0 \sum_{i,j=1}^{6} C_{ij} \epsilon_i \epsilon_j, \tag{2.9}$$

where U_0 is the equilibrium energy and V_0 is the equilibrium volume. According to Born's paper[52], the necessary and sufficient stability conditions are: 1) $|\mathbf{C}| > 0$; 2) all eigenvalues of $\mathbf{C}$ are positive; 3) Sylvester's criterion: the determinants of the upper-left k by k sub-matrices are positive; (4) an arbitrary set of minors of $\mathbf{C}$ are positive. Mouhat and Coudert [53] formulated closed form expressions of these criteria for different crystal systems. Taking into account the symmetry of these systems, the number of criteria reduces, and becomes very useful to

[3]The thickness of the monolayer is taken the interlayer distance of its corresponding layered structure.

check the mechanical stability of a new crystal system. For example, for a 2D hexagonal crystal, the criteria become: $C_{11} > |C_{22}|$ and $C_{66} > 0$.

Chapter 3

Results of Physical Properties Calculations in Novel 2D Materials

In this and the next chapter, the main results of the thesis will be presented. In **??**, I have reviewed some of the early post-graphene 2D materials, and their physical properties in chapter 2. As it has been defined, the properties discussed before belong to the basic property category. In this chapter, I will present my work on the determination of some of the advanced physical properties, namely thermal, piezoelectric, and magnetic properties and Li battery related properties. In addition, I will also introduce several new 2D materials: phosphorene, monolayer titanium trisulfide, penta-hexa-graphene and MXenes. Each of the sections below resulted in a research paper.

3.1 Thermal properties of black and blue phosphorene[1]

3.1.1 Introduction

Black phosphorene (black P) is a single atomic layer of black phosphorus and has been successfully exfoliated [54, 55]. Similar to the multiphase structures in phosphorus, at least six different possible stable 2D allotropes of phosphorene were proposed[56–58]. This multi-phase nature is because in contrast to the C

[1]This work is published: P3.

atoms of graphene, the P atoms in phosphorene have sp^3-hybridized orbitals. This is mainly caused by the extra valence electron of P atoms in comparison to C atoms. Indeed, if this extra electron is placed in a sp^2-hybridized structure, they would occupy the energetically unfavourable (antibonding) π^* band. However, with sp^3-hybridization, a σ-bond network can be formed with three sp^3 orbitals and the other sp^3 orbital is used to host the remaining electron pair. This leads to an essentially tetragonal coordination of the P atoms and results in a buckled nature of sp^3-hybridized sheets, see Fig. 3.1 for the structures. The out-of-plane positions of the atoms in sp^3-hybridized sheets give rise to various possible structural phases which are absent in sp^2-hybridized systems. Among those, black P, also referred as the α phase, is the most stable allotrope. However, the cohesive energy of blue phosphorene (blue P), or the β phase, is only a few meV/atom higher than that of black P, while other crystal structures are much less favourable with energy at least by $\sim$ 80 meV/atom higher.

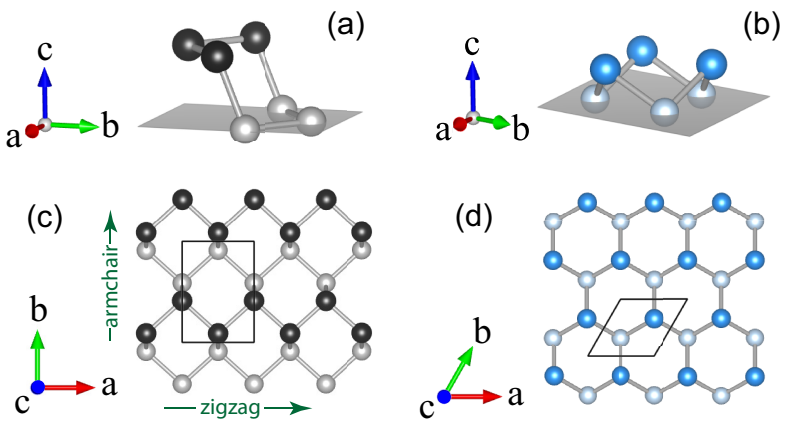

Fig. 3.1 (a) and (b) show the hexagonal rings of black P and blue P. Their top viewed structures are shown in (c) and (d), respectively. Atoms are coloured in accordance with the names of the structures. Lighter coloured atoms mean they are lower in vertical position. Black boxes in top views are the primitive unit cells used in our calculations.

Triggered by its experimental realization, various physical properties of phosphorene have been explored. Electronically, black P is a semiconductor with a direct band gap at the Γ point[56, 59]. Experimentally, photoluminescence excitation spectroscopy measured a quasi-particle band gap of 2.2 eV[60], which is

larger than its bulk band gap, i.e. 0.31-0.33 eV[61, 62]. Due to its electronic structure, black P has been proposed as a potential novel material in nanoelectronics and optoelectronics, especially in the infrared regime. High performance black P based transistors with a mobility up to 1000 $cm^2/V{\cdot}s$ and an on/off ratio up to 10^4 at room temperature have been reported[54, 55]. Similar to black P, blue P was predicted to be a semiconductor material with an indirect band gap around 2.00 eV[56]. Therefore, it can be potentially used for field-effect transistor applications. The high mobility and tunable finite band gap of phosphorene, among other promising properties[63–67], make it an interesting new member of the 2D materials. Despite the mentioned studies that aimed to explore the physical properties of phosphorene, a more comprehensive knowledge of finite temperature effects on their properties has not been reported. Given the fact that this knowledge could contribute to the acceleration in the progress towards its proposed applications, this study[P3] is urgently needed. To this end, here we explore the thermal properties of black p and blue p, their temperature-dependent lattice constant, thermal expansion coefficient (TEC), free energy and specific heat.

3.1.2 Thermal expansion and quasi-harmonic approximation

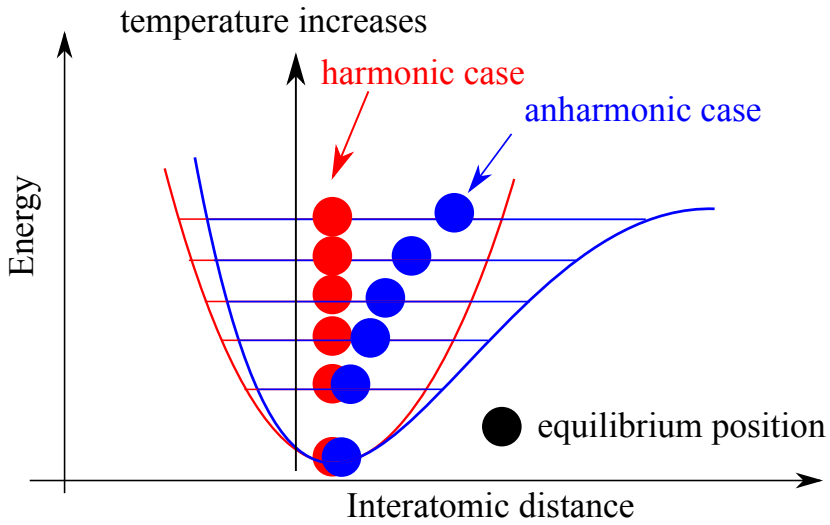

Fig. 3.2 Schematic illustration of the relation between asymmetric interatomic potential and thermal expansion.

The thermal expansion is the expansion of a material's volume at finite temperature. As shown in Fig. 3.2, it is directly related to the asymmetry of the interatomic potential where the equilibrium position shifts towards the flatter side of the potential energy profile and stays far away from the steeper side as the temperature increases. Below we will see how we can include this anharmonic potential using an approximation. The TEC $\alpha(T)$ is defined through the following formula:

$$\alpha(T) = \frac{1}{a_0(T)} \frac{da_0(T)}{dT}, \tag{3.1}$$

where T is the temperature, $a_0(T)$ is the equilibrium lattice parameter corresponding to the minimum of the Helmholtz free energy.

In order to describe the thermal expansion within DFT, one needs to go beyond the harmonic approximation that is used to calculate the phonon frequency as we discussed in chapter 2. The harmonic approximation gives infinite thermal conductivity, infinite phonon lifetimes and temperature-independent vibrational and elastic properties, which contradict to the experiment. The quasi-harmonic approximation (QHA) [68–71] is a way to include the approximated anharmonic effect through volume-dependent frequencies within the non-interacting phonons approximation. Although it is an implicit inclusion of anharmonic effect, its dominant role in the thermal properties, that is two orders of magnitude larger than explicit anharmonic effects, make sure it can correctly describe the thermal properties up to melting point. Beyond this temperature, anharmonic effect will become important. QHA has been applied to various compounds from semiconductors to metals and to earth materials under extreme conditions[68, 72, 73] . In Fig. 3.3, the applications of the QHA for graphite and graphene are shown. The agreement between experiment and QHA is good in a wide range of temperature up to 2000 K. Another interesting point is that the negative thermal expansion, where the $\alpha(T)$ is negative, is presented in both materials, especially, graphene keeps such a feature up to 2000 K. This is a common character of layered materials where layers are weakly bonded. The origin of this is related to the ZA mode in layered materials as discussed in chapter 2. At low temperature, ZA mode will be excited and this out-of-plane vibration effectively shrinks the in-plane dimension of the materials and thus gives negative thermal expansion.

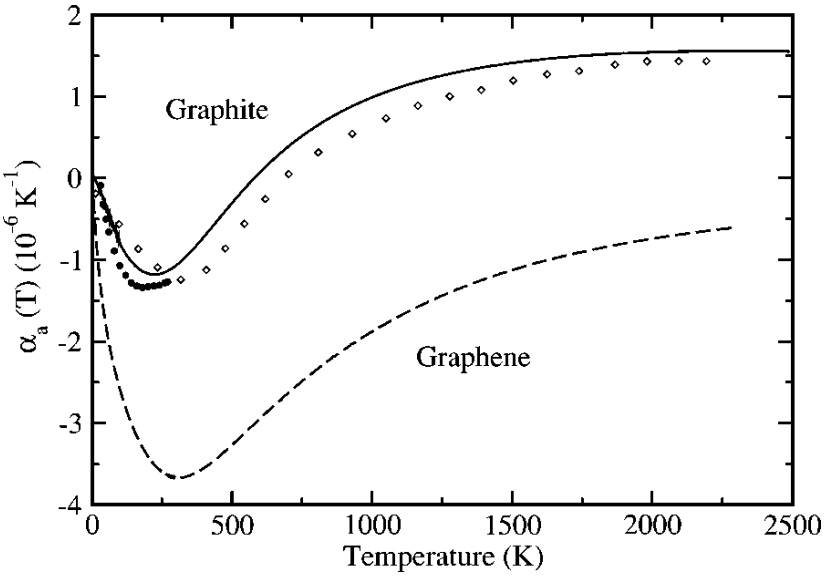

Fig. 3.3 TEC of graphite and graphene calculated using QHA (solid line) and experimental result for graphite (points). Image source: [68]

Equilibrium lattice constants at any temperature $a_0(T)$ are calculated by direct minimization of the Helmholtz free energy $F(a,T)$ with respect to its independent lattice vector, i.e. in this case, **a** and **b** for black P, and **a** for blue P. For the minimization process, $F(a,T)$ is obtained by fitting the discrete data points of $F(a_i,T)$ to the third-order Birch-Murnaghan equation of state, where i is the label for different lattice constants or equivalently different strains. The $F(a_i,T)$ is constructed from $\omega^i_{\mathbf{q},j}$ and $E[a_i]$ through the following formula[68, 74]:

$$F(a_i,T) = E[a_i] + \sum_{\mathbf{q},j} \frac{\hbar\omega^i_{\mathbf{q},j}}{2} + k_B T \sum_{\mathbf{q},j} \ln\left(1 - \exp\left[-\frac{\hbar\omega^i_{\mathbf{q},j}}{k_B T}\right]\right). \tag{3.2}$$

Here, T is the temperature, k_B is the Boltzmann constant, $E[a_i]$ is the DFT ground state energy. $\omega^i_{\mathbf{q},j}$ is the phonon frequency at the q point **q** with band index j. The sums run over all q points and all bands of the whole Brillouin zone. Since the structural instabilities arise especially for the armchair direction when under compressive strain values larger than 4%, the calculation of phonon dispersions for both structures are performed under small strains, namely $\pm$ 2%, in order to evaluate $\omega^i_{\mathbf{q},j}$ and $E[a_i]$. Considering two independent lattice vectors **a** and **b** of black P two uniaxial strains are applied for these directions. While for blue

P, only biaxial strain is applied to keep its hexagonal symmetry unchanged. The whole calculation process was carried out using the phonopy-qha script[75].

3.1.3 Computational details

Simulation program: VASP and Phonopy[76]
Energy cut-off: 500 eV
Pseudopotentials: PBE-GGA(PAW)
k points (*Gamma* centered): 15×11×1 and 15×15×1 for black P and blue P, respectively
Vacuum: 25 Å
Energy and force convergence criterion: 10^{-5} eV and 10^{-7} eV/Å, respectively
Supercell for phonon calculation: 7×3×1 and 5×5×1 for black P and blue P, respectively
q points for phonon calculation: 200×200×1

3.1.4 Phonon modes and dispersion

Different from a pure planar graphene, black P and blue P have a buckled non-planar structure due to the sp^3 hybridization, yet all three structures share the same hexagonal lattice base. Given an almost identical local environment in the unit cell, see Fig. 3.1, it is not surprising that blue P and black P having similar total energy. The only significant difference is the plane, marked as grey shown in Fig. 3.1, on which the system extends to form an infinite 2D crystal. Therefore, thermal expansion on these different planes are expected to be different and will carry insight and information on the different finite temperature properties. The primitive unit cell of black P is a rectangular lattice with a four-atom basis and a space group of D^7_{2h}, and that of blue P is a hexagonal lattice with a two-atom basis and a space group of D^3_{3d}. Therefore, besides the three acoustic modes with the in-phase vibrations of atoms, there are nine and three optical modes for black P and blue P, respectively.

The calculated phonon dispersions along the high symmetric q lines corresponding to these modes are depicted in Fig. 3.4(a) and (b) for both structures. Parallel with the previous calculations [77, 78], the calculated phonon dispersions are free from imaginary frequencies, which ensures the structural stability of the materials. The lowest acoustic mode ZA displays a q^2 relation as we discussed in chapter 2. The other two acoustic modes, LA and TA, still have a linear dependence with respect to the q wavevector since the situation is the same

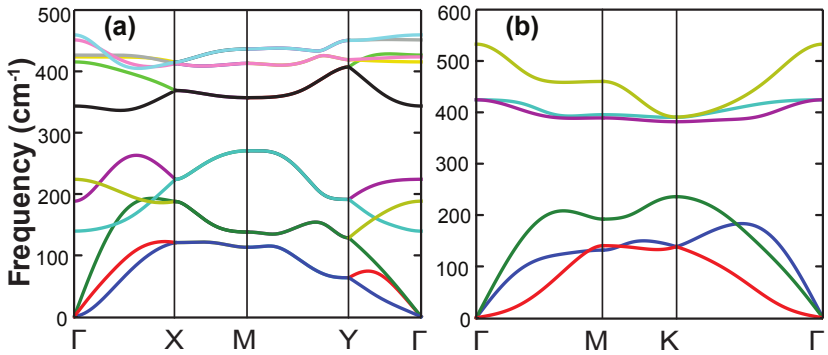

Fig. 3.4 Calculated phonon dispersions for prinstine (a) black and (b) blue P.

here as in the bulk. The total frequency range of the phonon dispersion is larger by an amount of about 100 cm^{-1} in blue P as compared to black P.

3.1.5 Temperature-dependent thermal properties

The equilibrium lattice constants at zero K, a_0 and b_0 of black P and a_0 of blue P, are predicted as a_0 = 3.298 Å, b_0=4.625 Å, and a_0 = 3.277 Å, respectively, in good agreement with previously reported results (a_0 = 3.297 Å, b_0=4.640 Å for black P[59, 79], and a_0 = 3.330 Å for blue P[56]). The expansion of these lattice parameters due to zero-point vibration is around 0.2% at 0 K, which is smaller than that of other well-known 2D materials like graphene and *h*-BN, but it is comparable with that of MoS_2 and $MoSe_2$. This result is reasonable due to the difference in the maximum phonon frequency between these materials: that of graphene and *h*-BN is around 1600 cm^{-1} and that of MoS_2, $MoSe_2$, black P and a_0 of blue P is around 600 cm^{-1}.

The temperature dependence of the lattice constants $a_0(T)$, $b_0(T)$ and TEC $\alpha(T)$ of both structures are shown in Fig. 3.5. The anisotropic nature of the structure of black P leads to different lattice constant expansion rates. A faster thermal expansion along the armchair direction (i.e. **b**) is found, see Fig. 3.5(a). While a small negative TEC appears for all structures in all directions at temperatures lower than 100 K, black P along the zigzag direction has a more apparent negative expansion. The lattice constant of both phases varies linearly when T $>$ 200 K, see Fig. 3.5(a). The TEC increases rapidly with temperature up to 300 K. After that, all TECs changes slowly with temperature starting from around 400 K

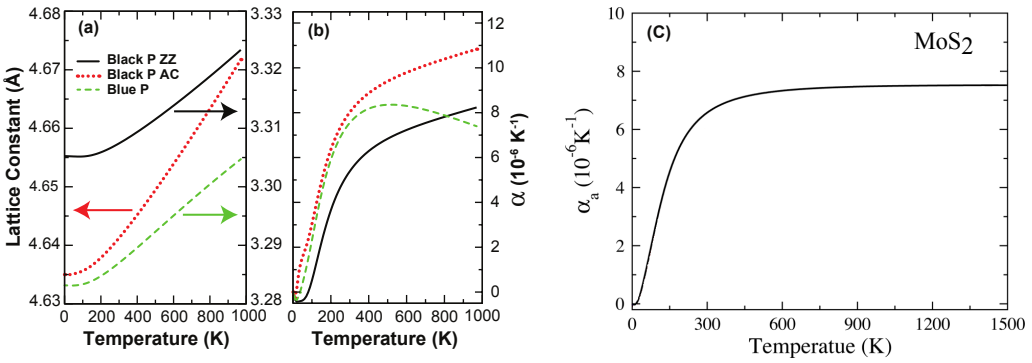

Fig. 3.5 (a) Lattice constants and (b) TEC of black P and blue P as a function of temperature. Here, ZZ and AC are denoted for the zigzag and armchair directions, respectively. (c) TEC of monolayer MoS_2 for comparison from Ref. [70].

in agreement with predictions for 2D-TMDs [69, 70], for example see Fig. 3.5(c) for monolayer MoS_2. Different from MoS_2, we do not observe any saturation of the TEC for black P at high temperatures. While black P expands at most 0.02 Å along the zigzag direction as T approaches 1000 K, it expands 0.04 Å along the armchair direction. As is clear from Fig. 3.1, a uniaxal expansion along the armchair direction may result in a structural phase transition from black P to blue P because of the similar hexagonal arrangement of P atoms[80].

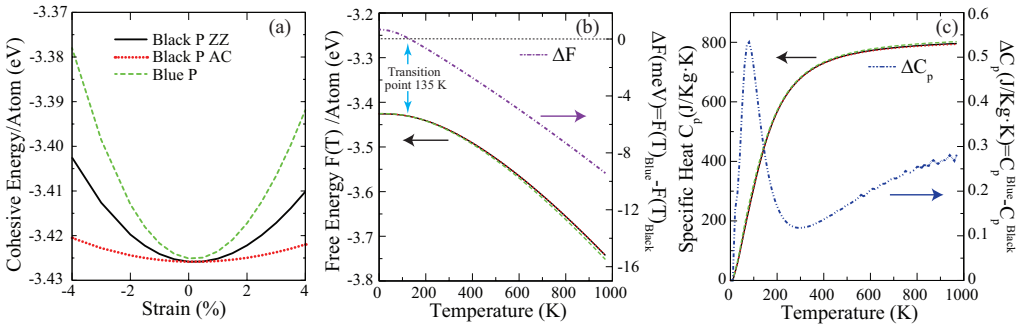

Fig. 3.6 (a) Cohesive energy, including zero point energy, as a function of applied strain at T = 0 K and (b) Helmholtz free energy ($F(T)$) as a function of temperature. Here, ZZ and AC are used for the zigzag and armchair directions, respectively. $\Delta F(T)$ is the difference between $F(T)$ of black P and blue P. The blue arrow (b) denotes the transition point, after which blue P becomes thermodynamically more stable over black P. The specific heat at constant pressure (C_p) and the difference (ΔC_p) between C_p of black P and blue P are shown in (c).

In Fig. 3.6, the variation of the cohesive energy as a function of strain at 0 K (a) and the variation of the Helmholtz free energy (F(T)) as a function of temperature (b) are presented. In Fig. 3.6(b), we also show $\Delta F(T)$ which is defined as $\Delta F(T)$=$F_{blueP}(T)$ - $F_{blackP}(T)$. Here, $F_{blueP}(T)$ and $F_{blackP}(T)$ are the Helmholtz free energy of black P and blue P, respectively. As the zero-point energy continuously decreases with strain from minus to plus, the variation of the zero-point energy results in an asymmetric behaviour in cohesive energy with strain. In addition, the curvature of this total energy gives the in-plane stiffness of the material as a measure of the response to mechanical deformation. It is clear that blue P is a stiffer material as compared to black P. Moreover, the deformation along the zigzag direction of black P is harder than that along the armchair direction at 0 K, and this is consistent with the finite temperature behaviour as we concluded from the previous section in connection with Fig. 3.5(a).

The $F(T)$ decreases as temperature increases due to the entropy term (the last term in equation (3.2)). Inclusion of the zero-point energy gives rise to a slightly higher ground state energy for blue P over black P since its optical phonon modes have larger frequencies. However, as temperature increases, a crossing of the free energy curves around 135 K occurs, which makes the blue P energetically more favorable at high temperatures, see Fig. 3.6(b). The free energy difference between the two phases is of the order of 4 meV at room temperature, meaning that the two phases can coexist. In addition, it is possible to observe a phase transition driven by temperature from black P to blue P or visa verse at T=135 K.

In Fig. 3.6(c), we present constant pressure heat capacity, C_p, results for both structures, which is generally a few percent different from constant volume heat capacity in similar structures[68]. The C_p difference (ΔC_p) between two phases is significantly small for the whole temperature range as represented with a blue dash-dot line in Fig. 3.6(c), which shows essentially very similar Debye temperature for these two different phases. At high temperatures, C_p approaches its classical value of 12 k_B. When T=300 K, C_p already reaches about 80 % of its classical value, meaning that most of the phonon modes are activated at this temperature.

3.1.6 Summary

In summary, we systematically investigated the lattice thermal properties of black and blue P. Similar to its electronic properties, black P has direction dependent mechanical and thermal properties. The calculated TEC demonstrates that a much larger expansion along the armchair direction with temperature is observed for black P. While black P is thermodynamically more stable than blue P, the latter becomes more stable when T $>$ 135 K. Yet their free energy difference is small due to their structural similarities. It is possible to observe a structural phase transition from black P to blue P by increasing the temperature beyond 135 K, and therefore the coexistence of these two phases is possible.

3.2 Piezoelectric properties of 2D-TMDs and 2D-TMDOs[2]

3.2.1 Introduction

We have seen the general properties of 2D-TMDs in **??** and the vibrational and electronic properties of one member: 2D-MoS_2 in chapter 2. When the S atom is replaced with O, TMDs become TMDOs, whose monolayers have similar properties as 2D-TMDs. Although 2D-TMDOs are proven to be stable, they have not been synthesised yet. Sharing similar electronic structure, 2D-TMDs and 2D-TMDOs already promise various potential applications, such as nanoelectronic and nanophotonic devices owe to their direct finite band gaps[81, 82]. In addition to these exciting applications, 2D-TMDs, in the noncentrosymmetric 2H crystal structure with D_{3h} symmetry, have also been shown to have remarkable piezoelectric properties that can then be used in pressure sensors, transducers, high voltage generators, energy harvesters, energy conversion and piezotronic applications. Many layered materials have a centrosymmetry which suppresses piezoelectricity. However, this symmetry will be broken at the monolayer level, and then piezoelectricity is recovered. For example, graphene preserves centrosymmetry as in graphite, or inversion symmetry, due to its non-polar nature, thus it does not display piezoelectricity. Whereas, 2D-BN and 2D-TMDs break

[2] This work is published: P5.

such symmetry and become noncentrosymmetric systems where piezoelectric effects can manifest themselves.

Duerloo et al. [83] calculated the piezoelectric properties of a single layer of BN, MoS_2, $MoSe_2$, $MoTe_2$, WS_2, WSe_2, and WTe_2 by using first-principles calculations. They reported that piezoelectricity of the 2D-TMDC monolayers in the H phase are comparable or even better than that of conventional bulk piezoelectric materials. Zhu et al. [84] reported experimental evidence of piezoelectricity in free-standing MoS_2 and they found that this material exhibits piezoelectricity for an odd number of layers in which case inversion symmetry is broken. Their measured piezoelectric coefficient is 2.9×10^{-10} C/m, which agrees well with previous theoretical calculations[83]. Similarly, by using DFT based theoretical calculations, it has been predicted that group IIIA monodichalcogenides, namely GaS, GaSe and InSe, have piezoelectric stress coefficients of 1.34×10^{-10}, 1.34×10^{-10} and 1.47×10^{-10} C/m, respectively[85]. In addition, reducing the dimensionality has been shown to enhance piezoelectricity in ZnO[86]. These studies indicate that TMDs are promising candidates as low dimensional piezoelectric materials.

Since previous calculations and experiments were only focused on Mo and W based TMDs, the potential of other 2D-TMDs and 2D-TMDOs for piezoelectric device applications have remained an open question so far. To reveal such potential, first principles calculations are performed in order to systematically investigate the piezoelectric properties of single layer 2H-MX_2 compounds, where M= Cr, Mo, W, Ti, Zr, Hf, Sn and X=O, S, Se, Te. Lattice parameters, atomic positions, electronic band-gap values, elastic stiffness constants (C_{11} and C_{12}), Young modulus (Y), Poisson's ratios (ν), piezoelectric stress coefficients (e_{11}) and piezoelectric strain coefficients (d_{11}) are calculated.

3.2.2 Piezoelectric constants

Piezoelectricity is the ability of some materials to generate an internal electric field in response to applied mechanical stress. Two types of piezoelectric phenomena can be observed for piezoelectric materials: 1) direct piezoelectric effect: separation of opposite charge due to stress and 2) converse piezoelectric effect: occurrences of stress and strain under external electric field. In Fig. 3.7, the mechanism of direct piezoelectric effect is shown.

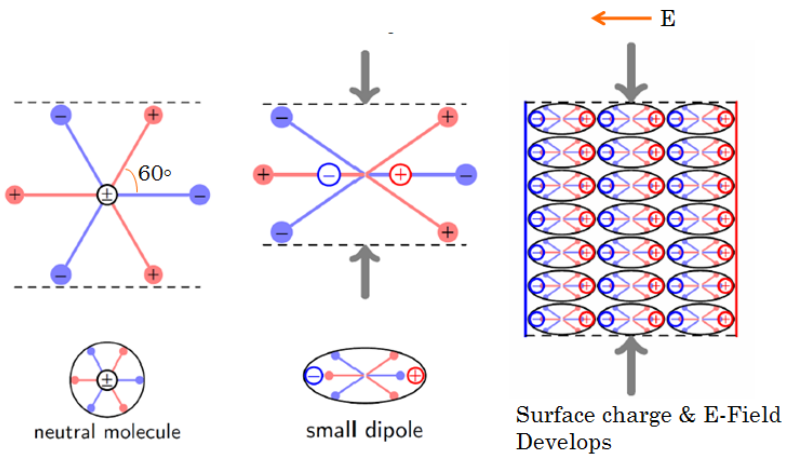

Fig. 3.7 Mechanism of direct piezoelectric effect. Image source: [87]

To investigate the piezoelectric properties, we follow the same theoretical approach as Ref. [83]. The piezoelectric tensor[88, 89], e_{ij}, can be defined in terms of the induced polarization in the direction i due to a strain (ε_j) change along the direction j as follows

$$e_{ij} = \partial P_i/\partial \varepsilon_j = \partial P_i/\partial \varepsilon_j \,|_u + \sum_k (\partial P_i/\partial u_{ik})(\partial u_{ik}/\partial \varepsilon_j). \tag{3.3}$$

where P_i is the induced polarization along the direction i as a result of an applied strain ε_j along the direction j. The P_i is calculated using the Berry Phase approach[90] as implemented in the VASP package with applied uniform strain, ranging from 1 % to -1 % in steps of 0.5 %, along the armchair side of the rectangular cell. At this point, in order to apply strain in a desired direction, the hexagonal primitive cell structure of each material is transformed to a tetragonal one composed of two hexagonal primitive cells[83], see Fig. 3.8. The first term in equation (3.3) is the clamped-ion or homogeneous strain contribution to the piezoelectric tensor and it mainly arises from the electronic contribution. The second term represents the contribution from the internal relaxation of ions. Here, u_{ik} is the fractional coordinate of the k^{th} atom along the i direction of the unit cell.

Since TMDs and TMDOs compounds have a non-centrosymmetric crystal structure, the inclusion of internal relaxation becomes essential in order to obtain re-

alistic piezoelectric properties. In addition, it is clear that the relaxed-ion piezoelectric coefficients are experimentally relevant quantities that can be measured. From the theoretical point of view, since the relaxed-ion piezoelectric coefficients include both electronic and relaxation effects, the calculation of the clamped-ion piezoelectric coefficients helps to separate the electronic and relaxation contributions from the relaxed-ion piezoelectric coefficients. The number of independent piezoelectric tensor coefficients is deduced from the symmetry of the crystal. For TMDs and TMDOs, we only need to calculate the e_{11} component of the piezoelectric stress tensor. e_{11} relates in-plane strain to in-plane electrical polarization. The piezoelectric coefficient e_{31} is zero due to the presence of an inversion centre between the two layers of chalcogenides. However, it is found to be non-zero for the unsymmetrical H and F co-decorated graphene[91, 92].

The corresponding piezoelectric strain tensor (d_{11}) of each material is predicted from the following relation[83]:

$$d_{11} = e_{11}/(C_{11} - C_{12}). \tag{3.4}$$

For each applied strain, the ions are kept in their strained positions or allowed to relax to their new equilibrium positions, and consequently the clamped-ion or relaxed-ion piezoelectric properties are calculated, respectively.

3.2.3 Computational details

Simulation program: VASP
Energy cut-off: 600 eV
Pseudopotentials: PBE-GGA(PAW), HSE06
k points (*Gamma* centered): 26×26×1
Vacuum: 15 Å
Energy and force convergence criterion: 10^{-3} eV and 10^{-7} eV/Å, respectively
strain applied: 1% to -1% in steps of 0.5%
stress and force: finite displacement method
polarization: Berry Phase expression [90] in VASP

3.2.4 Accurate band gaps from HSE06 hybrid functional

It is mandatory that a piezoelectric material has to be an insulator or semiconductor with a sufficiently wide band gap to avoid current leakage. Thus, we

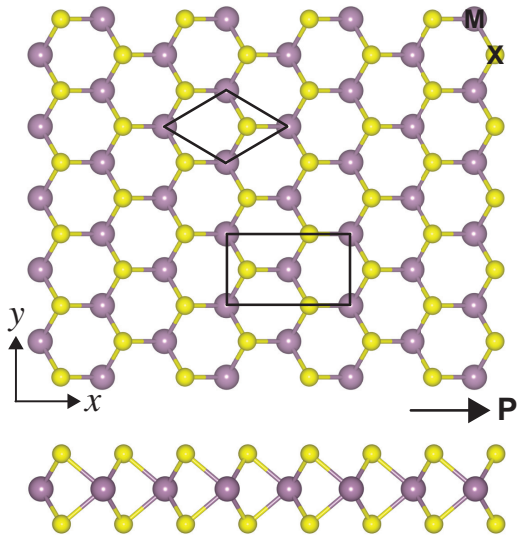

Fig. 3.8 Top and side views of MX_2 where M= Cr, Mo, W, Ti, Zr, Hf, Sn and X=O, S, Se, Te. P denotes the direction of the polarization. Piezoelectric calculations are done in a rectangular cell.

first calculate the electronic properties of twenty eight single layer MX_2 compounds, where M= Cr, Mo, W, Ti, Zr, Hf, Sn and X=O, S, Se, Te. We discard the metallic structures, namely $SnSe_2$, $SnTe_2$, and $TiTe_2$. Actually, G_0W_0 calculations predicted that 2H-$TiTe_2$ is a small band gap semiconductor material[93]. Since semi-local functionals are used in the Berry's phase calculations, 2H-$TiTe_2$ is excluded. For electronic structure calculations, we also applied the HSE06 hybrid functionals in order to obtain realistic electronic band gap values for TMDs and TMDOs. Fig. 3.9 shows the calculated PBE-GGA and HSE06 band gap values E_{gap}. The materials, except Cr, Mo, and W based TMDs, have indirect band gaps and the predicted values and trends are in good agreement with previous theoretical calculations[83, 94, 95]. Generally, the band gap increases when moving upwards in the chalcogens family from Te to S and with increasing atomic number in the transition metals. However, the latter trend is only partially valid when the compounds with O are included. The difference is that within the same row of the transition metals, TMDOs with a larger atomic number tend to have smaller band gaps which is in contrast to the TMDs case.

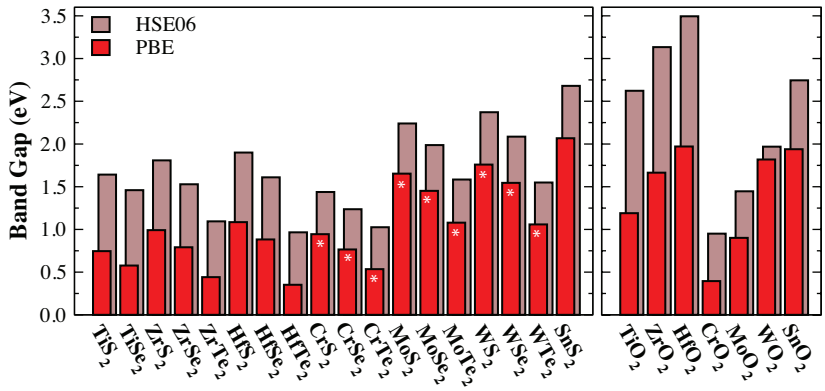

Fig. 3.9 The calculated PBE-GGA and HSE06 E_{gap} values for TMDs and TMDOs. Here, the white * sign indicates that it is a direct band gap material.

3.2.5 Elastic constants

As previously mentioned, we need to calculate the elastic constants in order to obtain the piezoelectric strain, d_{11} coefficients, see equation (3.4). Therefore, the relaxed-ion and clamped-ion elastic stiffness coefficients (C_{11} and C_{12}), Young modulus (Y= (C_{11}^2-C_{12}^2)/C_{11}) and Poisson's ratios (ν=C_{12}/C_{11}) for all 2D-TMDC and 2D-TMDO materials considered in this study are obtained and are listed in table 3.1. Our results are in good agreement with available data[50, 83, 96, 97]. The first observation from table 3.1 is that C_{11}, C_{12} and Y decrease with increasing row number of the chalcogenide atom. Except Zr, in each chalcogenide group, the MX_2 monolayer becomes stiffer with increase of the row number of the metal atom. Structures considered in this study are found to be less stiff when compared to graphene (Y=341 N/m)[69] and single layer *h*-BN (Y=275.9 N/m)[69]. Also it should be noticed that the calculated elastic constants are positive and satisfy the Born stability criteria for crystals having hexagonal symmetry[45, 98]. Note that the relaxed-ion elastic constants, i.e. C_{11} and C_{12}, are always smaller than the clamped-ion ones since the internal relaxation of ions allows to release some of the stress in the former, see table 3.1.

3.2.6 Piezoelectric stress/strain coefficients

Piezoelectric coefficients (e_{11}) are derived from the slope of the polarization change in Fig. 3.10) with applied uniform strain, ranging from 0.01 % to -0.01

Table 3.1 Calculated clamped and relaxed-ion elastic constants (in units of N/m), Young modulus Y (in units of N/m) and Poisson's ratio ν.

Material	Clamped Ion				Relaxed Ion			
	C_{11}	C_{12}	Y	ν	C_{11}	C_{12}	Y	ν
TiS_2	100.3	34.2	88.6	0.34	89.9	28.6	80.8	0.32
$TiSe_2$	84.8	29.3	74.7	0.35	74.4	24.4	66.4	0.33
ZrS_2	96.3	37.7	81.5	0.39	84.2	31.8	72.2	0.38
$ZrSe_2$	83.3	31.0	71.8	0.37	71.4	26.0	61.9	0.36
$ZrTe_2$	66.2	22.8	58.35	0.34	53.1	18.6	46.6	0.35
HfS_2	104.4	39.1	89.8	0.37	92.8	33.8	80.5	0.36
$HfSe_2$	89.7	32.2	78.1	0.36	78.8	27.8	69.0	0.35
$HfTe_2$	71.0	23.5	63.2	0.33	59.3	19.7	52.8	0.33
CrS_2	136.9	42.6	123.6	0.31	120.6	32.3	111.9	0.27
$CrSe_2$	111.3	37.5	98.7	0.34	96.6	28.9	87.9	0.30
$CrTe_2$	86.5	32.7	74.1	0.38	73.0	25.8	63.9	0.30
MoS_2	157.2	50.1	141.2	0.32	132.7	33.0	124.5	0.25
$MoSe_2$	133.2	40.8	120.7	0.31	106.9	25.6	100.8	0.24
$MoTe_2$	106.3	32.8	96.2	0.31	84.1	19.8	79.4	0.24
WS_2	174.7	51.9	159.3	0.30	146.5	31.8	139.6	0.22
WSe_2	147.4	41.1	135.9	0.28	102.4	23.1	115.9	0.23
WTe_2	115.4	31.6	106.8	0.27	89.2	15.7	86.4	0.18
SnS_2	92.8	23.1	87.1	0.25	91.0	22.2	85.6	0.24
TiO_2	178.9	80.9	142.3	0.45	173.7	75.7	141.7	0.44
ZrO_2	163.5	83.0	121.5	0.51	157.4	77.5	119.2	0.49
HfO_2	181.7	86.7	140.3	0.48	174.2	81.5	136.1	0.47
CrO_2	233.8	87.4	201.1	0.37	218.6	74.4	193.3	0.34
MoO_2	253.3	104.0	210.6	0.41	230.2	84.5	199.2	0.37
WO_2	286.2	109.0	244.7	0.38	261.2	87.8	231.7	0.34
SnO_2	165.7	52.4	149.1	0.32	160.2	53.3	142.5	0.33

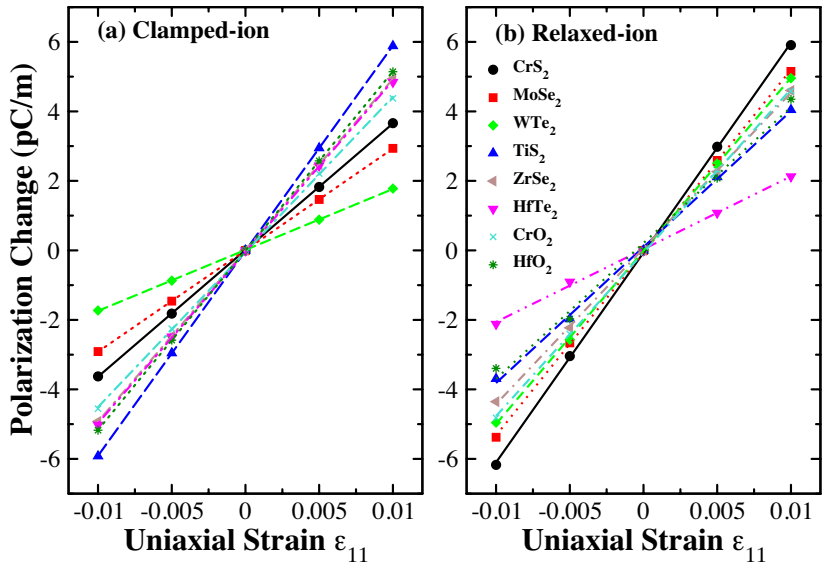

Fig. 3.10 (a) Clamped-ion and (b) relaxed-ion polarization change under applied uniaxial strain (ε_{11}) along the x direction for the selected 2D-TMDs and 2D-TMDOs structures. Piezoelectric coefficient is determined from the slope of the curves.

% in steps of 0.005 %, along the armchair side of the rectangular cell via Berry's Phase approximation[90]. The clamped-ion and relaxed-ion d_{11} coefficients are obtained by using the calculated e_{11} coefficients, and the elastic constants (C_{11} and C_{12}) via equation (3.4). Fig. 3.11 shows the calculated e_{11} and d_{11} coefficients for both TMDs and TMDOs. The materials are ordered along the x-axis by considering the period and group number of the transition metal element in the periodic table. The predicted relaxed-ion e_{11} and d_{11} coefficients are consistent with the available reference data[83, 99], see results for Cr, Mo and W based TMDs, which are comparable with the piezoelectric properties of single layer and bulk h-BN[83, 100–102]. In addition, the relaxed-ion e_{11} coefficient of single layer MoS_2 (4.91×10^{-10} C/m) is comparable with the experimentally measured piezoelectric coefficient of 2.90×10^{-10} C/m[84] and agrees well with the reported value of 3.64×10^{-10} C/m.[83]. In addition, the trends found for the e_{11} and d_{11} coefficients of Mo and W based TMDs are consistent with those found in Ref.[83]. The difference between our calculated piezoelectric coefficients and previous calculations is likely due to the use of different pseudopotentials, small differences in elastic constants, and other computational parameters (for instance k-mesh).

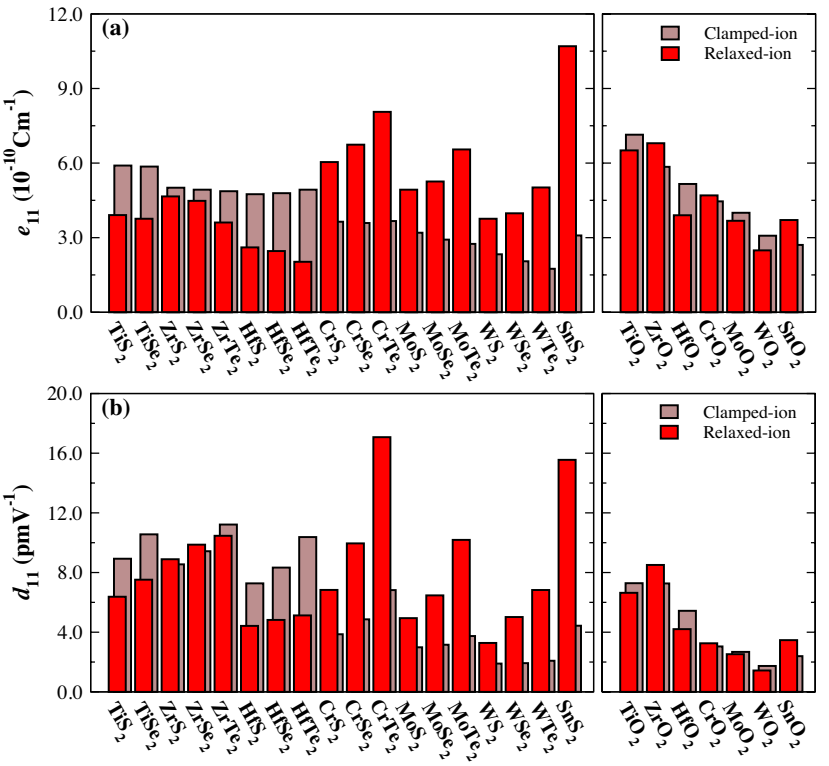

Fig. 3.11 The calculated clamped and relaxed-ion (a) piezoelectric stress (e_{11}) and (b) piezoelectric strain (d_{11}) coefficients.

SnS_2 has the highest e_{11} coefficient for the relaxed-ion (10.7×10^{-10} C/m) calculation. WO_2 has the smallest relaxed-ion piezoelectric stress coefficient (2.49×10^{-10} C/m) among TMDOs and WTe_2 has the smallest clamped-ion piezoelectric stress coefficient (1.75×10^{-10} C/m). From Fig. 3.11, we predict several periodic trends in clamped-ion e_{11} and d_{11} coefficients for TMDC and TMDO monolayers. The clamped-ion e_{11} coefficients of TMDs usually increase when moving from right to left in the periodic table (i.e., from CrX_2 to TiX_2) and upward in an individual group of both transition metal and chalcogen atoms. This trend is nearly the same for TMDOs. However, for TMDs, the trend (i.e., the increase in the calculated clamped-ion e_{11} coefficients when moving upward in the group of chalcogen elements) becomes reversed for the relaxed-ion calculations of group VIB elements as clearly seen in Fig. 3.11(a). The clamped and relaxed ion d_{11} coefficients increase when moving downward in the group of chalcogen elements (i.e. from S to Te) in each metal group. This trend can be

correlated to the polarizability of chalcogen atoms since the atoms are easily polarized when going downward in a specific group of the periodic table. We notice that the chalcogenide atoms have a much larger impact on the d_{11} coefficients as compared to the metal atoms. Especially in group VI, the d_{11} coefficient is maximized if one uses a smaller metal atom and a larger chalcogen atom. In group IVB, Zr does not exhibit the same trend that is found for the group VIB elements. This is partially because the C_{11} elastic constant of Zr based TMDs for a particular chalcogen atom is smaller that that of Ti and Hf based TMDs. Since TMDOs pose larger elastic constants, they usually have smaller d_{11} coefficients as compared to TMDs. In other words, the stronger the material the smaller the d_{11} coefficient.

Among the group VIB elements (i.e., Cr, Mo and W), Cr based TMDs and TMDOs are found to have much better piezoelectric properties in each chalcogenide group and $CrTe_2$ possesses the largest relaxed-ion e_{11} (8.06×10^{-10} C/m) and d_{11} (17.1 pm/V) coefficients. On the other hand, the relaxed-ion e_{11} and d_{11} coefficients of SnS_2 are almost the same as those of $CrTe_2$. The predicted relaxed-ion e_{11} values are much larger than the values previously predicted for surface decorated graphene structures[103]. Furthermore, when the piezoelectric coefficients of the extensively used bulk piezoelectric materials, namely 2.3 pm/V for α-quartz[104], 3.1 pm/V for wurtzite GaN[105] and 5.1 pm/V for AlN[105], are considered, we predict that TMDs and TMDOs have comparable or even larger relaxed-ion piezoelectric coefficients.

3.2.7 Importance of internal relaxation

It is essential to discuss the effect of the internal relaxation on the piezoelectric properties of TMDs and TMDOs. Relaxing the ion positions after applying strain significantly reduces (increases) the polarization of the Ti, Zr and Hf (Cr, Mo and W) based TMDs. As a result, the clamped-ion piezoelectric coefficients of the Ti, Zr and Hf (Cr, Mo and W) based TMDs monolayers are much larger (smaller) than that of the relaxed-ion coefficients. This means that the electronic contribution, i.e. the first term in equation (3.3), and strain contribution, i.e. the second term in equation (3.3), have opposite (the same) sign for the Ti, Zr and Hf (Cr, Mo and W) based TMDs. The calculated elastic constants suggest that Ti, Zr and Hf based

TMDs are more brittle materials that are expected to exhibit larger response to an applied strain, thereby giving rise to higher clamped-ion piezoelectric constants. For TMDOs, the contribution of internal relaxation to the e_{11} coefficient decreases when moving downward in an individual metal group. However, in each chalcogen group, the internal relaxation becomes generally less important when going from Te to S. This can be attributed to the large strain-induced ionic motion in response to an applied strain. In other words, after applying strain, the amount of the internal relaxation of the chalcogen atoms increases from S to Te, giving rise to a larger internal relaxation contribution to the piezoelectric coefficients in Te based TMDs. Since Te is the most easily polarizable atom among the chalcogenide atoms (due to its larger size), the polarization effects (and hence electronic contribution to the e_{11} coefficient) are found to be large in Te based TMDs as compared to S and Se counterparts. However, the increase in piezoelectricity effects competes with the degradation of stability.

3.2.8 Summary

In summary, we presented a detailed theoretical investigation of the piezoelectric properties of semiconductor TMDC and TMDO monolayers. Our calculations show that TMDC and TMDO structures are strong candidates for future atomically thin piezoelectric applications. We show that Ti, Zr, Sn and Cr based TMDs and TMDOs have much better piezoelectric properties as compared to Mo and W based TMDs and TMDOs and the well-known conventional bulk piezoelectric materials. The usage of these 2D piezoelectric materials in ultra sensitive sensors, low-power electronics and nanoscale electromechanical systems are expected to have an impact on the size reduction, weight and energy consumption of such devices.

3.3 Magnetic properties of penta-hexa-graphene[3]

3.3.1 Introduction

In **??**, we have seen that graphene derivatives [106, 107] are also the subject of intensive research to either modify their known properties or to increase their functionality. Considering the very low SOC and long spin relaxation time in these systems, substantial effort has been devoted to the induction of magnetism in these metal-free materials with the aim for future spintronic devices[108, 109]. Intrinsic magnetism in graphene is absent, but extrinsic magnetism has been achieved by means of partial hydrogenation[110, 111], foreign atom substitution[112, 113] and the introduction of defects[114, 115].

Three types of orbital hybridization are usually found in carbon allotropes, namely sp, sp^2 and sp^3. While graphene is made of a network of sp^2 hybridized atoms connected through σ and π bonds of p_z orbitals, diamond is exclusively held together by σ bonds between sp^3 bonded atoms. Another class of carbon allotropes is formed by the graphynes and graphdiynes[116, 117]. These flat materials contain a mixture of sp and sp^2 hybridized C atoms. Structures containing a mixture of sp^2 and sp^3 atoms, such as penta-graphene[118], have been studied as well. This last structure contains a mixture of threefold and fourfold coordinated C atoms. This leads to a distorted structure with non-ideal bond angles that has higher formation energy than the non-distorted graphene and diamond crystals with their ideal planar and tetrahedral bonding geometry. Therefore, a system with a local bond structure resembling that of graphene or diamond will have lower energy.

None of the above mentioned materials are magnetic because they contain only paired electrons. Local magnetic moments usually originate from lone electrons that are not involved in chemical bonding. Single atomic defects such as vacancies break covalent bonds and create lone electrons that can give rise to magnetism. It is interesting to investigate whether a structural modification with a proper mixing of three- and fourfold coordinated C atoms can lead to local magnetic moments in a stable crystalline structure. In this work, we propose such a new type of 2D carbon allotrope with non-trivial magnetic properties. This

[3]This work is published: P8.

structure is composed of a mixture of pentagonal and hexagonal rings of carbon atoms and will be called penta-hexa-graphene (ph-graphene). This new material has an antiferromagnetic (AFM) ground state which transforms to a ferromagnetic (FM) state under strain. The latter state is protected by a small strain-induced energy barrier. These findings can initiate further research to induce magnetism and spin-flip barriers through strain in other metal-free 2D materials.

While finishing this work, Zhang et al. [119] reported our proposed structure in their supplementary materials. However, a detailed study of the physical properties, especially the magnetic properties, of this structure was not reported.

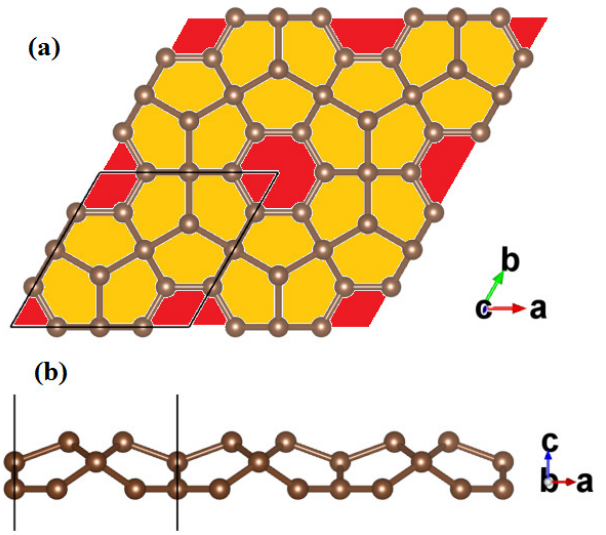

Fig. 3.12 Atomic structure of a 2×2 supercell of monolayer ph-graphene. (a) Top view with hexagonal and pentagonal rings marked with red and yellow color, respectively; (b) Side view of the buckled structure. (Visualisation using VESTA [120])

3.3.2 Computational details

Simulation program: VASP
Energy cut-off: 500 eV
Pseudopotentials: PBE-GGA(PAW)
k points (*Gamma* centered): 15×15×1
Vacuum: 25 Å

Energy and force convergence criterion: 10^{-8} eV and 10^{-7} eV/Å, respectively
Supercell for phonon calculation: 3×3×1
phonon calculation: Density functional perturbation theory (DFPT)

3.3.3 Bond hybridization and magnetic moment

The structure of the proposed 2D material is schematically shown in Fig. 3.12. It consists of hexagonal rings of C atoms surrounded by six pentagonal rings which share one edge with the hexagon and four with other pentagons. These hexagonal and pentagonal rings are arranged in a hexagonal lattice to form an infinite monolayer sheet. Considering the complex structure of this system, it is important to understand the hybridization of the electronic orbitals. For this, we calculate the hybridization index of the three C atoms that have a unique local environment, namely C1, C2 and C3 in Fig. 3.13, through Coulson's theorem: $1 + \sqrt{n_1 n_2}\, cos\theta_{12} = 0$, where θ_{12} is the interorbital angle between orbital 1 and 2 (see Fig. 3.13) and n is the hybridization index. n corresponds to the index in the sp^n notation and determines the relative fraction of p orbitals with respect to the s orbital. The sum of the s fractions in all hybridized orbitals should equal 1, while it should be 3 for the sum of the p fractions.

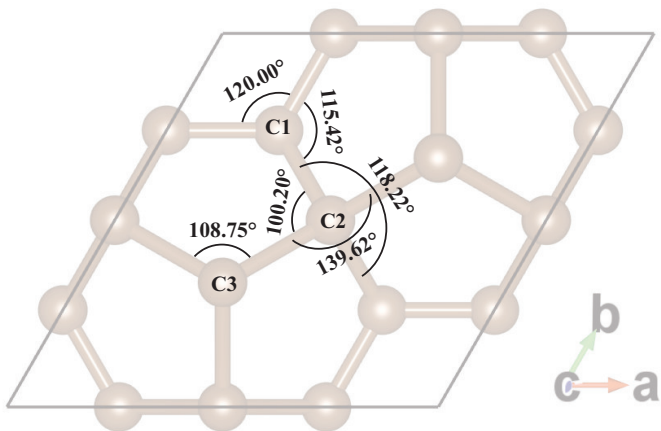

Fig. 3.13 Bond angles in the unit cell of monolayer ph-graphene.

In table 3.2, we list the hybridization indices of the C1 and C3 orbitals, φ. The C1 atom has two sp^2 orbitals with 120° interorbital angle and one $sp^{2.72}$. The latter gives rise to a partly buckled structure. The fourth C1 orbital has a large

Table 3.2 Orbital hybridization indices n for four orbitals φ of the C atoms in ph-graphene.

Atom	φ_1	φ_2	φ_3	φ_4
C1	2.00	2.00	2.72	14.58
C3	3.11	3.11	3.11	2.70

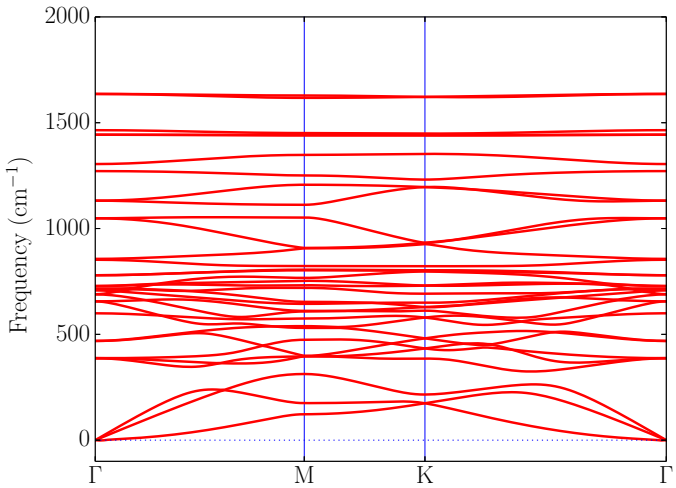

Fig. 3.14 Phonon dispersion relation of monolayer ph-graphene.

p contribution, indicating that it is close to a p_z orbital with little s contribution, and induces π bonding in the hexagonal rings. The C2 atoms have fourfold coordination and their hybridization should be close to sp^3. Due to geometric constraints, the bonds have strained angles[32]. Finally, the C3 atom has four quasi-sp^3 orbitals of which three are used for nearest-neighbor σ bonding. The electron in the fourth orbital remains unpaired and can give a local magnetic moment of 1 μ_B (Bohr magneton). There are two C3 atoms per unit cell which form a graphene-like subcrystal. The maximal magnetic moment per unit cell is therefore $2\mu_B$ if the system is ferromagnetic. However, when we align these two magnetic moments antiparallel, the total energy is lowered by 12 meV per magnetic atom, which gives an AFM ground state.

In comparison to penta-graphene, ph-graphene has a 76 mev/atom lower formation energy. However, it is about 0.9 eV/atom higher than that of graphene. The relatively high formation energy of ph-graphene as compared to graphene

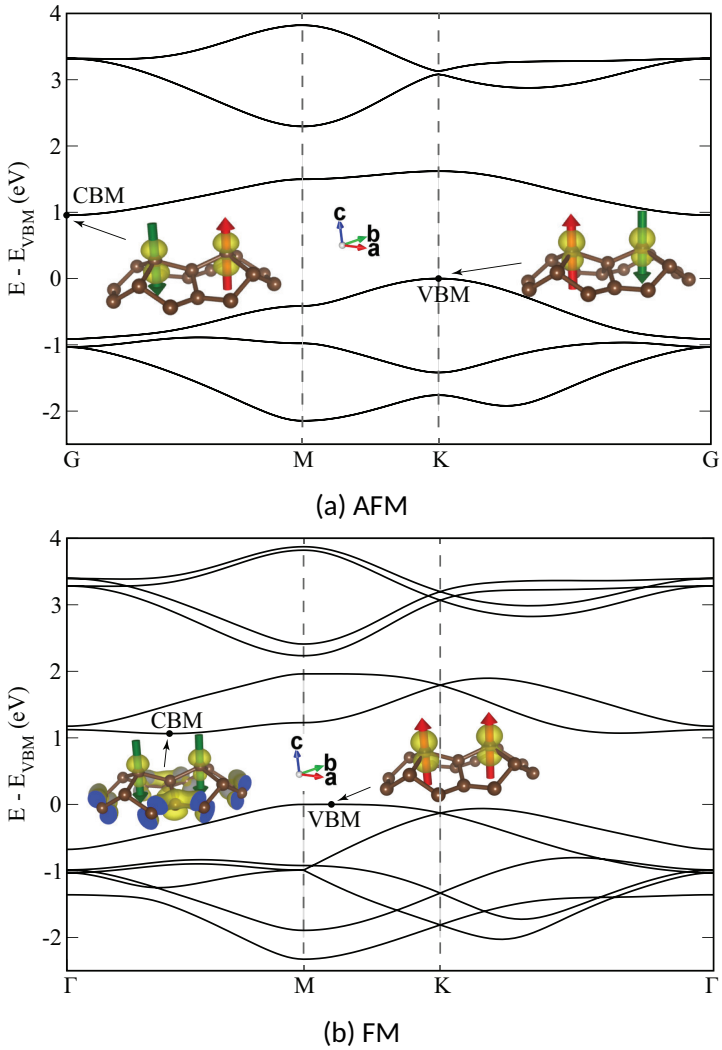

Fig. 3.15 Electronic band structure of monolayer ph-graphene. The charge densities at the VBM and CBM in the unit cell are shown as insets. The arrows on the atoms indicate the orientation of their magnetic moments.

can be mainly attributed to the "bent" bonds of the C2 atoms due to geometric constraints.

To check the dynamical stability of the ph-graphene structure we calculated its phonon spectrum (see Fig. 3.14). Since there are no imaginary frequencies, we can conclude that the structure is dynamically stable.

The electronic band structure and the charge densities at the VBM and CBM are shown in Fig. 3.15. Both the FM and AFM states exhibit indirect semiconducting character with a band gap (PBE) of 1.06 eV and 0.96 eV, respectively. The band edge states are mainly located on the magnetic atoms and the band gap separates states of opposite spin orientation. The hybridized φ_4 states (see above) on these atoms form a π bonding network that resembles the p_z π bonding in graphene. For the FM state, the typical graphene-like band structure that results from this can be observed for the valence and conduction bands. These bands are separated due to the ferromagnetic exchange splitting in spin-up and spin-down states with a large gap in between. Note that the splitting between bonding and anti-bonding states at the Γ point is strongly reduced with respect to graphene because of the larger interatomic distance separating the C3 atoms (3.1 Å in ph-graphene *vs* 1.4 Å in graphene). Due to this increased bonding distance, the exchange interaction exceeds the bonding interaction and the system is magnetic in stark contrast to graphene where the π bonding is much stronger.

3.3.4 Summary

In this work, we proposed a new type of stable monolayer carbon allotrope composed of pentagonal and hexagonal rings of carbon atoms. We explained the symmetry and the structure of the bonds that result in local magnetic moments. By comparing the total energy of the FM and AFM state, we conclude that the latter is the ground state. Our theoretical calculations give insight in the magnetic mechanism in this metal-free material, which can initiate further work on the exploration of magnetic properties of other 2D metal-free material.

3.4 Lithium battery related properties of MXenes/ graphene heterostructure[4]

3.4.1 Introduction

Lithium ion batteries (LIBs) are widely used for electrochemical energy storage in electrical vehicles and portable electronic devices such as cell phones. The speed of development in these state of the art products mostly hinges on the progress in battery technology. The energy density and rate capability of both LIBs and sodium ion batteries (NIBs) are currently insufficient to satisfy costumers' needs. Therefore, the demand for metal based new generation batteries that have large reversible energy/power capacity, good cyclic stability and long life span is growing. Recently, rechargeable batteries based on 2D materials have received great attention because of their promising potential as anode materials with enhanced gravimetric and volumetric energy densities which is a key challenge in current rechargeable ion battery technology. For instance Mo_2C was shown to exhibit much better electrochemical properties in lithium-ion battery applications,[121]. Moreover, other 2D layered materials such as transition metal dichalcogenides,[122, 123], black phosphorus[124, 125], and MXenes (with M = Ti, V, Nb, Mo and X = C, N)[126] have also been widely investigated because of their high energy storage density and high rate capacity. However, experimental studies have shown that single type layered nanosheets inevitably restack during the cycling process, resulting in a rapid capacity fading and poor rate performance.

Therefore, current interest has been directed towards heterostructured[127, 128] 2D materials. A clever design of vertical heterostructures from different 2D materials is expected to be beneficial for rapid electron transport and accelerated cation transport in the electrodes, and thus is expected to improve the rate performance in current battery technology[128]. In addition, the negligible volumetric changes of in particular TMDs and MXenes under lithiation/delithiation processes, such that there is only 5% in-plane lattice expansion in the Mo_2C lattice caused by Li intercalation[129], can minimize the intrinsic volumetric changes during charging/discharging processes which prolongs the cycling lifetime of the rechargeable batteries. Furthermore, combining different 2D ma-

[4]This work is submitted: P10.

terials is a promising way to adjust the interlayer distance to accommodate much larger (i.e. Na^+) and more polarized (i.e. Mg^{2+}) ions. For instance, lithium-ion capacity in excess of 750 mAh g^{-1}[130] has already been demonstrated for the batteries with MXene electrodes, optimized with CNTs.

To this end, we systematically investigated Li intercalation in vertical (van der Waals) heterostructures of MXenes and graphene for rechargeable battery applications. We only considered MXenes functionalized with OH and O, since the experimentally synthesized MXenes are often functionalized with various radicals due to chemical exfoliation. In addition, MXenes with low formula weights, such as Ti_2C, Nb_2C, V_2C and Sc_2C have been found to be most promising[131] materials in battery applications due to their theoretically stated gravimetric capacity, which represents the amount of charge that can be stored per gram of material. Therefore, we considered only M_2CX_2 (where M=Sc, Ti, V and X=OH, O) monolayers in this study. V_2CX_2 is particularly important since it shows the largest Li^+ capacity of all MXenes tested under similar conditions[132]. Another advantageous is that, compared to bilayer M_2CX_2, M_2CX_2/graphene hetorostructure has a much smaller weight, offering much larger storage capacity.

We introduce the following nomenclatures in the following sections: M stands for the transition metal in MXenes; X stands for the functionalized group, i.e. OH or O; Gr stands for graphene; Li is intercalated Li atom (unless the concentration is stated it means only single Li atom intercalation); Monolayer and bilayer are denoted with mono- or bi- prefixes. For instance: bi-Ti_2CO_2+Li stands for bilayer Ti_2CO_2 with a single Li atom intercalation, and Ti_2CO_2+Gr+Li stands for heterostructure of Ti_2CO_2 on graphene with a single Li atom intercalation.

3.4.2 Computational details

Simulation program: VASP
Energy cut-off: 500 eV
Pseudopotentials: PBE-GGA(PAW)
k points (Γ centered): $7\times7\times1$ to $11\times11\times1$
Vacuum: 30 Å
Energy and force convergence criterion: 10^{-5} eV and 10^{-3} eV/Å, respectively
vdW interactions: DFT-D3 method Grimme et al. [133] including Becke-Johnson damping
Charge analysis: Bader analysis [134–137]

In addition, we calculated diffusion barriers for Li ions using the climbing-image nudge elastic (cNEB) method as implemented in the VASP transition state tools[138, 139]. The cNEB method is an efficient method to determine the minimum energy diffusion path between two given positions. We used at least 7 images, including initial and final positions, for cNEB calculations. The atomic positions and energy of the images were then relaxed until the largest norm of the force orthogonal to the path is smaller than 0.01 eV/Å.

3.4.3 Heterostructure stacking types

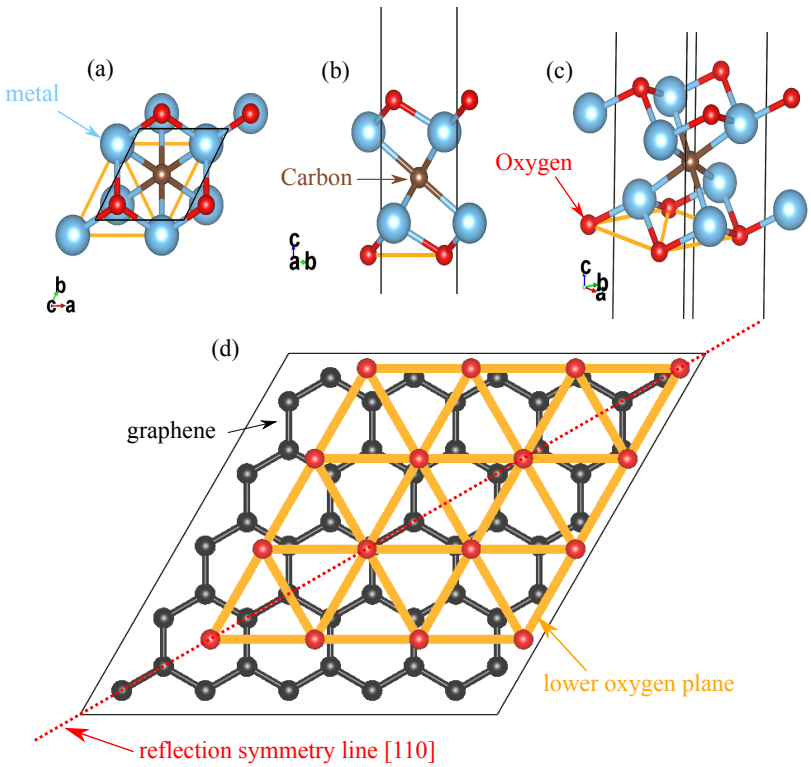

Fig. 3.16 An example structure of mono-Ti_2CO_2 with (a) top view, (b) side view, and (c) tilted view. (d) Simplified example of the M_2CX_2+Gr heterostructure in its ground state stacking.

First of all, we constructed the MXene-Graphene heterostructures by considering super cells such that we have a minimum lattice mismatch between the

Table 3.3 A comparison of different MXenes systems: monolayer, bilayer, and heterostructure. d is the interlayer distance and is defined as shown in Fig. 3.17. E_b is the binding energy of the system with respect to its components, e.g bilayer with respect to monolayers. Only the ground state stacking of M_2CX_2+Gr is reported.

Material	Structure	d Å	E_b eV/atom
graphene	bi-Gr (AB)	3.277	-0.024
	bi-Gr (AA)	3.325	-0.020
Sc_2CO_2	bi-Sc_2CO_2	2.294	-0.029
	Sc_2CO_2+Gr	3.067	-0.022
$Sc_2C(OH)_2$	bi-$Sc_2C(OH)_2$	0.598	-0.025
	$Sc_2C(OH)_2$+Gr	2.191	-0.027
Ti_2CO_2	bi-Ti_2CO_2	2.396	-0.027
	Ti_2CO_2+Gr	3.000	-0.018
$Ti_2C(OH)_2$	bi-$Ti_2C(OH)_2$	0.399	-0.024
	$Ti_2C(OH)_2$+Gr	2.097	-0.034
V_2CO_2	bi-V_2CO_2	2.394	-0.025
	V_2CO_2+Gr	2.867	-0.022
$V_2C(OH)_2$	bi-$V_2C(OH)_2$	0.398	-0.011
	$V_2C(OH)_2$+Gr	2.779	-0.035

layers. Therefore, heterostructures with a 3×3 super cell of Sc_2CO_2 or $Sc_2C(OH)_2$ with a 4×4 super cell of graphene, a 4×4 super cell of Ti_2CO_2 or $Ti_2C(OH)_2$ with a 5×5 super cell of graphene, and a 5×5 super cell of V_2CO_2 or $V_2C(OH)_2$ with a 6×6 super cell of graphene were constructed, see Fig. 3.16 for a representative example. In order to find out the ground state stacking type of these, M_2CX_2+Gr heterostructures, we calculated the binding energy of possible stacking configurations by shifting the M_2CX_2 layer over the unit cell of graphene on a uniform mesh. In the course of these simulations, each layer in the heterostructure is regarded rigid where only the interlayer distance is allowed to relax. The corre-

sponding binding energy per atom, E_b was calculated as follows:

$$E_b = \frac{1}{N}[E(M_2CX_2 + Gr) - E(M_2CX_2) - E(Gr)], \tag{3.5}$$

where $E(M_2CX_2$+Gr), $E(M_2CX_2)$ and E(Gr) are the total energies of M_2CX_2+Gr, mono-M_2CX_2 and Gr, respectively. N is the total number of atoms in the super cell. In table 3.3, the calculated E_b and the interlayer distance for M_2CX_2+Gr are given for all the considered systems. The results for graphene bilayer are also given as reference. The interlayer binding energy and the distance of AB stacked bilayer graphene are 24 meV/atom and 3.28 Å, respectively. Our calculations agree very well with a recent work in which quantum Monte Carlo simulations predicted a 18 meV/atom binding energy and 3.38 Å interlayer separation for bilayer graphene[140]. The calculated binding energies (i.e. E_b) are negative for all the considered heterostructures, demonstrating the stability of each system against phase separation. The magnitude of E_b for the ground state stacking in MXene oxides/graphene are comparable to that of bilayer graphene, whereas the hydroxides/graphene are slightly stronger bonded due to the extra hydrogen bonds. The differences in binding energy among different MXenes that have the same functionalized group are negligible.

3.4.4 Single Li intercalation and its binding energy

Using the calculated ground state stacking types of all the M_2CX_2+Gr heterostructures, we investigated the Li intercalation in these structures. To systematically uncover the potential of M_2CX_2+Gr heterostructures for battery applications, we also considered Li intercalation on mono-M_2CX_2, within bi-M_2CX_2 and within bi-Gr. These additional reference calculations were performed with the same system dimensions, or equivalently the same Li atom concentration, as in the corresponding heterostructures.

Previous studies[141–143] pointed out that the strongest binding of the Li atoms occurs for bilayer heterostructure. They reported a non-binding character of Li atoms on the surface of few-layer graphene. Therefore, in this study, we limited ourselves to the intercalation between M_2CX_2 and graphene. In addition, inspired by the previous study[144] on the location of the Li absorption site in M_2CX_2 multilayer system, we found that the intercalated Li atom is bound close

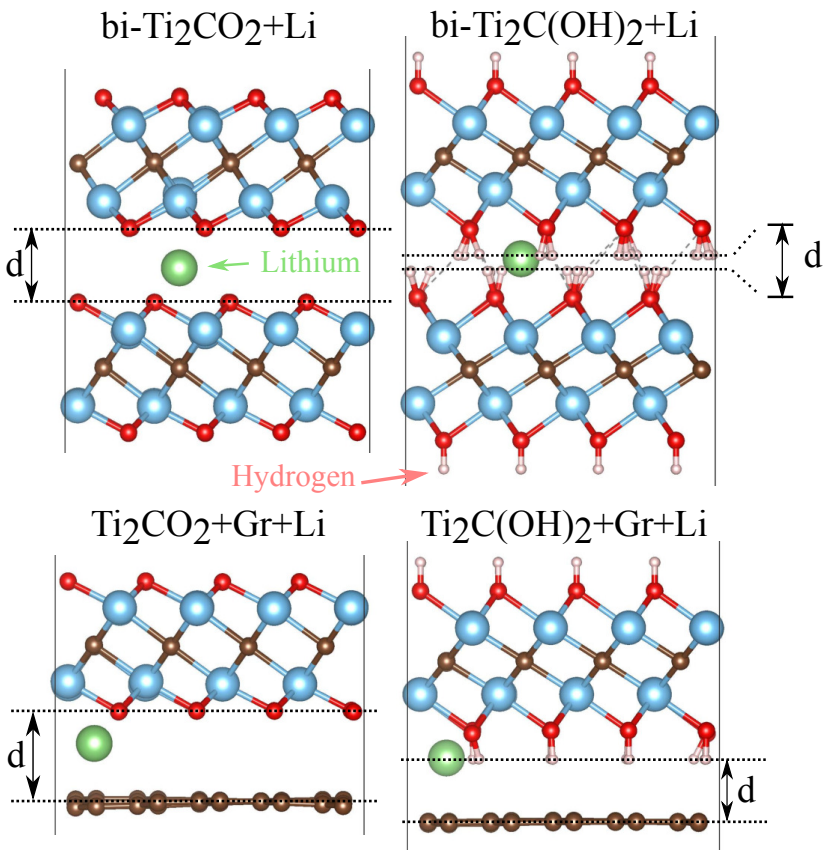

Fig. 3.17 The optimized locations of single Li atoms in different structures and the definition of interlayer distance d, which ignores the Li atom layer..

to the M_2CX_2 layer and far from graphene, and it resides between three O atoms. Thus, each formula unit of M_2CX_2 in heterostructure can accommodate one Li atom. Additional Li atoms occupy the same position in other unit cells, as shown in Fig. 3.18. Note that the ground state stacking has reflection symmetry, and therefore we may limit ourselves to investigate Li positions only on one side of the symmetry line [110] for single Li absorption. A strong binding between Li and M_2CX_2+Gr bilayer is necessary to avoid the formation of metallic lithium, which well improves the safety and reversibility of lithium-ion batteries. Therefore, we need to make sure that the reported Li binding energy as large as possible. We calculated all the possible adsorption sites between the two layers, here I only present the ground state configuration.

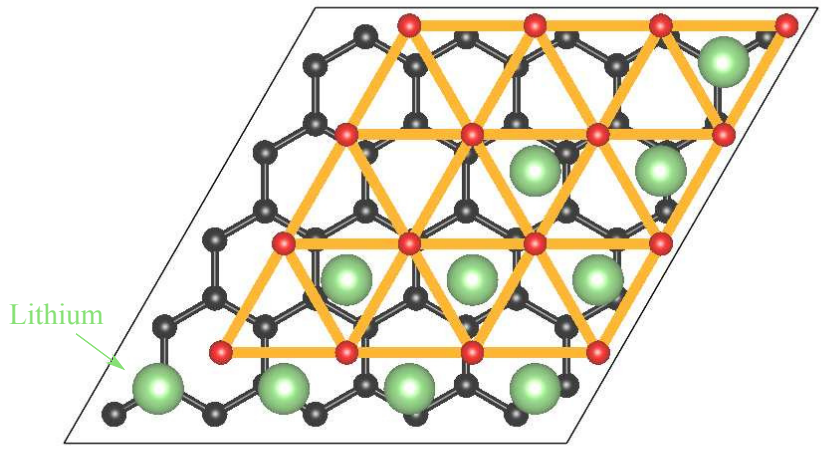

Fig. 3.18 The locations of Li atoms intercalation between Ti_2CO_2+Gr heterostructure as an example.

The binding energy, E_b^{Li}, for Li intercalated systems is defined through the following equation:

$$E_b^{Li} = \frac{1}{x}[E(\text{with } x\text{Li}) - E(\text{without Li}) - xE(\text{Li})], \tag{3.6}$$

where $E(\text{with } x\text{Li})$ and $E(\text{without Li})$ are the total energies of system with and without x Li atoms, respectively. $E(\text{Li})$ is the total energy of a Li atom in its most stable bcc bulk structure. Here, a more negative binding energy indicates a more favourable exothermic binding of Li.

In table 3.4, the results for three different promising systems are shown. For comparison, we also calculated Li intercalation in AA and AB stacked graphene bilayers. While the latter is more stable than the former for the pristine systems, the former is energetically more favorable for Li intercalation, which is consistent with previous calculations[145], see table 3.4. The LiC_{64} (4×4 bilayer graphene) in AA configuration is energetically favorable to accommodate single Li between bilayer, while the Li atom will not bind at all in the AB stack bilayer configuration. However, the magnitude of the binding energy generally is small as compared to the heterostructure due to the strong interaction of Li with the M_2CO_2 layer.

Our results can be summarized as follows: (1) All the systems related to Sc_2CO_2 experience severe structural distortion upon Li interactions. Two or three of the C atoms in the Sc_2CO_2 move towards each other and show the tendency

to cluster. Therefore, this type of system is unstable for Li intercalation. (2) The binding of a Li atom on mono-$M_2C(OH)_2$ is not favorable. This can be attributed to the Coulomb repulsion between positively charged Li ion and H atoms. (3) When going from mono- to bi-$M_2C(OH)_2$+Li, Li adsorption is made stable again through the van der Waals interaction that competes with foregoing repulsive interaction. (4) Mono-M_2CO_2+Li, bi-M_2CX_2+Li and M_2CX_2+Gr+Li exhibit the strongest adsorption for Li atoms. The calculated E_b^{Li} value at the largest binding energy site is -1.87 eV/atom for the mono-Ti_2CO_2 and -2.97 eV/atom for the mono-V_2CO_2. In the case of M_2CX_2+Gr+Li, we observed that E_b^{Li} slightly decreases for M=Ti and V and X=O. This may be correlated to the reduced vdW interaction with respect to the pristine bilayers due to the increase in interlayer separation. (5) We have identified three promising candidates with large Li atom adsorption energy, namely $Sc_2C(OH)_2$+Gr+Li, Ti_2CO_2+Gr+Li and V_2CO_2+Gr+Li. Therefore, for the rest of the paper, we will focus on these three systems and will study the kinetics of Li diffusion.

3.4.5 Effect of Li concentration

As a next step, we investigated the effect of Li ion concentration on the physical properties of M_2CX_2+Gr+Li heterostructures. Here, the concentration is defined as the ratio of the number of Li atoms and the number of formula unit of M_2CX_2 in the heterostructures (e.g. 100% corresponds to one Li atom for each formula unit). Fig. 3.19(a) shows the variation of the average E_b^{Li} as a function of concentration of Li ions (i.e. x). As the number of intercalated Li increases, the average E_b^{Li} decreases gradually. The reduction in binding energy is due to two main factors; One is the weak electrostatic attraction between M_2CX_2+Gr host and the Li cations, and the other one is the enhanced Li-Li repulsion at high Li concentration. The former is correlated with the reduction of charge transfer from the Li atom to M_2CX_2+Gr complex at high concentrations, as shown in Fig. 3.19(b). Similarly, the latter is due to the reduction of interatomic distances between positively charged Li ions. Above a critical concentration value, namely 80%, E_b^{Li} becomes positive for $Sc_2C(OH)_2$+Gr+Li, and the system becomes energetically unstable for further Li insertion. E_b^{Li} is always negative for Ti_2CO_2+Gr+Li and V_2CO_2+Gr+Li, suggesting that these heterostructures are stable against Li in-

Table 3.4 A comparison of different MXenes systems: monolayer, bilayer, and heterostructure with Li intercalation. d is the interlayer distance and is defined as shown in Fig. 3.17. E_b^{Li} is the binding energy of a single Li atom. Only the largest binding energy of Li atom is reported, i.e. ground state adsorption site. L_{min} is the shortest bond length of a Li atom with others. The charge transfer from a Li atom to a heterostructure is in units of e. For consistency of the Li concentrations, all monolayer and bilayer systems use the same dimensions as in the corresponding heterostructures. Three different sizes of bi-Gr are presented to compare with the heterostructures with corresponding size of Gr.

Material	Structure	d Å	E_b^{Li} eV/atom	L_{min} Å	Li charge transfer e
graphene	4×4 bi-Gr (AB)+Li	3.591	0.030	2.060	0.873
	4×4 bi-Gr (AA)+Li	3.616	-0.232	2.344	0.868
	5×5 bi-Gr (AA)+Li	3.617	-0.283	2.344	0.878
	6×6 bi-Gr (AA)+Li	3.636	-0.336	2.352	0.879
Sc_2CO_2 (unstable)	mono-Sc_2CO_2+Li	-	-9.986	2.024	0.898
	bi-Sc_2CO_2+Li	1.791	-32.646	2.208	0.902
	Sc_2CO_2+Gr+Li	2.874	-19.885	1.958	0.887
$Sc_2C(OH)_2$	mono-$Sc_2C(OH)_2$+Li	-	0.048	1.918	0.869
	bi-$Sc_2C(OH)_2$+Li	0.548	-0.309	2.050	0.885
	$Sc_2C(OH)_2$+Gr+Li	2.278	-0.941	1.953	0.877
Ti_2CO_2	mono-Ti_2CO_2+Li	-	-1.870	1.994	0.912
	bi-Ti_2CO_2+Li	2.480	-2.308	2.047	0.886
	Ti_2CO_2+Gr+Li	2.976	-1.729	1.993	0.887
$Ti_2C(OH)_2$	mono-$Ti_2C(OH)_2$+Li	-	0.146	1.926	0.792
	bi-$Ti_2C(OH)_2$+Li	0.599	-0.431	2.004	0.879
	$Ti_2C(OH)_2$+Gr+Li	2.090	-0.229	1.941	0.875
V_2CO_2	mono-V_2CO_2+Li	-	-2.791	1.975	0.921
	bi-V_2CO_2+Li	2.500	-3.573	2.009	0.887
	V_2CO_2+Gr+Li	2.779	-2.537	1.957	0.891
$V_2C(OH)_2$	mono-$V_2C(OH)_2$+Li	-	-0.175	1.878	0.860
	bi-$V_2C(OH)_2$+Li	0.395	-1.336	1.995	0.878
	$V_2C(OH)_2$+Gr+Li	2.080	-0.304	1.912	0.878

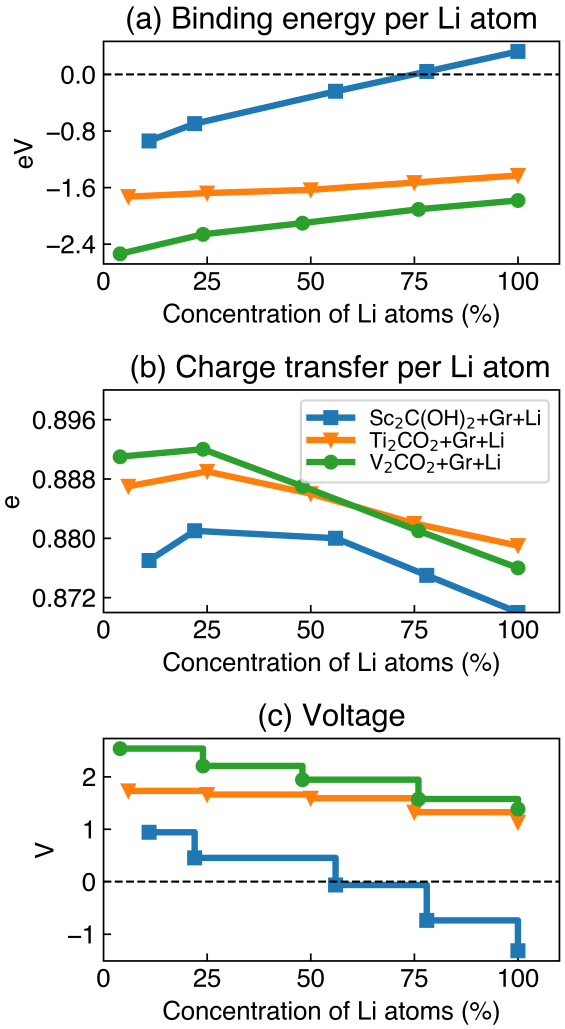

Fig. 3.19 The average binding energy (a), the average charge transfer (b) of Li atoms, and the voltage profile of M_2CX_2+Gr heterostructure as a function of Li concentration.

tercalation, and thus we can safely disregard the phase separation into individual monolayers and bulk Li at high concentrations. In other words, the Ti_2CO_2+Gr+Li and V_2CO_2+Gr+Li structures are highly stable even for high Li concentrations. For V_2CO_2+Gr+Li (Ti_2CO_2+Gr+Li), E_b^{Li} may vary by about 1 (0.5) eV as a function of Li concentration. Recently, Sun et al. [146]reported that V_2CO_2 undergoes a reversible structural transformation during the adsorption of Li. We also checked the possibility of such structural transformation for V_2CO_2+Gr bilayer and we found that the presence of graphene prevents the transformation of V_2CO_2. Our results clearly demonstrated that Ti_2CO_2+Gr+Li and V_2CO_2+Gr+Li can be utilized as an anode material for high capacity Li ion batteries.

Another important point is how the structural stability of Ti_2CO_2+Gr+Li and V_2CO_2+Gr+Li is affected as the Li ion concentration is increased. We found that an increase in the number of Li ions leads to a small expansion in the in-plane lattice constants. For instance, the in-plane lattice constant of both V_2CO_2+Gr+Li and Ti_2CO_2+Gr+Li increase by less than 1%. Besides, we did not observe any severe lengthening of the surface Ti/V-O bonds and shortening of Li-O bonds for both Ti_2CO_2+Gr+Li and V_2CO_2+Gr+Li heterostructures. For instance, Li-O bond length decreases with most 3% with increasing Li concentration. It is also found that Li intercalation slightly enlarges and later reduces the interlayer separation as the Li concentration increases. The calculated interlayer separation suggests that we can have at most 0.5 Å expansion as a result of Li intercalation. These results clearly show that these layered M_2CX_2+Gr heterostructures possess a reversible reaction process, which is necessary for rechargeable ion batteries and thus they can effectively defy the volume expansion problem faced by present day electrode materials. However, $Sc_2C(OH)_2$+Gr is unstable against Li loading at higher concentration.

3.4.6 Electrochemical properties

In order to gain insight into the electrochemical properties of the Li intercalation process into the M_2CX_2+Gr heterostructure, the open-circuit-voltage was obtained by calculating the averaged half cell voltage over a range of metal ion

concentrations x, where $x_1 \leq x \leq x_2$, using,

$$V \approx \frac{E_{M_2CX_2+Gr+x_1Li} - E_{M_2CX_2+Gr+x_2Li} + (x_2 - x_1)E_{Li}}{(x_2 - x_1)e} \tag{3.7}$$

where $E_{M_2CX_2+Gr+Li_{x_1}}$ and $E_{M_2CX_2+Gr+Li_{x_2}}$ are the total energies of the M_2CX_2+Gr heterostructure with x_1 and x_2 Li intercalated, respectively. E_{Li} is the total energy of bulk bcc Li. First of all, our calculations show that the charging voltage for Li intercalation decreases with increasing in Li ion concentration, as clearly seen in Fig. 3.19(c). The calculated average voltage corresponding to $Sc_2C(OH)_2$+Gr+Li is negative for a Li ion concentration x larger than 55%. As mentioned above, a phase transition should be expected for the concentrations larger than this critical value. Our results are consistent with a recent work reporting that H and/or OH should be avoided if possible since they result in a lower capacity and negative cell voltage[147, 148]. On the other hand, the available intercalation sites in Ti_2CO_2+Gr+Li and V_2CO_2+Gr+Li composites can be fully occupied. As we increase the Li concentration from x=50% to 100%, the open-circuit voltage decreases from 1.59 (1.94) V to 1.13 (1.38) V for Ti_2CO_2+Gr+Li (V_2CO_2+Gr+Li). The binding energy change (i.e E_b^{Li}) with the Li ion concentration which can be correlated with the voltage value. Since V_2CO_2+Gr+Li has the largest Li binding energy, the calculated voltage value is also the largest. The calculated average voltage profile is 1.49 V for Ti_2CO_2+Gr+Li and 1.93 V for V_2CO_2+Gr+Li, which are higher than those of Mo_2C[129], graphite[149] and TiO_2 electrode [150] and lower than for phosphorene[151]. Experimentally measured maximum voltages for pure V_2CO_2 and Ti_2CO_2 anodes are 3.0 V and 2.5 V, respectively[131, 152]. Combining graphene with V_2CO_2 or Ti_2CO_2 reduces the maximum voltages by about 0.5 V. Approximately 50% of the capacity of V_2CO_2+Gr+Li (Ti_2CO_2+Gr+Li) is intercalated above 2 (1.6) V, with the rest intercalating at lower voltages. Our results clearly demonstrate that Ti_2CO_2+Gr+Li can be exploited in low voltage applications and V_2CO_2+Gr+Li are suitable for high charging voltage applications.

3.4.7 Diffusion properties

A low diffusion barrier and high mobility are the requirements of an efficient electrode material. In particular, the mobility of a metal atom on an electrode

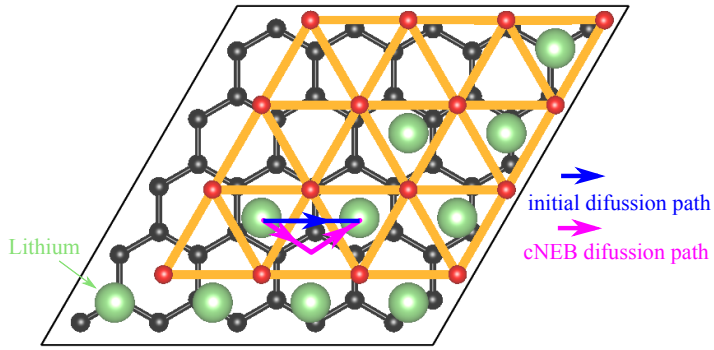

Fig. 3.20 Initial guessed and final resulted Li diffusion path between Ti_2CO_2+Gr heterostructure.

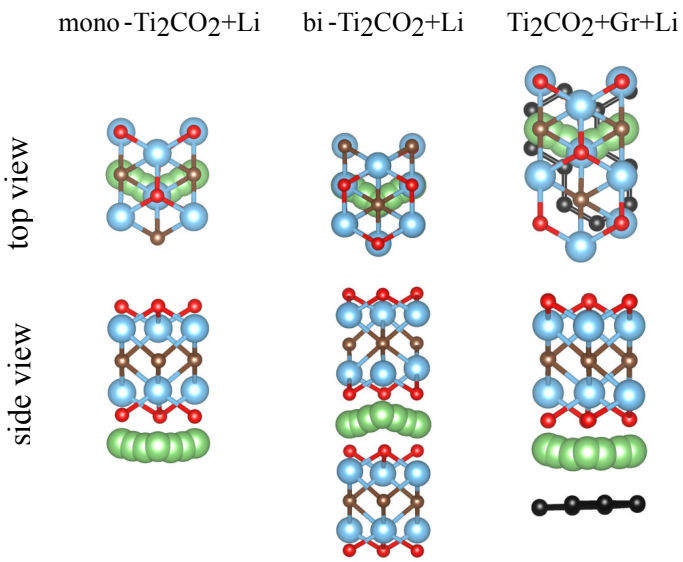

Fig. 3.21 Top and side view of the lowest energy diffusion path of Li in Ti_2CO_2 related systems.

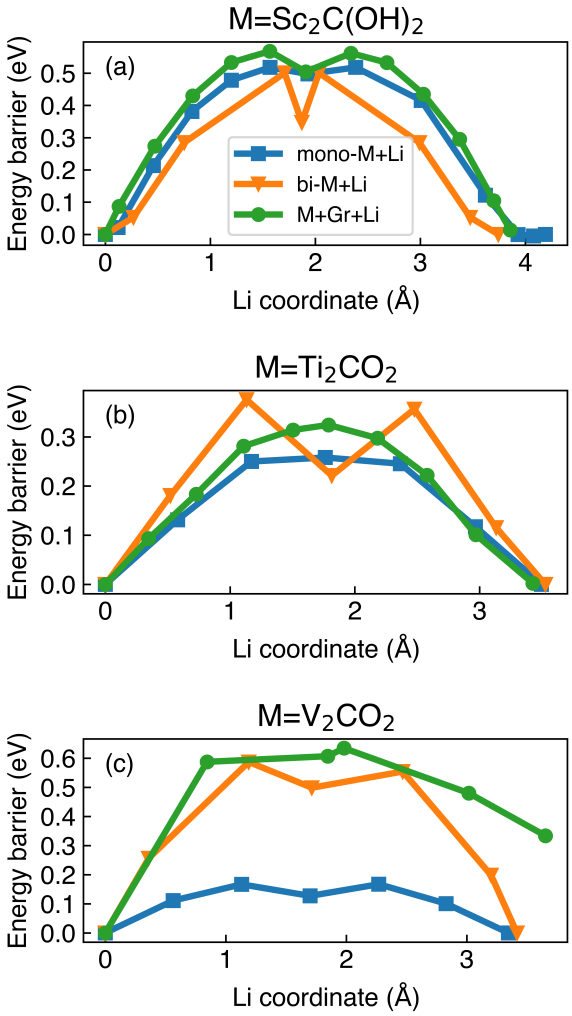

Fig. 3.22 Energy profiles of Li diffusion in different systems composed of (a) $Sc_2C(OH)_2$, (b) Ti_2CO_2 and (c) V_2CO_2 along the lowest energy diffusion path as indicated in Fig. 3.21.

material is a key factor determining the rate performance during charging and discharging of a battery. Following the thermodynamic consideration of Li intercalation, we investigated the single Li kinetics on mono-M+Li, within bi-M+Li and within M+Gr+Li heterostructures, where M=$Sc_2C(OH)_2$, Ti_2CO_2 and V_2CO_2, by calculating the lowest energy Li atom diffusion path connecting two adjacent binding sites using the cNEB method, see Fig. 3.21. The determined energy profiles of the paths are shown in Fig. 3.22. Compared to the bilayer systems, Li displays relatively smaller diffusion barriers on the pristine monolayers. In other words, energy barriers of Li ions in a M_2CX_2+Gr+Li heterostructure are always higher than those of monolayers. For instance, while the energy barrier is calculated to be 0.16 eV on mono-V_2CO_2+Li, it becomes 0.6 eV for bi-V_2CO_2+Li and V_2CO_2+Gr+Li heterestructure. Since the multilayer system has the advantage of having higher capacity than the single monolayer system for given volume, and also the synthesized M_2CX_2+Gr will mostly be multilayered, we believe that the monolayer structures represent the lower limit for the energy barriers. However, to obtain realistic kinetics properties we should consider the diffusion of ions between layers not only on isolated monolayers. Another important point is that surface functionalization increases the barrier considerably[153]. Interestingly, energy barriers for Ti based systems are similar, varying in the range of 0.22-032 eV. Our calculated energy barriers for mono-Ti_2CO_2+Li are consistent with a recent work[153]. Energy barriers for Ti-based systems are lower than that of graphite 0.5 eV[154] and high-capacity bulk silicon anode materials with a diffusion barrier around 0.57 eV, comparable to the commercially used anode materials based on TiO_2 which have a barrier of 0.35-0.65 eV[155–157], suggesting that heterostructures of Ti-based MXenes with graphene are promising candidates for electrode materials in battery applications. The diffusion barriers can be reduced by weakening the interaction of Li ions with the constituent layers. This can be achieved by fabricated pillar structures in which the interlayer distance of graphene and MXenes is enlarged by the help of intercalated molecules [158]. This method can also improve the storage capacity by multilayer absorption between the layers.

3.4.8 Summary

We carried out first-principles calculations to systematically investigate Li atoms intercalation in MXenes/graphene vertical bilayer heterostructures for Li battery application. Six members in the MXenes family were considered to form heterostructures with graphene: M_2CX_2+Gr (where M=Sc, Ti, V and X=OH, O). The ground state stacking types of bilayer and the strongest binding sites of Li atoms were first determined. The strength of the binding of the bilayer heterostructure is comparable to that of bilayer graphene, and is stronger than for MXenes bilayers. Due to a finite mismatch of the lattice constant of MXenes and graphene, the relative motion of the bilayer in the heterostructure require less energy as compared with the other two cases and give a low friction between them.

We identified two promising heterostructure for Li intercalation: Ti_2CO_2+Gr and V_2CO_2+Gr. The stability of the heterostructure upon Li intercalation is confirmed through; 1) small variations of the structural parameters , e.g. in-plane lattice parameters ($<$1%) and interlayer separation ($<$0.5 Å); 2) Large negative binding energies of Li atoms, e.g. larger than that in bilayer graphene; 3) Li atom donates a significant amount of charge to the host material and exists in the cationic state. We found that all the possible Li absorption sites can be occupied without destroying stability, namely 100% Li intercalation, leading to an average open circuit voltage of 1.49 V for Ti_2CO_2+Gr and 1.93 V for V_2CO_2+Gr. Especially, Ti_2CO_2 MXene offers a compromise between capacity and kinetics since the calculated diffusion barriers are the lowest among the other considered systems and which is lower than that of graphene. A balance between the storage capacity and kinetics should be made for practical applications when selecting a promising candidate. Due to their lower molecular weights as compared to bare MXenes bilayers, MXene+Gr heterostructure offer higher storage density, they also have the advantage of good electrical conductivity which is an essential property for a proper operation of a battery.

Chapter 4

Results of Modification of Physical Properties in Novel 2D materials

This is the second part of the results of this thesis. Here we will discuss some of the possible ways to modify the physical properties of 2D materials. As before, each section will be focused on an unique way to change the properties of materials, namely through the number of layers, mechanical strain, heterostructuring and defect introduction. Following the theme of the thesis, which is about novel 2D materials, we will continue to introduce other new 2D materials that have been discovered and whose properties will be modified.

4.1 Number of layers: Few-layer of Calcium hydroxide[1]

4.1.1 Introduction

We have seen several monolayer systems that were extracted from layered materials such as 2D-BN, 2D-MoS_2. In this section, we further explore this process for alkaline earth metal hydroxides (AEMHs), which pose a layered structure in the bulk form and are exfoliated to few-layer form. The experimental synthesis and the theoretical modelling is reported in this section. In contrast to the abundant literature on graphene-like ultra-thin structures, few-layer AEMHs have not

[1]This work is published: P2.

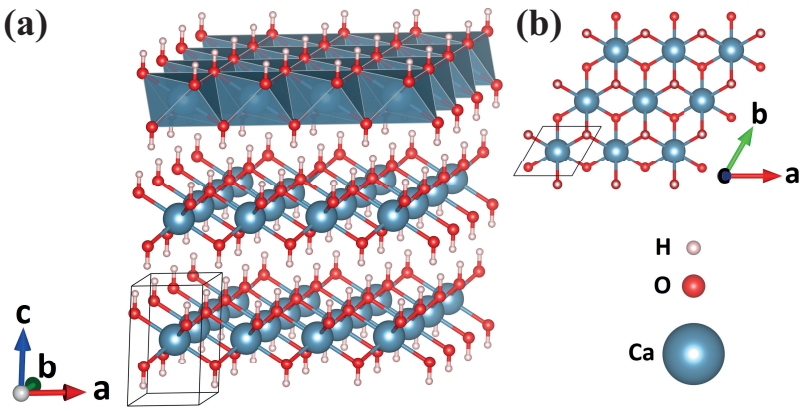

Fig. 4.1 Atomic structure of bulk $Ca(OH)_2$: (a) tilted view, (b) top view of one layer.

been investigated so far. Bulk forms of AEMHs are layered structures belonging to the $P\bar{3}m1$ space group[159] and the crystal structure of layered AEMHs comprise stacked sheets of MO_6 (M=alkaline earth metals) edge-sharing octahedra, see Fig. 4.1. At each corner of an octahedron, each O atom binds to one H atom and the latter interacts with three neighbouring hydroxyl groups of the adjacent layer. Early studies on bulk AEMHs revealed that the application of temperature and pressure may result in dramatical changes in their crystal structure and electronic properties[160–167] . Moreover, early theoretical studies showed the reliability of the use of first-principles calculations with a plane-waves basis set in combination with the GGA exchange-correlation functional for the investigation of structural and electronic properties of these materials[168–171].

Although the structural and electronic properties of bulk AEMHs have been investigated before [170, 172, 173] , single layers of these materials have never been studied before and their stability is still an open question. However, advances in experimental techniques made exfoliation and growth of such structures possible[174, 175]. Especially the Portlandite material, $Ca(OH)_2$, which has been the main product of hydration of Portland cement, CaO, is one of the most well-known AEHMs. Characteristic properties of ultra-thin structures of Portlandite have not been reported yet. In this study we investigate, both experimentally and theoretically, the structural, electronic, magnetic, vibrational and mechanical characteristics of bulk, bilayer and monolayer $Ca(OH)_2$ and discuss how these properties change with the number of layers. Particularly, the result

of the phonon calculations is presented for the confirmation of the stability of the newly proposed 2D material.

To assess the mechanical strength of the material, in addition to the elastic moduli that we have introduced in chapter 2, here we calculate another useful parameter that is closely related to the Young's modulus, which is called the in-plane stiffness of the materials. We focused on the harmonic range of the elastic deformation, where the structure responded linearly to strain ϵ. The stretching of the $Ca(OH)_2$ is achieved by increasing the equilibrium lattice constant a_0 by Δa, to attain the axial strain $\epsilon = \Delta a/a_0$. We optimized the atomic structure at each increment of the strain, $\Delta\epsilon$ =0.01 and calculated the total energy under strain $E_T(\epsilon)$. Then the strain energy can be given by, $E_S = E_T(\epsilon) - E_T(\epsilon=0)$; namely, the total energy at a given strain ϵ minus the total energy at zero strain. Then, using the following formula, one can calculate the in-plane stiffness:

$$C = (\frac{1}{A_0})(\frac{d^2 E_S}{d\epsilon^2}), \tag{4.1}$$

where A_0 is the equilibrium area of the supercell.

As explained in detail in the following sections, unit cells including one Ca, two O, and two H form the primitive cells of both monolayer and bulk structures, while it is doubled for a bilayer. The cohesive energy per unit cell, E_{coh} is presented in table 4.2 and is calculated according to the formula: $E_{coh} = E_{tot} - nE_{Ca} - 2nE_O - 2nE_H$, where E_{tot} is the total energy of the unit cell of $Ca(OH)_2$, E_X is the single atom total energy of atom X and n is the number of Ca atoms for the corresponding unit cell, i.e. $n = 1$, $n = 2$ and $n = 1$ for monolayer, bilayer and bulk, respectively.

4.1.2 Computational details

Simulation program: VASP and PHON[176]
Energy cut-off: 500 eV
Pseudopotentials: PBE-GGA(PAW)
k points (Monkhorst-Pack): 35×35×1 and 25×25×11 for few-layer and bulk $Ca(OH)_2$, respectively
Vacuum: 25 Å
Energy and force convergence criterion: 10^{-5} eV and 10^{-2} eV/Å, respectively
vdW corrections: DFT-D2 method of Grimme [177]

Charge analysis: Bader's charge analysis method[134–136]

4.1.3 Experimental measurements

Before our theoretical investigation of few-layer $Ca(OH)_2$, we present the experimental realization and detailed theoretical analysis of the characteristics of bulk $Ca(OH)_2$ crystals.

$Ca(OH)_2$ crystals were grown using the hydrolysis technique by using Ca_3SiO_5 micro-pallets. Ca_3SiO_5 was mixed at different water to solid ratios ranging from 0.2 to 0.9 by molar weight. The mixture was heated up to 40 °C in a controlled reaction chamber for 3 hours and controllably cooled down to 5 °C for 24 hours using a temperature controller. The growth time depends on the total water to solid ratio as well as the growth temperature. Growth time was around 8 hours for 0.6 water to solid ratio and 40 °C growth temperature. Longer growth time typically resulted in a dendritic morphology where the growth was mostly in the c-axis direction. Synthesized crystals displayed rather sharp (the full width at half maximum is around 7 cm^{-1}) Raman feature at 280 cm^{-1} and our XRD measurements displayed sharp (00l) reflections at 19.1, 39, 56.2, 77.7 degrees implying that crystals have lamellar nature.

Synthesized crystals were around 0.1-2 mm in size and they were filtered from the solution. After the filtering process, crystallites were washed off using 18.2 MOhm.cm DI wafer multiple times and dried under inert Ar gas. Crystallites were exfoliated using micro-mechanical exfoliation technique onto thermal silicon oxide / Si substrates. We find that the contrast was improved for an oxide thickness around 265-285 nm. Exfoliated flakes displayed rather sharp edges (see Fig. 4.2) with well-defined angles of 120° and 60° implying that the materials are highly crystalline. Interestingly, synthesized $Ca(OH)_2$ flakes are layered in agreement with theoretical calculations and these flakes can be easily exfoliated using the Scotch tape technique on different substrates. The exfoliated flakes do not show any signs of structural imperfection, pit formation, and overall rather flat surfaces can be obtained. In Fig. 4.2, the yellowish looking regions actually correspond to regions where the thickness is around 50-100 nm (50-100 layers) while the blue features are only 10-50 nm in thickness. Considering the ease to

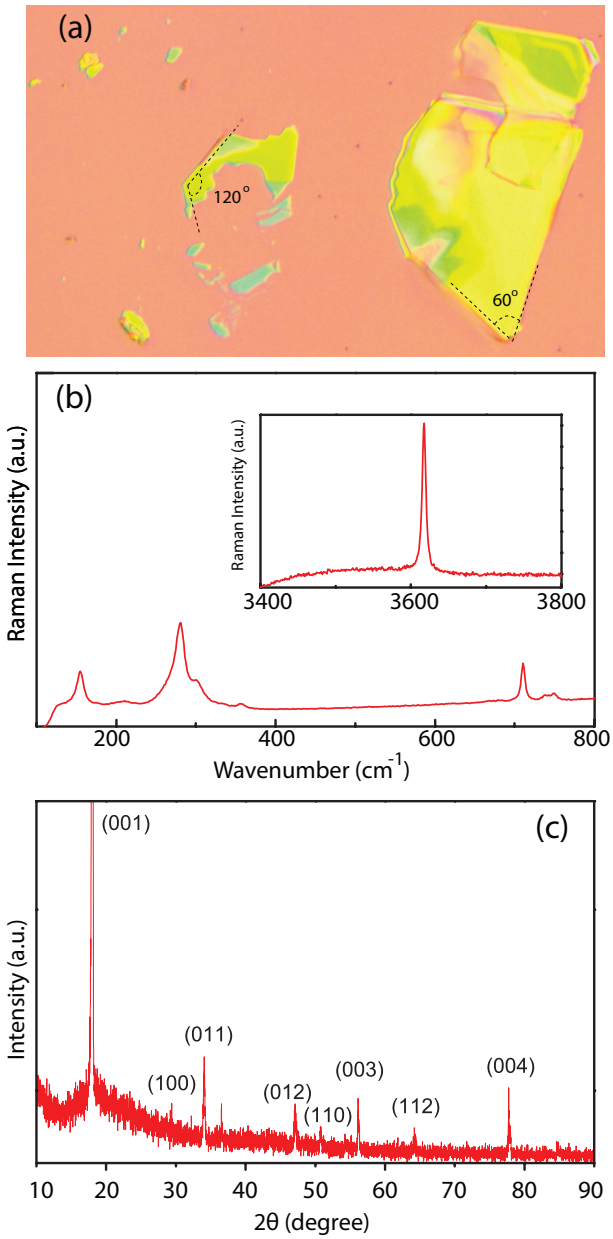

Fig. 4.2 (a) Optical image of the crystal structure and (b) Raman spectrum measured using 488 nm laser in the low and the high frequency region. The fundamental phonon branches located at the low frequency (100-400 cm^{-1} range) and the high frequency (3620 cm^{-1}) are associated with the OH stretching mode. (c) XRD measurements

exfoliate this material, experimentally and theoretically we predict that they can be eventually isolated down to mono- and few-layers on various substrates.

In addition, micro-Raman measurements were performed using a 488 nm laser on a 2 micron square spot using a high intensity laser of 10 mW. We noticed that few-layers of $Ca(OH)_2$ were not subject to local over-heating / decomposition effects unlike TMDs (MoS_2, WS_2, etc.) which typically decompose around 100 microWatt power using a similar laser excitation spot. We attribute this to the low absorption of the material associated with the rather large band gap. Raman measurements displayed various peaks in the 100-1000 cm^{-1} range. The high frequency peak at 3620 cm^{-1} is associated with the O-H stretching mode A_{1g}. In addition, the low frequency $E_u(T)$ mode is found at 280 cm^{-1}.

Here, we note that even though this material is a direct gap semiconductor, their band gap is well beyond our detectors range and since the insulators cannot be excited with such high laser wavelength, PL measurements are virtually impossible.

4.1.4 Structure properties

The bulk structure of Portlandite is formed by the stacking of individual $Ca(OH)_2$ monolayers on top of each other, see Fig. 4.1. As we will examine and discuss the stacking in detail in the following paragraphs, we learned that the AA stacking is the ground state atomic configuration for bulk and multilayer structures of $Ca(OH)_2$. In table 4.1, optimized lattice parameters of the bulk structure together with experiments and other theoretical calculation are presented. Our results are consistent with reference [172] and together they have good agreement with experiments. This justifies the reliability of our calculations.

In the 5-atomic hexagonal primitive unit cell of bulk $Ca(OH)_2$, the Ca atom sits at the geometrical center of the cell, i.e. $\{1/2a, 1/2b, 1/2c\}$. Two O and two H atoms form two hydroxyl groups (-OH^-) located symmetrically with respect to the Ca atom. In this arrangement, coordinates of H and O only differ by their positions along the **c** lattice axis and their fractional coordinates can be given as $\{1/6a, 1/6b, (1/2c - c_O)\}$ and $\{1/6a, 1/6b, (1/2c - c_H)\}$ for one hydroxyl, $\{5/6a, 5/6b, (1/2c + c_O)\}$ and $\{5/6a, 5/6b, (1/2c + c_H)\}$ for the other

Table 4.1 Comparison of calculated results for structures parameter of bulk $Ca(OH)_2$ with experimental results and with theoretical results from other reference: lattice constants a and c, volume V and c/a ratio.

Structure parameters	Exp. [a]	Exp. [b]	PBE-PAW (this work)	PBE-PAW [c]
a (Å)	3.589	3.592	3.614	3.612
c (Å)	4.911	4.906	4.982	4.942
V (Å^3)	54.78	54.82	56.35	55.85
c/a	1.368	1.366	1.379	1.368

[a] Ref. [178]
[b] Ref. [179]
[c] Ref. [172]

one, where c_O and c_H are the vertical shifts of the positions of O and H atoms from the Ca plane in units of Å , respectively.

In the optimized structure, the lattice constants a and c are 3.61 Å and 4.98 Å in the bulk structure and the parameters c_O and c_H are calculated to be 1.15 Å and 2.12 Å. The bond lengths of Ca-O and O-H are 2.36 Å and 0.97 Å. The interlayer distance which is defined as the distance between the uppermost H layer of the underlying layer and the lowermost H layer of the top-lying layer is found to be 0.49 Å . Differing from other lamellar bulk crystal structures such as graphite (3.58 Å) and MoS_2 (3.42 Å)[180] , $Ca(OH)_2$ layers are more closely stacked on top of each other.

Our calculations revealed that going from bulk to monolayer the in-plane lattice parameter a changes to 3.62 Å . In our calculations, the c lattice parameter in the hexagonal unit cell of the monolayer is set to 25 Å in order to avoid interlayer interaction between the adjacent layers. In the monolayer $Ca(OH)_2$, parameters c_O and c_H are calculated to be c_O=1.14 Å and c_H=2.10 Å , respectively. Ca-O and O-H bond distances are 2.38 Å and 0.97 Å in the monolayer, respectively. We observed only a small change as the system goes from bulk to monolayer, and some of the structure parameters are even left unchanged. From this we can conclude there in quite weak interlayer interaction in $Ca(OH)_2$. In order to study the interlayer interaction we further investigate its effect on stacking, and by including the vdW correction in the functional we are able to identify the nature of this interaction.

Table 4.2 Calculated results for different structures of $Ca(OH)_2$: lattice constants a, vertical shift of O and H atom c_O c_H, Ca-O and O-H bond length, energy band gap E_{gap}, cohesive energy per atom E_{coh}, charge transfer from Ca atom to O atom ΔQ, in-plane Young's modulus E_{xx}, E_{yy}, in-plane Poisson's ratio ν_{xy}, in-plane shear modulus G_{xy} and in-plane stiffness C. For comparison, theoretical calculation on same quantities of BN are shown in the last row.

System	a (Å)	c_O/c_H (Å/Å)	Ca-O/O-H (Å/Å)	E_{gap} (eV)	E_{coh} (eV)	ΔQ (e)	E_{xx}, E_{yy} (N/m)	ν_{xy}	G_{xy} (N/m)	C (J/m^2)
Bulk $Ca(OH)_2$	3.61	1.15/2.12	2.36/0.97	4.08	4.52	1.6	55.0	0.30	21.23	60.1
2L $Ca(OH)_2$	3.62	1.15/2.12	2.38/0.97	3.70	4.48	1.6	50.7	0.32	19.16	55.6
1L $Ca(OH)_2$	3.62	1.14/2.11	2.38/0.97	3.67	4.39	1.6	50.7	0.33	19.08	53.2
1L BN	2.51[a]	-	1.45[a b]	4.64[a]	8.82[a]	0.43[a c]	278.2[d]	0.22[d]	113.5[d]	267[e]

[a] Ref. [181]
[b] B-N bond length
[c] charge transfer from B to N
[d] Ref. [182]
[e] Ref. [183]

Individual layers of layered structures such as graphite, hex-BN and TMDs are held together mainly by the vdW force in order to form a bulk layered structure. Such a weak interaction stems from dynamical correlations between fluctuating charge distributions in neighboring layers. Here we investigated the energies of various bilayer configurations. As presented in Fig. 4.3 there are six possible types of stacking between two $Ca(OH)_2$ monolayers. Similar to the stacking nomenclature of bilayer graphene, we classify the stacking types to be either AA or ABn (n=1,2,...,5). The same type of atoms from different monolayers are on top of each other in AA stacking whereas AB stackings can be reached by shifting one of the layers along certain lattice vectors directions. One set of AB stackings could be realized by shifting the second layer in the AA stacking towards $[\overline{1}\overline{1}0]$, which gives stacking AB1, and by shifting towards the [110] direction, which gives stacking AB2, see first row in Fig. 4.3. Another set of bilayers is achieved by first flipping the second layer upside down in AA stacking, which gives stacking AB3, then AB4 and AB5 can be constructed by doing the same shifting on the second layer of AB3 towards $[\overline{1}\overline{1}0]$ and [110] directions of the 1st layer, respectively. After relaxation of all stackings, the variation of the **a** lattice constant among the different stacking types is less than 0.01 Å . The smallest interlayer distance, as defined previously for bulk, is for AA stacking and equals 0.49 Å , i.e. the same as in bulk. For AB stacking the interlayer distance is $1\sim2$ Å larger than that for AA

stacking. As depicted in Fig. 4.3, AA stacking is 96∼137 meV per formula more favorable than all other possible stacking types and hence it corresponds to the lowest energy configuration.

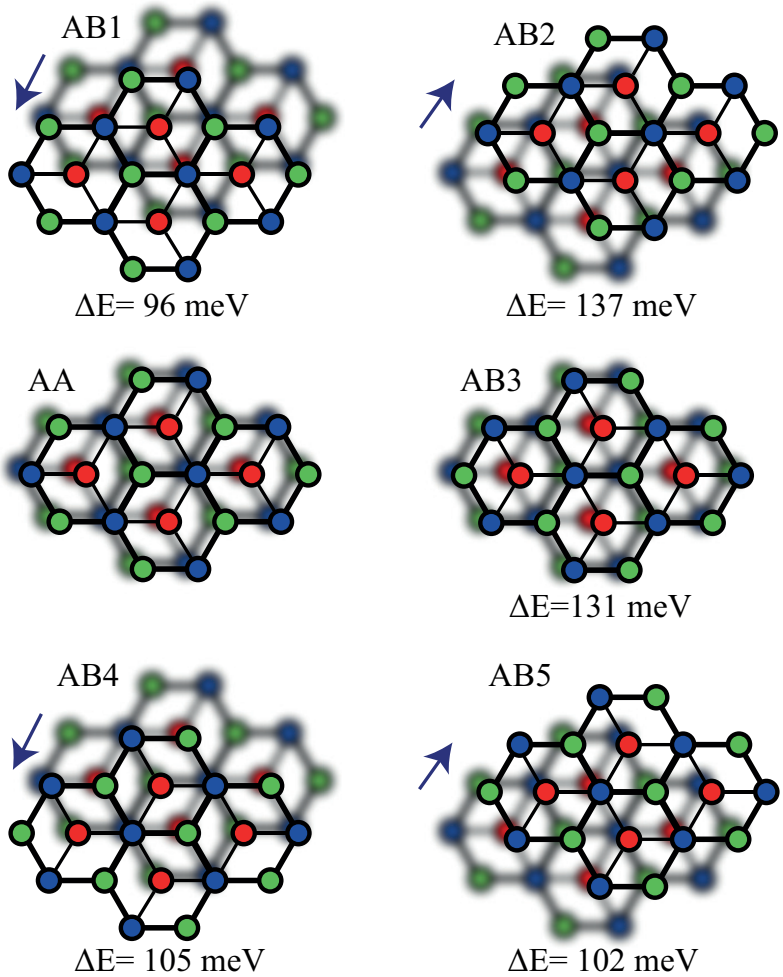

Fig. 4.3 Different stacked bilayers (bottom layer is blurred) and their energy difference with respect to the AA stacking of $Ca(OH)_2$, i.e. $\Delta E=E_{ABX}-E_{AA}$, (X=1,2,...,5). Energies are given per formula of $Ca(OH)_2$. Blue, green and red circles are for Ca atom, upper hydroxyl group and lower hydroxyl group, respectively. For clarity, the bottom layer is shifted slightly.

To investigate the nature of the interlayer interaction, we have calculated the interlayer interaction energy (IE) for the AA stacked bilayer structure of $Ca(OH)_2$. The IE is the energy difference between the total energy at a specific interlayer

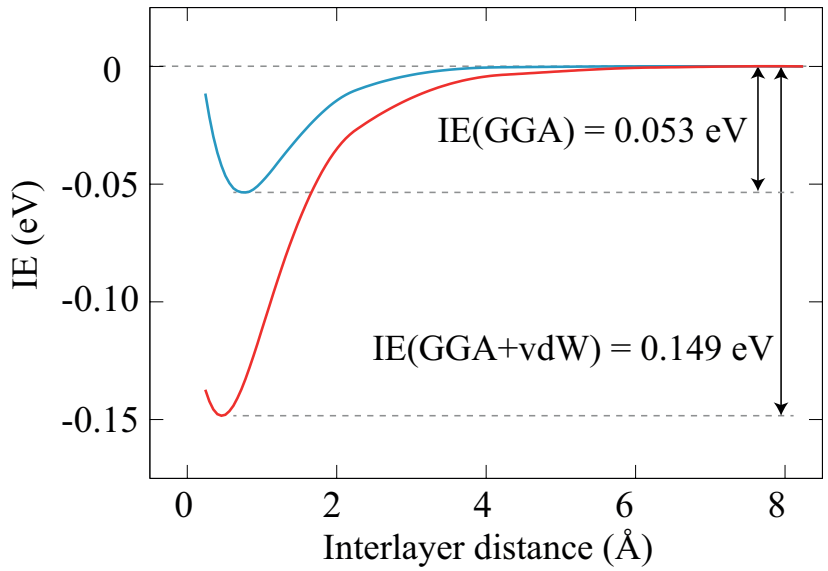

Fig. 4.4 Interlayer interaction energy per formula of AA-stacked bilayer $Ca(OH)_2$. Blue and red curves are for GGA calculations without and with vdW correction, respectively.

distance and that of a well separated bilayer. The plot of IE versus interlayer distance is shown in Fig. 4.4, where the energy of the well separated bilayer is defined as 0 eV. Two sets of calculations were performed: one set only considers GGA exchange correlation; while another set considers both the GGA and vdW interaction. At the optimized interlayer distance for the bilayer structure, almost 2/3 of the attractive interaction comes from the vdWs interaction, which is consistent with D'Arco et al. [171] . They stated that interlayer interaction of Brucite, one of the isomorphous of Portlandite, is mainly a dispersion-type interaction. The nature of interlayer interaction in $Ca(OH)_2$ is mainly vdW type weak interaction. Our GGA+vdW calculations revealed that the interlayer interaction between two layers of $Ca(OH)_2$ (149 meV per formula) is much stronger than that of bilayers of MoS_2 (76 meV per formula).

4.1.5 Electronic properties

Our Bader charge transfer analysis showed that the final (initial) electron charge on Ca, O and H atoms after (before) the formation of the crystal are 6.4e (8.0e), 7.4e (6.0e) and 0.4e (1.0e), respectively. Therefore, in the bulk structure of

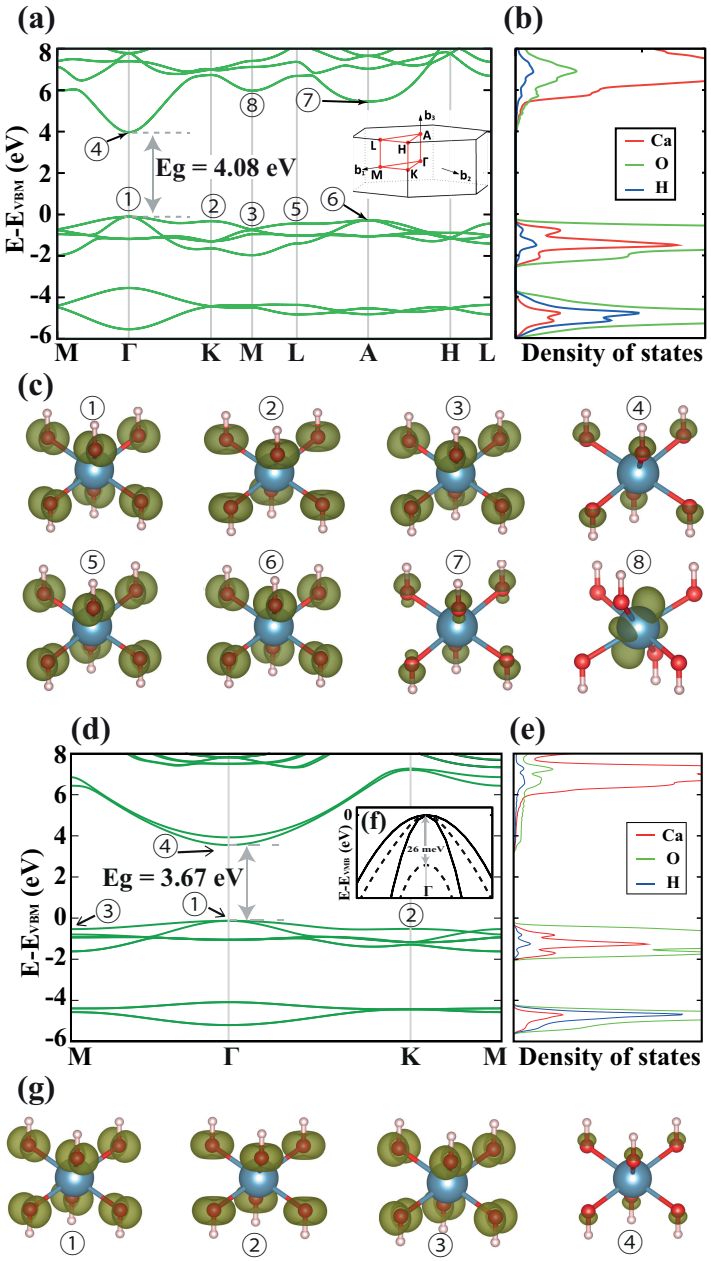

Fig. 4.5 (a) and (d) are the Band structures, (b) and (e) are the partial DOS and (c) and (g) are the band and *k*-point decomposed charge densities of the bulk (c) and monolayer (g) $Ca(OH)_2$, respectively. The charge density are the band edges indicated in (a) and (d), isovalues are kept constant. (f) Band structure around Γ point is shown with (dashed line) and without (solid line) spin orbit coupling.

$Ca(OH)_2$, Ca-O bonds, which are mostly in ionic character, are formed through $0.8e$ charge transfer from each Ca to O atom. The charge transfer is kept unchanged when it comes to the monolayer structure, except that the rest charge on H atoms is $0.6e$ in monolayers.

Our calculations on the electronic structure reveal that bulk $Ca(OH)_2$ is an insulator with a 4.37 eV direct band gap. As shown in Fig. 4.5(a), the VBM and the CBM are located at the Γ point. The partial density of states (DOS) shown in Fig. 4.1(b) indicates that the major contribution to the states at the valence and conduction band edge originate from the O atoms, while deeper in the conduction band, states are mainly composed of the orbitals of Ca. The orbital character of a state at a particular band can also be deduced from a band and k-point decomposed charge density. As seen from Fig. 4.5(c), edges in the top of VBM have O-p_x and O-p_y orbital character, and the hybridization of these states are also shown in the same figure. While the CBM has some p_z orbital character from the O atoms, but as the energy of the state increases, the d orbitals from Ca atoms start to contribute, see ⑧ in the same figure.

Electronic properties of $Ca(OH)_2$ are quite different from similar 2D graphene-like structures. Unlike TMDs (such as MoS_2 and WSe_2) that exhibit indirect-to-direct band gap crossover when going from bulk to a single layer structure, $Ca(OH)_2$ is a direct band gap semiconductor which is independent of the number of layers. Although the energy band gap at the Γ point decreases from 4.03 to 3.67 eV for a monolayer structure, the electronic dispersion of the valence band edge remains almost unchanged, see Fig. 4.5(d). As shown in Fig. 4.5(e) the conduction band states mainly originate from Ca atoms, while the valence states are mainly composed of the orbitals of O atoms.

Our magnetic state analysis shows that unless a defect is formed in/on the structure, there is no spin polarization in the ground state of both bulk and monolayer $Ca(OH)_2$. Therefore, $Ca(OH)_2$ is a non-magnetic insulator regardless of its dimension for the structure.

Moreover, it was seen that the spin-orbit interaction has no considerable effect on the bond lengths and the overall electronic dispersion (except for a 26 meV splitting in the VBM at the Γ point, see Fig. 4.5(f)). Due to the presence of inversion symmetry of $Ca(OH)_2$, the degeneracy of spin-up and spin-down states still remains, this is also confirmed by the results of our calculation.

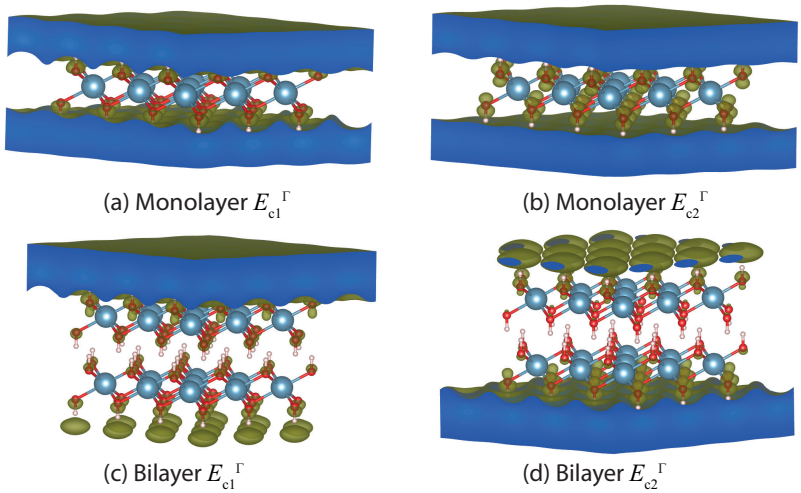

Fig. 4.6 Two lowest conduction band charge density of monolayer and bilayer $Ca(OH)_2$ at the Γ point.

Band and *k*-point decomposed charge density in Fig. 4.5 are kept with the same isosurface level for comparison. However, as we further reduced the isosurface level at ④ in (d) and (g) of Fig. 4.5, which is the lowest conduction band of the monolayer at the Γ point, E_{c1}^{Γ}, charge density forms a planar state parallel to the layer on both sides, see Fig. 4.6(a). This is also the case for the second lowest non-spin-resolved conduction band at the same *k*-point, E_{c2}^{Γ}, see Fig. 4.6(b). These two states are important due to their unique character and having energies right below the ionization energy. Such exceptional states having free-electron-like dispersion were reported before[184, 185] for doped graphite. To study the trend in these states, the same states were plotted for bilayer $Ca(OH)_2$, see (c) and (d) in Fig. 4.6. E_{c1}^{Γ} and E_{c2}^{Γ} have lower energies than ionization energy. Therefore, electrons are still close and bind to both sides of monolayers as seen from the charge density. In the case of bilayers, interestingly, these states appear only on one side of the bilayer.

4.1.6 Mechanical properties

We present the quantities that describe the mechanical properties of $Ca(OH)_2$ in table 4.2. First, the in-plane Young's modulus of the bulk structure is calculated.

Bulk $Ca(OH)_2$ has an in-plane Young's modulus of 55.0 N/m and an in-plane shear modulus of 21.23 N/m. Both these quantities indicate a flexible nature to in-plane tensile and shear deformation of bulk $Ca(OH)_2$. In addition, bulk $Ca(OH)_2$ has an in-plane Poisson's ratio of 0.30. Additionally, the value of the in-plane stiffness for bulk $Ca(OH)_2$ is calculated to be 60.1 J/m^2.

If we go from bulk to bilayer $Ca(OH)_2$, we see a reduction in both the in-plane Young's modulus or the in-plane shear modulus, which are 50.7 N/m and 19.16 N/m, respectively. The in-plane Poisson's ratio on the other hand is slightly increased to 0.32 and becomes more spongy-like as opposed to more cork-like character[186]. In addition, the in-plane stiffness value of bilayer $Ca(OH)_2$ is calculated to be 55.6 J/m^2.

We found that monolayer $Ca(OH)_2$ has a quite low in-plane Young's modulus (50.7 N/m) when compared to BN (278.2 N/m). The in-plane Poisson's ratio (0.33) and the in-plane shear modulus (19.08 N/m) of the monolayer are similar with those for bilayer, and for BN, they are 0.22 and 113.5 N/m respectively. The calculated values of the in-plane stiffness of monolayer $Ca(OH)_2$ is 53.2 J/m^2.

4.1.7 Vibrational properties

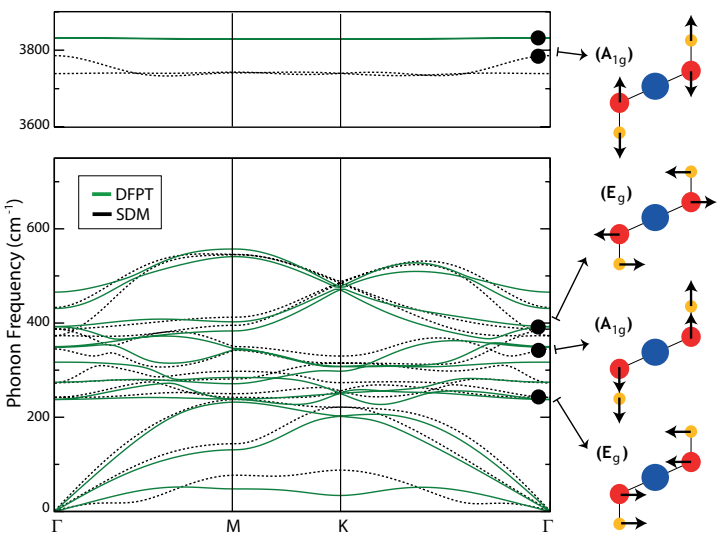

Fig. 4.7 Phonon dispersion of monolayer $Ca(OH)_2$.

Lastly, for the analysis of the vibrational spectrum and further examination of the dynamical stability of monolayer $Ca(OH)_2$, we performed a calculation of the phonon spectrum using both the first-principles small displacement methodology (SDM)[176] and density functional perturbation methodology (DFPT)[88]. Here the non-quadratic dispersion of the flexural mode around the zone center is directly related to the insufficient FFT grid along the vacuum direction. It is seen from Fig. 4.7 that similar to the Raman shift measurements observed from the bulk crystal structure, the monolayer material has also high-frequency OH stretching modes at 3700-3800 cm^{-1}.

Further analysis of the analysis of the phonon branches shows that the decomposition of the vibrational representation of optical modes at the zone center is $\Gamma = 4E_u + 2A_{2u} + 4E_g + 2A_{1g}$. As shown in the right panel of Fig. 4.7 there are four Raman-active phonon branches around 240, 350, 390 and 3700-3800 cm^{-1}. It is also worth to note that differing from other TMD structures having 1T phase, the presence of H atoms results in the existence of two different E_g and A_{1g} modes. Here the phonon dispersion has real eigenfrequencies in the whole Brillouin Zone, which is another indication of the stability of monolayer $Ca(OH)_2$.

4.1.8 Summary

By performing first-principles calculations on bulk, bilayer and monolayer $Ca(OH)_2$ and experimental confirmation of the bulk crystal layered structure, we have predicted several important properties of this material and its stability. We found that: (i) $Ca(OH)_2$ crystals are environmentally stable and their stable structures can be synthesized by experimental methods; (ii) Experimentally, we also demonstrated that $Ca(OH)_2$ crystals can be grown in layered form and also be exfoliated on arbitrary substrates; (iii) The dimensionality of $Ca(OH)_2$ will not change the electronic, structural and magnetic properties qualitatively. Nevertheless, intrinsic mechanical stiffness of each layer will become slightly stiffer as the system goes from monolayer to bilayer. (iv) Interlayer interaction is mainly a vdWs dispersion-type force, and the strength of the interaction is stronger than that of similar layered materials (e.g MoS_2 and graphite). (v) The conduction states which have a free-electron-like character may be utilized for high-mobility electron transfer.

We believe that the stable structure and the unique electronic properties of ultra-thin $Ca(OH)_2$, predicted for the first time here, will trigger interest in this new class of materials.

4.2 Number of layers: Few-layer of pentasilicene[2]

4.2.1 Introduction

Recently, a new 2D structure for carbon was proposed, called penta-graphene[118]. This crystal is composed entirely of pentagonal rings of C atoms with mixed sp^2/sp^3 orbital hybridization. However, the silicon counterpart of this structure, penta-silicene, contains a dynamical instability in its monolayer form. A few attempts have been made to stabilize this new Si structure by hydrogenation[187] and chemical doping[188].

In the present work, we construct multilayer structures of penta-silicene. We use density functional theory to explore their stability and physical properties. Two types of stacking for the penta-silicene layers are found to give stable few-layer structures. These different stacking types lead to completely different electronic properties since one leads to metallic and the other to semiconducting behavior. Somewhat surprisingly, we found that bilayer penta-silicene has lower formation energy than the most stable hexagonal silicene bilayers. Furthermore, we found that the band gaps of these semiconducting penta-silicene bilayers can be tuned by mechanical strain. We first explore the stability of monolayer penta-silicene and demonstrate its dynamical instability. This forms the motivation to study few-layer systems. Then we investigate different stacking possibilities and the resulting stability. Further, we study their mechanical properties by calculating their elastic constants. We also compare bilayer penta-silicene to the most stable bilayer hexagonal silicene structures. Lastly, The electronic properties of multilayered penta-silicene are discussed.

4.2.2 Computational details

Simulation program: VASP and Phonopy

[2]This work is published: P7.

Energy cut-off: 500 eV
Pseudopotentials: PBE-GGA(PAW)
k points (Monkhorst-Pack): 17×17×1 and 23×23×1 for insulating and metallic systems, respectively
Vacuum: 20 Å
Energy and force convergence criterion: 10^{-8} eV and 10^{-7} eV/Å, respectively
phonon calculation: finite displacement method
Supercell for phonon calculation: 4 × 4 × 1 and 3 × 3 × 2 for few-layer and bulk systems, respectively
***Ab initio* molecular dynamics:** Parrinello-Rahman (NpT) dynamics [189, 190] and a Langevin thermostat [191]
***Ab initio* molecular dynamics (Energy cut-off):** 300 eV
***Ab initio* molecular dynamics (time step):** 2 fs
***Ab initio* molecular dynamics (temperature):** 100 K
***Ab initio* molecular dynamics (simulation time):** 6 ps

4.2.3 Monolayer pentasilicene

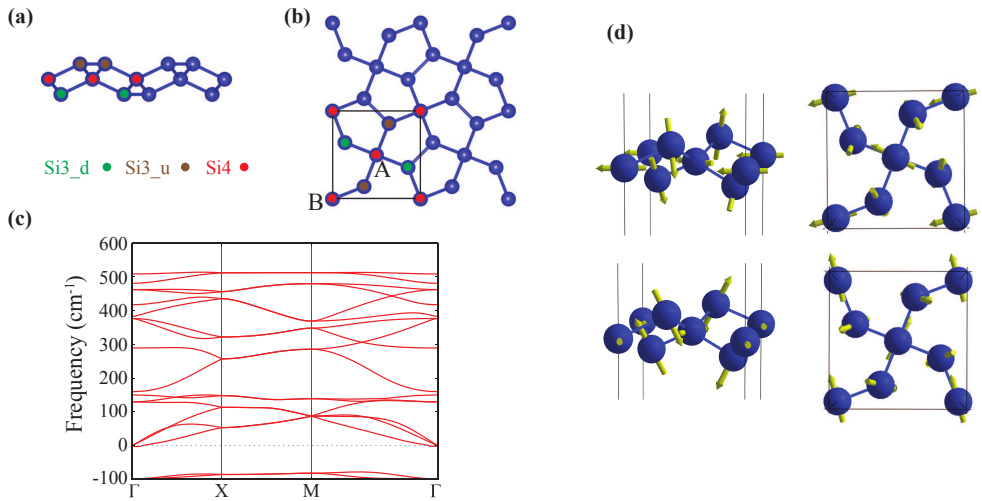

Fig. 4.8 (a) Side view and (b) top view of the atomic structure, (c) phonon spectrum and (d) two vibration modes with imaginary frequency of monolayer pentasilicene. Visualization of vibration modes is done with the V_Sim package [192].

The layer group symmetry of monolayer penta-silicene (p-Si) is $p\bar{4}2_1m$ (58). As shown in Fig. 4.8(a) and Fig. 4.8(b), the primitive cell contains six silicon atoms,

of which two have fourfold coordination (Si4) and four have threefold coordination (Si3). Two of the Si3 atoms reside above the Si4 atoms, denoted as Si3_u, while the other two are below the Si4 atoms, denoted as Si3_d. The Si4 atoms are bonded to four Si3 atoms while the Si3 atoms are connected to two Si4 atoms and one neighboring Si3 atom. Note that the two Si4 atoms have equivalent environments which are rotated by approximately 41° with respect to each other. Therefore, in analogy to graphene, we can relate these two equivalent Si4 atoms to sublattices which in the following will be referred to as the A and B sublattice.

The dynamical stability of this structure can be studied through its phonon spectrum. As noted before[187, 188] the phonon spectrum of monolayer p-Si contains imaginary frequencies, as shown in Fig. 4.8(c), which is a clear signature of its instability. The corresponding atomic vibrations of the two imaginary frequencies at the Γ point are shown in Fig. 4.8(d). These modes correspond mainly to out-of-plane vibrations of the Si3 atoms with respect to the Si4 atoms. As a consequence, the structure is found to fall apart, indicating that there is no stable form of monolayer p-Si. However, the addition of extra layers could reduce these out of plane vibrations and stabilize the structure. This is the motivation to study few-layer p-Si.

4.2.4 Multilayers of pentasilicene structures

Table 4.3 The cohesive energy (E_{coh}), the interlayer binding distance (d_{inter}), the interlayer binding energy (E_{inter}), number of interlayer bonds (N_b) and energy per bond (E_{bond}) of the four possible stacking types of bilayer p-Si. The interlayer binding energy per unit cell is defined as $E_{inter} = E_{bi} - 2E_{mono}$.

structure	E_{coh} (eV/atom)	d_{inter} (Å)	E_{inter} (eV)	N_b -	E_{bond} (eV)
AA	-4.129	0.795	-3.502	4	-0.875
AA_r	-4.113	2.379	-3.318	2	-1.659
AB	-3.968	2.174	-1.574	2	-0.787
AB_r	-4.147	1.893	-3.725	2	-1.862
AB_r^d	-4.185	1.896	-4.174	2	-2.087

When considering two layers, different stacking configurations are possible. Here we focus on the so-called AA and AB stacking modes of the aforementioned

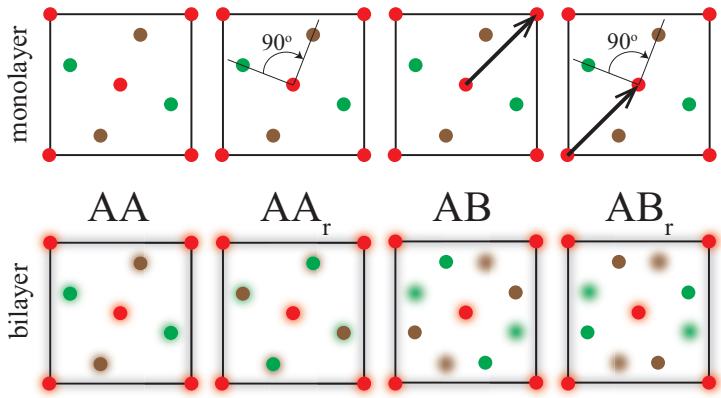

Fig. 4.9 Schematic illustration of the four stacking types for bilayer p-Si. The colors of the symbols correspond to those of the monolayer in Fig. 4.8(a) and Fig. 4.8(b). The bottom layer in the bilayer is blurred for clarity. The arrow represents translation and the angle represents the rotation of the top layer with respect to the bottom layer.

sublattices (see Fig. 4.9). The stacking in which both layers have the same in-plane orientation and the Si atoms are put right on top of each other is called AA stacking. AB stacking arises by shifting the A sublattice of one layer to the B sublattice of the other. This nomenclature was also used by Wang et al. [193] for bilayer penta-graphene. Although penta-silicene has a tetragonal lattice symmetry, the highest proper rotational symmetry order is two. Therefore, there are also two different possible orientations of the upper layer with respect to the lower one: One in which the two layers have the same orientation and another in which one layer is rotated over 90° with respect to the other one. We denote this last orientation with a subscript r to show that it results from a 90° rotation, e.g. AA_r. Therefore, there are four possible stacking types for bilayer p-Si. Note that AB_r stacking corresponds to the recently proposed bulk T12 phase for group IVA elements[194]. However, as discussed in more detail below, perfect AB_r stacking is not stable in the case of multilayer penta-silicene. A considerable distortion of the outer layers is required to stabilize AB_r stacking. The distorted structure, which will be referred to as AB_r^d in the following, is obtained by breaking the symmetry between the two Si3 atoms at each surface side in AB_r multi-

layer. In this way, one of the two Si3 atoms acquires sp^2 hybridization and looses an electron to the other Si3 atom that has sp^3 hybridization.

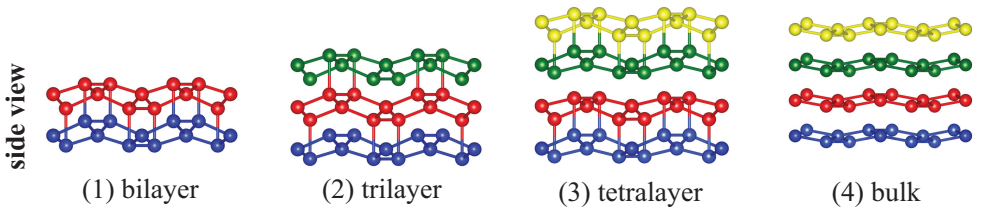

(a) AA stacked structures

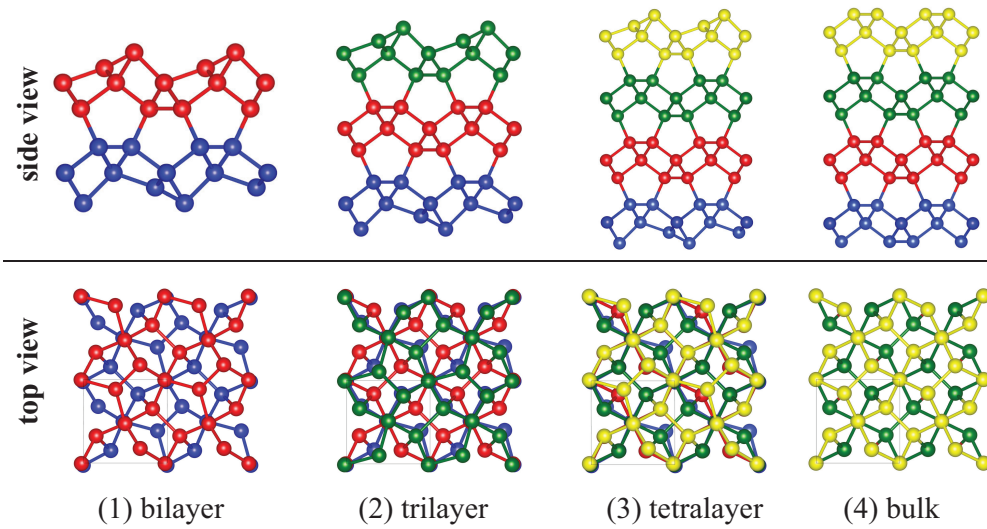

(b) AB_r^d stacked few-layer and AB_r stacked bulk structures

Fig. 4.10 Atomic structure of the 2×2 supercell of few-layer p-Si. The number of atomic layers in the bulk structure is fixed to four for comparison (i.e. $2 \times 2 \times 4$ and $2 \times 2 \times 2$ supercells for AA and AB_r stacked bulk p-Si). (Visualisation using VESTA [120]).

Table 4.4 The layer (space) group for few-layer (bulk) systems. The lattice constant (a), the interlayer distance (d_{inter}), the nearest-neighbor bond length range ($d_{min/max}$), the cohesive energy (E_{coh}), and the band gap (PBE) of few-layer and bulk p-Si.

stacking	structure	layer/space group	a (Å)	d_{inter} (Å)	d_{min} (Å)	d_{max} (Å)	E_{coh} (eV/atom)	band gap (eV)
-	monolayer	$p\bar{4}2_1m$ (58)	5.587	-	2.233	2.363	-3.837	0.046 (M→ Σ)
AA	bilayer	$p\bar{4}2_1m$ (58)	5.907	0.795	2.363	2.468	-4.129	metal
	trilayer		5.887	1.085	2.330	2.606	-4.108	metal
	tetralayer		5.980	0.996/1.794[a]	2.368	2.478	-4.150	metal
	bulk	$P\bar{4}2_1m$ (113)	6.234	1.769	2.398	2.463	-4.204	metal
AB_r^d	bilayer	pb2b (30) pm2a (31)	5.222	1.896	2.303	2.403	-4.185	0.119 (M→ Σ)
	trilayer	p1 (1)	5.222	1.989	2.298	2.413	-4.291	0.247 (M→ Σ)
	tetralayer	pb2b (30) pm2a (31)	5.221	1.997	2.298	2.413	-4.345	0.232 (M→ Σ)
AB_r	bulk	$P4_2/ncm$(138)	5.220	1.999	2.358	2.413	-4.508	1.329 (M→ Δ)

[a] The first and the second number indicate the interlayer distance between two monolayers and two bilayers, respectively.

In table 4.3, we compare the energies of the different stacking modes. In all cases the Si4 atoms are not involved in interlayer bonding since their possible number of bonds is already saturated. Except for the AA stacking where all Si3 atoms are bound to Si3 atoms from the other layer, only half of the Si3 atoms are bonded to the other layer in the other cases. In table 4.3, the size of the interlayer binding energy and the strength per bond are given. The size of the bond energies indicate strong chemical bonding. The AB_r^d stacking mode clearly forms the most stable structure. For the rest of the section, we will only focus on the most stable AA and AB-type stacking, i.e. AA and AB_r^d.

We also investigated the stability of trilayer, tetralayer and bulk p-Si structures by adding extra layers to the stable bilayers mentioned above, their structures are shown in Fig. 4.10(a) and Fig. 4.10(b). We list their structural and energetic properties in table 4.4. Extra layers increase the cohesive energy per atom due to a smaller ratio of surface atoms. For AA stacking, adding a 4th layer to a trilayer system results in a double bilayer system with lesser bonding between them. Going to AA bulk, the interlayer interaction appears to be further reduced and the buckled layers become more flat. Adding extra layers to an AB_r^d bilayer results in similar structures in which the Si3 atoms of the surface layers become distorted. For bulk, the undistorted AB_r structure is found in which $\overline{4}$-fold symmetry is restored.

4.2.5 Stabilities

In this section we investigate the stability of the different multilayer structures discussed above. Phonon calculations for the AA and AB_r stacking modes reveal that only the AA bilayer is dynamically stable at low temperature. The extra bonds of the Si3 atoms in AA-stacked structures effectively reduce out-of-plane vibrations and stabilize the structure. Although the AA-stacked bulk structure has weaker interlayer bonding, its phonon spectrum contains no imaginary frequencies, indicating its dynamical stability. The AB_r-stacked layers, on the other hand, exhibit similar out-of-plane vibrations of the outermost Si atoms as a monolayer. For AB_r^d-stacking the distortion of the outermost layer removes the instabilities from the phonon spectrum, so that these structures are also dynamically stable.

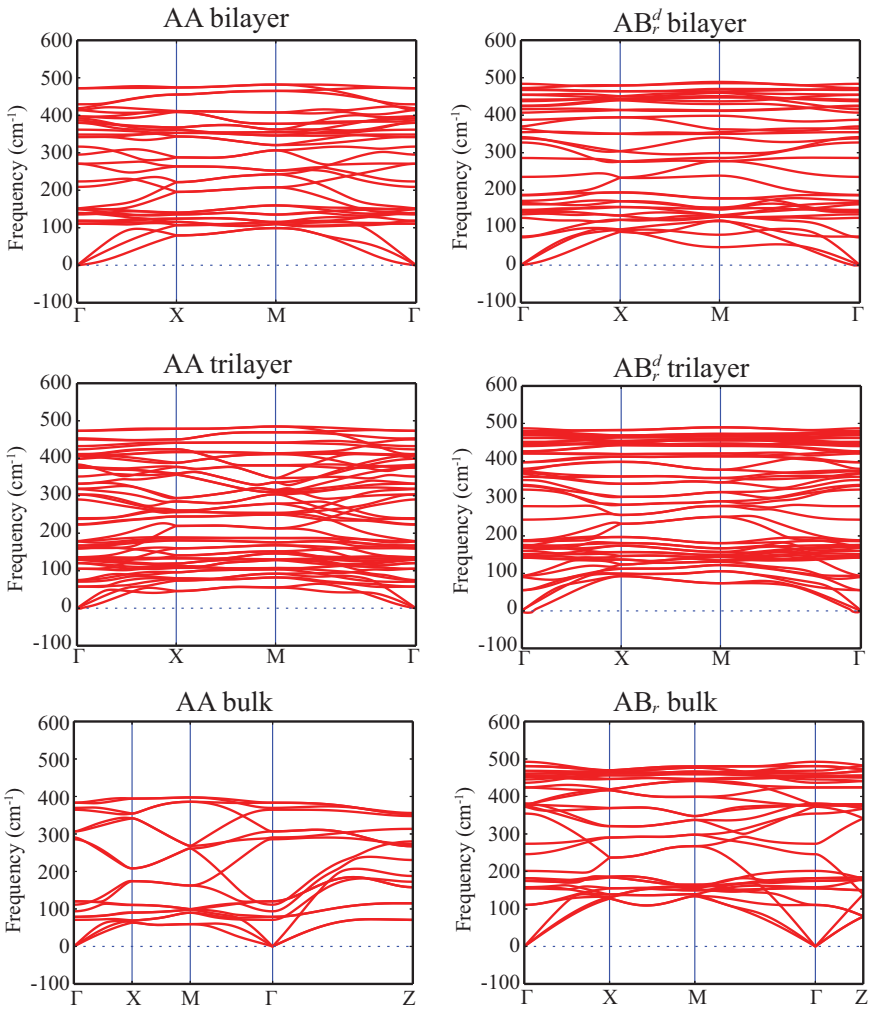

Fig. 4.11 Phonon spectra of different-stacked few-layer p-Si.

It is also interesting to see whether these structures remain stable at finite temperature. To this end, we performed *ab initio* molecular dynamics calculations at a temperature of 100 K. The evolution of the cohesive energy as a function of simulation time is shown in Fig. 4.12. For comparison, the results for the dynamically unstable monolayer are also shown. The monolayer laterally shrinks and becomes a disordered multilayered system. The AA and AB$_r^d$ bilayer systems, on the other hand, remain stable and retain their crystalline structure.

As a final stability check, we investigate the mechanical stability of bilayer p-Si which is determined by the elastic constants of the structures. If the elastic constants satisfy the necessary and sufficient Born criteria generalized by

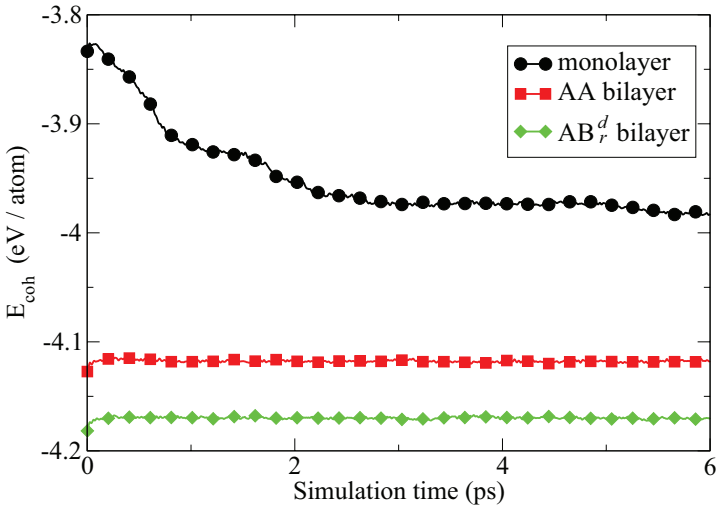

Fig. 4.12 The cohesive energy of monolayer and AA and AB_r^d stacked bilayer p-Si as a function of time at a temperature of 100 K under NpT-ensemble.

Mouhat and Coudert [53], the structures are mechanically stable. AA bilayer p-Si belong to the layer group symmetry of $p\bar{4}2_1m$, which belongs to the tetragonal symmetry groups, and the independent elastic constants in 2D are: C_{11}= 101.43 N/m, C_{12}= 36.36 N/m and C_{66} = 39.53 N/m. In the case of AB_r^d bilayer p-Si, the crystal possesses pb2b or pm2a layer group symmetry which belongs to the orthorhombic crystal systems, and the independent elastic constants are: C_{11}=C_{22}= 63.83 N/m, C_{12}=26.92 N/m and C_{66} = 50.43 N/m. As discussed in chapter 2, the following criteria must be fulfilled for 2D tetragonal systems to be stable:

$$C_{11} > |C_{12}|, C_{66} > 0, \tag{4.2}$$

while 2D orthorhombic systems should satisfy:

$$C_{11} > 0, C_{11}C_{22} > C_{12}^2, C_{66} > 0. \tag{4.3}$$

As one can see, these criteria are satisfied by AA and AB_r^d bilayer p-Si which ensures their mechanical stability. Additionally, in table 4.5, we list the (2D) Young's modulus, shear modulus and Poisson's ratio of bilayer p-Si systems. An interesting aspect of the Possion's ratio of AB_r^d is that it is quite high and close to the theoretical limit of 0.5. This means that this 2D material, prefers to change its

shape rather than its surface area under strain, similar to the 3D cases of rubber and water.

Table 4.5 Mechanical properties of AB_r^d bilayer p-Si

Stacking	$E[N/m]$	$G[N/m]$	ν
AA	88.40	39.53	0.36
AB_r^d	52.47	50.41	0.42

4.2.6 Relative phase stability

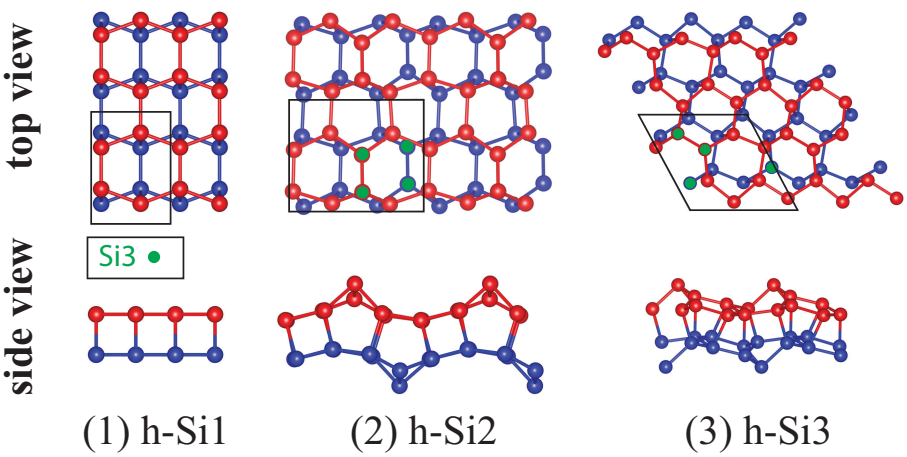

Fig. 4.13 Top and side views of the atomic structures of the 2 × 2 supercell of the three examined hexagonal silicene bilayers.

In this section we compare the cohesive energy of bilayer p-Si to the more familiar bilayer hexagonal silicene structures (h-Si). We examined 3 different stacking types for h-Si bilayers, denoted as h-Si1, h-Si2, and h-Si3. To the best of our knowledge, these are the most stable hexagonal bilayer structures of silicene predicted so far. The h-Si2 structure corresponds to the re-DL-Si structure suggested by Morishita et al. [195] and the h-Si3 is the hex-OR-2×2 structure that was recently proposed by Sakai and Oshiyama [196]. These structures are constructed from the structure information provided by the authors in the supplementary material of the corresponding papers and re-optimized with our computational procedure. The h-Si1 is a new stable bilayer h-Si structure that we

Table 4.6 The interlayer distance d_{inter}, the nearest-neighbor bond length range ($d_{min/max}$) and the cohesive energy per atom E_{coh} of the most stable hexagonal bilayer silicene and bilayer p-Si.

structure	d_{inter} (Å)	d_{min} (Å)	d_{max} (Å)	E_{coh} (eV/atom)
AA bilayer p-Si	0.795	2.363	2.468	-4.129
AB_r^d bilayer p-Si	1.896	2.303	2.403	-4.185
h-Si1	2.175	2.358	2.418	-4.115
h-Si2	1.579	2.298	2.453	-4.165
h-Si3	1.378	2.288	2.473	-4.175

discovered. It is composed of two planar, non-buckled, compressed hexagonal silicene planes that are shifted along the crystal plane. This structure is interesting because although its cohesive energy is close to the former two cases, it has a non-buckled nature. To the best of our knowledge, it is the most stable non-buckled bilayer silicene discovered so far.

The cohesive energies of all the stable bilayer Si systems are given in table 4.6. It is seen that the AB_r^d bilayer p-Si system has the lowest energy, about 10 meV/atom less than the most stable hexagonal silicene bilayer h-Si3. This means that the AB_r^d p-Si structure is the most stable bilayer silicon structure predicted so far, which is a very surprising result. The AA-stacked p-Si has slightly higher energy than h-Si2 and h-Si3.

4.2.7 Electronic properties

In the last part of this work, we investigate the electronic properties of few-layer and bulk p-Si. These electronic properties are mainly determined by the electronic spectrum. In Fig. 4.14 and Fig. 4.15, the electronic band structure of respectively AA and AB_r^d p-Si multilayers and their bulk counterpart is shown. The band structure of the unstable monolayer is also calculated for comparison. Monolayer p-Si is an indirect semiconductor with a band gap of 0.046 eV (PBE). The band-edge states are mainly composed of p_z orbitals of Si3 atoms. In contrast to this, all AA-stacked multilayers are metallic. In the case of the AB_r^d structure, the semiconducting properties of monolayer p-Si are preserved, but the band gap changes somewhat with the number of layers. This can be understood from

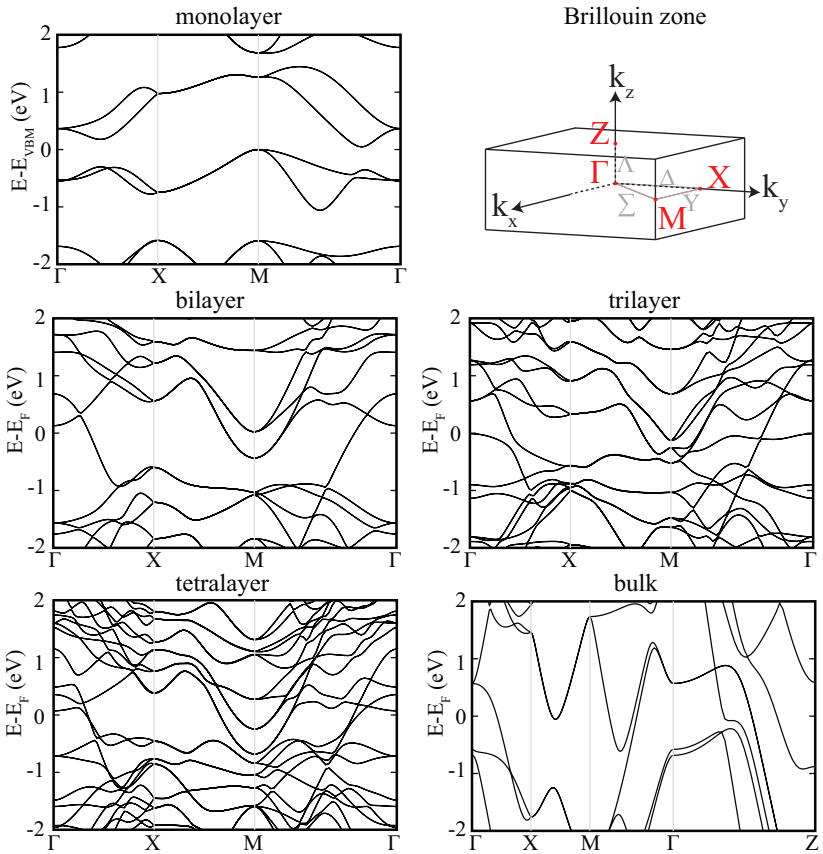

Fig. 4.14 Electronic band structure of AA stacked few-layer and bulk p-Si, and a schematic of the first Brillouin zone.

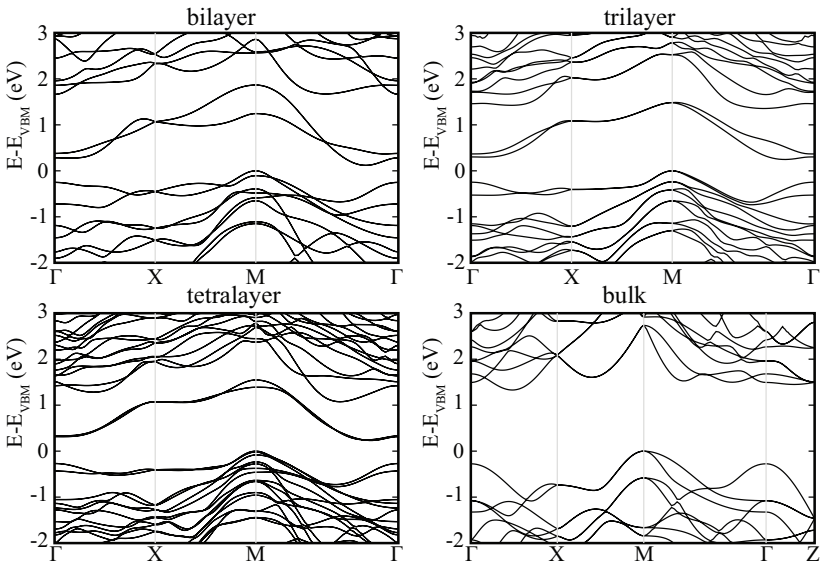

Fig. 4.15 Electronic band structures of AB_r^d stacked few-layer and AB_r stacked bulk p-Si. The results for the monolayer are shown for comparison.

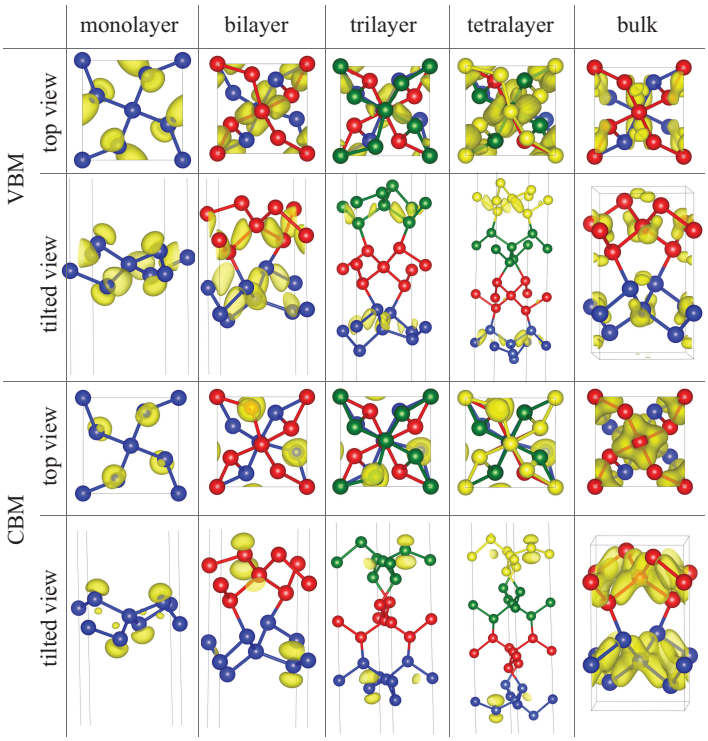

Fig. 4.16 The charge distribution of CBM and VBM in AB_r^d stacked few-layer and AB_r stacked bulk p-Si. The results for the monolayer are shown for comparison.

the position of the electron and hole states which correspond to the CBM and the VBM, respectively. As seen in Fig. 4.15, the VBM and CBM states are always localized on the outermost layers. In other words, the electronic properties are mainly determined by the surface region which is nearly independent of the slab thickness. For AB_r-stacked bulk p-Si, there is no surface and the VBM and CBM correspond to bulk states. This explains the much larger band gap (1.33 eV) in the bulk case.

4.2.8 Summary

In this work, we proposed several stable structures for few-layer pentasilicene. The stability of these structures was confirmed via their phonon spectrum, finite-temperature molecular dynamics, and their mechanical properties. The type of stacking mode, AA or AB, of few-layer pentasilicene has a crucial influence on the electronic properties: AA-stacked systems are metallic, while AB_r^d stacked ones are semiconducting . Surprisingly, the AB_r^d stacked bilayer pentasilicene has lower energy than the most stable bilayer hexagonal silicene structures, which makes it the most stable predicted form of bilayer silicon.

4.3 Mechanical strain: Carrier mobility enhancement in TiS_3 monolayer with strain[3]

4.3.1 Introduction

Recently, monolayers of TiS_3[197, 198] are synthesized as a new type of promising 2D material having high carrier mobility for high-performance electronic device applications. Here, we will study how strain can be utilized to modify the mobility of the carriers in this material. Enhancement of the mobility under strain has been reported and measured before for silicon layers on Si_xGe_{1-x} substrates [199, 200]. According to which, a mobility enhancement up to about 76 % at room temperature was achieved. First-principles calculations have been frequently used to determine the intrinsic mobility of 2D materials.[201–203].

[3]This work is published: P6.

There are also several works that investigated the mobility of monolayer materials under strain[79, 204, 205], including the strain-controlled anisotropic of the mobility in phosphorene [79]. The vertical compression of phosphorene bilayers leads to a two orders of magnitude increase of the mobility[204], strain-enhanced mobility of MoS_2 up to a factor of 10 [205]. In the last two cases, enhancement of the mobility results from the decrease of deformation potential constant (DPC) which is consistent with our situation that will be discussed in our results. Inspired by significant improvements of the transport properties of 2D materials under strain, we investigate the strain dependence of the carrier mobility of TiS_3 monolayers under mechanical strain at 300 K. We find that more than an order of magnitude enhancement of the electron mobility can be achieved by the tensile strain. Furthermore the hole mobility also has moderate enhancement effects.

4.3.2 Computational details

Simulation program: VASP and Phonopy
Energy cut-off: 700 eV
Pseudopotentials: PBE-GGA(PAW)
k points (Monkhorst-Pack): $25\times25\times1$ for insulating and metallic systems, respectively
Vacuum: 20 Å
Energy and force convergence criterion: 10^{-8} eV and 10^{-7} eV/Å, respectively
phonon calculation: finite displacement method
Supercell for phonon calculation: $2 \times 3 \times 1$

As discussed before, band gap is underestimated due to the well-known semilocal functional band gap problem. However, for the position shifts of the valence and conduction band edges with an applied tensile strain, the semilocal functional can provide consistent results and trends when compared to hybrid functionals and has been successfully used in previous studies for the determination of the mobility in 2D materials[79, 203, 206].

To determine the mobility of electrons and holes, we use the deformation potential theory together with the effective mass approximation [207], which has been previously applied to several 2D systems[208–211]. The mobility, μ, of

a 2D system is given by:

$$\mu = \frac{2e\hbar^3 C}{3k_B T|m^*|^2 E_d^2}. \tag{4.4}$$

where e is the electron charge and $\hbar$ is the reduced planck constant. C is the elastic modulus along the transport direction. It is defined as $C = (\partial^2 E_{total}/\partial\varepsilon^2)/S_0$, where E_{total} is the calculated total energy of TiS_3, ε is the strain applied along the transport direction and S_0 is the equilibrium 2D area of the unit cell. k_B is the Boltzmann constant. T is the temperature, which is equal to 300 K throughout the section unless stated otherwise. m^* is the effective mass of the carrier along the transport direction calculated from $1/m^*_{e(h)} = \partial^2 E_{c(v)}(k)/\partial k^2\hbar^2$, where $E_{c(v)}(k)$ is the energy dispersion near the CBM (VBM). E_d is the DPC along the transport direction. It is defined as $E_d^{e(h)} = \Delta E_{CBM(VBM)}/(\delta l/l)$, where $\Delta E_{CBM(VBM)}$ is the energy shift of the band edges with respect to the vacuum level under a small dilation δl of the lattice constant l. We fix $\delta l/l$ to 0.005 as in previous calculations [210]. In this theory, the dominant scattering process is the longitudinal acoustic phonon scattering (AS). However, for a polar material, scattering on optical phonon modes and other scattering sources should be taken into account at high temperatures[201]. Nevertheless, in this work, we will focus solely to the effect of AS on the mobility and its dependence on the strain for the following reasons: 1) The dominant role of AS is not suppressed in polar materials, so it is still an important part that determines the mobility, 2) To separately study different mobility-controlled mechanisms, specially their strain dependence, and 3) It is computationally less expensive.

4.3.3 Unstrained system

The atomic structure of a TiS_3 monolayer is shown in Fig. 4.17. The unit cell has a monoclinic crystal structure. The calculated lattice constants are a = 5.03 Å and b = 3.41 Å, in good agreement with previous calculations [211, 212] and close to the experimental values for the bulk structure (a=4.958, b=3.401)[213]. The monolayer is constructed of connecting quasi-one-dimensional chains of TiS_3 triangular prisms extending along the b direction, as shown in Fig. 4.17. One can spot a significant structural anisotropy in the system along the chain direction (green arrow) and the perpendicular direction (red arrow). Therefore, we can

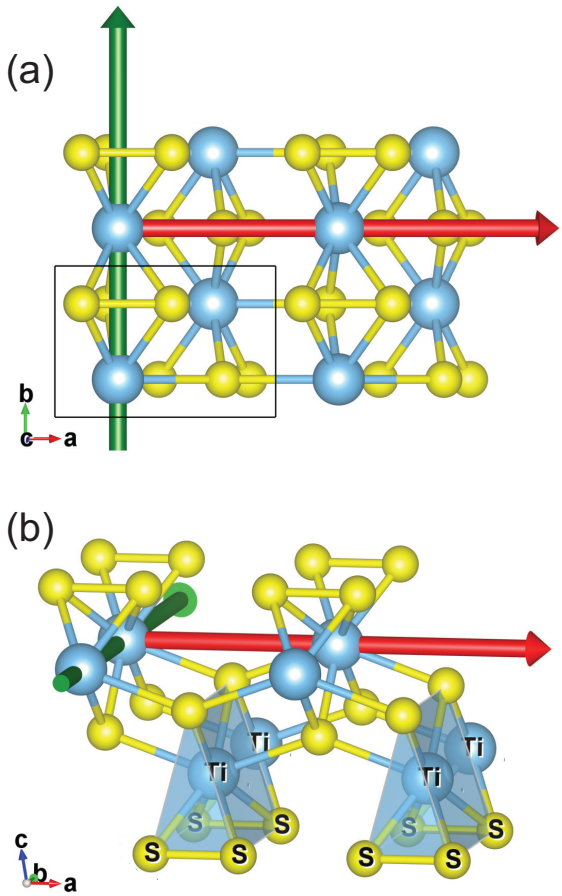

Fig. 4.17 (a) Top and (b) tilted views of a 2×2 supercell of monolayer TiS_3. Two crystallographic directions (where the strain is applied or the mobility is calculated) are shown with red and green arrows.

make a clear distinction when discussing between these two directions throughout the section.

As shown in Fig. 4.18, monolayer TiS_3 is a direct band gap semiconductor having a band gap of 0.29 eV (1.06 eV [210]) that is calculated with PBE (HSE06) functional at the Γ-point. The CBM has the largest contribution from $d_{x^2-y^2}$ and d_{z^2} orbitals of the Ti atoms, while the VBM is mostly dominated by the p_x orbital of the S atoms and the d_{xz} orbitals of the Ti atoms. The x and y directions coincide with the a and b directions, respectively. The z direction is taken perpendicular

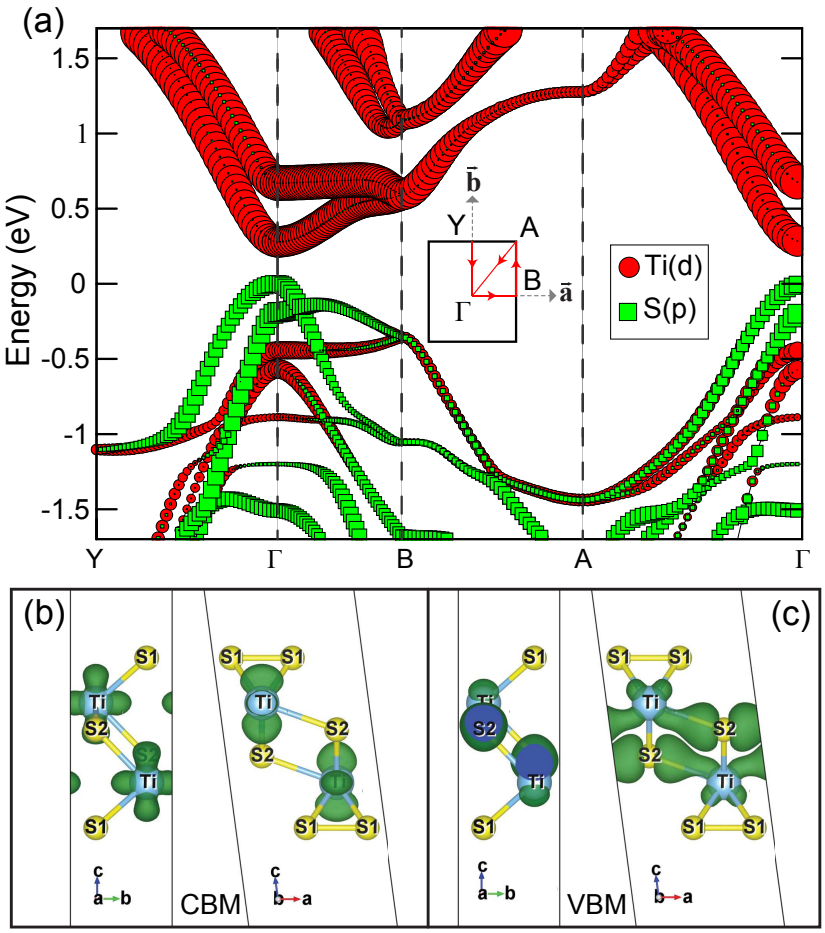

Fig. 4.18 (a) The site and orbital-projected band structure (calculated using PBE functional) of the unstrained TiS_3 monolayer. Decomposed charge density of CMB (b) and VBM (c) at the Γ point are presented.

to the xy plane. Later, we will discuss in detail how these states change their energies when they are exposed to mechanical strain.

To gain deeper insight about the binding nature in the TiS_3 monolayer, we calculate the Bader charges[134–137]. According to the Bader analysis, each Ti atom donates 1.61 e^- to eight S atoms surrounding it. Each of the surface S atoms, labelled as S1 in Fig. 4.18, binds only with two Ti atoms and gains 0.34 e^- net charge. Two of these S1 atoms form a covalent bond between them. While each of the S atoms between two Ti layers, S2 in Fig. 4.18, binds with four neighbouring Ti atoms, and has 0.81 e^- net charge accumulated on it. The electronegativity differences between S (2.58) and Ti (1.54) is calculated as 1.04, and thus

belongs to the polar covalent bond class [214]. This value is large as compared to that of MoS_2 where Mo (2.16) and S (2.58) have a difference in electronegativity of 0.41. Therefore, S-Ti bonds are considered as covalent bonds.

Table 4.7 The electron (hole) effective mass (m^*), the elastic modulus (C), the DPC (E_d), and the electron (hole) mobility (μ) of phosphorene and monolayer TiS_3.

Material	Carrier type	Direction	$m^*(m_e)$	C(N/m)	E_d(eV)	$\mu(10^3$ $cm^2V^{-1}s^{-1})$
Phosphorene	electron	armchair	0.20	24.30	0.65	1.93
	hole	zigzag	6.89	103.14	0.11	25.36
TiS_3 monolayer	electron	*a*	1.52	82.68	0.53	1.82
		b	0.40	133.76	0.84	17.08
	hole	*a*	0.30	82.68	2.53	2.00
		b	0.99	133.76	4.10	0.11

Before applying strain to our system, we summarize the mobility and related parameters for the unstrained TiS_3 in table 4.7, which are in agreement with previous calculations [210]. Similar data for phosphorene are presented for comparison. The results for phosphorene are recalculated with the same computational parameters as TiS_3. The mobility of the electron in a TiS_3 monolayer has an impressive level, which is an order of magnitude larger than that in phosphorene. However, resulting from very small DPC, the hole mobility in phosphorene is an order of magnitude larger than that in TiS_3. Moreover, the anisotropy of the effective mass along different crystallographic directions is much more pronounced for phosphorene as compared to that in TiS_3. Overall, phosphorene is softer than TiS_3 as far as the elastic modulus is concerned.

4.3.4 Dynamical stability under mechanical strain

Applying mechanical strain may have important effects on the stability of a structure. Therefore, it is crucial to know if strain applied to the system does not induce any structural instability. To this purpose, we calculate the elastic modulus and phonon spectrum for the TiS_3 monolayer under various strain values in order to confirm its dynamical stability. Fig. 4.19 shows the elastic modulus along the *a* and *b* directions as a function of applied strain. These values correspond to the elastic constants, i.e. C_{11} and C_{22}. Here, C_{11} (C_{22}) reflects the mechani-

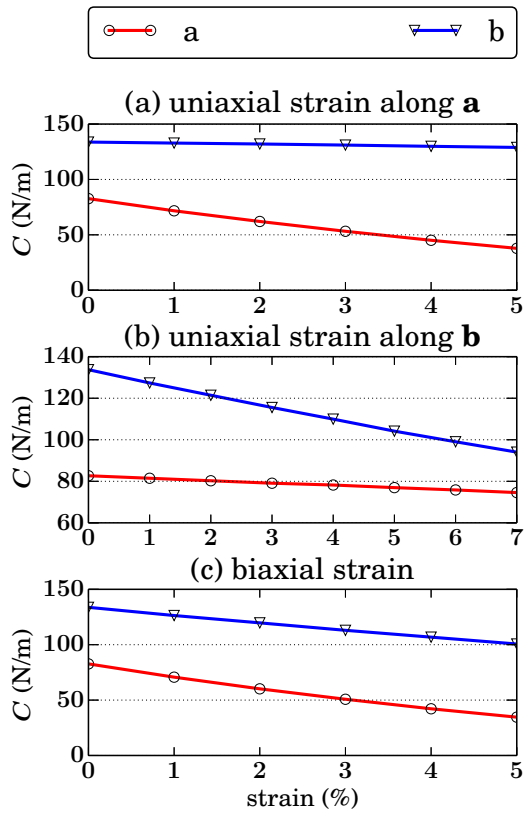

Fig. 4.19 Calculated elastic modulus along the *a* and *b* directions under mechanical strain.

cal response of the TiS_3 monolayer to a strain applied along the *a* (*b*) direction. The calculated value of C_{11} (C_{22}) for the unstrained TiS_3 is 133.76 (82.68) N/m, in good agreement with previous calculations [210, 215]. Note that the calculated elastic constants are all positive and they fulfill the mechanical stability criteria, i.e. C_{11} and $C_{22} > 0$. These results clearly imply that monolayer TiS_3 is less stiff than graphene and single layer h-BN. However, it is mechanically superior as compared to MoS_2 and phosphorene[69]. Furthermore, C_{11} is always larger than C_{22}, meaning that the *a* direction is stiffer than the *b* direction.

In order to gain further insight into the stability of TiS_3 monolayer, we calculate the phonon dispersion under different types of strain. As shown in Fig. 4.20, uniaxial strain applied along the *a* and *b* direction induce dynamical instability in the system at strain values of 6% and 8%, respectively. Note that the highest opti-

cal mode reaches up to 550 cm^{-1} and does not vary with strain. Consistent with our results of the elastic constants, the optical phonon modes are more sensitive to strain applied along the *b* direction, see Fig. 4.20. Except for the topmost mode, phonon branches move downward with strain applied along the *b* direction. We observe an average downward shift of 25 cm^{-1} at 8%, which can be easily detected by Raman spectroscopy. The observed instability at large strain values is due to the presence of imaginary vibrational frequencies, suggesting a structural phase transition. The dynamical stable range of black phosphorus is 15% which is much larger than that of TiS_3[216]. Due to its puckered structure, the former is able to sustain large mechanical deformations. The biaxial case is the combination of two uniaxial strains applied along the *a* and *b* directions, and the stable range is determined by the lowest strain value, i.e. 6% applied along the *a* direction.

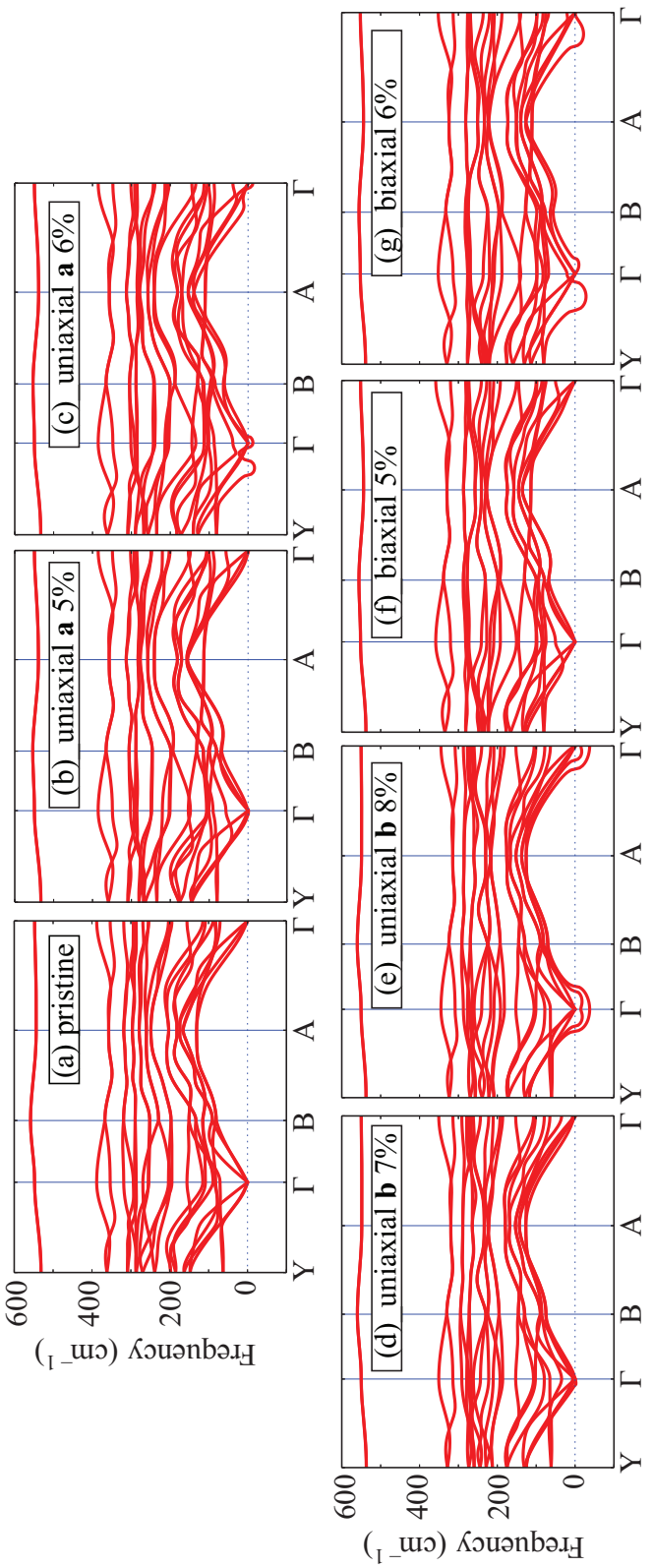

Fig. 4.20 Calculated phonon spectrum of (a) pristine monolayer TiS_3 and that under strain (b-g).

4.3.5 Bond lengths and band gap under mechanical strain

The foremost consequence of the mechanical strain is the change of the structure parameters in the unit cell. Strain is applied by manually changing the lattice constant along the desired direction. After that, the cell parameters are kept fixed whereas the internal atomic positions are allowed to fully relax. Therefore, the latter can be considered as the response of the material to the external strain, which would carry important information about the consequential effects. The variation of the bond length provides information about how the local environment of atoms in the unit cell changes with strain. Considering this, we plot the bond lengths with respect to the different types of strain in Fig. 4.21.

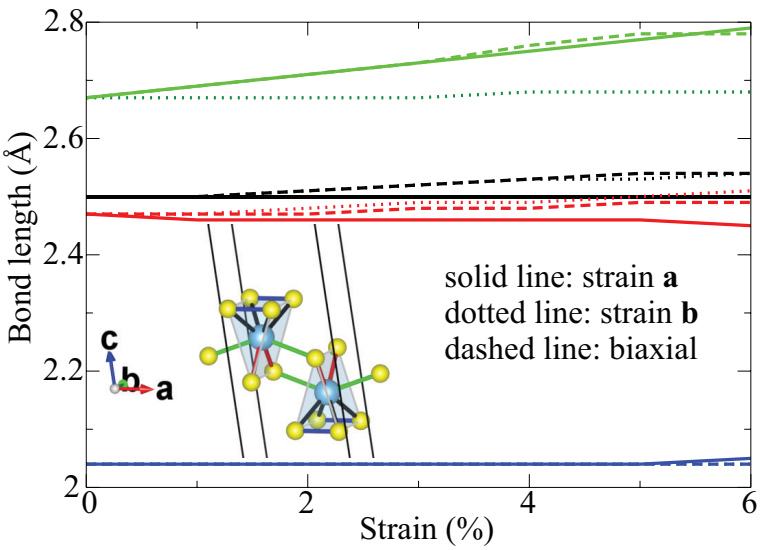

Fig. 4.21 Variation of bond lengths with strain. Color of the curves matches with the color of the bonds in the structure depicted in the inset.

In the following discussion, we correlate the variation of the CBM and VBM, as shown in Fig. 4.22, with the change of bond length by investigating their bonding character. Let us first focus on strain applied along the *a* direction. The most significant change occurs for the Ti-S bond between two neighboring prisms. As the strain increases, the local environment inside the prism hardly changes, in contrast to the bond lengths of Ti-S bonds between prisms. On the other hand, it can be seen from the decomposed charge density of the VBM at the Γ point for the unstrained TiS_3 (see Fig. 4.18(c)) that the Ti-S distance between two prisms

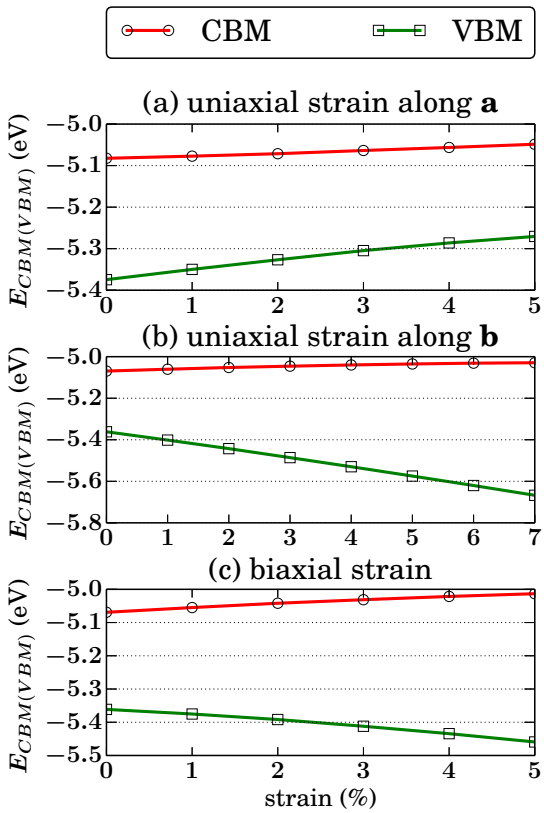

Fig. 4.22 Variation of the band edges with respect to vacuum with strain.

is controlled by the Ti-S bonding state at the VBM. Therefore, we would expect that the energy of this state increases (i.e. its binding energy decreases) with tensile strain, which can be seen in Fig. 4.22. For strain applied along the *b* direction, one can note from Fig. 4.18(c) that the VBM charge distribution along the *b* direction has a node between two prisms. Given the fact that atoms sit close to each other, this is an anti-bonding state. Therefore, we would expect that its energy decreases (i.e. its binding energy increases by depopulating the anti-bonding state) when strain along the *b* direction increases. This is true when we see the trend of the VBM with the strain applied along the *b* direction in Fig. 4.22. The CBM mostly gives a nonbonding state regardless of the direction, see Fig. 4.18(b). This results in a much slower variation of the energy of the CBM under tensile strain, but an overall small change is observed.

Fig. 4.22 also provides information about the variation of the band gap under strain, which agrees well with previous calculations [217, 218]. While the band gap decreases under strain applied along the *a* direction, it increases with strain applied along the *b* direction. The band gap increase in the latter case was experimentally confirmed [217]. By the help of strain engineering, it is possible to tune the optical gap from far infrared to near infrared. The nature of the band gap remains direct within the considered tensile strain range where TiS_3 is dynamically stable. We find that biaxial strain is a superposition of the above two situations as can be seen from Fig. 4.22.

4.3.6 Effective mass, DPC and mobility under mechanical strain

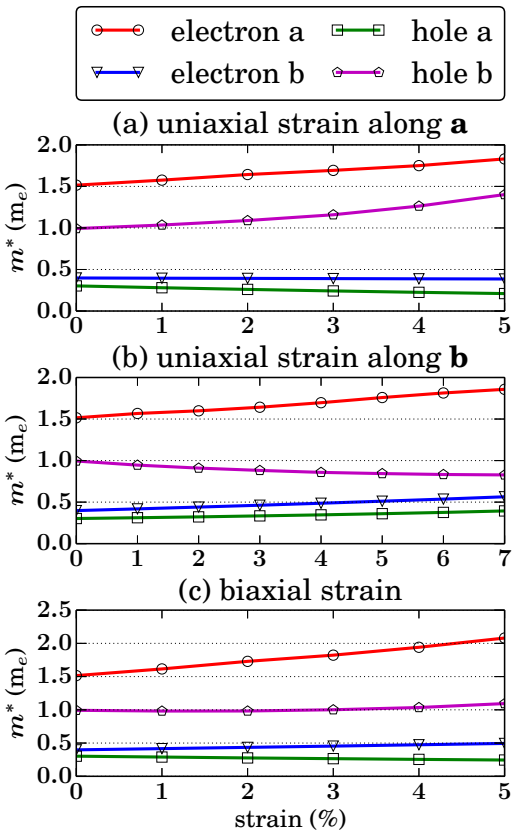

Fig. 4.23 Variation of the effective mass of electrons and holes along the *a* and *b* directions at the Γ-point with strain.

Using the computational setup described above, we estimate the acoustic-phonon-limited mobility of monolayer TiS_3 under strain via equation (4.4). According to this equation, at a particular temperature (e.g. 300 K), three different physical parameters, namely the elastic modulus C, the carrier effective mass m^* and the DPC or E_d, are subjected to a change under strain. Previously, we already discussed the variation of the elastic modulus with strain, which is shown in Fig. 4.19. Now we discuss how the effective mass and DPC change under strain. Fig. 4.23 shows the effective mass of both hole and electron for different directions and strain values. All curves change monotonically. There is no abrupt change of the slope of the curves since there is no band crossing in the considered strain range, and one would expect a smooth variation for the band edges with strain. The electron mass along the *a* direction increases regardless of the direction of applied strain, and the magnitude of this change is the largest among both carrier effective masses along the other directions. Because of this, the degree of anisotropy in the effective mass increases as TiS_3 is subjected to strain. As for the hole effective mass, the difference along the *a* and *b* directions increases for strain applied along the *a* direction whereas this difference decreases for strain applied along the *b* direction. Such anisotropy can be utilized to modify the electronic and thermoelectric properties of TiS_3.

Our calculations unveil that one of the most important factors that determines the mobility is the DPC. In order to evaluate the DPC, we need to apply a small dilation along the direction where the DPC is calculated. The ratio of the CBM (VBM) shift to the amount of this dilation gives DPC for electrons (holes), see Fig. 4.24. Mathematically, as shown in equation (4.4), it is the square of a small number in the denominator. Thus the variation of DPC determines the whole ratio in equation (4.4) and hence the mobility, unless other quantities change dramatically, which is not the case as we have discussed. For example, in the work of Fei and Yang [79], the direction of the highest mobility change by 90° was reported, which was a result of the change in the smallest effective mass in a particular direction. In our case, we observe no band crossing and the variation of the effective mass with strain is rather small for the highest mobility directions, see Fig. 4.23.

Next, we explore the mobility variation under strain, see Fig. 4.25. For uniaxial strain along the *a* direction, the two most apparent changes are the mod-

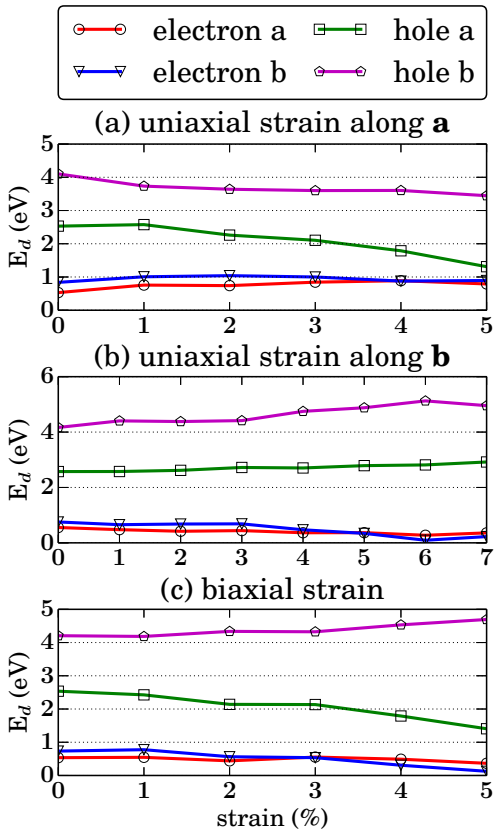

Fig. 4.24 Variation of the (a) DPC (E_d) with strain.

erate enhancement of the hole mobility along the *b* direction, from 2.00×10^3 to 7.08×10^3 $cm^2V^{-1}s^{-1}$ and the drop of the electron mobility along the same direction, from 1.82×10^3 to 0.25×10^3 $cm^2V^{-1}s^{-1}$. Although the electron mobility along the *a* direction for strainless TiS_3 is close to the hole mobility along the same direction, an order of magnitude difference can be realized by the help of tensile strain. Therefore, uniaxial strain applied along the *a* direction would be helpful to select the carrier type based on their different transport properties. For uniaxial strain along the *b* direction, we find a dramatic enhancement of the electron mobility along the *a* direction, from 1.71×10^4 to 5.53×10^5 $cm^2V^{-1}s^{-1}$ at 300 K. This corresponds to a mobility enhancement from 5.13×10^4 to 1.66×10^6 $cm^2V^{-1}s^{-1}$ at 100 K. The subsequent drop at 7 % can be ascribed to being close to the edge of the dynamically stable region. Furthermore, the electron mobility in the other direction (i.e. *b*) has a moderate enhancement

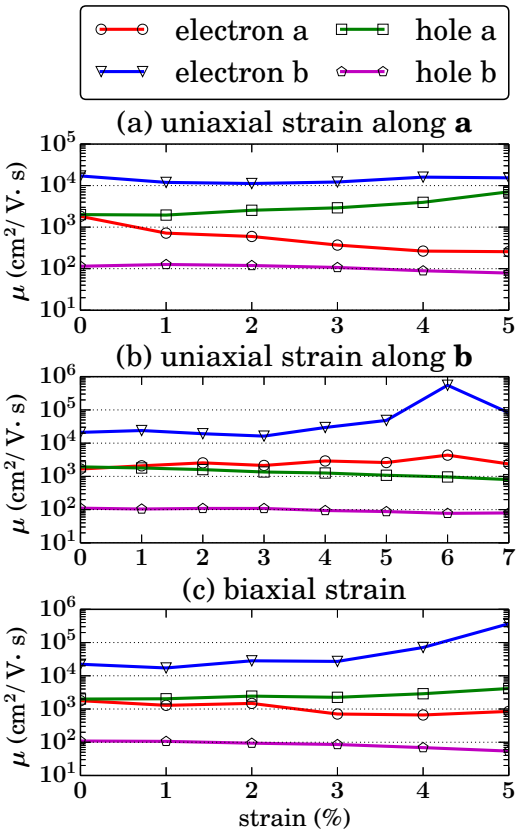

Fig. 4.25 Variation of the mobility (μ) with strain.

at strain value of 6 % as well. The electron mobility along the *b* direction has a considerable increase when tensile strain is applied along the *b* direction. The hole mobility generally tends to decrease in both directions. As stated before, the biaxial case is an effective combination of two uniaxial strains applied along the *a* and *b* directions. The electron mobility along the *a* direction reaches up to 3.68 $\times 10^5$ cm^{2}V^{-1}s^{-1} at 5% biaxial strain.

Lastly, we discuss the effect of the optical phonon scattering on the mobility. Using a Drude-like expression, μ can be expressed as $\sim q\langle\tau\rangle/m^*$, where $\langle\tau\rangle$ is the average scattering time, and in the Matthiessen's Rule, it is given as the sum of all scattering process, i.e. $1/\tau$=$1/\tau_{ph}$+ $1/\tau_{el}$+$1/\tau_{imp}$+ $\cdots$. Here, τ_{ph}, τ_{el} and τ_{imp} are the scattering times related to electron-phonon, electron-electron and electron-impurity scattering, respectively. In a rough estimate (i.e using Einstein's model), τ_{ph} for the longitudinal optical phonon scattering is inversely pro-

portional to the frequency of the optical modes. According to our calculations, the frequency of the phonon modes is subject to a redshift under strain. This means that the contribution of the optical phonon scattering reduces with increasing tensile strain. As a result, we can claim that our trends are persistent against the contribution of the different scattering processes.

4.3.7 Summary

In this work, we have demonstrated that, by the help of tensile strain, it is possible to enhance the carrier mobility of the TiS_3 monolayer more than an order of magnitude at 300 K and two orders of magnitude at 100 K. Phonon dispersion calculations revealed that TiS_3 becomes dynamically unstable for an uniaxial tensile strain larger than 6% (8%) applied along the *a* (*b*) direction. The degree of effective mass anisotropy can be controlled with uniaxial strain. The determining role of the DPC on the mobility in this material is confirmed. The variation of the CBM and VBM with strain was explained through the bonding character within the TiS_3 monolayer. Here, we also showed that strain engineering appears to be a quite exciting way to tune the electrical conductivity of TiS_3.

4.4 Heterostructures: Electrical transport in 1T/2H/1T MoS2 lateral heterostructure[4]

Another way to enrich the properties of materials is to combine different materials to form heterostructures[219–221]. They can be composites made of materials with complementary characters those perform better than each of the material individually, or materials which display new phenomena and promising properties only when acting together. Given the obvious structure anisotropy in 2D materials, there are two types of heterostructures: vertical and lateral[222], see for example Fig. 4.26. The vertical heterostructures are composed of stacks of different 2D materials. We have already seen a vertical heterostructure in the last chapter. They are held together via what holds graphite layers together: the vdW force. Thus, this type of construction is referred as vdW heterostruc-

[4]This work is submitted: P9.

tures. On the other hand, a lateral heterostructure[223, 224] is made by joining the edges of different 2D materials and the connection is mostly made through strong bonding, e.g. covalent or ionic. For this case, all the new properties result from the interface. In this section, I will present our work on the transport properties in lateral heterostructure that is made of the 1T and 2H phase of MoS_2.

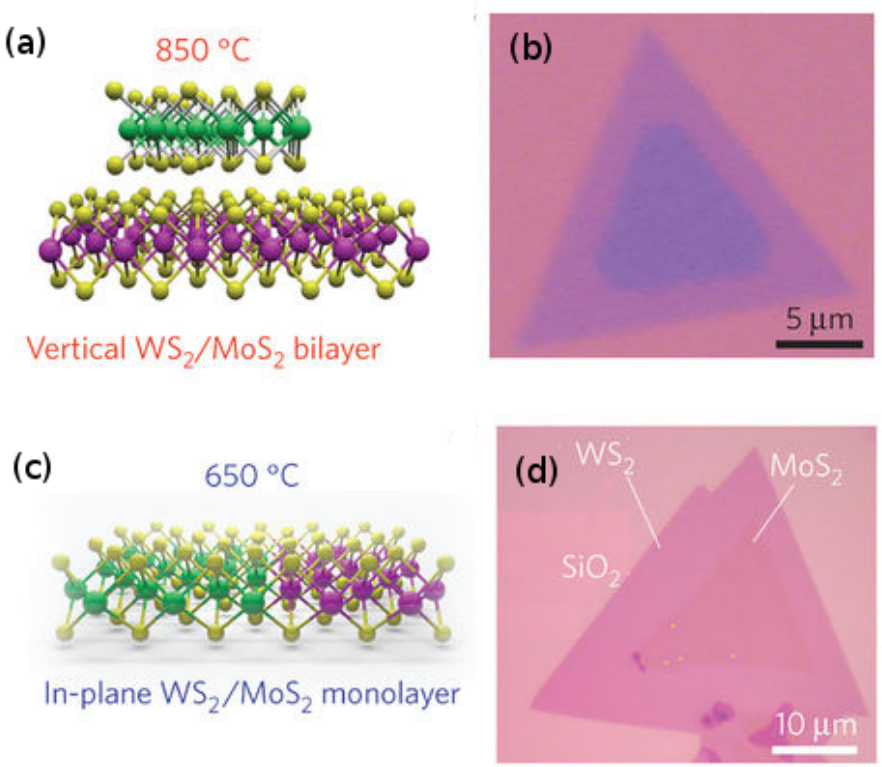

Fig. 4.26 (a) and (d) vertical and (c) and (d) lateral WS_2/MoS_2 heterostructures. Image adapted from: [225]

4.4.1 Introduction

Heterostructures are the essential components of a wide range of solid-state devices, such as transistors, solar cells, and sensors[226, 227]. They are fabricated by combining different types of materials, e.g. metals, semiconductors, and insulators. Therefore, the physical properties of the combined system are enhanced or become more controllable as compared to that of each material individually. These tailored properties are strongly related to the interface of the

two different materials where all interesting and new phenomena occur. However, along with the emergence of nanostructured materials, dimensionality has become another major factor affecting the physical properties of materials and devices along with the interface. Thus, solid-state device fabrication with heterostructures based on low-dimensional nanomaterials has attracted significant attention and a new research area in material design has been initiated where researchers are expecting unprecedented results, phenomena and physics[228–230]. Indeed, several advantages of 2D phase engineering over the 3D counterpart has already been demonstrated.[231]

As discussed before, In a vertical heterostructure, an overlapping portion of two materials is glued together mainly via interlayer vdWs interaction, while in a lateral heterostructure one-dimensional edges of two materials are contacted with covalent bonds without overlapping. The vdWs interaction in a vertical heterostructure introduces a potential gap between the two layers, which electrons have to tunnel through, resulting in higher resistance due to the reduced carrier transmission probability. Naturally, this resistance is much lower in a lateral heterostructure owing to the formation of covalent bonds that provide a path for carriers to travel across the interfaces[232, 233]. Recently, Eda et al. [234] have discovered the coexistence of multi-phase MoS_2 that is a promising material for heterostructure device fabrication due to their natural metal-semiconductor-metal structure with clear a lateral heterostructure interface[234]. Considering the distinct electronic nature of these phases, the physical properties of these heterostructures[235, 236] can be tuned by phase engineering and novel solid-state device architectures can be realized for several different future applications.

The same research group has synthesized 2D semiconducting heterostructure devices[118, 237] by using metal contacts. As a result of their experimental analysis, they have particularly pointed out the vital importance on the device performance of the geometry and electronic nature consistency between the metal contact and the heterostructure [234, 238]. Considering this fact, Kappera et al. [235] have locally induced 1T metallic phase of MoS_2 in the 1H semiconducting phase, and they measured that the edge resistance was lower than that of metal contacts by more than a factor of two. Subsequently, 1T|1H lateral heterostructures have been drawn attention as a promising contact structure hav-

ing a higher carrier injection rate. Different arrangements of the interfaces between 1T and 1H phases were investigated through theoretical calculations[239, 240] and the structure formed by the connection of armchair edges of 1T and 1H phases has been determined as an energetically more favorable configuration. However, in these calculations the more stable metallic structure ($1T_d$), which arises from a small distortion of the 1T phase, was considered.

The present work aims to investigate the electronic transport properties of MoS_2 multi-phase lateral junctions when the more stable metallic phase of MoS_2 (i.e. $1T_d$) acts as the contact and is compared with the 1T phase. Besides this, this work mainly focuses on the effect of doping on the electrical transport properties. In the results section, we first construct three junction models and calculate their transmission without external bias . Then we calculate the electronic properties for different levels of doping.

4.4.2 Computational details

Simulation program: VASP
Energy cut-off: 500 eV
Pseudopotentials: PBE-GGA(PAW)
k points (Monkhorst-Pack): $25\times25\times1$ for 2D systems and $9\times1\times1$ for lateral heterostructures
Vacuum: 15 Å
Energy and force convergence criterion: 10^{-5} eV and 10^{-2} eV/Å, respectively

Transmission spectrum calculation Electronic transport across the $1T_d$/1T-MoS_2 |1H-MoS_2 interfaces is calculated using the self-consistent non-equilibrium Green's functions (NEGF) technique as implemented in TranSIESTA[241] which is interfaced with the SIESTA code.[242] Double-zeta (plus polarization) numerical orbital basis sets are used for all atoms. We employed norm-conserving pseudopotentials[243], the GGA/PBE functional, and an energy cutoff for the real-space mesh of 250 Ry. In order to get accurate transmission spectra, the 2D Brillouin zone normal to the transport direction is sampled by meshes composed of 100 k-points in the periodic direction. While the SIESTA code uses a localized basis set and norm-conserving pseudopotentials, the calculated lattice parameters for different phases of MoS_2 agree well with those obtained from the VASP code.

4.4.3 Structures

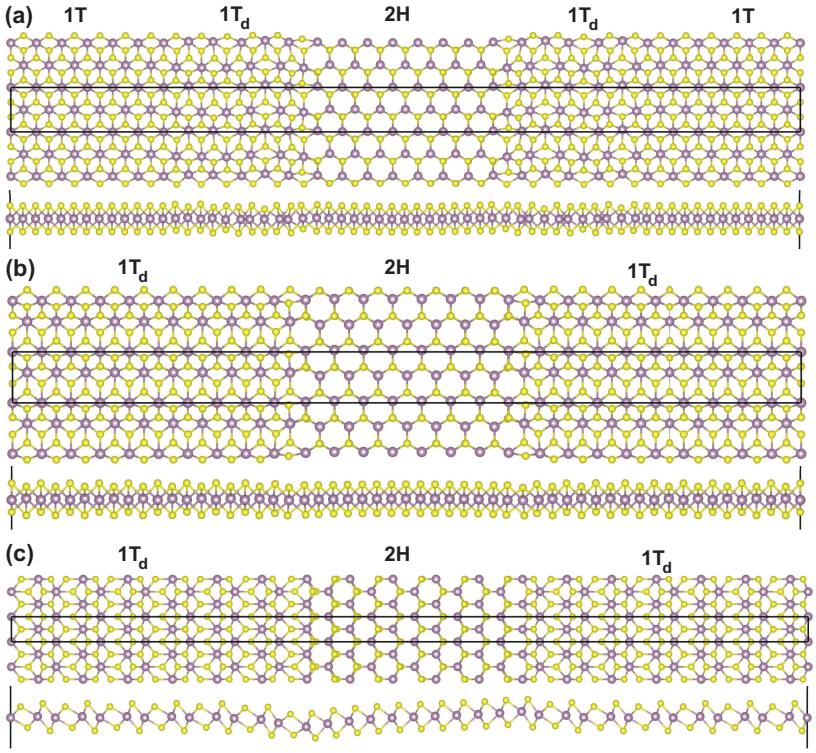

Fig. 4.27 Device models where the 2H phase of MoS_2 is sandwiched between the metallic MoS_2 electrodes: (a) the α-device, (b) the β-device, and (c) the γ-device. For the α and β devices, the interfaces between metallic and semiconducting MoS_2 have an armchair termination while a zigzag termination in the γ-device.

The use of metallic TMDCs as metal electrodes are expected to offer a breakthrough in the semiconductor industry as they have negligible heat dissipation and therefore are energy efficient. Among metallic TMDCs, metallic phases of MoS_2 (1T- and $1T_d$-MoS_2) have attracted a growing interest due to their smooth interface with the semiconductor phase of MoS_2 (1H-MoS_2). However, the 1H phase is thermodynamically more stable than both 1T and $1T_d$ phases. Therefore, the stabilization of 1T and $1T_d$ over the 1H phase becomes an essential requirement for the successful experimental realization of configurable device structures such as 1T/T_d-MoS_2 |1H-MoS_2. On the other hand, 1T MoS_2 is meta-stable and undergoes a Peierls transition to a lower-energy state $1T_d$ (or distorted 1T) and thus, metal contacts with the $1T_d$ structure are more stable than those with

the 1T phase. However, the MoS_2 $1T_d$ phase retransforms to the 1H phase at room temperature. As far as the relative stability is considered, choosing $1T_d$ as metal contact further stabilized the junction. Therefore, understanding the effect of different physical mechanisms on the stability of multiple phases (H, T, T_d) of this material is of vital importance to develop a proper control on phase transitions. To this end we mainly focus on the effect of doping (either with charge or atoms) on the stability, electronic and transport properties of $1T/T_d$-MoS_2 $|$1H-MoS_2 interfaces. For the 1T and 1H hexagonal unit cells, the optimized in-plane lattice constant is obtained as 3.18 Å . On the other hand, the optimized lattice constants are a=3.18 Å and b=5.72 Å for the tetragonal $1T_d$ unit cell. These values are in good agreement with previous calculations[244]. It was previously discovered that the coexistence of the $1T_d$ phase with the other two phases indicates their experimental stability, yet it is also possible to relax the $1T_d$ phase to 1T phase using an external source, such as electron beam irradiation[234]. In experiment, 1T and $1T_d$ are indistinguishable, because the S atoms are the same in these two cases. Only the Mo atom form clusters that can not be differentiated in STM image.

In this work, we systematically investigate the electronic and transport properties of three different device architectures, called α, β, and γ, denoted in Fig. 4.27. In all device models, the semiconducting 1H-MoS_2 phase is sandwiched between two $1T_d$ metal electrodes to create Schottky contacts at the interfaces. In the α structure, the metallic part consists of both 1T and $1T_d$-MoS_2 phases. The size of metallic and semiconducting parts are larger than 20 Å along the transport direction. The interface between the $1T_d$-MoS2 and 1H-MoS_2 phases have either an armchair termination, as in the case of the α and β structures, or a zigzag termination as in the case of the γ structure, in order to investigate the influence of the contact type on the calculated properties. We predict that the γ structure significantly deviates from a planar geometry after structural relaxation, see Fig. 4.27. To check whether such distortion is due to a calculation artefact, we started from a complete planar geometry and allowed both atomic coordinates and cell parameters to relax to their equilibrium values (or lowest energy configuration). We observed that the planar structure is not stable and structural relaxation brought back the original distorted structure. Indeed, such buckling or deviation from a planar structure is mainly restricted to the left in-

terface, in line with a recent work that proposed a new crystal structure model for MoS_2[244]. The observed buckling helps to reduce repulsive interaction between S atoms at the left interface, thereby enhancing the stability of this interface.

4.4.4 Transmission spectra and DOS

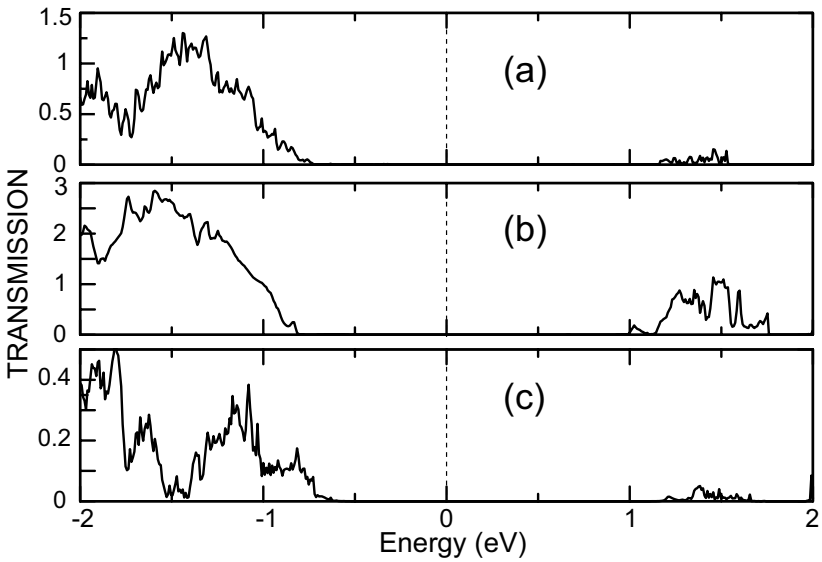

Fig. 4.28 The zero bias transmission spectra for (a) the α device, (b) the β device, and (c) the γ device.

The transmission spectra for all three device models at zero bias are depicted in Fig. 4.28. In these plots, the Schottky barrier for holes (electrons) is defined as the difference between Fermi level and the VBM(CBM) of the semiconductor 1H phase of MoS_2. The first clear observation is that there is a large barrier height at the pristine interfaces and there is no transmission within an energy range of 1.8 eV around the Fermi level, corresponding to the band gap of 1H-MoS_2. The Schottky barrier heights for the α, β and γ structures are predicted as 0.72, 0.80, and 0.63 eV for holes and 1.16, 0.99 and 1.19 eV for electrons, respectively. The estimated size of the scattering region along the transport direction is larger than 23 Å, which is much smaller than the mean free path of electrons in MoS_2[245] and therefore, the transport properties of these systems can be estimated with ballistic transport calculations. The β structure has the largest transmission over

the calculated energy range. The Mo atoms form a zigzag chain perpendicular to the interface (or along the transport direction) in the β and γ structures which enhances the electrical transport in these systems. However, the non-symmetric Mo zigzag chain lying parallel to the transport direction leads to scattering of electrons at the interface and gives rise to a lower transmission as compared to the α and β structures. Similar anisotropic electron transport has also been observed for ReS_2 where the resistance is the lowest along the Re cluster direction[246]. Comparing the α and β devices, the coexistence of 1T and $1T_d$ regions in the former device contributes to lowering the transmission due to additional scattering at the $1T/1T_d$ interface as compared to the latter device where we only have $1T_d$ phase in the electrode region.

4.4.5 The effect of doping

Next, we turn to the calculations of the electronic properties as a function of doping. The central part of 1H-MoS_2 is the least affected from the interface formation and determining the band gap and the position of the band edges with respect to the Fermi level. The calculated band gap value of 1.75 eV clearly indicates that the size of the 1H part is large enough to achieve the monolayer limit and eliminates the electrode-electrode interaction. In fact, the band gap of the pristine 1H-MoS_2 monolayer calculated with the same functional is around 1.7 eV. In line with the transport calculations, the Fermi level appears within the band gap of the central region of 1H-MoS_2. The calculated Schottky barriers are 0.75 eV for holes and 0.99 eV for electrons in the β structure. In the following discussion, we mainly focus on the β structure due to its better transport properties as compared to the α and γ devices. Other device models exhibit similar properties. Our results contradict experimental findings in the sense that, in experiments, it was shown that 1T (or $1T_d$)|1H-MoS_2 interfaces exhibit a superior performance over the 3D metal-MoS_2 interfaces. However, we predict large Schottky barriers which give rise to a large contact resistance. In order to shed light on this contradiction, we calculate the electronic properties of the β structure as a function of electron doping. First of all, the electron doping stabilizes the $1T_d$ phase over the 1H-MoS_2 and prevents the structural phase transition to the semiconducting 1H-MoS_2 phase[247]. Also, the electron doping decreases the Schottky bar-

rier height for electrons at the interface, leading to the formation of an *n*-type Schottky barrier. This is attributed to the increase of the density of electrons in the *d*-orbital of the metallic $1T_d$ MoS_2 phase. Fig. 4.29 and Fig. 4.30 show the variation of the partial density of states (pDOS) and Schottky barrier as a function of the electron concentration, respectively. We find that the Schottky barrier already diminishes for electron concentrations larger than 0.1 electron (per $1T_d$ MoS_2 formula unit). The Fermi level rises about 1 eV when 0.28 electron is placed on the $1T_d$ part, which is corresponding to 2.05×10^{14} cm^{-2} in the heavily doped regime. The Schottky barrier can be reduced by half with 0.05 electron per 1T-MoS_2, and that is 5.72×10^{13} cm^{-2}. Direct electron doping can be achieved by using electron beams in experiments or Li/Na adsorption on the metallic phase[247, 248] . Here, the considered alkali atoms donate electrons to the $1T_d$ phase and enhance the stability and electronic properties of the metallic part[247]. In addition, absorption of hydrogen atoms on the 1T part of MoS_2 has been shown to reduce the barrier at the interface of 1T-MoS_2 |1H-MoS_2[249, 250].

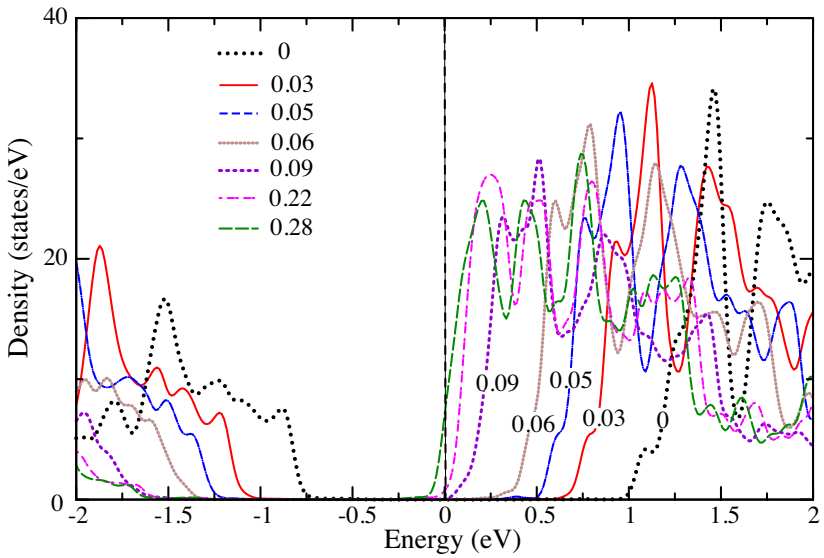

Fig. 4.29 pDOS of the valence and conduction band of 1H-MoS_2 as a function of electron concentration for the β-device. Here, we only show the PDOS of the central part of 1H-MoS_2 where the effect of the interface is minimal. The Fermi level marks the zero energy. Electron concentrations (per formula unit of $1T_d$ phase) are given.

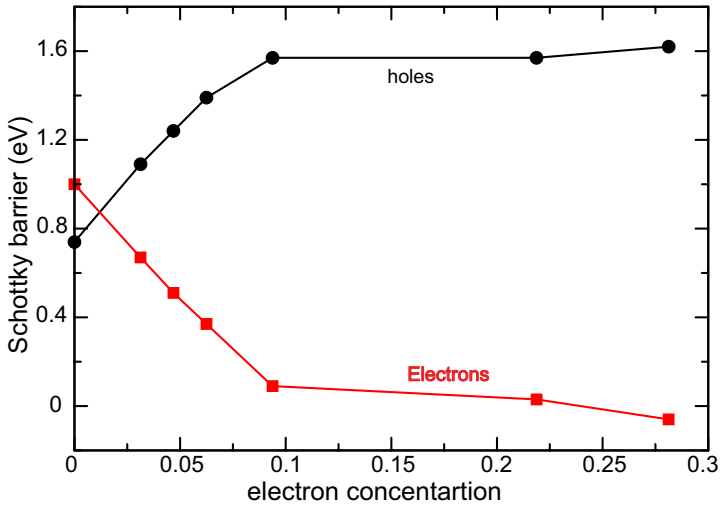

Fig. 4.30 Variation of Schottky barrier for the β-device as a function of electron concentration (per formula unit of $1T_d$ part) for both electrons (red) and holes (black).

Another possible strategy to enhance the stability of metallic phases and electrical conduction at the metal-semiconductor MoS_2 interface is to dope the metallic phase with transition metal atoms. Most of the well known TMDCs are either in the 1H or 1T phase when in their ground state. However, the single layer ReS_2 has neither H nor T as ground state, but it is stabilized in $1T_d$ structure[251]. Therefore, alloying MoS_2 with Re may stabilize the $1T_d$ structure of MoS_2 and leads to *n*-type doping of the crystal as similarly proposed by Raffone et al. [252] for Sn doped 1T phase. Meanwhile, we have previously shown that doping of ReS_2 with Mo results in a *p*-type doping of a ReS_2 monolayer[251]. Therefore, we investigate the effect of substitutional doping of Re at Mo sites of $1T_d$-MoS_2 on the transport properties. Here, we also consider the group VB element Ta since the pristine TaS_2 monolayer crystallizes in the 1T phase and results in a *p*-type doped $1T_d$ MoS_2 structure. Indeed, in a recent work, it was shown that the distorted phase of MoS_2 becomes energetically stable over 1H phase when the Re concentration exceeds 50%[253]. In this work, we did not consider such large dopant concentrations for two reasons. First of all, the lattice mismatch between 1H-MoS_2 and doped 1T-MoS_2 phases can be kept minimal for small dopant concentrations. At large concentrations, the relaxation of the cell parameters leads to artificial enlargement of the lattice parameters of 1H-MoS_2.

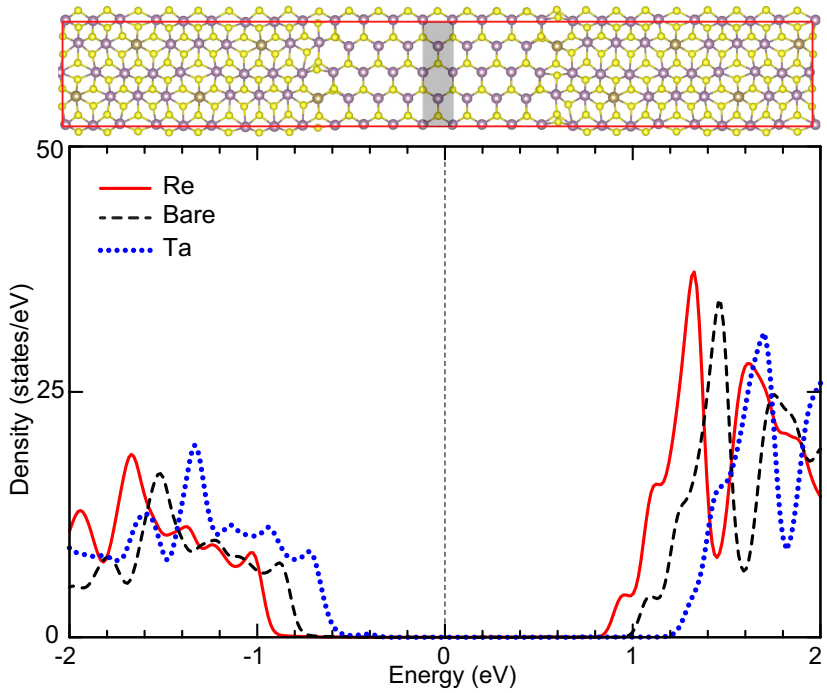

Fig. 4.31 pDOS of the valence and conduction band of the central part of 1H-MoS_2 for Re and Ta doped devices. In the top figure, gray region highlights the central part of 1H phase for which PDOS is calculated. For comparison, PDOS of bare device is also shown.

Secondly, Re doped 1T_d-MoS_2 becomes a semiconductor. To show the effect of doping, we only considered concentrations smaller than 20%. In this work, we assumed that doping of 1T-MoS_2 with Re or Ta may avoid the structural transition to 1H phase due to, for instance, temperature effects. Fig. 4.31 shows the PDOS for the central part of 1H-MoS_2 for Re and Ta doped β structure. In the case of Re doping, the Fermi level approaches the conduction band of 1H-MoS_2, accompanied by a significant decrease in *n*-type Schottky barrier height. On the other hand Ta doping reduces the *p*-type Schottky barrier height as expected. For a concentration of 14% (per electrode), the *n*-type Schottky barrier becomes 0.85 eV for Re and the *p*-type Schottky barrier becomes 0.58 eV for Ta.

Since Re and Ta doping give rise to different electronic properties, we can design metal-semiconductor junctions with different type of Schottky barrier heights (i.e. *n*- and -*p* type) in the same device geometry. This allows us to design optical and photovoltaic applications. While a Re doped junction effectively

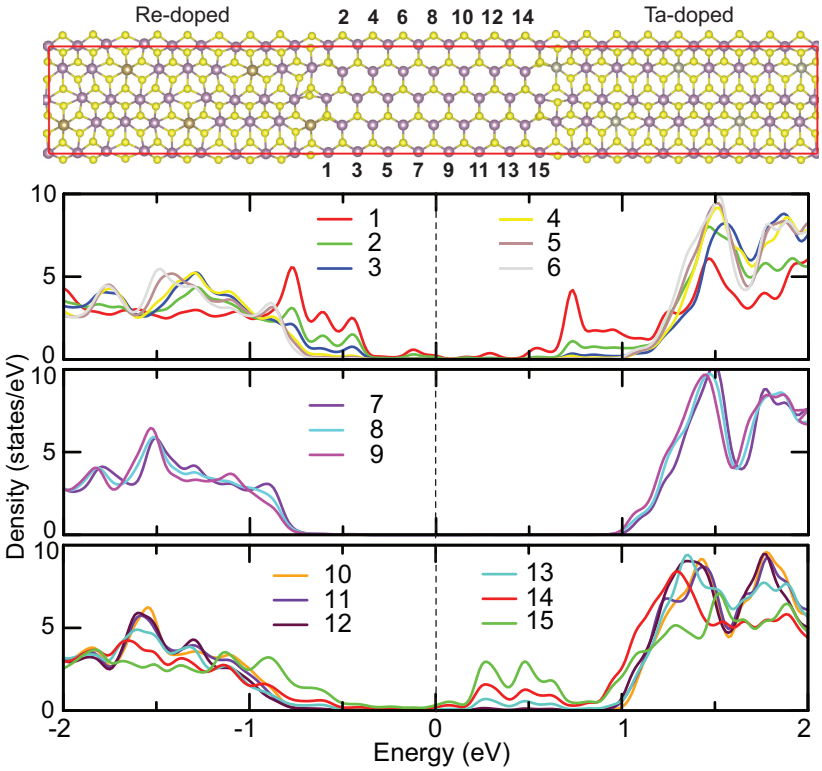

Fig. 4.32 pDOS of 1H-MoS_2 at the different position on 1H-MoS_2. The Fermi level marks the zero energy.

blocks holes Ta doped junction hampers the easy passage of electrons across the junction. In this device geometry, we can separate photo-generated charge carriers for instance. Fig. 4.32 shows the device model and pDOS as a function of position in 1H-MoS_2. While the left electrode is doped with Re, the right electrode is alloyed with Ta. The central part of 1H-MoS_2 clearly has a PDOS similar to free-standing 1H-MoS_2 monolayers with a band gap of 1.75 eV. However, we have different electronic properties in the right and left side of the central region. Due to Re (Ta) doping, the left (right) part has a *n* (*p*)-type Schottky barrier. The presence of $1T_d$-1H MoS_2 interfaces develops mid-gap states that mainly come from the atoms in the boundary region. The electronic properties gradually change from metallic to semiconducting when moving away from the interfaces. For the atoms far away from the interface region (i.e. central region of 1H-MoS_2), we observe a clear band gap which is close to that of pristine 1H-MoS_2. While the mid-gap states appear below the Fermi level at the left interface (Re-doped

side), they are unoccupied and reside above the Fermi level at the right interface (Ta-doped side). About 3.2 Å from the interface, the mid-gap states start to disappear.

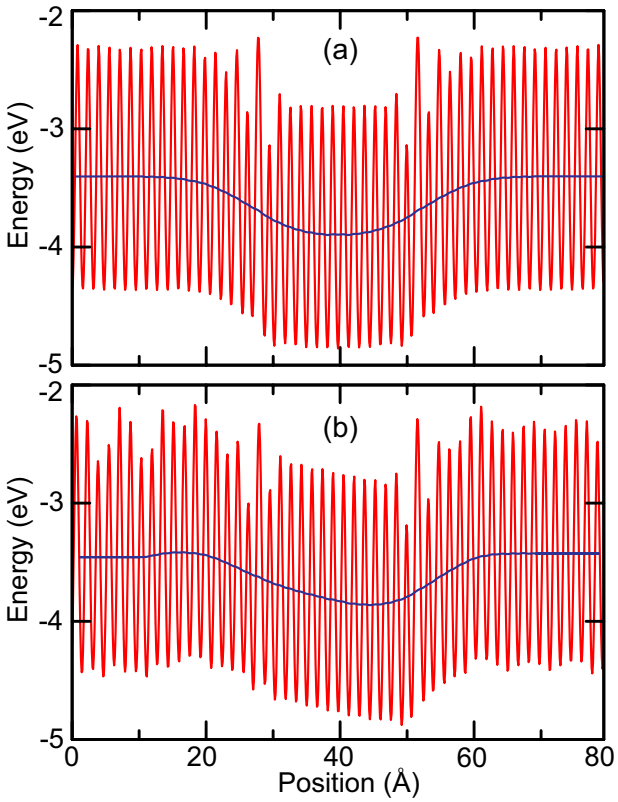

Fig. 4.33 Self-consistent EP profile along the interface of armchair (a) pristine and (b) doped $1T_d$-1H-$1T_d$ MoS_2 heterostructure. The right (left) $1T_d$ MoS_2 is doped with Re (Ta). Blue curve denotes the plane average potential along the heterostructure.

Fig. 4.33 shows the electrostatic potential (EP) along the heterojunction. We consider both pristine and doped β-devices. For an undoped heterojunction, the average potential is symmetric at the left and right interfaces. However, doped heterojunctions have a different EP, especially, within 1H-MoS_2. Due to its valence configuration, Re (Ta) acts as a donor (an acceptor). This is reflected in the average effective potential shown in Fig. 4.33(b). The average EP does not have a sharp variation at the $1T_d$-1H interface, extending along the 2-3 atomic rows. This is due to the fact that we form interfaces between two different crystal structures of MoS_2 (i.e $1T_d$ and 1H). The EP converges to the same value at

the left and right electrodes. If one considers a photovoltaic device using the β structure co-doped with Re and Ta, an electron-hole pair is generated after absorbing a photon in the 1H part. the Re-doped interface has a higher potential as compared to the Ta-doped interface, producing a driving force for dissociation of the electron-hole pair. The electron flows along the potential decline (i.e. towards Ta-doped electrode) and the hole in the opposite direction (i.e. towards Re-doped electrode). In this way, a photocurrent can be generated by the photovoltaic effect. Thus, by proper control of doping and interface roughness, we can control the quantum efficiency of electron-hole dissociation[254].

4.4.6 Summary

In this work, we explored the impact of doping on the electronic and charge transport properties across $1T_d$-1H MoS_2 interfaces by considering various device models. Doping and alloying (with charge, atoms or molecules) appear to be the effective methods to tailor and improve the physical-chemical properties and stability of not only $1T/1T_d$ phases of MoS_2 but also other 2D materials. The interface structure between $1T_d$ and 1H phases is one of the decisive factors in the determination of the electrical transport across the heterojunction. We found that the Schottky barrier height of electrons for pristine heterojunctions can even disappear as a result of electron doping. While charge doping only reduces the Schottky barrier for electrons, co-doping is able to tune the barriers for hole and electrons at the same time.

4.5 Defect induction: Faceted blue phosphorene nanotube formed by line defects[5]

4.5.1 Introduction

Previously we have introduced phosphorene as a new member of 2D materials family. In contrast to the C atoms of graphene, the P atoms in phosphorene have sp^3-hybridization. This is mainly caused by the extra valence electron of phosphorus in comparison to carbon. Indeed, if these extra electrons are placed

[5]This work is published: P4.

in a sp^2-hybridized structure, they would occupy the energetically unfavourable (antibonding) π^* band. However, with sp^3-hybridization, a σ-bond network can be formed with three sp^3 orbitals and the other sp^3 orbital is used to host the remaining electron pair. This leads to an essentially tetragonal coordination of the P atoms and results in a buckled nature of sp^3-hybridized sheets. The out-of-plane positions of the atoms in sp^3-hybridized sheets give rise to various possible structural phases which are absent in sp^2-hybridized systems. In the case of phosphorene, this extra freedom leads to a plethora of structural phases[57, 58] of which black (α-phase) and blue (β-phase) phosphorene (see Fig. 4.34) are the most stable ones.

Most 2D crystals, such as graphene and boron nitride, can also be used to create nanotubes by rolling up the sheets. Due to the buckled nature of the phosphorene family, the traditionally rolled-up nanotubes can be modified in various ways. As shown by Guan *et al.*[57], it is possible to join different structural phases of phosphorene to create so-called faceted nanotubes with lower formation energies than simple rolled nanotubes. These faceted tubes are made up of different phases that form well-defined angles when they are joined together. When a suitable combination of such structural phases is used, the structure can be closed to form a tube without inducing bending strain as in rolled nanotubes.

In the present work, we have taken a different approach to reduce the formation energy of phosphorene nanotubes (PNT). We start from (single-phase) blue phosphorene sheets and introduce various defect lines to induce kinks with well-defined angles in the system. Combining the defect lines in appropriate ways leads to faceted blue PNT with low formation energies. The advantage of this approach is that the energetically unfavorable phases are kept to a minimum. Here, we investigate the stability and electronic properties of these faceted tubes and compare them to the traditional rolled tubes and to the faceted multiphase tubes.

This work is organized as follows: First we study rolled blue PNTs. Then we introduce various defect lines and calculate the corresponding formation energies and the angles of the resulting kinks. We use this information to create energetically interesting faceted PNTs in the next section. Finally, we investigate the electronic properties of the obtained structures and summarize our results.

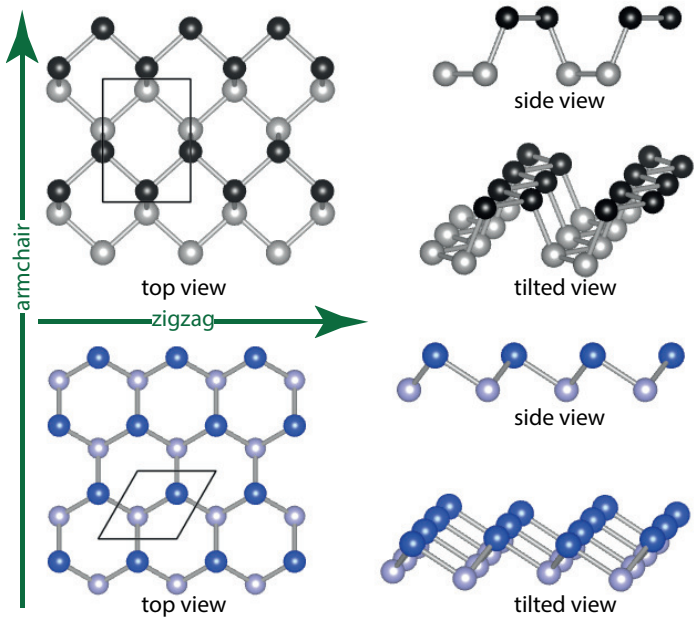

Fig. 4.34 Monolayer structures of black (first row) and blue (second row) phosphorenes. Atoms are colored according to the names of the allotropes, and are lighter in color for the bottom layer of the buckled structure. The black boxes indicate the unit cell of each stucture.

4.5.2 Computational details

Simulation program: VASP
Energy cut-off: 500 eV
Pseudopotentials: PBE-GGA(PAW)
k points (Monkhorst-Pack): 15×15×1 for 2D systems and 1×1×15 for nanotubes
Vacuum: 15 Å
Energy and force convergence criterion: 10^{-5} eV and 10^{-3} eV/Å, respectively

4.5.3 Rolled PNT

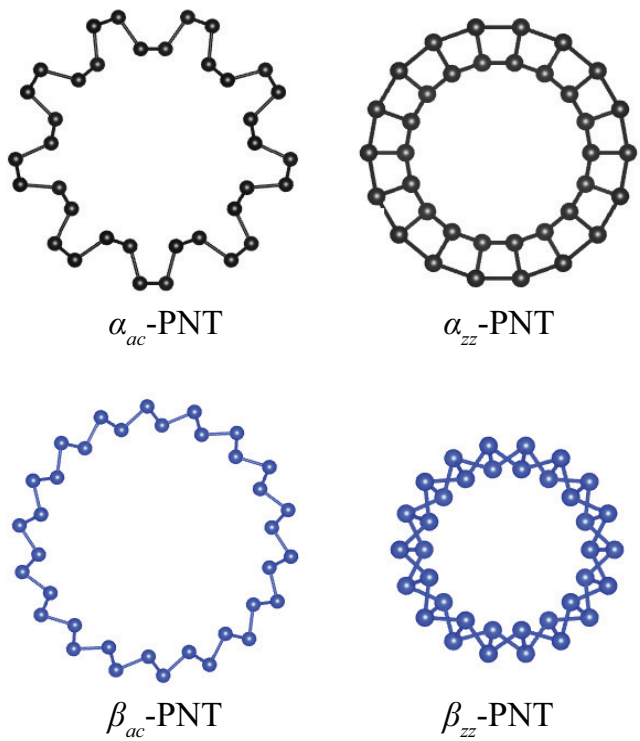

Fig. 4.35 Rolled structures of α-PNT and β-PNT seen from the axial direction. The subscripts indicate the directions of the chiral vector, i.e. *ac* for armchair and *zz* for zigzag.

As a reference, we first investigate the rolled α-PNT and β-PNT that result from rolling up black and blue phosphorene sheets, respectively. A cross section of the structure of some typical examples is shown in Fig. 4.35. In principle, there is an infinite number of possible tubes but we restrict our study to

the chiral tubes rolled up along the armchair and zigzag directions. Such PNTs were also studied previously[57, 255] and our results compare well with those recent calculations as shown below. For large tubes, the formation energy of the tubes can be mainly attributed to the strain energy that results from bending the phosphorene sheets. It has been demonstrated with a simple continuum elastic model that the bending energy follows a R^{-2} dependence, in which R denotes the radius of the nanotube[256, 257]. Deviations from this ideal behavior can be expected for small tubes where the finite thickness of the phosphorene sheet and the interatomic interactions between non-nearest neighbours become important.

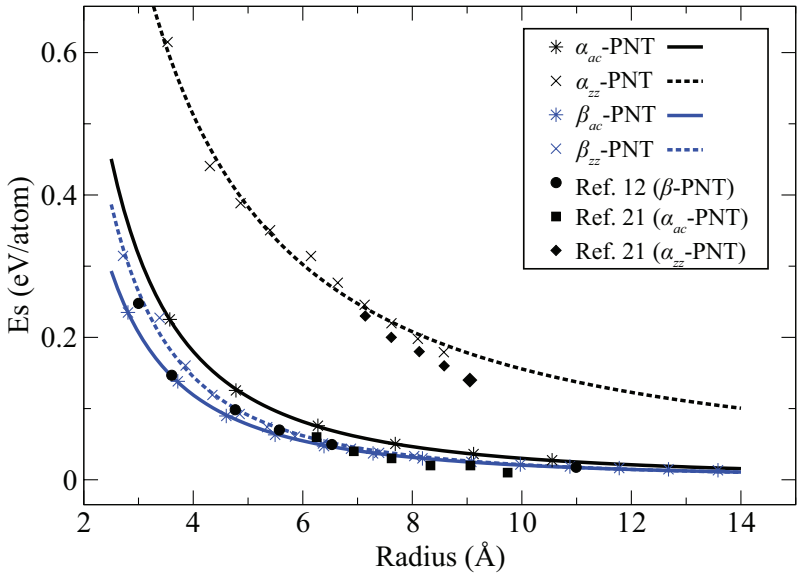

Fig. 4.36 Strain energy versus radius of rolled nanotubes. The curves correspond to aR^{-b} fits, where the fitting parameters are listed in table 4.8.

We calculated the strain energy for armchair and zigzag nanotubes of α-PNT and β-PNT as a function of their radii and show the results in Fig. 4.36 together with the results of Ref. [57] and Ref. [255]. The strain energy is here defined as the energy difference per P atom between the rolled PNT and a corresponding phosphorene sheet, i.e. $E_S^x = (E_{\text{PNT}}^x - E_{\text{sheet}}^x)/N$, in which N denotes the number of atoms and $x = \alpha, \beta$. Since the strain energy of ideal nanotubes follows a R^{-2} law, we try to fit data by a power law of the form $E_S = aR^{-b}$. In table 4.8, we show the coefficients of this fitting function for all the different

nanotubes. It is clear that the strain energy of the rolled PNT approximately follows the inverse-square law based on the bending energy. Note, however, that a substantial deviation from this trend is observed for zigzag nanotubes made of black phosphorene. This can be attributed to the large buckling in the transverse direction which effectively increases the thickness of the bended sheet. Another interesting observation is that the blue phosphorene phase becomes more stable than black phosphorene for small nanotubes: The cohesive energy of 2D black phosphorene sheets is about 10 meV/atom larger than that of blue phosphorene[57] and this is easily compensated by the reduced bending energy of blue phosphorene.

Table 4.8 Fitting coefficients for the strain energy $E_S = aR^{-b}$ of rolled PNTs shown in Fig. 4.36.

	α_{zz}-PNT	α_{ac}-PNT	β_{zz}-PNT	β_{ac}-PNT
a	3.11	2.70	2.63	1.70
b	1.30	1.95	2.09	1.92

The strain energy of all the round nanotubes increases rapidly as the tube radius decreases. At some point the strain energy might become so large that it is more favorable to alter the structure in order to release some of the built-up energy. As discussed in the introduction, Guan *et al.*[57] showed that specific partial structural phase transitions can lead to substantial energy gains. As a result, the PNTs loose their round character and acquire a faceted appearance. The different facets of the tube consist of nearly flat phosphorene nanoribbons with well-defined structural phases that are glued together at almost no expense. The structural phase transitions raise the energy, but this is more than compensated by the reduced strain energy for small PNTs.

4.5.4 Defect lines

Here, we take another approach to release the strain energy. In contrast to the faceted tubes of Guan *et al.*[57] that contain considerable large parts with unfavorable structural phases, we try to maximize the amount of the low-energy blue phosphorene (β phase) in the nanotubes. This can be done by the introduction of defect lines that create kinks in the phosphorene sheet. We will use

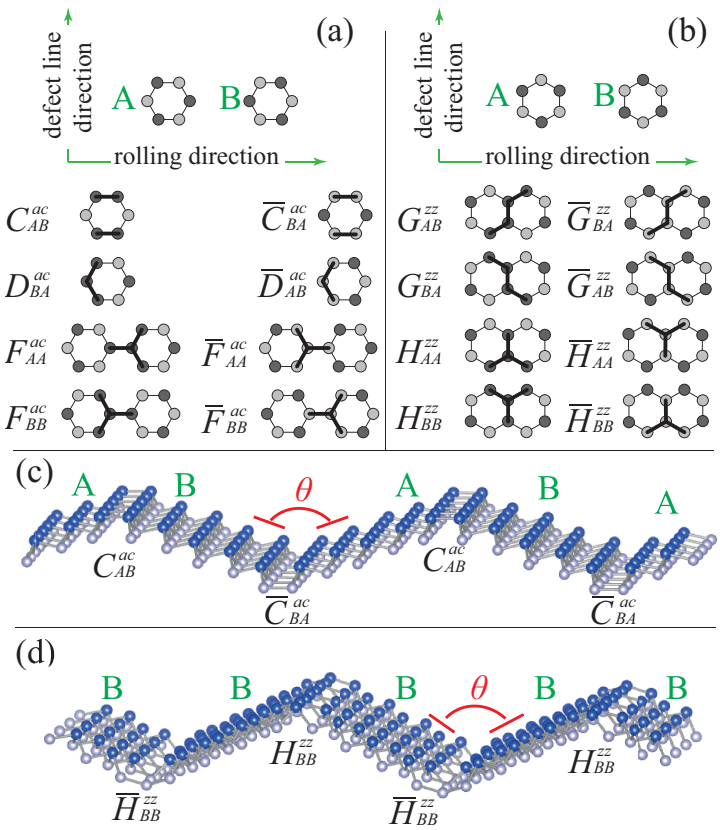

Fig. 4.37 Different types of defect for (a) armchair and (b) zigzag directions. The dark and light shaded atoms indicate that they are buckled up or down, respectively. Effective location of the defect is represented by a thick black line. Overlined defect name refer to the same defect but with an opposite opening direction of the angle. (c) and (d) are tilted view of the C and H defect lines incorporated in the β phase.

the β phase for this purpose for two different reasons: (i) as discussed above, the β phase has lower energy for small tubes, and (ii) it is easier to introduce defect lines in the β phase than in the α phase (black phosphorene). The β phase consists of P atoms that are alternately shifted up and down with respect to the crystal plane (i.e. one sublattice (A) buckles up, while the other (B) buckles down). Defect lines are created by breaking this ordered pattern along 1D lines, which can be done in several ways. We restrict our study to lines in the zigzag and armchair directions in order to create armchair and zigzag nanotubes, respectively. Three types of defect lines, C, D, and F, in the zigzag direction are

considered and two, G and H, in the armchair direction. The structure of these defect lines is depicted in Fig. 4.37 and we give their formation energies in table 4.9. The defect lines induce kinks in the phosphorene sheets and the angle of these kinks is also given in table 4.9. The formation energy of a defect line is defined as $E_f^l = (E_{\text{defect}} - E_{\text{sheet}})/L$ in which L is the length of the defect line. Practically, this property can be calculated in a system that combines two defects of the same kind but with opposite orientation (i.e. angle) in a periodic structure, as illustrated in Fig. 4.37. The following nomenclature will be applied in order to distinguish between the different defects: superscripts (ac or zz) are used to indicate the type of tubes that are produced by the defects (armchair or zigzag); and subscripts (AA, AB, BA, and BB) correspond to the buckling on the two sides of the defect line, A (B) meaning sublattice A up and B down (B up and A down).

Table 4.9 The formation energy E_f^l, and the kink angle θ of the different defect lines that are illustrated in Fig. 4.37.

	C^{ac}	D^{ac}	F^{ac}	G^{zz}	H^{zz}
E_f^l (eV/Å)	0.05	-0.003	0.08	0.09	0.19
θ (°)	139.7	112.4	89.5	118.5	126.7
E_{gap} (eV)	1.56	1.64	1.43	1.28	1.20

Note that one can distinguish two kinds of defects: (i) defects that leave the β phase unaltered on both sides of the defect line and (ii) those defects that invert the buckling orientation on one side with respect to the other. $F^{ac}_{AA/BB}$ and $H^{zz}_{AA/BB}$ belong to the first type, while C^{ac}_{AB}, D^{ac}_{BA}, and $G^{zz}_{AB/BA}$ belong to the second type.

4.5.5 Defect-induced faceted PNTs

The different defect lines discussed above can now be combined to create defect-induced faceted PNTs (DIF-PNTs). According to the type, the formation energy, and the preferred angles of the defects, we can make intuitive guesses about which defect combinations are possible and energetically favorable. Some examples of DIF-PNTs are pictured in Fig. 4.38.

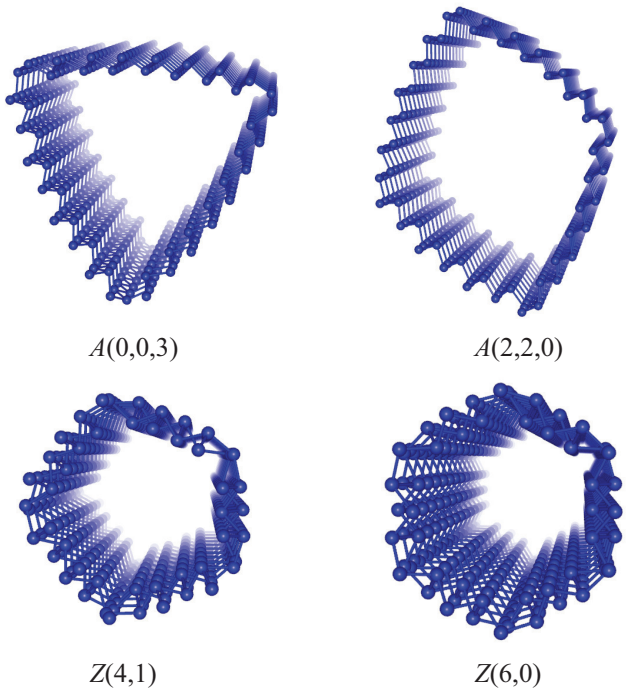

Fig. 4.38 Selected examples of defect-induced faceted PNTs

Not all defect combinations are possible or favorable and we therefore used the following guidelines to make potentially interesting tubes: (i) An even number of defects that invert the buckling (i.e. the second type of defects discussed in previous section) must be included to make closed nanotubes. (ii) The total number of defects should be as small as possible because every defect line has a finite formation energy. (iii) For a nanotube with N defects, the sum of the defect angles should be close to $(N-2)\times 180^\circ$ in order to avoid straining the angles too much.

To compare the DIF-PNTs with round tubes, we need to define some radius for the faceted tubes. To this end, we use the radius of a rolled tube with the same orientation and number of P atoms as the DIF-PNT. The radius of the DIF-PNTs is not only determined by the present defect lines, but also by the size of the defect-free β-phase regions which can also be varied. The formation energy of the DIF-PNT is defined as $E_f^t = (E_{\text{DIF-PNT}} - E_{\text{sheet}})/N$, where N is the number of atoms. When the angles are perfectly matched in some ideal faceted tube, the formation energy of the tube is expected to decrease as R^{-1} instead of the R^{-2}

dependence of round tubes. This R^{-1} dependence simply follows from the fact that the formation energy of the defects is (nearly) independent of the radius, while the number of atoms increases linearly with the size of the radius of the tube. The different behavior of the formation energies of (ideal) faceted and round nanotubes as a function of radius implies that there will be a crossover radius R_0 such that faceted tubes with $R < R_0$ are more stable than round ones.

We will first take a look at armchair PNTs and consider zigzag PNTs in the next section.

armchair PNTs For armchair nanotubes, we need defect lines along the zigzag direction. We discussed three of such defects above and we will combine them to make energetically favorable armchair DIF-PNTs. The first two defects, C^{ac}_{AB} and D^{ac}_{BA}, have opposite effects on the buckling of the P atoms and should always appear in pairs in order to match the buckling at the two edges of the nanoribbon. The third defect, $F^{ac}_{AA/BB}$, can be regarded as a combination of the first two and can always be added to an existing tube. In order to distinguish the different defected nanotubes we introduce the notation $A(m, m, n)$ to indicate an armchair (A) DIF-PNT with m defects of the first and second kind and n of the third. To keep the strain on the defect angles low, we need at least three defects (triangular tube).

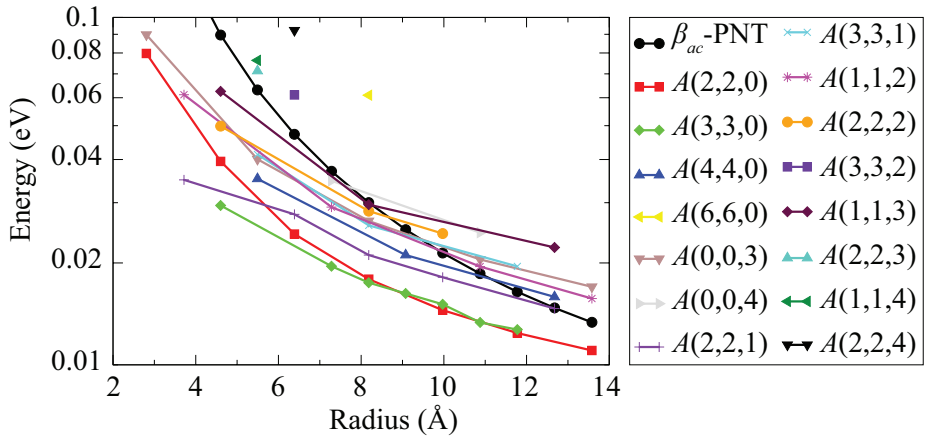

Fig. 4.39 The formation energy E^t_f of armchair DIF-PNTs compared with the strain energy E^β_S of β_{ac}-PNT (black curve with circle symbols).

The only possibilities for such tubes are $A(1,1,1)$ and $A(0,0,3)$. The strain on the first one is considerable and this kind of tube is therefore not considered. Quadrilateral tubes can be made from the following combinations: $A(2,2,0)$, $A(1,1,2)$, and $A(0,0,4)$. Pentagons and hexagons can be formed with $A(2,2,1)$, $A(1,1,3)$, $A(0,0,5)$, $A(3,3,0)$, $A(2,2,2)$, $A(1,1,4)$, and $A(0,0,6)$. The 3th and 7th type of tubes are not considered because of the excessive incorporation of the most energetically unfavorable F^{ac} defects. Adding more defect lines becomes unfavorable because in this case large tubes are required to incorporate such number of defects. Therefore, we only investigate the smallest possible nanotubes as typical examples and do not consider their behavior as a function of the tube radius.

In Fig. 4.39, the formation energy of the different armchair PNTs is shown as a function of tube radius for both faceted and round tubes. The crossover in the formation energy between the faceted and round tubes is nicely observed for several faceted nanotubes such as $A(0,0,3)$. The point where the crossover occurs depends on the type and number of defects and ranges from approximately 7 to more than 15 Å. The most favorable armchair DIF-PNTs are the quadrilateral A(2,2,0) and the hexagonal A(3,3,0) nanotubes with a slight preference for the latter. Due to their larger formation energy, F^{zz} defects are rarely included in the energetically favorable armchair DIF-PNTs.

zigzag PNTs For zigzag nanotubes, only two kinds of defect lines are included to make faceted tubes, namely G^{zz} and H^{zz}. We use the notation $Z(m,n)$ to indicate a zigzag (Z) DIF-PNT with m defects of the first and n of the second kind, see Fig. 4.38 for examples. The total number of G^{zz} defects should be even, while the number of H^{zz} defects is arbitrary. Again, we need at least three defect lines and the only possibility is $Z(0,3)$ in this case. Quadrilateral tubes can be made from $Z(4,0)$, $Z(2,2)$, and $Z(0,4)$. Other tubes that we considered are $Z(4,1)$, $Z(6,0)$, and $Z(8,0)$.

In Fig. 4.40, the formation energy of the different zigzag PNTs is shown as a function of tube radius for both faceted and round tubes. It is seen that the crossover in the formation energy between the faceted and round tubes also occurs for the zigzag nanotube, but at much smaller radii as compared to the

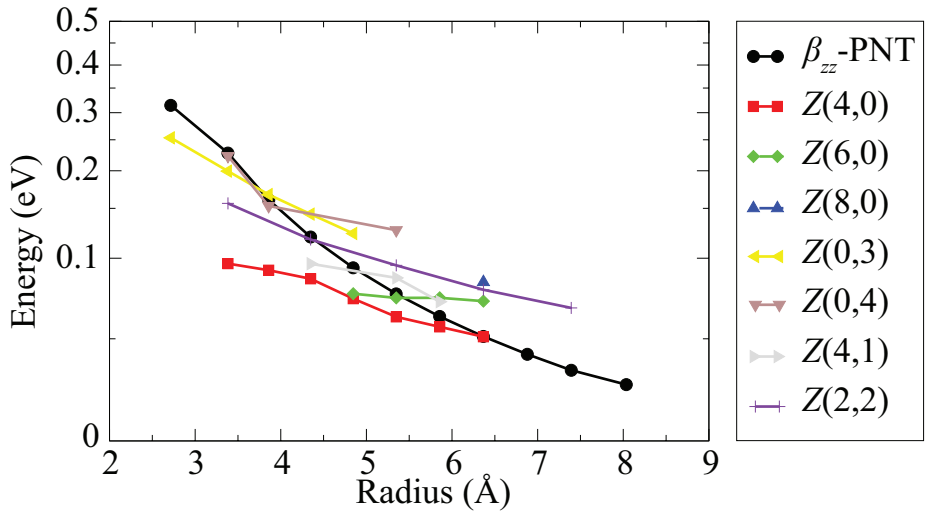

Fig. 4.40 The formation energy E_f^t of zigzag DIF-PNTs compared with the strain energy E_S^β of β_{zz}-PNT (black curve with circle symbols).

armchair nanotubes (from approximately 4 to 6.5 Å). The quadrilateral Z(4,0) tubes are found to be the most stable zigzag DIF-PNTs.

Table 4.10 Fitting coefficients for the formation energy $E_f^t = aR^{-b}$ of DIF-PNTs.

Direction	β_{ac}-PNT	$A(2,2,0)$	$A(3,3,0)$	$A(0,0,3)$	$A(0,0,4)$	$A(2,2,1)$	$A(3,3,1)$
a	1.70	0.33	0.12	0.28	0.19	0.16	0.24
b	1.92	1.37	0.89	1.12	0.86	0.93	1.04

Direction	β_{zz}-PNT	$Z(4,0)$	$Z(6,0)$	$Z(0,3)$	$Z(0,4)$	$Z(4,1)$
a	2.63	0.61	0.30	0.87	0.34	3.70
b	2.09	1.36	0.88	1.23	0.59	2.25

It is interesting to examine the formation energy of the faceted armchair and zigzag PNTs in more detail. We can fit the formation energy of the different tubes with the function $E_f^t = aR^{-b}$. This function has the same form as the strain energy (E_S) defined in subsection 4.5.4, but it now includes both strain energy and defect energy. A b parameter close to 2 indicates that the strain energy dominates in the system, while $b \approx 1$ is expected for non-strained defected tubes. In table 4.10, we give the fitting parameters as obtained for some typical types of DIF-PNT. The round tubes (β_{ac}-PNT and β_{zz}-PNT) have indeed parameters close to 2 and the defected tubes have fitting parameters close to 1, although there

are some substantial deviations in the case of faceted zigzag nanotubes because of the limited number of data points and the smallness of the tubes.

4.5.6 Electronic properties

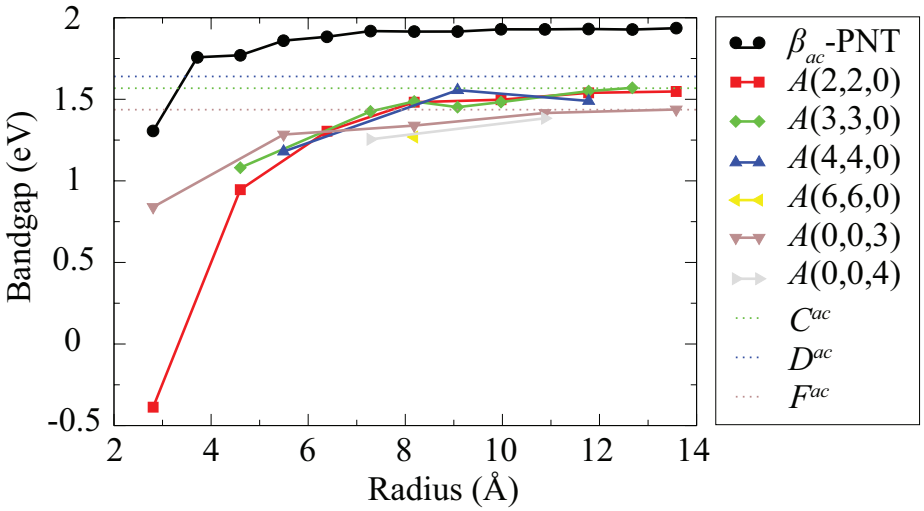

Fig. 4.41 Armchair DIF-PNTs band gaps compared with rolled β_{ac}-PNT (black curve with circle symbols).

In the next section, we will investigate the electronic properties of the DIF-PNTs with a focus on the electronic band gap. In contrast to the inverse proportionality of the band gap with diameter in carbon nanotubes[258], the band gap of round PNTs increases with the size of the radius . For multiphase faceted PNTs, it was shown previously that the band gap does not show any clear dependence on the radius but rather spans the range between the composing structural phases[57].

In Fig. 4.41 we show the band gaps of the armchair DIF-PNTs together with the results for the rolled β_{ac}-PNT. A clear dependence of the band gap on the radius can be observed. The band gap increases with radius and converges to two different limits, well below the limit of the round tubes. The origin of this behavior lies in the character of the VBM and CBM states of the DIF-PNTs which determine the size of the band gap. As illustrated in the insets of Fig. 4.42, the VBM and CBM states are localized on the defect lines. In other words, the de-

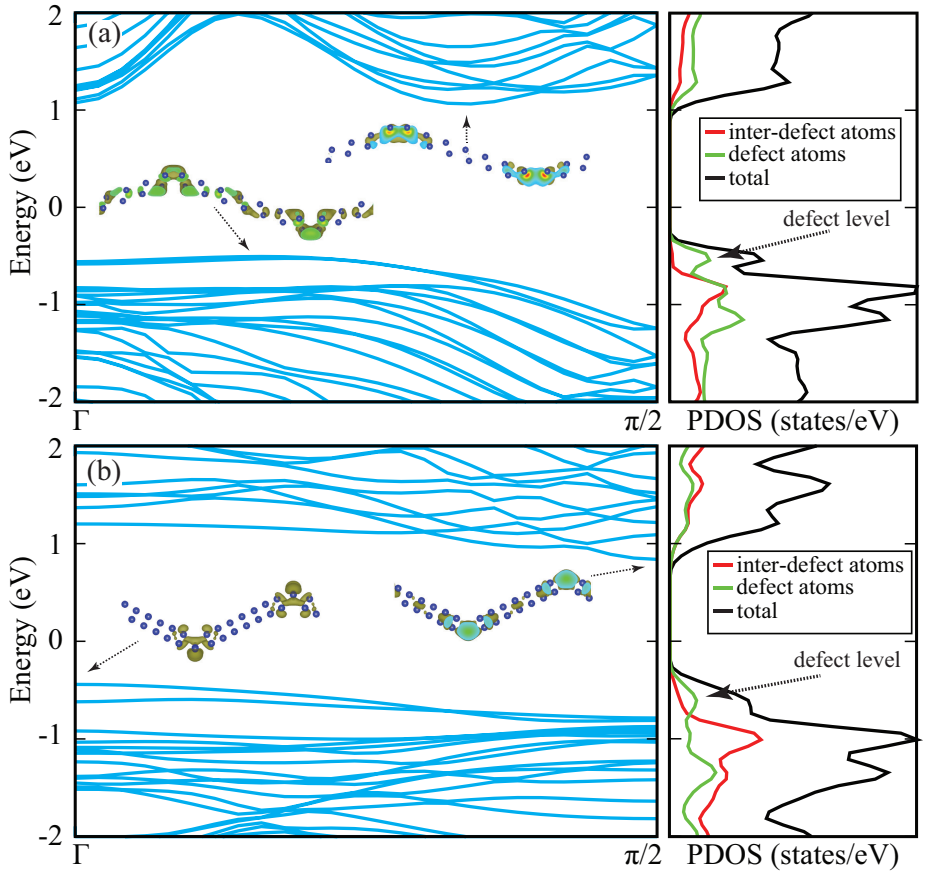

Fig. 4.42 Band structure (along defect line) and PDOS of selected DIF-PNTs, (a) for C^{av} and (b) for G^{zz}. Insets: Charge density at CBM and VBM.

fect levels associated with the defect lines fall inside the blue phosphorene gap and determine the band gap of the defect-induced faceted PNTs. This is confirmed by the pDOS in Fig. 4.42, where a clear defect peak in the PDOS can be found inside the band gap of pure (inter-defect) blue phosphorene. Therefore, the electronic band gap will not converge to the blue phosphorene limit, but rather to the gap size of the isolated defects as calculated in subsection 4.5.4 (table 4.9). The tubes contain various types of defects, but the defect with the smallest gap determines the total band gap of the tube. The decreased band gaps for smaller tubes can be attributed to inter-defect interactions and possibly to some remaining bending stresses. The decrease in the band gap when the distance between the defect lines decreases was also observed for the de-

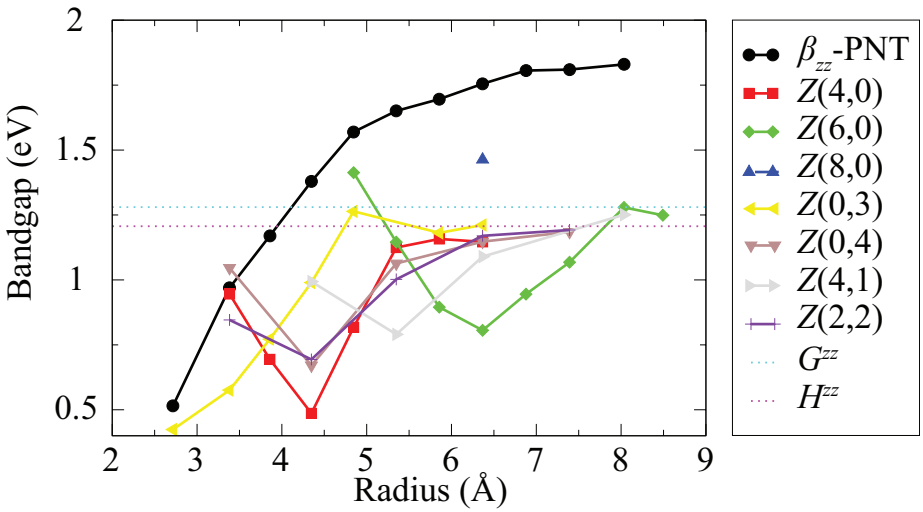

Fig. 4.43 Zigzag DIF-PNTs band gaps compared with rolled β_{zz}-PNT (black curve with circle symbols).

fected phosphorene sheets, illustrated in Fig. 4.37, in which no bending strain was present.

The dependence of the band gap on the radius of the zigzag DIF-PNTs is shown in Fig. 4.43. As for the zigzag DIF-PNTs, the band gaps converge to that of the isolated defects for large radii. When compared to armchair DIF-PNTs, a different behavior can be observed for tubes with small radii: with decreasing radius the band gap first decreases, but then it increases again for very small radii. The first decrease can be attributed to the interaction between the different defect states. The increase of the band gap for very small radii might be attributed to the structural interaction between the defects: the defects of the zigzag nanotubes are wider (i.e. they distort the blue phosphorene phase over a wider range) than the armchair ones and become structurally distorted when the distance between them becomes smaller.

4.5.7 Comparison to multiphase faceted PNT

In the last part of this work, we will compare our results of DIF-PNTs to the multiphase faceted PNTs proposed by Guan et al. [57]. These last tubes are made of fixed combinations of α, β, γ, and δ-phase phosphorene with variable widths, as depicted in Fig. 1 of Ref. [57]. Our most favorable armchair DIF-PNTs, namely the

A(3,3,0) tubes, are closely related to some of the tubes of Guan *et al.* and have similar symmetry and formation energies. The (nearly) equally stable quadrilateral A(2,2,0) tubes, on the other hand, fall outside their description due to the different number of facets. The DIF-PNTs are not restricted to the triangular symmetry of the multiphase PNTs and allow therefore for a much larger variety of possible low-energy nanotubes.

For zigzag PNTs the differences are even larger. Our zigzag DIF-PNTs have no analogues in the multiphase description because the multiphase zigzag PNTs are exclusively built from the energetically less favorable γ and δ phases. The multiphase description provides only one structure with lower formation energy than rolled β-PNT (see Fig. 3(a) of Ref. [57]), in contrast to the multitude of zigzag DIF-PNTs with lower formation energies that we found (see Fig. 4.40). Blue (β) phosphorene is significantly better suited to make small zigzag PNTs than the other structural phases (α, γ, and δ).

4.5.8 Summary

In this work, we investigated a new class of faceted PNT using first-principles calculations. We started our study by examining round armchair and zigzag PNTs of black and blue phosphorous and showed that blue phosphorene is better suited to make small nanotubes. Then we proposed five different type of defect lines to create kinks in β phosphorene sheets. We investigated the formation energy and kink angle of these defects and used this information to create defect-induced faceted PNTs. After identifying some suitable defect combinations, we calculated the formation energy as a function of the PNT radius and demonstrated the enhanced stability of the DIF-PNTs with respect to round tubes. We showed that the VBM and CBM states of the DIF-PNTs are localized on the defect lines and that these states control the electronic properties of the tubes. The band gap of armchair DIF-PNTs increases with the radius and converges to the gap corresponding to isolated (infinitely separated) defect lines. For zigzag DIF-PNTs, a more complicated behavior was observed which originates from the wider structural distortions associated with the defect lines.

Finally, we compared our defect-induced PNTs with the multiphase faceted PNTs proposed by Guan *et al.*[57]. We found similar formation energies for arm-

chair PNTs, but more favorable DIF-PNTs can be created with small radii due to less stringent restrictions regarding the structure (symmetry) of the tubes. For zigzag PNTs, the DIF-PNTs are significantly more stable in comparison to rolled β-PNTs and previously reported multiphase faceted PNTs. Furthermore, we found a much larger variety of stable zigzag PNTs.

Chapter 5

Summary and outlook

Summary This thesis started with an introduction to graphene and several early 2D materials such as functionalized graphene, group-IVA 2D materials and other 2D materials from layered materials, and briefly covered their diverse physical properties. Inspired by these new materials and new properties, in chapter 3 and chapter 4, the determination of higher level physical properties of several newly discovered or proposed 2D materials were presented as the main results of the thesis. These new 2D materials are phosphorene, 2D-TiS_3, MXenes, 2D-$Ca(OH)_2$, pentasilicene and penta-hexa-graphene, and additionally, faceted blue PNT. Among these, the last four materials are the theoretically proposed ones from this thesis. The higher level physical properties of these materials that were investigated in this thesis include thermal, piezoelectric, magnetic and transport properties, and lithium battery-related properties. Moreover, several ways to modify the properties of these materials were introduced, such as varying the number of layers, application of mechanical strain, forming a heterostructure and the presence of defects. The main results are summarized as follows.

Phosphorene is one of the new 2D materials. It has several allotropes among which blue and black phosphorene are the most stable ones. They have band gaps around 2 eV and high carrier mobilities, which makes them ideal for electronic device application. In section 3.1, we saw the highly anisotropic thermal expansion rate in black phosphorene, in contrast to the isotropic blue phosphorene. This is consistent with their structural properties. There is a less significant negative thermal expansion in these materials in comparison to graphene. Based on the free energy calculations at finite temperature, we also observed a

possible phase transition from black to blue phosphorene as the temperature is increased. In this study, we combined the results from DFT for phonon calculations with the QHA to access the thermal expansion coefficient.

The piezoelectric properties of 2D-TMDs and 2D-TMDOs were evaluated in section 3.2. A number of candidates were identified to deliver better piezoelectricity as compared to the conventional bulk materials. The general trend shows the Ti, Zr, Sn and Cr based TMDs and TMDOs have much better piezoelectric properties than Mo and W based ones. The reduction of the size and weight when using 2D materials will enhance the efficiency of electromechanical applications.

In section 3.3, we constructed a new type of all-carbon 2D materials through structure and bond engineering. A stable configuration can be realized such that on each of the two C atoms in the unit cell, the local magnetic moment is one Bohr magneton . This structure is a mixed composition of penta- and hexagonal C rings, and it has an AFM ground state.

Properties related to Li battery applications were studied in section 3.4 on our proposed heterostructure, which is a bilayer of MXene and graphene. The presence of graphene breaks the stacking symmetry, such that Li atoms bind stronger to MXenes and stay far away from the graphene layer. The binding energy is larger than that in multilayer MXenes, while the diffusion barriers in these two cases are comparable.

2D-$Ca(OH)_2$ is another 2D material proposed in this thesis. In section 4.1, we have seen negligible influence of the dimension of these materials, despite having a hydrogen-enhanced interlayer interaction. Interestingly, a free-electron-like planar surface state exists in the monolayer and this state has a symmetric charge density distribution with respect to the layer. This symmetry is broken when the system is transformed to a bilayer.

Pentasilicene is a variation of pentagraphene in which carbon atoms are replaced with silicon ones. However, it is not stable as has been indicated by the phonon dispersion having imaginary frequencies. In section 4.2, we stabilized it by transforming it into a bilayer structure where the interlayer bonds are covalent. Surprisingly, the resulting structure is the most stable bilayer silicene to the best of our knowledge.

Strain can also be used to alter the properties of materials. In section 4.3, we used it to enhance the acoustic-phonon limited mobility in 2D-TiS_2. From the deformation potential theory, we explained the proportional relationship of the DPC with the band edge shifts with respect to vacuum under the application of homogeneous strain. The latter is small at a finite strain, which implies the mobility of the material can be large when strain is applied. In this way, more than an order of magnitude increase of the mobility was achieved for this material.

Another way to modify the properties of 2D materials is to construct a heterostructure. In section 4.4, we studied the electrical transport properties of such a system. Taking advantage of the coherent interface of the T and H phase of MoS_2, we formed a lateral heterostructure where two metallic T phases form the electrodes and one semiconducting H phase is the scattering center. The transmission was studied under various electron concentrations to reduce the Schottky barrier height which has been the main obstacle for electron transport at the metal-semiconducting interface. A n-type doping at one electrode and a p-type at the other can reduce the barrier height for both electron and hole.

Finally, a new type of faceted nanotube was designed from blue phosphorene in section 4.5. By introducing line defects in the 2D plane, kinks can be formed to close a faceted tube surface. The advantage of this faceted tube is the fact that flat edges almost do not cost elastic energy to form. This is energetically more favourable than a curved surface of conventional nanotubes. The most important part of the structure are the corners of the faceted tubes, which determines the energy and the electronic band gap of the tubes.

Outlook Nowadays, more and more stable 2D materials are being proposed and synthesized. They need to be explored to fully reveal their potential in both applications and fundamental research. For example, the MXenes family has more than 60 members with a broad range of properties waiting to be characterized. Moreover, with the increase of the number of different 2D materials increasing, the possible combinations of forming heterostructures exhibit a factorial increase. In addition, these heterostructures do not have to be limited to 2D, if one stacks them to a macroscopic thickness, one will end up with layered bulk materials, or nanocomposites, with tailored properties that are designed at

the microscale. On the other hand, DFT software packages are being optimized for higher efficiency and broader capabilities to take full advantage of modern supercomputing facilities. Therefore, the determination of high-level properties of materials of larger simulated systems become accessible and will overcome the barriers that previously limited our understanding of new 2D materials and opens the door to use them in new applications.

Bibliography

[1] S. Kirklin, J. E. Saal, B. Meredig, A. Thompson, J. W. Doak, M. Aykol, S. Rühl, and C. Wolverton, "The Open Quantum Materials Database (OQMD): assessing the accuracy of DFT formation energies", npj Comput. Mater. **1**, 15010 (2015) (cit. on p. 2).

[2] P. Hohenberg and W. Kohn, "Inhomogeneous Electron Gas", Phys. Rev. **136**, B864–B871 (1964) (cit. on p. 2).

[3] W. Kohn and L. J. Sham, "Self-Consistent Equations Including Exchange and Correlation Effects", Phys. Rev. **140**, A1133–A1138 (1965) (cit. on p. 2).

[4] N. Drummond, *QMC Studies of Real Systems*, (2017) http://slideplayer.com/slide/4763755/ (visited on 05/10/2017) (cit. on p. 2).

[5] M. Born and R. Oppenheimer, "Zur Quantentheorie der Molekeln", Annalen der Physik **389**, 457–484 (1927) (cit. on p. 3).

[6] M. Levy, "Universal variational functionals of electron densities, first-order density matrices, and natural spin-orbitals and solution of the v-representability problem", Proceedings of the National Academy of Sciences **76**, 6062–6065 (1979) (cit. on p. 3).

[7] J. P. Perdew, *Electronic structure of solids' 91*, Vol. 11 (Akademie Verlag, 1991) (cit. on p. 6).

[8] J. P. Perdew, J. A. Chevary, S. H. Vosko, K. A. Jackson, M. R. Pederson, D. J. Singh, and C. Fiolhais, "Atoms, molecules, solids, and surfaces: Applications of the generalized gradient approximation for exchange and correlation", Phys. Rev. B **46**, 6671–6687 (1992) (cit. on p. 6).

[9] J. P. Perdew, K. Burke, and M. Ernzerhof, "Generalized Gradient Approximation Made Simple [Phys. Rev. Lett. 77, 3865 (1996)]", Phys. Rev. Lett. **78**, 1396–1396 (1997) (cit. on p. 6).

[10] V. Van Doren, C. Van Alsenoy, and P. Geerlings, *Density Functional Theory and Its Application to Materials: Antwerp, Belgium, 8-10 June 2000*, AIP conference proceedings (American Institute of Physics, 2001) (cit. on p. 6).

[11] Q. Peng, F. Duarte, and R. S. Paton, "Computing organic stereoselectivity - from concepts to quantitative calculations and predictions", Chem. Soc. Rev. **45**, 6093–6107 (2016) (cit. on p. 7).

[12] C. Adamo and V. Barone, "Toward reliable density functional methods without adjustable parameters: The PBE0 model", The Journal of Chemical Physics **110**, 6158–6170 (1999) (cit. on p. 6).

[13] J. Heyd, G. E. Scuseria, and M. Ernzerhof, "Hybrid functionals based on a screened Coulomb potential", The Journal of Chemical Physics **118**, 8207–8215 (2003) (cit. on p. 6).

[14] M. J. Lucero, T. M. Henderson, and G. E. Scuseria, "Improved semiconductor lattice parameters and band gaps from a middle-range screened hybrid exchange functional", J. Phys.: Condens. Matter **24**, 145504 (2012) (cit. on p. 8).

[15] D. C. Langreth and J. P. Perdew, "Theory of nonuniform electronic systems. I. Analysis of the gradient approximation and a generalization that works", Phys. Rev. B **21**, 5469–5493 (1980) (cit. on p. 7).

[16] C. Fiolhais, F. Nogueira, and M. A. L. Marques, eds., *A Primer in Density Functional Theory* (Springer Berlin Heidelberg, Berlin, 2003) (cit. on p. 9).

[17] R. W. Godby, M. Schlüter, and L. J. Sham, "Self-energy operators and exchange-correlation potentials in semiconductors", Phys. Rev. B **37**, 10159–10175 (1988) (cit. on p. 9).

[18] D. Vanderbilt, "Soft self-consistent pseudopotentials in a generalized eigenvalue formalism", Phys. Rev. B **41**, 7892–7895 (1990) (cit. on p. 11).

[19] P. E. Blöchl, "Projector augmented-wave method", Phys. Rev. B **50**, 17953–17979 (1994) (cit. on p. 11).

[20] G. Kresse and D. Joubert, "From ultrasoft pseudopotentials to the projector augmented-wave method", Phys. Rev. B **59**, 1758–1775 (1999) (cit. on p. 11).

[21] *List of quantum chemistry and solid-state physics software*, (2017) https://en.wikipedia.org/wiki/List_of_quantum_chemistry_and_solid-state_physics_software (cit. on p. 12).

[22] K. Lejaeghere, G. Bihlmayer, T. Björkman, P. Blaha, S. Blügel, V. Blum, D. Caliste, I. E. Castelli, S. J. Clark, A. Dal Corso, S. de Gironcoli, T. Deutsch, J. K. Dewhurst, I. Di Marco, C. Draxl, M. Dułak, O. Eriksson, J. A. Flores-Livas, K. F. Garrity, L. Genovese, P. Giannozzi, M. Giantomassi, S. Goedecker, X. Gonze, O. Grånäs, E. K. U. Gross, A. Gulans, F. Gygi, D. R. Hamann, P. J. Hasnip, N. A. W. Holzwarth, D. Iuşan, D. B. Jochym, F. Jollet, D. Jones, G. Kresse, K. Koepernik, E. Küçükbenli, Y. O. Kvashnin, I. L. M. Locht, S. Lubeck, M. Marsman, N. Marzari, U. Nitzsche, L. Nordström, T. Ozaki, L. Paulatto, C. J. Pickard, W. Poelmans, M. I. J. Probert, K. Refson, M. Richter, G.-M. Rignanese, S. Saha, M. Scheffler, M. Schlipf, K. Schwarz, S. Sharma, F. Tavazza, P. Thunström, A. Tkatchenko, M. Torrent, D. Vanderbilt, M. J. van Setten, V. Van Speybroeck, J. M. Wills, J. R. Yates, G.-X. Zhang, and S. Cottenier, "Reproducibility in density functional theory calculations of solids", Science **351** (2016) 10.1126/science.aad3000 (cit. on p. 12).

[23] G. Kresse and J. Hafner, "*AB INITIO* MOLECULAR-DYNAMICS SIMULATION OF THE LIQUID-METAL-AMORPHOUS-SEMICONDUCTOR TRANSITION IN GERMANIUM", Phys. Rev. B **49**, 14251–14269 (1994) (cit. on p. 13).

[24] G. Kresse and J. Furthmüller, "Efficiency of *ab-initio* total energy calculations for metals and semiconductors using a plane-wave basis set", Computational Materials Science **6**, 15–50 (1996) (cit. on p. 13).

[25] J. D. van der Waals, "Over de Continuiteit van den Gas- en Vloeistoftoestand (on the continuity of the gas and liquid state)", Ph.D. thesis (University of Leiden, 1873) (cit. on p. 15).

[26] B. Partoens and F. M. Peeters, "From graphene to graphite: Electronic structure around the K point", Phys. Rev. B **74**, 075404 (2006) (cit. on pp. 16–17).

[27] K. F. Mak, M. Y. Sfeir, J. A. Misewich, and T. F. Heinz, "The evolution of electronic structure in few-layer graphene revealed by optical spectroscopy", Proceedings of the National Academy of Sciences **107**, 14999–15004 (2010) (cit. on p. 16).

[28] R. Saito, G. Dresselhaus, and M. Dresselhaus, *Physical Properties of Carbon Nanotubes* (Imperial College Press, Weinheim, 1998) (cit. on p. 17).

[29] K. F. Mak, C. Lee, J. Hone, J. Shan, and T. F. Heinz, "Atomically Thin MoS_2: A New Direct-Gap Semiconductor", Physical Review Letters **105** (2010) 10.1103/physrevlett.105.136805 (cit. on p. 18).

[30] J. E. Padilha, H. Peelaers, A. Janotti, and C. G. V. de Walle, "Nature and evolution of the band-edge states in MoS_2: From monolayer to bulk", Physical Review B **90** (2014) 10.1103/physrevb.90.205420 (cit. on p. 19).

[31] Fotolia.com, *sp^3 sp^2 sp hybrid orbitals*, (2016) https://www.fotolia.com/id/128894654 (cit. on p. 20).

[32] C. Coulson and W. Moffitt, "I. The properties of certain strained hydrocarbons", Phil. Mag. **40**, 1–35 (1949) (cit. on pp. 19, 56).

[33] T. Wassmann, A. P. Seitsonen, A. M. Saitta, M. Lazzeri, and F. Mauri, "Clar's Theory, π-Electron Distribution, and Geometry of Graphene Nanoribbons", Journal of the American Chemical Society **132**, PMID: 20178362, 3440–3451 (2010) (cit. on p. 21).

[34] T. Cole, *Double bond*, (2004) http://images.slideplayer.com/14/4339766/slides/slide_7.jpg (cit. on p. 22).

[35] A. H. C. Neto, F. Guinea, N. M. R. Peres, K. S. Novoselov, and A. K. Geim, "The electronic properties of graphene", Reviews of Modern Physics **81**, 109–162 (2009) (cit. on p. 23).

[36] Z. Liu, J. Wang, and J. Li, "Dirac cones in two-dimensional systems: from hexagonal to square lattices", Phys. Chem. Chem. Phys. **15**, 18855–18862 (2013) (cit. on pp. 23–24).

[37] J. Wang, S. Deng, Z. Liu, and Z. Liu, "The rare two-dimensional materials with Dirac cones", Natl. Sci. Rev. **2**, 22–39 (2015) (cit. on p. 23).

[38] Y. Hasegawa, R. Konno, H. Nakano, and M. Kohmoto, "Zero modes of tight-binding electrons on the honeycomb lattice", Phys. Rev. B **74**, 033413 (2006) (cit. on p. 24).

[39] G. J. Ackland, M. C. Warren, and S. J. Clark, "Practical methods in *ab initio* lattice dynamics", J. Phys. Condens. Matter **9**, 7861–7872 (1997) (cit. on p. 26).

[40] K. Parlinski, "Phonons calculated from first-principles", École thématique la Société Française la Neutron. **12**, 161–166 (2011) (cit. on p. 26).

[41] C. Kittel, *Introduction to Solid State Physics* (John Wiley & Sons, Inc., New York, 2004) (cit. on p. 27).

[42] M. Neek-Amal and F. M. Peeters, "Lattice thermal properties of graphane: Thermal contraction, roughness, and heat capacity", Phys. Rev. B **83**, 235437 (2011) (cit. on p. 27).

[43] J. Brivio, D. T. L. Alexander, and A. Kis, "Ripples and Layers in Ultrathin MoS_2 Membranes", Nano Lett. **11**, 5148–5153 (2011) (cit. on p. 27).

[44] A. Togo and I. Tanaka, "First principles phonon calculations in materials science", Scr. Mater. **108**, 1–5 (2015) (cit. on p. 29).

[45] J. Nye, *Physical Properties of Crystals: Their Representation by Tensors and Matrices*, Oxford science publications (Clarendon Press, Oxford, 1985) (cit. on pp. 30, 47).

[46] C. Lee, X. Wei, J. W. Kysar, and J. Hone, "Measurement of the elastic properties and intrinsic strength of monolayer graphene", Science **321**, 385–388 (2008) (cit. on p. 31).

[47] K. N. Kudin, G. E. Scuseria, and B. I. Yakobson, "C_2F, BN, and C nanoshell elasticity from *ab initio* computations", Physical Review B **64** (2001) 10.1103/physrevb.64.235406 (cit. on p. 31).

[48] M. Topsakal, S. Cahangirov, and S. Ciraci, "The response of mechanical and electronic properties of graphane to the elastic strain", Appl. Phys. Lett. **96**, 091912 (2010) (cit. on p. 31).

[49] S. Bertolazzi, J. Brivio, and A. Kis, "Stretching and Breaking of Ultrathin MoS_2", ACS Nano **5**, 9703–9709 (2011) (cit. on p. 31).

[50] R. C. Cooper, C. Lee, C. A. Marianetti, X. Wei, J. Hone, and J. W. Kysar, "Nonlinear elastic behavior of two-dimensional molybdenum disulfide", Phys. Rev. B **87**, 035423 (2013) (cit. on pp. 31, 47).

[51] C. U. E. Department, *Materials Data Book*, (2003) http://www-mdp.eng.cam.ac.uk/web/library/enginfo/cueddatabooks/materials.pdf (cit. on p. 31).

[52] M. Born, “On the stability of crystal lattices. I”, Mathematical Proceedings of the Cambridge Philosophical Society **36**, 160–172 (1940) (cit. on p. 31).

[53] F. Mouhat and F.-X. Coudert, “Necessary and sufficient elastic stability conditions in various crystal systems”, Phys. Rev. B **90**, 224104 (2014) (cit. on pp. 31, 98).

[54] H. Liu, A. T. Neal, Z. Zhu, Z. Luo, X. Xu, D. Tomanek, and P. D. Ye, “Phosphorene: An Unexplored 2D Semiconductor with a High Hole Mobility”, ACS Nano **8**, 4033–4041 (2014) (cit. on pp. 33, 35).

[55] L. Li, Y. Yu, G. J. Ye, Q. Ge, X. Ou, H. Wu, D. Feng, X. H. Chen, and Y. Zhang, “Black phosphorus field-effect transistors.”, Nature Nanotech. **9**, 372–7 (2014) (cit. on pp. 33, 35).

[56] Z. Zhu and D. Tománek, “Semiconducting Layered Blue Phosphorus: A Computational Study”, Phys. Rev. Lett. **112**, 176802 (2014) (cit. on pp. 33–35, 39).

[57] J. Guan, Z. Zhu, and D. Tománek, “Phase Coexistence and Metal-Insulator Transition in Few-Layer Phosphorene: A Computational Study”, Phys. Rev. Lett. **113**, 046804 (2014) (cit. on pp. 33, 132, 135–136, 143, 145–146).

[58] M. Wu, H. Fu, L. Zhou, K. Yao, and X. C. Zeng, “Nine New Phosphorene Polymorphs with Non-Honeycomb Structures: A Much Extended Family”, Nano Lett. **15**, 3557–3562 (2015) (cit. on pp. 33, 132).

[59] D. Çakır, H. Sahin, and F. M. Peeters, “Tuning of the electronic and optical properties of single-layer black phosphorus by strain”, Phys. Rev. B **90**, 205421 (2014) (cit. on pp. 34, 39).

[60] X. Wang, A. M. Jones, K. L. Seyler, V. Tran, Y. Jia, H. Zhao, H. Wang, L. Yang, X. Xu, and F. Xia, “Highly anisotropic and robust excitons in monolayer black phosphorus”, Nat. Nanotechnol. **10**, 517–521 (2015) (cit. on p. 34).

[61] Y. Maruyama, S. Suzuki, K. Kobayashi, and S. Tanuma, “Synthesis and some properties of black phosphorus single crystals”, Physica B+C **105**, 99–102 (1981) (cit. on p. 35).

[62] S. Narita, Y. Akahama, Y. Tsukiyama, K. Muro, S. Mori, S. Endo, M. Taniguchi, M. Seki, S. Suga, A. Mikuni, and H. Kanzaki, “Electrical and optical properties of black phosphorus single crystals”, Physica B+C **117**, 422–424 (1983) (cit. on p. 35).

[63] A. Jain and A. J. H. McGaughey, “Strongly anisotropic in-plane thermal transport in single-layer black phosphorene”, Sci. Rep. **5**, 8501 (2015) (cit. on p. 35).

[64] Q. Wei and X. Peng, “Superior mechanical flexibility of phosphorene and few-layer black phosphorus”, Applied Physics Letters **104**, 251915 (2014) (cit. on p. 35).

[65] L. Kou, T. Frauenheim, and C. Chen, "Phosphorene as a Superior Gas Sensor: Selective Adsorption and Distinct I–V Response", J. Phys. Chem. Lett. **5**, 2675–2681 (2014) (cit. on p. 35).

[66] M. Tahir, P. Vasilopoulos, and F. M. Peeters, "Magneto-optical transport properties of monolayer phosphorene", Phys. Rev. B **92**, 045420 (2015) (cit. on p. 35).

[67] X. Y. Zhou, R. Zhang, J. P. Sun, Y. L. Zou, D. Zhang, W. K. Lou, F. Cheng, G. H. Zhou, F. Zhai, and K. Chang, "Landau levels and magneto-transport property of monolayer phosphorene", Scientific Reports **5** (2015) 10.103 8/srep12295 (cit. on p. 35).

[68] N. Mounet and N. Marzari, "First-principles determination of the structural, vibrational and thermodynamic properties of diamond, graphite, and derivatives", Phys. Rev. B **71**, 205214 (2005) (cit. on pp. 36–37, 41).

[69] D. Çakır, F. M. Peeters, and C. Sevik, "Mechanical and thermal properties of h-MX_2 (M = Cr, Mo, W; X = O, S, Se, Te) monolayers: A comparative study", Appl. Phys. Lett. **104**, 203110 (2014) (cit. on pp. 36, 40, 47, 109).

[70] C. Sevik, "Assessment on lattice thermal properties of two-dimensional honeycomb structures: Graphene, h-BN, h-MoS_2, and h-$MoSe_2$", Physical Review B **89**, 035422 (2014) (cit. on pp. 36, 40).

[71] S. Baroni, P. Giannozzi, and E. Isaev, "Density-Functional Perturbation Theory for Quasi-Harmonic Calculations", Reviews in Mineralogy and Geochemistry **71**, 39–57 (2010) (cit. on p. 36).

[72] B. Grabowski, L. Ismer, T. Hickel, and J. Neugebauer, "*AB INITIO* UP TO THE MELTING POINT: ANHARMONICITY AND VACANCIES IN ALUMINUM", Phys. Rev. B **79**, 134106 (2009) (cit. on p. 36).

[73] B. B. Karki, R. M. Wentzcovitch, S. de Gironcoli, and S. Baroni, "High-pressure lattice dynamics and thermoelasticity of MgO", Phys. Rev. B **61**, 8793–8800 (2000) (cit. on p. 36).

[74] P. Pavone, K. Karch, O. Schütt, D. Strauch, W. Windl, P. Giannozzi, and S. Baroni, "*AB INITIO* LATTICE DYNAMICS OF DIAMOND", Phys. Rev. B **48**, 3156–3163 (1993) (cit. on p. 37).

[75] A. Togo, L. Chaput, I. Tanaka, and G. Hug, "First-principles phonon calculations of thermal expansion in Ti_3SiC_2, Ti_3AlC_2, and Ti_3GeC_2", Phys. Rev. B **81**, 174301 (2010) (cit. on p. 38).

[76] A. Togo, *phonopy*, (2017) https://atztogo.github.io/phonopy/ (cit. on p. 38).

[77] B. Sa, Y.-L. Li, J. Qi, R. Ahuja, and Z. Sun, "Strain Engineering for Phosphorene: The Potential Application as a Photocatalyst", The Journal of Physical Chemistry C **118**, 26560–26568 (2014) (cit. on p. 38).

[78] R. Fei and L. Yang, "Lattice vibrational modes and Raman scattering spectra of strained phosphorene", Appl. Phys. Lett. **105**, 083120 (2014) (cit. on p. 38).

[79] R. Fei and L. Yang, "Strain-Engineering the Anisotropic Electrical Conductance of Few-Layer Black Phosphorus", Nano Lett. **14**, 2884–2889 (2014) (cit. on pp. 39, 104, 115).

[80] J.-W. Jiang and H. S. Park, "Negative poisson's ratio in single-layer black phosphorus", Nat. Commun. **5**, 4727 (2014) (cit. on p. 40).

[81] D. Jariwala, V. K. Sangwan, L. J. Lauhon, T. J. Marks, and M. C. Hersam, "Emerging Device Applications for Semiconducting Two-Dimensional Transition Metal Dichalcogenides", ACS Nano **8**, 1102–1120 (2014) (cit. on p. 42).

[82] Q. H. Wang, K. Kalantar-Zadeh, A. Kis, J. N. Coleman, and M. S. Strano, "Electronics and optoelectronics of two-dimensional transition metal dichalcogenides", Nat. Nanotechnol. **7**, 699–712 (2012) (cit. on p. 42).

[83] K.-A. N. Duerloo, M. T. Ong, and E. J. Reed, "Intrinsic Piezoelectricity in Two-Dimensional Materials", The Journal of Physical Chemistry Letters **3**, 2871–2876 (2012) (cit. on pp. 43–47, 49).

[84] H. Zhu, Y. Wang, J. Xiao, M. Liu, S. Xiong, Z. J. Wong, Z. Ye, Y. Ye, X. Yin, and X. Zhang, "Observation of piezoelectricity in free-standing monolayer MoS_2", Nature nanotechnology **10**, 151–155 (2015) (cit. on pp. 43, 49).

[85] W. Li and J. Li, "Piezoelectricity in two-dimensional group-III monochalcogenides", Nano Research **8**, 3796–3802 (2015) (cit. on p. 43).

[86] H. J. Xiang, J. Yang, J. G. Hou, and Q. Zhu, "Piezoelectricity in ZnO nanowires: A first-principles study", Appl. Phys. Lett. **89**, 223111 (2006) (cit. on p. 43).

[87] G. Tomasz and W. Zielinski, *How does a piezoelectric igniter work?*, (2013) https://qph.ec.quoracdn.net/main-qimg-b9c33a87f3be9dd104214145364cfaf2 (cit. on p. 44).

[88] S. Baroni, S. de Gironcoli, A. Dal Corso, and P. Giannozzi, "Phonons and related crystal properties from density-functional perturbation theory", Rev. Mod. Phys. **73**, 515–562 (2001) (cit. on pp. 44, 89).

[89] X. Wu, D. Vanderbilt, and D. R. Hamann, "Systematic treatment of displacements, strains, and electric fields in density-functional perturbation theory", Phys. Rev. B **72**, 035105 (2005) (cit. on p. 44).

[90] D. Vanderbilt, "Berry-phase theory of proper piezoelectric response", J. Phys. Chem. Solids **61**, 147–151 (2000) (cit. on pp. 44–45, 49).

[91] M. T. Ong, K.-A. N. Duerloo, and E. J. Reed, "The Effect of Hydrogen and Fluorine Coadsorption on the Piezoelectric Properties of Graphene", The Journal of Physical Chemistry C **117**, 3615–3620 (2013) (cit. on p. 45).

[92] H. J. Kim, M. Noor-A-Alam, J. Y. Son, and Y.-H. Shin, "Origin of piezoelectricity in monolayer halogenated graphane piezoelectrics", Chem. Phys. Lett. **603**, 62–66 (2014) (cit. on p. 45).

[93] F. A. Rasmussen and K. S. Thygesen, "Computational 2D Materials Database: Electronic Structure of Transition-Metal Dichalcogenides and Oxides", The Journal of Physical Chemistry C **119**, 13169–13183 (2015) (cit. on p. 46).

[94] C. Ataca, H. Şahin, and S. Ciraci, "Stable, single-Layer MX_2 transition-metal oxides and dichalcogenides in a honeycomb-like structure", The Journal of Physical Chemistry C **116**, 8983–8999 (2012) (cit. on p. 46).

[95] H. Guo, N. Lu, L. Wang, X. Wu, and X. C. Zeng, "Tuning Electronic and Magnetic Properties of Early Transition-Metal Dichalcogenides via Tensile Strain", The Journal of Physical Chemistry C **118**, 7242–7249 (2014) (cit. on p. 46).

[96] Q. Peng and S. De, "Outstanding mechanical properties of monolayer MoS_2 and its application in elastic energy storage", Phys. Chem. Chem. Phys. **15**, 19427–19437 (2013) (cit. on p. 47).

[97] J. Kang, S. Tongay, J. Zhou, J. Li, and J. Wu, "Band offsets and heterostructures of two-dimensional semiconductors", Appl. Phys. Lett. **102**, 012111 (2013) (cit. on p. 47).

[98] M. Born and K. Huang, *Dynamical Theory of Crystal Lattices*, International series of monographs on physics (Clarendon Press, Oxford, 1998) (cit. on p. 47).

[99] H. L. Zhuang, M. D. Johannes, M. N. Blonsky, and R. G. Hennig, "Computational prediction and characterization of single-layer CrS_2", Appl. Phys. Lett. **104**, 022116 (2014) (cit. on p. 49).

[100] K. H. Michel and B. Verberck, "Theory of elastic and piezoelectric effects in two-dimensional hexagonal boron nitride", Phys. Rev. B **80**, 224301 (2009) (cit. on p. 49).

[101] K. H. Michel and B. Verberck, "Phonon dispersions and piezoelectricity in bulk and multilayers of hexagonal boron nitride", Phys. Rev. B **83**, 115328 (2011) (cit. on p. 49).

[102] K. H. Michel and B. Verberck, "Theory of phonon dispersions and piezoelectricity in multilayers of hexagonal boron-nitride", physica status solidi (b) **248**, 2720–2723 (2011) (cit. on p. 49).

[103] M. T. Ong and E. J. Reed, "Engineered Piezoelectricity in Graphene", ACS Nano **6**, 1387–1394 (2012) (cit. on p. 51).

[104] R. Bechmann, "Elastic and Piezoelectric Constants of Alpha-Quartz", Phys. Rev. **110**, 1060–1061 (1958) (cit. on p. 51).

[105] C. M. Lueng, H. L. W. Chan, C. Surya, and C. L. Choy, "Piezoelectric coefficient of aluminum nitride and gallium nitride", J. Appl. Phys. **88**, 5360–5363 (2000) (cit. on p. 51).

[106] V. Georgakilas, M. Otyepka, A. B. Bourlinos, V. Chandra, N. Kim, K. C. Kemp, P. Hobza, R. Zboril, and K. S. Kim, "Functionalization of Graphene: Covalent and Non-Covalent Approaches, Derivatives and Applications", Chem. Rev. **112**, 6156–6214 (2012) (cit. on p. 53).

[107] M. Inagaki and F. Kang, "Graphene derivatives: graphane, fluorographene, graphene oxide, graphyne and graphdiyne", J. Mater. Chem. A **2**, 13193–13206 (2014) (cit. on p. 53).

[108] E. Kan, Z. Li, and J. Yang, "Magnetism in graphene systems", Nano **03**, 433–442 (2008) (cit. on p. 53).

[109] K. Xu, X. Li, P. Chen, D. Zhou, C. Wu, Y. Guo, L. Zhang, J. Zhao, X. Wu, and Y. Xie, "Hydrogen dangling bonds induce ferromagnetism in two-dimensional metal-free graphitic-C_3N_4 nanosheets", Chem. Sci. **6**, 283–287 (2015) (cit. on p. 53).

[110] J. Zhou, Q. Wang, Q. Sun, X. S. Chen, Y. Kawazoe, and P. Jena, "Ferromagnetism in semihydrogenated graphene sheet", Nano Lett. **9**, 3867–3870 (2009) (cit. on p. 53).

[111] A. Y. S. Eng, H. L. Poh, F. Šaněk, M. Maryško, S. Matějková, Z. Sofer, and M. Pumera, "Searching for Magnetism in Hydrogenated Graphene: Using Highly Hydrogenated Graphene Prepared via Birch Reduction of Graphite Oxides", ACS Nano **7**, 5930–5939 (2013) (cit. on p. 53).

[112] S. Okada and A. Oshiyama, "Magnetic Ordering in Hexagonally Bonded Sheets with First-Row Elements", Phys. Rev. Lett. **87**, 146803 (2001) (cit. on p. 53).

[113] Q. Miao, L. Wang, Z. Liu, B. Wei, F. Xu, and W. Fei, "Magnetic properties of N-doped graphene with high Curie temperature", Sci. Rep. **6**, 21832 (2016) (cit. on p. 53).

[114] V. M. Pereira, F. Guinea, J. M. B. Lopes dos Santos, N. M. R. Peres, and A. H. Castro Neto, "Disorder Induced Localized States in Graphene", Phys. Rev. Lett. **96**, 036801 (2006) (cit. on p. 53).

[115] O. V. Yazyev and L. Helm, "Defect-induced magnetism in graphene", Phys. Rev. B **75**, 125408 (2007) (cit. on p. 53).

[116] R. Baughman, H. Eckhardt, and M. Kertesz, "Structure-property predictions for new planar forms of carbon: Layered phases containing sp^2 and sp atoms", The Journal of chemical physics **87**, 6687–6699 (1987) (cit. on p. 53).

[117] A. Ivanovskii, "Graphynes and graphdyines", Prog. Solid State Chem. **41**, 1–19 (2013) (cit. on p. 53).

[118] X.-Q. Zhang, C.-H. Lin, Y.-W. Tseng, K.-H. Huang, and Y.-H. Lee, "Synthesis of Lateral Heterostructures of Semiconducting Atomic Layers", Nano Letters **15**, 410–415 (2015) (cit. on pp. 53, 90, 120).

[119] X. Zhang, L. Wei, J. Tan, and M. Zhao, "Prediction of an ultrasoft graphene allotrope with Dirac cones", Carbon N. Y. **105**, 323–329 (2016) (cit. on p. 54).

[120] K. Momma and F. Izumi, "*VESTA3* for three-dimensional visualization of crystal, volumetric and morphology data", J. Appl. Cryst. **44**, 1272–1276 (2011) (cit. on pp. 54, 94).

[121] E. Yoo, J. Kim, E. Hosono, H.-s. Zhou, T. Kudo, and I. Honma, "Large Reversible Li Storage of Graphene Nanosheet Families for Use in Rechargeable Lithium Ion Batteries", Nano Letters **8**, PMID: 18651781, 2277–2282 (2008) (cit. on p. 59).

[122] Y. Jing, Z. Zhou, C. R. Cabrera, and Z. Chen, "Metallic VS_2 Monolayer: A Promising 2D Anode Material for Lithium Ion Batteries", The Journal of Physical Chemistry C **117**, 25409–25413 (2013) (cit. on p. 59).

[123] E. Yang, H. Ji, and Y. Jung, "Two-Dimensional Transition Metal Dichalcogenide Monolayers as Promising Sodium Ion Battery Anodes", The Journal of Physical Chemistry C **119**, 26374–26380 (2015) (cit. on p. 59).

[124] J. Sun, H.-W. Lee, M. Pasta, H. Yuan, G. Zheng, Y. Sun, Y. Li, and Y. Cui, "A phosphorene–graphene hybrid material as a high-capacity anode for sodium-ion batteries", Nat. Nano. **10**, 980–985 (2015) (cit. on p. 59).

[125] V. V. Kulish, O. I. Malyi, C. Persson, and P. Wu, "Phosphorene as an anode material for Na-ion batteries: a first-principles study", Phys. Chem. Chem. Phys. **17**, 13921–13928 (2015) (cit. on p. 59).

[126] J. Hu, B. Xu, S. A. Yang, S. Guan, C. Ouyang, and Y. Yao, "2D Electrides as Promising Anode Materials for Na-Ion Batteries from First-Principles Study", ACS Applied Materials & Interfaces **7**, PMID: 26461467, 24016–24022 (2015) (cit. on p. 59).

[127] X. Wang, Q. Weng, Y. Yang, Y. Bando, and D. Golberg, "Hybrid two-dimensional materials in rechargeable battery applications and their microscopic mechanisms", Chem. Soc. Rev. **45**, 4042–4073 (2016) (cit. on p. 59).

[128] E. Pomerantseva and Y. Gogotsi, "Two-dimensional heterostructures for energy storage", Nature Energy **2**, 17089 (2017) (cit. on p. 59).

[129] D. Çakır, C. Sevik, O. Gülseren, and F. M. Peeters, "Mo_2C as a high capacity anode material: a first-principles study", J. Mater. Chem. A **4**, 6029–6035 (2016) (cit. on pp. 59, 70).

[130] C. E. Ren, M.-Q. Zhao, T. Makaryan, J. Halim, M. Boota, S. Kota, B. Anasori, M. W. Barsoum, and Y. Gogotsi, "Porous Two-Dimensional Transition Metal Carbide (MXene) Flakes for High-Performance Li-Ion Storage", ChemElectroChem **3**, 689–693 (2016) (cit. on p. 60).

[131] M. Naguib, J. Halim, J. Lu, K. M. Cook, L. Hultman, Y. Gogotsi, and M. W. Barsoum, "New Two-Dimensional Niobium and Vanadium Carbides as Promising Materials for Li-Ion Batteries", Journal of the American Chemical Society **135**, 15966–15969 (2013) (cit. on pp. 60, 70).

[132] C. Eames and M. S. Islam, "Ion Intercalation into Two-Dimensional Transition-Metal Carbides: Global Screening for New High-Capacity Battery Materials", Journal of the American Chemical Society **136**, 16270–16276 (2014) (cit. on p. 60).

[133] S. Grimme, S. Ehrlich, and L. Goerigk, "Effect of the damping function in dispersion corrected density functional theory", Journal of Computational Chemistry **32**, 1456–1465 (2011) (cit. on p. 60).

[134] W. Tang, E. Sanville, and G. Henkelman, "A grid-based Bader analysis algorithm without lattice bias", J. Phys.: Condens. Matter **21**, 084204 (2009) (cit. on pp. 60, 78, 107).

[135] E. Sanville, S. D. Kenny, R. Smith, and G. Henkelman, "Improved grid-based algorithm for Bader charge allocation", J. Comput. Chem. **28**, 899–908 (2007) (cit. on pp. 60, 78, 107).

[136] G. Henkelman, A. Arnaldsson, and H. Jónsson, "A fast and robust algorithm for Bader decomposition of charge density", Computational Materials Science **36**, 354–360 (2006) (cit. on pp. 60, 78, 107).

[137] M. Yu and D. R. Trinkle, "Accurate and efficient algorithm for Bader charge integration", The Journal of Chemical Physics **134** (2011) 10.1063/1.3553716 (cit. on pp. 60, 107).

[138] G. Henkelman, B. P. Uberuaga, and H. Jansson, "A climbing image nudged elastic band method for finding saddle points and minimum energy paths", The Journal of Chemical Physics **113**, 9901–9904 (2000) (cit. on p. 61).

[139] G. Henkelman and H. Jansson, "Improved tangent estimate in the nudged elastic band method for finding minimum energy paths and saddle points", The Journal of Chemical Physics **113**, 9978–9985 (2000) (cit. on p. 61).

[140] E. Mostaani, N. D. Drummond, and V. I. Fal'ko, "Quantum Monte Carlo Calculation of the Binding Energy of Bilayer Graphene", Phys. Rev. Lett. **115**, 115501 (2015) (cit. on p. 63).

[141] G.-C. Guo, D. Wang, X.-L. Wei, Q. Zhang, H. Liu, W.-M. Lau, and L.-M. Liu, "First-Principles Study of Phosphorene and Graphene Heterostructure as Anode Materials for Rechargeable Li Batteries", The Journal of Physical Chemistry Letters **6**, 5002–5008 (2015) (cit. on p. 63).

[142] A. Samad, M. Noor-A-Alam, and Y.-H. Shin, "First principles study of a SnS_2 /graphene heterostructure: a promising anode material for rechargeable Na ion batteries", J. Mater. Chem. A **4**, 14316–14323 (2016) (cit. on p. 63).

[143] E. Lee and K. A. Persson, "Li Absorption and Intercalation in Single Layer Graphene and Few Layer Graphene by First Principles", Nano Lett. **12**, 4624–4628 (2012) (cit. on p. 63).

[144] M. Ashton, R. G. Hennig, and S. B. Sinnott, "Computational characterization of lightweight multilayer MXene Li-ion battery anodes", Applied Physics Letters **108**, 023901 (2016) (cit. on p. 63).

[145] S. N. Shirodkar and E. Kaxiras, "Li intercalation at graphene/hexagonal boron nitride interfaces", Phys. Rev. B **93**, 245438 (2016) (cit. on p. 65).

[146] D. Sun, Q. Hu, J. Chen, X. Zhang, L. Wang, Q. Wu, and A. Zhou, "Structural transformation of MXene (V_2C, Cr_2C, and Ta_2C) with O groups during lithiation: a first-principles investigation", ACS Applied Materials & Interfaces **8**, 74–81 (2016) (cit. on p. 69).

[147] Y. Xie, M. Naguib, V. N. Mochalin, M. W. Barsoum, Y. Gogotsi, X. Yu, K.-W. Nam, X.-Q. Yang, A. I. Kolesnikov, and P. R. C. Kent, "Role of Surface Structure on Li-Ion Energy Storage Capacity of Two-Dimensional Transition-Metal Carbides", J. Am. Chem. Soc. **136**, 6385–6394 (2014) (cit. on p. 70).

[148] Q. Tang, Z. Zhou, and P. Shen, "Are MXenes Promising Anode Materials for Li Ion Batteries? Computational Studies on Electronic Properties and Li Storage Capability of Ti_3C_2 and $Ti_3C_2X_2$ (X = F, OH) Monolayer", J. Am. Chem. Soc. **134**, 16909–16916 (2012) (cit. on p. 70).

[149] K. Persson, Y. Hinuma, Y. S. Meng, A. Van der Ven, and G. Ceder, "Thermodynamic and kinetic properties of the Li-graphite system from first-principles calculations", Phys. Rev. B **82**, 125416 (2010) (cit. on p. 70).

[150] M. V. Koudriachova, N. M. Harrison, and S. W. de Leeuw, "Open circuit voltage profile for Li-intercalation in rutile and anatase from first principles", Solid State Ionics **152–153**, 189–194 (2002) (cit. on p. 70).

[151] W. Li, Y. Yang, G. Zhang, and Y.-W. Zhang, "Ultrafast and Directional Diffusion of Lithium in Phosphorene for High-Performance Lithium-Ion Battery", Nano Letters **15**, 1691–1697 (2015) (cit. on p. 70).

[152] M. Naguib, J. Come, B. Dyatkin, V. Presser, P.-L. Taberna, P. Simon, M. W. Barsoum, and Y. Gogotsi, "MXene: a promising transition metal carbide anode for lithium-ion batteries", Electrochemistry Communications **16**, 61–64 (2012) (cit. on p. 70).

[153] S. Zhao, W. Kang, and J. Xue, "Role of strain and concentration on the Li adsorption and diffusion properties on Ti_2C layer", The Journal of Physical Chemistry C **118**, 14983–14990 (2014) (cit. on p. 73).

[154] S. Thinius, M. M. Islam, P. Heitjans, and T. Bredow, "Theoretical study of Li migration in lithium-graphite intercalation compounds with dispersion-corrected DFT methods", The Journal of Physical Chemistry C **118**, 2273–2280 (2014) (cit. on p. 73).

[155] S. Lunell, A. Stashans, L. Ojamae, H. Lindstrom, and A. Hagfeldt, "Li and Na diffusion in TiO_2 from quantum chemical theory versus electrochemical experiment", Journal of the American Chemical Society **119**, 7374–7380 (1997) (cit. on p. 73).

[156] H. Lindström, S. Södergren, A. Solbrand, H. Rensmo, J. Hjelm, A. Hagfeldt, and S.-E. Lindquist, "Li^+ ion insertion in TiO_2 (Anatase). 1. Chronoamperometry on CVD films and nanoporous films", The Journal of Physical Chemistry B **101**, 7710–7716 (1997) (cit. on p. 73).

[157] C. L. Olson, J. Nelson, and M. S. Islam, "Defect chemistry, surface structures, and lithium insertion in Anatase TiO_2", The Journal of Physical Chemistry B **110**, 9995–10001 (2006) (cit. on p. 73).

[158] J. Luo, W. Zhang, H. Yuan, C. Jin, L. Zhang, H. Huang, C. Liang, Y. Xia, J. Zhang, Y. Gan, and X. Tao, "Pillared Structure Design of MXene with Ultralarge Interlayer Spacing for High-Performance Lithium-Ion Capacitors", ACS Nano **11**, 2459–2469 (2017) (cit. on p. 73).

[159] R. Lieth, *Preparation and crystal growth of materials with layered structures*, Vol. 1 (Springer, Dordrecht, 1977) (cit. on p. 76).

[160] C. Meade and R. Jeanloz, "Static compression of $Ca(OH)_2$ at room temperature: Observations of amorphization and equation of state measurements to 10.7 GPa", Geophys. Res. Lett. **17**, 1157–1160 (1990) (cit. on p. 76).

[161] M. B. Kruger, Q. Williams, and R. Jeanloz, "Vibrational spectra of $Mg(OH)_2$ and $Ca(OH)_2$ under pressure", The Journal of Chemical Physics **91**, 5910–5915 (1989) (cit. on p. 76).

[162] J. H. Nguyen, M. B. Kruger, and R. Jeanloz, "Evidence for "Partial" (sublattice) amorphization in $Co(OH)_2$", Physical Review Letters **78**, 1936–1939 (1997) (cit. on p. 76).

[163] S. Raugei, P. L. Silvestrelli, and M. Parrinello, "Pressure-Induced Frustration and Disorder in $Mg(OH)_2$ and $Ca(OH)_2$", Physical Review Letters **83**, 2222–2225 (1999) (cit. on p. 76).

[164] T. S. Duffy, C. Meade, Y. Fei, H.-K. Mao, and R. J. Hemley, "High-pressure phase transition in brucite, $Mg(OH)_2$", Am. Mineral. **80**, 222–230 (1995) (cit. on p. 76).

[165] S. Ekbundit, K. Leinenweber, J. Yarger, J. Robinson, M. Verhelst-Voorhees, and G. Wolf, "New high-pressure phase and pressure-induced amorphization of $Ca(OH)_2$: grain size effect", J. Solid State Chem. **126**, 300–307 (1996) (cit. on p. 76).

[166] K. Catalli, S.-H. Shim, and V. B. Prakapenka, "A crystalline-to-crystalline phase transition in $Ca(OH)_2$ at 8 GPa and room temperature", Geophys. Res. Lett. **35**, L05312 (2008) (cit. on p. 76).

[167] R. Iizuka, H. Kagi, K. Komatsu, D. Ushijima, S. Nakano, A. Sano-Furukawa, T. Nagai, and T. Yagi, "Pressure responses of portlandite and H–D isotope effects on pressure-induced phase transitions", Phys. Chem. Miner. **38**, 777–785 (2011) (cit. on p. 76).

[168] B. Winkler, V. Milman, B. Hennion, M. Payne, M.-H. Lee, and J. Lin, "*AB INITIO* TOTAL ENERGY STUDY OF BRUCITE, DIASPORE AND HYPOTHETICAL HYDROUS WADSLEYITE", Phys. Chem. Miner. **22**, 461–467 (1995) (cit. on p. 76).

[169] P. Baranek, A. Lichanot, R. Orlando, and R. Dovesi, "Structural and vibrational properties of solid $Mg(OH)_2$ and $Ca(OH)_2$ – performances of various hamiltonians", Chemical Physics Letters **340**, 362–369 (2001) (cit. on p. 76).

[170] K. Azuma, T. Oda, and S. Tanaka, "Vibration analysis of O–H stretching mode in $Mg(OH)_2$, $Ca(OH)_2$, LiOH, and NaOH by plane-wave pseudopotential DFT calculation", Comput. Theor. Chem. **963**, 215–220 (2011) (cit. on p. 76).

[171] P. D'Arco, M. Causà, C. Roetti, and B. Silvi, "Periodic Hartree-Fock study of a weakly bonded layer structure: Brucite $Mg(OH)_2$", Physical Review B **47**, 3522–3529 (1993) (cit. on pp. 76, 84).

[172] A. Pishtshev, S. Z. Karazhanov, and M. Klopov, "Materials properties of magnesium and calcium hydroxides from first-principles calculations", Computational Materials Science **95**, 693–705 (2014) (cit. on pp. 76, 80–81).

[173] A. Pishtshev, S. Z. Karazhanov, and M. Klopov, "Excitons in $Mg(OH)_2$ and $Ca(OH)_2$ from *ab initio* calculations", Solid State Commun. **193**, 11–15 (2014) (cit. on p. 76).

[174] W. Ren and H.-M. Cheng, "The global growth of graphene", Nature Nanotechnology **9**, 726–730 (2014) (cit. on p. 76).

[175] Y. Yu, C. Li, Y. Liu, L. Su, Y. Zhang, and L. Cao, "Controlled scalable synthesis of uniform, high-quality monolayer and few-layer MoS_2 films", Scientific Reports **3** (2013) 10.1038/srep01866 (cit. on p. 76).

[176] D. Alfè, "PHON: A program to calculate phonons using the small displacement method", Comput. Phys. Commun. **180**, 40 YEARS OF CPC: A celebratory issue focused on quality software for high performance, grid and novel computing architectures, 2622–2633 (2009) (cit. on pp. 77, 89).

[177] S. Grimme, "Semiempirical GGA-type density functional constructed with a long-range dispersion correction", J. Comput. Chem. **27**, 1787–1799 (2006) (cit. on p. 77).

[178] L. Desgranges, D. Grebille, G. Calvarin, G. Chevrier, N. Floquet, and J.-C. Niepce, "Hydrogen thermal motion in calcium hydroxide: $Ca(OH)_2$", Acta Crystallographica Section B **49**, 812–817 (1993) (cit. on p. 81).

[179] W. R. Busing and H. A. Levy, "Neutron Diffraction Study of Calcium Hydroxide", The Journal of Chemical Physics **26**, 563–568 (1957) (cit. on p. 81).

[180] C. Ataca, M. Topsakal, E. Aktürk, and S. Ciraci, "A comparative study of lattice dynamics of three- and two-dimensional MoS_2", The Journal of Physical Chemistry C **115**, 16354–16361 (2011) (cit. on p. 81).

[181] M. Topsakal, E. Aktürk, and S. Ciraci, "First-principles study of two- and one-dimensional honeycomb structures of boron nitride", Phys. Rev. B **79**, 115442 (2009) (cit. on p. 82).

[182] Q. Peng, W. Ji, and S. De, "Mechanical properties of the hexagonal boron nitride monolayer: *Ab initio* study", Computational Materials Science **56**, 11–17 (2012) (cit. on p. 82).

[183] H. Şahin, S. Cahangirov, M. Topsakal, E. Bekaroglu, E. Akturk, R. T. Senger, and S. Ciraci, "Monolayer honeycomb structures of group-IV elements and III-V binary compounds: First-principles calculations", Phys. Rev. B **80**, 155453 (2009) (cit. on p. 82).

[184] M. Posternak, A. Baldereschi, A. J. Freeman, and E. Wimmer, "Prediction of Electronic Surface States in Layered Materials: Graphite", Phys. Rev. Lett. **52**, 863–866 (1984) (cit. on p. 87).

[185] M. Posternak, A. Baldereschi, A. J. Freeman, E. Wimmer, and M. Weinert, "Prediction of Electronic Interlayer States in Graphite and Reinterpretation of Alkali Bands in Graphite Intercalation Compounds", Phys. Rev. Lett. **50**, 761–764 (1983) (cit. on p. 87).

[186] G. N. Greaves, A. L. Greer, R. S. Lakes, and T. Rouxel, "Poisson's ratio and modern materials", Nat. Mater. **10**, 823–837 (2011) (cit. on p. 88).

[187] Y. Ding and Y. Wang, "Hydrogen-induced stabilization and tunable electronic structures of penta-silicene: a computational study", J. Mater. Chem. C **3**, 11341–11348 (2015) (cit. on pp. 90, 92).

[188] X. Li, Y. Dai, M. Li, W. Wei, and B. Huang, "Stable Si-based pentagonal monolayers: high carrier mobilities and applications in photocatalytic water splitting", J. Mater. Chem. A **3**, 24055–24063 (2015) (cit. on pp. 90, 92).

[189] M. Parrinello and A. Rahman, "Crystal Structure and Pair Potentials: A Molecular-Dynamics Study", Phys. Rev. Lett. **45**, 1196–1199 (1980) (cit. on p. 91).

[190] M. Parrinello and A. Rahman, "Polymorphic transitions in single crystals: A new molecular dynamics method", J. Appl. Phys. **52**, 7182–7190 (1981) (cit. on p. 91).

[191] M. Allen and D. Tildesley, *Computer Simulation of Liquids* (Clarendon Press, Oxford, 1989) (cit. on p. 91).

[192] D. Caliste, *V_Sim atomic visualization package available online*, http://inac.cea.fr/L_Sim/V_Sim/index.en.html (cit. on p. 91).

[193] Z. Wang, F. Dong, B. Shen, R. Zhang, Y. Zheng, L. Chen, S. Wang, C. Wang, K. Ho, Y.-J. Fan, B.-Y. Jin, and W.-S. Su, "Electronic and optical properties of novel carbon allotropes", Carbon **101**, 77–85 (2016) (cit. on p. 93).

[194] Z. Zhao, F. Tian, X. Dong, Q. Li, Q. Wang, H. Wang, X. Zhong, B. Xu, D. Yu, J. He, H.-T. Wang, Y. Ma, and Y. Tian, "Tetragonal Allotrope of Group 14 Elements", JACS **134**, 12362–12365 (2012) (cit. on p. 93).

[195] T. Morishita, M. J. Spencer, S. P. Russo, I. K. Snook, and M. Mikami, "Surface reconstruction of ultrathin silicon nanosheets", Chem. Phys. Lett. **506**, 221–225 (2011) (cit. on p. 99).

[196] Y. Sakai and A. Oshiyama, "Structural stability and energy-gap modulation through atomic protrusion in freestanding bilayer silicene", Phys. Rev. B **91**, 201405 (2015) (cit. on p. 99).

[197] J. O. Island, M. Buscema, M. Barawi, J. M. Clamagirand, J. R. Ares, C. Sánchez, I. J. Ferrer, G. A. Steele, H. S. J. van der Zant, and A. Castellanos-Gomez, "Ultrahigh photoresponse of few-layer TiS_3 nanoribbon transistors", Advanced Optical Materials **2**, 641–645 (2014) (cit. on p. 103).

[198] J. O. Island, M. Barawi, R. Biele, A. Almazán, J. M. Clamagirand, J. R. Ares, C. Sánchez, H. S. J. van der Zant, J. V. Álvarez, R. D'Agosta, I. J. Ferrer, and A. Castellanos-Gomez, "TiS_3 transistors with tailored morphology and electrical properties", Advanced Materials **27**, 2595–2601 (2015) (cit. on p. 103).

[199] T. Vogelsang and K. R. Hofmann, "Electron transport in strained Si layers on $Si_{1-x}Ge_x$ substrates", Applied Physics Letters **63**, 186–188 (1993) (cit. on p. 103).

[200] J. Welser, J. Hoyt, S. Takagi, and J. Gibbons, "Strain dependence of the performance enhancement in strained-Si n-MOSFETs", in Electron Devices Meeting, 1994. IEDM '94. Technical Digest., International (Dec. 1994), pp. 373–376 (cit. on p. 103).

[201] K. Kaasbjerg, K. S. Thygesen, and K. W. Jacobsen, "Phonon-limited mobility in n-type single-layer MoS_2 from first principles", Physical Review B **85** (2012) 10.1103/physrevb.85.115317 (cit. on pp. 103, 105).

[202] W. Zhang, Z. Huang, W. Zhang, and Y. Li, "Two-dimensional semiconductors with possible high room temperature mobility", Nano Res. **7**, 1731–1737 (2014) (cit. on p. 103).

[203] Y. Cai, G. Zhang, and Y.-W. Zhang, "Polarity-reversed robust carrier mobility in monolayer MoS_2 nanoribbons", J. Am. Chem. Soc. **136**, 6269–6275 (2014) (cit. on pp. 103–104).

[204] H. M. Stewart, S. A. Shevlin, C. R. A. Catlow, and Z. X. Guo, "Compressive Straining of Bilayer Phosphorene Leads to Extraordinary Electron Mobility at a New Conduction Band Edge", Nano Lett. **15**, 2006–2010 (2015) (cit. on p. 104).

[205] S. Yu, H. D. Xiong, K. Eshun, H. Yuan, and Q. Li, "Phase transition, effective mass and carrier mobility of MoS_2 monolayer under tensile strain", Appl. Surf. Sci. **325**, 27–32 (2015) (cit. on p. 104).

[206] M.-Q. Long, L. Tang, D. Wang, L. Wang, and Z. Shuai, "Theoretical Predictions of Size-Dependent Carrier Mobility and Polarity in Graphene", J. Am. Chem. Soc. **131**, 17728–17729 (2009) (cit. on p. 104).

[207] J. Bardeen and W. Shockley, "Deformation Potentials and Mobilities in Non-Polar Crystals", Phys. Rev. **80**, 72–80 (1950) (cit. on p. 104).

[208] J. Xi, M. Long, L. Tang, D. Wang, and Z. Shuai, "First-principles prediction of charge mobility in carbon and organic nanomaterials", Nanoscale **4**, 4348 (2012) (cit. on p. 104).

[209] J. Qiao, X. Kong, Z.-X. Hu, F. Yang, and W. Ji, "High-mobility transport anisotropy and linear dichroism in few-layer black phosphorus", Nat. Commun. **5**, 4475 (2014) (cit. on p. 104).

[210] J. Dai and X. C. Zeng, "Titanium Trisulfide Monolayer: Theoretical Prediction of a New Direct-Gap Semiconductor with High and Anisotropic Carrier Mobility", Angewandte Chemie International Edition **54**, 7572–7576 (2015) (cit. on pp. 104–106, 108–109).

[211] J. Kang, H. Sahin, H. D. Ozaydin, R. T. Senger, and F. M. Peeters, "TiS_3 nanoribbons: Width-independent band gap and strain-tunable electronic properties", Physical Review B **92** (2015) 10.1103/physrevb.92.075413 (cit. on pp. 104–105).

[212] Y. Jin, X. Li, and J. Yang, "Single layer of MX_3 (M = Ti, Zr; X = S, Se, Te): a new platform for nano-electronics and optics", Phys. Chem. Chem. Phys. **17**, 18665–18669 (2015) (cit. on p. 105).

[213] S. Furuseth, L. Brattås, A. Kjekshus, and A. F. Andresen, "On the Crystal Structures of TiS_3, ZrS_3, $ZrSe_3$, $ZrTe_3$, HfS_3, and $HfSe_3$.", Acta Chem. Scand. **29a**, 623–631 (1975) (cit. on p. 105).

[214] D. W. Oxtoby, H. P. Gillis, and A. Campion, *Principles of Modern Chemistry*, 7th ed. (Brooks Cole, Belmont(CA), May 2011) (cit. on p. 108).

[215] J. Kang, H. Sahin, and F. M. Peeters, "Mechanical properties of monolayer sulphides: a comparative study between MoS_2, HfS_2 and TiS_3", Phys. Chem. Chem. Phys. **17**, 27742–27749 (2015) (cit. on p. 109).

[216] G. Q. Huang and Z. W. Xing, "Band-gap tunability and dynamical instability in strained monolayer and bilayer phosphorenes", J. Phys.: Condens. Matter **27**, 175006 (2015) (cit. on p. 110).

[217] R. Biele, E. Flores, J. R. Ares, C. Sanchez, I. J. Ferrer, G. Rubio-Bollinger, A. Castellanos-Gomez, and R. D'Agosta, "Strain-induced band gap engineering in layered TiS_3", Nano Research (2017) 10.1007/s12274-017-1622-3 (cit. on p. 114).

[218] M. Li, J. Dai, and X. C. Zeng, "Tuning the electronic properties of transition-metal trichalcogenides via tensile strain", Nanoscale **7**, 15385–15391 (2015) (cit. on p. 114).

[219] A. K. Geim and I. V. Grigorieva, "Van der Waals heterostructures", Nature **499**, 419–425 (2013) (cit. on p. 118).

[220] Y. Liu, N. O. Weiss, X. Duan, H.-C. Cheng, Y. Huang, and X. Duan, "Van der Waals heterostructures and devices", Nat. Rev. Mater. **1**, 16042 (2016) (cit. on p. 118).

[221] E. Pomerantseva and Y. Gogotsi, "Two-dimensional heterostructures for energy storage", Nat. Energy **2**, 17089 (2017) (cit. on p. 118).

[222] A. Allain, J. Kang, K. Banerjee, and A. Kis, "Electrical contacts to two-dimensional semiconductors", Nat. Mater. **14**, 1195–1205 (2015) (cit. on p. 118).

[223] D. Jena, K. Banerjee, and G. H. Xing, "2D crystal semiconductors: Intimate contacts", Nat. Mater. **13**, 1076–1078 (2014) (cit. on p. 119).

[224] M. Chhowalla, D. Voiry, J. Yang, H. S. Shin, and K. P. Loh, "Phase-engineered transition-metal dichalcogenides for energy and electronics", MRS Bulletin **40**, 585–591 (2015) (cit. on p. 119).

[225] Y. Gong, J. Lin, X. Wang, G. Shi, S. Lei, Z. Lin, X. Zou, G. Ye, R. Vajtai, B. I. Yakobson, H. Terrones, M. Terrones, B. Tay, J. Lou, S. T. Pantelides, Z. Liu, W. Zhou, and P. M. Ajayan, "Vertical and in-plane heterostructures from WS_2/MoS_2 monolayers", Nature Materials **13**, 1135–1142 (2014) (cit. on p. 119).

[226] J. Singh, *Physics of semiconductors and their heterostructures*, Electrical engineering series (McGraw-Hill, New York, 1993) (cit. on p. 119).

[227] G. Agostini and C. Lamberti, *Characterization of Semiconductor Heterostructures and Nanostructures* (Elsevier Science, Oxford, 2011) (cit. on p. 119).

[228] L.-Y. Gan, Q. Zhang, Y. Cheng, and U. Schwingenschlögl, "Two-dimensional ferromagnet/semiconductor transition metal dichalcogenide contacts: *p*-type Schottky barrier and spin-injection control", Phys. Rev. B **88**, 235310 (2013) (cit. on p. 120).

[229] N. Wu, Z. Yang, W. Zhou, H. Zou, X. Xiong, Y. Chen, and F. Ouyang, "Collective electronic behaviors of laterally heterostructured armchair MoS_2-NbS_2 nanoribbons", Journal of Applied Physics **118**, 084306 (2015) (cit. on p. 120).

[230] A. Di Bartolomeo, "Graphene Schottky diodes: An experimental review of the rectifying graphene/semiconductor heterojunction", Physics Reports **606**, 1–58 (2016) (cit. on p. 120).

[231] K.-A. N. Duerloo and E. J. Reed, "Structural Phase Transitions by Design in Monolayer Alloys", ACS Nano **10**, 289–297 (2016) (cit. on p. 120).

[232] Y. Matsuda, W.-Q. Deng, and W. A. Goddard, "Contact Resistance for "End-Contacted" Metal-Graphene and Metal-Nanotube Interfaces from Quantum Mechanics", The Journal of Physical Chemistry C **114**, 17845–17850 (2010) (cit. on p. 120).

[233] J. Kang, W. Liu, D. Sarkar, D. Jena, and K. Banerjee, "Computational Study of Metal Contacts to Monolayer Transition-Metal Dichalcogenide Semiconductors", Phys. Rev. X **4**, 031005 (2014) (cit. on p. 120).

[234] G. Eda, T. Fujita, H. Yamaguchi, D. Voiry, M. Chen, and M. Chhowalla, "Coherent Atomic and Electronic Heterostructures of Single-Layer MoS_2", ACS Nano **6**, 7311–7317 (2012) (cit. on pp. 120, 123).

[235] R. Kappera, D. Voiry, S. E. Yalcin, B. Branch, G. Gupta, A. D. Mohite, and M. Chhowalla, "Phase-engineered low-resistance contacts for ultrathin MoS_2 transistors", Nature Materials **13**, 1128–1134 (2014) (cit. on p. 120).

[236] X. Fan, P. Xu, D. Zhou, Y. Sun, Y. C. Li, M. A. T. Nguyen, M. Terrones, and T. E. Mallouk, "Fast and Efficient Preparation of Exfoliated 2H MoS_2 nanosheets by Sonication-Assisted Lithium Intercalation and Infrared Laser-Induced 1T to 2H Phase Reversion", Nano Letters **15**, 5956–5960 (2015) (cit. on p. 120).

[237] C. Huang, S. Wu, A. M. Sanchez, J. J. P. Peters, R. Beanland, J. S. Ross, P. Rivera, W. Yao, D. H. Cobden, and X. Xu, "Lateral heterojunctions within monolayer $MoSe_2$–WSe_2 semiconductors", Nature Materials **13**, 1096–1101 (2014) (cit. on p. 120).

[238] Z. Bai, T. Markussen, and K. S. Thygesen, "Electron transport across a metal/MoS_2 interface: dependence on contact area and binding distance", arXiv, 1–7 (2013) (cit. on p. 120).

[239] Z. Hu, S. Zhang, Y.-N. Zhang, D. Wang, H. Zeng, and L.-M. Liu, "Modulating the phase transition between metallic and semiconducting single-layer MoS_2 and WS_2 through size effects", Phys. Chem. Chem. Phys. **17**, 1099–1105 (2015) (cit. on p. 121).

[240] G. Sivaraman, F. A. L. de Souza, R. G. Amorim, W. L. Scopel, M. Fyta, and R. H. Scheicher, "Electronic transport along hybrid MoS_2 monolayers", The Journal of Physical Chemistry C **120**, 23389–23396 (2016) (cit. on p. 121).

[241] M. Brandbyge, J.-L. Mozos, P. Ordejón, J. Taylor, and K. Stokbro, "Density-functional method for nonequilibrium electron transport", Phys. Rev. B **65**, 165401 (2002) (cit. on p. 121).

[242] J. M. Soler, E. Artacho, J. D. Gale, A. Garcia, J. Junquera, P. Ordejón, and D. Sanchez-Portal, "The SIESTA method for *ab initio* order-N materials simulation", Journal of Physics: Condensed Matter **14**, 2745 (2002) (cit. on p. 121).

[243] N. Troullier and J. L. Martins, "Efficient pseudopotentials for plane-wave calculations", Phys. Rev. B **43**, 1993–2006 (1991) (cit. on p. 121).

[244] F. Ma, G. Gao, Y. Jiao, Y. Gu, A. Bilic, H. Zhang, Z. Chen, and A. Du, "Predicting a new phase (T") of two-dimensional transition metal dichalcogenides and strain-controlled topological phase transition", Nanoscale **8**, 4969–4975 (2016) (cit. on pp. 123–124).

[245] B. Radisavljevic, A. Radenovic, J. Brivio, V. Giacometti, and A. Kis, "Single-layer MoS_2 transistors", Nature Nanotechnology **6**, 147–150 (2011) (cit. on p. 124).

[246] Y.-C. Lin, H.-P. Komsa, C.-H. Yeh, T. Björkman, Z.-Y. Liang, C.-H. Ho, Y.-S. Huang, P.-W. Chiu, A. V. Krasheninnikov, and K. Suenaga, "Single-Layer ReS_2: Two-Dimensional Semiconductor with Tunable In-Plane Anisotropy", ACS Nano **9**, 11249–11257 (2015) (cit. on p. 125).

[247] M. Kan, J. Y. Wang, X. W. Li, S. H. Zhang, Y. W. Li, Y. Kawazoe, Q. Sun, and P. Jena, "Structures and Phase Transition of a MoS_2 Monolayer", The Journal of Physical Chemistry C **118**, 1515–1522 (2014) (cit. on pp. 125–126).

[248] Y. Katagiri, T. Nakamura, A. Ishii, C. Ohata, M. Hasegawa, S. Katsumoto, T. Cusati, A. Fortunelli, G. Iannaccone, G. Fiori, S. Roche, and J. Haruyama, "Gate-tunable atomically thin lateral MoS_2 schottky junction patterned by electron beam", Nano Letters **16**, 3788–3794 (2016) (cit. on p. 126).

[249] A. Nourbakhsh, A. Zubair, R. N. Sajjad, A. Tavakkoli K. G., W. Chen, S. Fang, X. Ling, J. Kong, M. S. Dresselhaus, E. Kaxiras, K. K. Berggren, D. Antoniadis, and T. Palacios, "MoS_2 field-effect transistor with sub-10 nm channel length", Nano Letters **16**, 7798–7806 (2016) (cit. on p. 126).

[250] Q. Tang and D.-e. Jiang, "Stabilization and band-gap tuning of the 1T-MoS_2 Monolayer by covalent functionalization", Chemistry of Materials **27**, 3743–3748 (2015) (cit. on p. 126).

[251] D. Çakır, H. Sahin, and F. M. Peeters, "Doping of rhenium disulfide monolayers: a systematic first principles study", Phys. Chem. Chem. Phys. **16**, 16771–16779 (2014) (cit. on p. 127).

[252] F. Raffone, C. Ataca, J. C. Grossman, and G. Cicero, "MoS_2 enhanced T-phase stabilization and tunability through alloying", The Journal of Physical Chemistry Letters **7**, 2304–2309 (2016) (cit. on p. 127).

[253] T. L. Tan, M.-F. Ng, and G. Eda, "Stable Monolayer Transition Metal Dichalcogenide Ordered Alloys with Tunable Electronic Properties", The Journal of Physical Chemistry C **120**, 2501–2508 (2016) (cit. on p. 127).

[254] Z. Cao, M. Harb, S. Lardhi, and L. Cavallo, "Impact of Interfacial Defects on the Properties of Monolayer Transition Metal Dichalcogenide Lateral Heterojunctions", The Journal of Physical Chemistry Letters, 1664–1669 (cit. on p. 131).

[255] H. Guo, N. Lu, J. Dai, X. Wu, and X. C. Zeng, "Phosphorene Nanoribbons, Phosphorus Nanotubes, and van der Waals Multilayers", J. Phys. Chem. C **118**, 14051–14059 (2014) (cit. on p. 135).

[256] G. G. Tibbetts, "Why are carbon filaments tubular?", J. Cryst. Growth **66**, 632–638 (1984) (cit. on p. 135).

[257] D. H. Robertson, D. W. Brenner, and J. W. Mintmire, "Energetics of nanoscale graphitic tubules", Phys. Rev. B **45**, 12592–12595 (1992) (cit. on p. 135).

[258] T. W. Odom, J.-L. Huang, P. Kim, and C. M. Lieber, “Structure and Electronic Properties of Carbon Nanotubes”, J. Phys. Chem. B **104**, 2794–2809 (2000) (cit. on p. 143).

List of Publications

Published

[P1] A. Yimamu, S. Beysen, D. Peng, and Y. Aierken, "Mixed-solvent thermal synthesis and magnetic properties of flower-like microstructured nickel", Particuology **10**, 392–396 (2012).

[P2] Y. Aierken, H. Sahin, F. Iyikanat, S. Horzum, A. Suslu, B. Chen, R. T. Senger, S. Tongay, and F. M. Peeters, "Portlandite crystal: Bulk, bilayer, and monolayer structures", Phys. Rev. B **91**, 245413 (2015) (cit. on p. 75).

[P3] Y. Aierken, D. Çakır, C. Sevik, and F. M. Peeters, "Thermal properties of black and blue phosphorenes from a first-principles quasiharmonic approach", Phys. Rev. B **92**, 081408 (2015) (cit. on pp. 33, 35).

[P4] Y. Aierken, O. Leenaerts, and F. M. Peeters, "Defect-induced faceted blue phosphorene nanotubes", Phys. Rev. B **92**, 104104 (2015) (cit. on p. 131).

[P5] M. M. Alyörük, Y. Aierken, D. Çakır, F. M. Peeters, and C. Sevik, "Promising Piezoelectric Performance of Single Layer Transition-Metal Dichalcogenides and Dioxides", The Journal of Physical Chemistry C **119**, 23231–23237 (2015) (cit. on p. 42).

[P6] Y. Aierken, D. Çakır, and F. M. Peeters, "Strain enhancement of acoustic phonon limited mobility in monolayer TiS_3", Phys. Chem. Chem. Phys. **18**, 14434–14441 (2016) (cit. on p. 103).

[P7] Y. Aierken, O. Leenaerts, and F. M. Peeters, "A first-principles study of stable few-layer penta-silicene", Phys. Chem. Chem. Phys. **18**, 18486–18492 (2016) (cit. on p. 90).

[P8] Y. Aierken, O. Leenaerts, and F. M. Peeters, “Intrinsic magnetism in penta-hexa-graphene: A first-principles study”, Phys. Rev. B **94**, 155410 (2016) (cit. on p. 53).

Under Review

[P9] Y. Aierken, C. Sevik, O. Gülseren, F. M. Peeters, and D. Çakır, “In pursuit of barrierless transition metal dichalcogenides lateral heterojunctions”, submitted to PRB (cit. on p. 118).

[P10] Y. Aierken, C. Sevik, O. Gülseren, F. M. Peeters, and D. Çakır, “MXenes/graphene heterostructures for Li battery applications: a first principles study”, submitted to Journal of Materials Chemistry A (cit. on p. 59).

Curriculum vitae

YIERPAN AIERKEN

PERSONAL INFORMATION

Date of birth: June 9th 1986
Place of birth: Xinjiang, China
Gender: Male
Nationality: Chinese
Ethnic group: Uighur

Phone: +32-0485324566 (Cell)
E-mail: erpan14ar@gmail.com
Address: Condensed Matter Theory
Groenenborgerlaan 171
2020 Antwerp, Belgium

EDUCATION BACKGROUND

BS **University of Science and Technology Beijing, P. R. China** **Sept. 2006 - July 2010**
School of Materials Science and Engineering. Bachelor Degree in Materials Physics.

MS **University of Camerino, Italy** **Oct. 2010 - April 2013**
Department of Physics. Master Degree in Physics.

PhD **University of Antwerp, Belgium** **Dec. 2013 - Until now**
Condensed matter theory group, Department of Physics. PhD in Physics (Expected Dec. 2017).

THESES

Bachelor thesis

Title: A study on the anisotropies of Cobalt-based Thin Films in high performance magnetic sensor.
Supervisor: Professor HaiCheng Wang

Master thesis

Title: Effect of temperature on correlation in strong correlated two-dimensional quantum electron liquid.
Supervisor: Professor David Neilson

PhD thesis

Title: First-principles study of novel two-dimensional crystals and their properties.
Supervisor: Professor Francois Peeters

PUBLICATIONS

1. A. Yimamu, S. Beysen, D. Peng, and **Y. Aierken**: " Mixed-solvent thermal synthesis and magnetic properties of flower-like microstructured nickel ", Particuology 10, 392–396 (2012).
2. **Y. Aierken**, H. Sahin, F. Iyikanat, S. Horzum, A. Suslu, B. Chen, R. T. Senger, S. Tongay, and F. M. Peeters: " Portlandite crystal: Bulk, bilayer, and monolayer structures ", Phys. Rev. B 91, 245413 (2015).
3. **Y. Aierken**, D. Çakır, C. Sevik, and F. M. Peeters: "Thermal properties of black and blue phosphorenes from a first-principles quasiharmonic approach", Phys. Rev. B 92, 081408(R) (2015).
4. **Y. Aierken**, O. Leenaerts, and F. M. Peeters: "Defect-induced faceted blue phosphorene nanotubes", Phys. Rev. B 92, 104104 (2015).
5. M. M. Alyörük, **Y. Aierken**, D. Çakır, F. M. Peeters, and C. Sevik: "Promising Piezoelectric Performance of Single Layer Transition-Metal Dichalcogenides and Dioxides", J. Phys. Chem. C 119, 23231-23237 (2015).
6. **Y. Aierken**, D. Çakır, and F. M. Peeters: "Strain enhancement of acoustic phonon limited mobility in monolayer TiS_3", Phys. Chem. Chem. Phys. 18, 14434-14441 (2016).

7. **Y. Aierken**, O. Leenaerts, and F. M. Peeters: "A first-principles study of stable few-layer penta-silicene", Phys. Chem. Chem. Phys. 18, 18486-18492 (2016).
8. **Y. Aierken**, O. Leenaerts, and F. M. Peeters: "Intrinsic magnetism in penta-hexa-graphene: A first-principles study", Phys. Rev. B 94, 155410 (2016).

UNDER REVIEW

9. **Y. Aierken**, D. Çakır, and F. M. Peeters: "Impact of doping on the electrical transport properties of transition metal dichalcogenides lateral heterojunctions" (submitted to nanoscale) (2017)
10. **Y. Aierken**, D. Çakır, and F. M. Peeters: "MXenes/graphene heterostructures for Li battery applications: a first principles study" (finalizing) (2017)

CONFERENCE AND SCHOOLS

- 45th IFF Spring School: Computing Solids: " Models, *ab initio* methods and supercomputing ", Jülich, Germany, March 2014.
- **Y. Aierken**, O. Leenaerts, and F. M. Peeters: "Defect-induced faceted blue phosphorene nanotubes" poster presentations on:
  - Hands-on workshop density-functional theory and beyond: " First-principles simulations of molecules and materials ", Berlin, Germany, July 2015.
  - Psi-k 2015 Conference: " *ab initio* (from the electronic structure) calculations processes in materials ", San Sebastian, Spain, September 2015.

LANGUAGES

English (good), Mandarin (native), Uighur (mother tongue)

COMPUTER SKILLS

Fortran, Python, Mathematica, GitHub, Latex, Linux, OS X, Windows
Simulation packages: VASP, Quantum espresso, Siesta (Transiesta), Phonopy, Lammps, Atomic Simulation Environment, QuantumWise, Material studio. AiiDA high throughput computations

HONORS AND AWARDS

- Academic Progress Award 2005
- Outstanding Self-financed Students Award from Xinjiang Province, China 2012, 2014-2015
- Master Students Scholarship (borsa di studio) 2010-2013
- FWO Grant for participation in an international workshop or course 2015
- FWO Grant for participation in an international conference 2015

OTHER ACTIVATES AND INTERESTS

- The Champion band of the Outstanding Star Music Competition on campus. 2006
- Outstanding Performance Prize in YAMAHA Asian Beat Music competition. 2008
- The Champion team of the College Basketball Tournament. 2008